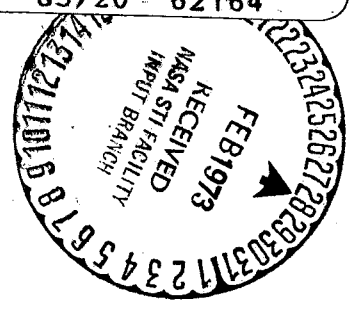


NASA CR-112137
GDCA-HAB-73-005
CONTRACT NAS 1-11111

(NASA-CR-112137) - MONITORING OF AIR POLLUTION BY SATELLITES (MAPS), PHASE 1
Final Report, 21 Sep. 1971 - 20 Mar. 1972 (General Dynamics/Astronautics)
195 p HC \$11.75

N73-17682
Unclas
G3/20 62164
CSCL 04B



MONITORING OF AIR POLLUTION BY SATELLITES (MAPS)

PHASE I
FINAL REPORT

GENERAL DYNAMICS
Convair Aerospace Division

Reproduced by
**NATIONAL TECHNICAL
INFORMATION SERVICE**
US Department of Commerce
Springfield, VA. 22151

195 pp

Final Report
MONITORING OF AIR POLLUTION BY SATELLITES (MAPS)
(Phase I)

April 1972

Prepared under Contract No. NAS1-11111
by

GENERAL DYNAMICS CORPORATION
Convair Aerospace Division
San Diego, California
for
Langley Research Center
NATIONAL AERONAUTICS AND SPACE ADMINISTRATION

C

J

Preceding page blank

FOREWORD

This is a report on work performed during Phase I of the MAPS program from 21 September 1971 to 20 March 1972. The contract was administered by NASA-Langley Research Center under the AAFE program and monitored by Dr. J. M. Russell, III.

The principal investigator was C. B. Ludwig, the co-investigators were W. Malkmus, M. Griggs, and E. R. Bartle. The following personnel have contributed to various subjects: W. Marggraf, J. Wang, C. N. Abeyta and R. M. Smith. Fruitful discussions were held with L. L. Acton and G. D. Hall of Convair Aerospace.

PRECEDING PAGE BLANK NOT FILMED

ABSTRACT

The present study has provided results upon which the design of a satellite "Remote Gas Filter Correlation (RGFC)" instrument can be based. Although a final decision about the feasibility of measuring some of the pollutants with the required accuracy is still outstanding and subject to further theoretical and experimental verifications, viable concepts are presented which permit the initiation of the design phase. The pollutants which are of concern in the troposphere and stratosphere were selected. The infrared bands of these pollutants were identified, together with the bands of interfering gases and the line parameters of the pollutants as well as interfering gases were generated through a computer program. Radiative transfer calculations (line-by-line) were made to establish the radiation levels at the top of the atmosphere and the signal levels at the detector of the RGFC instrument. Based upon these results the channels for the RGFC were selected. Finally, the problem areas, which need further investigations, were delineated and the supporting data requirements were established.

CONTENTS

FOREWORD	iii
ABSTRACT	iv
ILLUSTRATIONS	viii
TABLES	xiv
LIST OF SYMBOLS	xv
SUMMARY	xviii
1 INTRODUCTION	1
2 MODEL INPUT (Task 1)	4
2.1 THEORY OF SYMMETRIC AND NEARLY SYMMETRIC TOP MOLECULES	4
2.2 DESCRIPTION OF SYM TOP PROGRAM	7
2.3 RESULTS AND COMPARISON WITH LABORATORY DATA	8
2.3.1 Carbon Monoxide	8
2.3.2 Carbon Dioxide	11
2.3.3 Sulfur Dioxide	14
2.3.4 Nitrogen Dioxide	15
2.3.5 Nitric Oxide	17
2.3.6 Ammonia	18
2.3.7 Nitrous Oxide	25
2.3.8 Formaldehyde	28
2.3.9 Methane	28
2.3.10 Water	30
REFERENCES	30
3 MODEL STUDIES FOR GASEOUS POLLUTANTS (Task 2)	32
3.1 THEORY OF RADIATIVE TRANSFER	32
3.2 DESCRIPTION OF GAS FILTER CORRELATION INSTRUMENT	36
3.3 DESCRIPTION OF THE POLAYER PROGRAM	38
3.3.1 The Basic POLAYER Program	38
3.3.2 Test Calculation with POLAYER for the Solar Spectrum at 4.65 μ	39
3.3.3 Versions of POLAYER	41
3.3.4 Future Development of POLAYER	43
3.4 RESULTS	44

3.4.1	Carbon Monoxide	44
3.4.1.1	Comparison with Band Model Calculations	46
3.4.1.2	Influence of Stratospheric CO	46
3.4.1.3	Influence of Water Vapor	46
3.4.1.4	Influence of Stratospheric H ₂ O on CO Measurements	49
3.4.1.5	Model Calculations for CO with H ₂ O and N ₂ O	50
3.4.1.6	Model Calculations for CO with H ₂ O, N ₂ O, CO ₂ and O ₃	53
3.4.1.7	Comparison Between DV and Radiance Measurements	55
3.4.1.8	The Radiance as a Function of Sun Angle	55
3.4.1.9	ΔV as a Function of Sun Angle, Ground Emissivity and Temperature	60
3.4.1.10	Influence of Variable Ground Emissivity on ΔV	60
3.4.2	Carbon Dioxide	67
3.4.2.1	Model Calculations for CO ₂ at 1.6 μ	67
3.4.2.2	Model Calculations for CO ₂ at 2.1 μ	67
3.4.3	Sulfur Dioxide	69
3.4.3.1	Model Calculations for SO ₂ at 8.6 μ	69
3.4.3.2	Model Calculations for SO ₂ at 4 μ	69
3.4.4	Nitrogen Dioxide	70
3.4.4.1	Model Calculations for NO ₂ at 7.6 μ	70
3.4.4.2	Model Calculations for NO ₂ at 3.3 μ	70
3.4.5	Nitric Oxide	70
3.4.6	Ammonia	71
3.4.6.1	Model Calculations for NH ₃ at 10.5 μ	71
3.4.6.2	Model Calculations for NH ₃ at 3 μ	71
3.4.7	Formaldehyde	72
	REFERENCES	72
4	MODEL STUDIES FOR AEROSOL DETECTION (Task 3)	73
4.1	EARTH-ORIENTED OBSERVATIONS	73

4.1.1	Radiance Observations	73
4.1.2	Polarization Observations	76
4.1.3	Comparison of Radiance and Polarization Observations	80
4.1.4	Observations Over Land or Clouds	81
4.1.5	Problem Areas	87
	4.1.5.1 Sun Glitter	87
	4.1.5.2 Aerosol Properties	88
	4.1.5.3 Non-Lambertian Surfaces	88
	4.1.5.4 Surface Reflectance Gradient	88
4.2	SUN-ORIENTED OBSERVATIONS OF AEROSOLS	89
	4.2.1 Cloud Interference	89
	4.2.2 Atmospheric Attenuation	91
	REFERENCES	95
5	INVESTIGATION OF RGFC INSTRUMENT PARAMETERS (Task 4)	97
5.1	OPTIMIZATION PROCEDURE	97
5.2	LABORATORY CALIBRATION PROCEDURE	103
5.3	IN-FLIGHT CALIBRATION	115
5.4	INVESTIGATION OF RATIO TECHNIQUES	116
	5.4.1 Ratio of Signal Difference of One-Cell Pair to Signal	116
	5.4.2 Ratio of Signal Difference of Two-Cell Pairs	126
6	STUDY OF MISSION REQUIREMENTS (Task 5)	132
6.1	ATMOSPHERIC TEMPERATURE AND PRESSURE PROFILE	132
	6.1.1 Temporal and Spatial Variations of Temperature Profiles in the Real Atmosphere	132
	6.1.2 The Accuracy of Temperature Data	140
	6.1.3 Summary of Requirements for Atmospheric Temperature and Pressure Profile Data	143
6.2	WATER VAPOR PROFILE	150
	6.2.1 Temporal and Spatial Variations of Water Vapor Profiles in the Real Atmosphere	150
	6.2.2 Water Vapor from SIRS (NIMBUS IV)	154
6.3	CLOUD COVER	154
6.4	THEORETICAL SENSITIVITY OF GFC INSTRUMENT TO UNCERTAINTIES IN ATMOSPHERIC PARAMETERS	157

ILLUSTRATIONS

2-1	Monochromatic transmissivity of the R0 and R1 lines of the first overtone of CO for $u=9.0$ cm-atm, $T=300^\circ\text{K}$ and $p=1$ atm.	9
2-2	Degraded transmissivity (slit width of 0.11 cm^{-1} of the R0 and R1 lines of the first overtone of CO for $u=9.0$ cm-atm, $T=300^\circ\text{K}$ and $p=1$ atm (calculated spectrum solid, laboratory spectrum ⁽⁶⁾).	10
2-3	Monochromatic transmissivity of the band system at 1.6μ of CO_2 between 6330 and 6336 cm^{-1} for $u=800$ cm-atm, $p=0.5$ atm and $T=296^\circ\text{K}$.	13
2-4	Degraded transmissivity (slit width of 0.08 cm^{-1}) of spectrum from Figure 2-3 (calculated spectrum solid. laboratory spectrum ⁽⁸⁾ dashed).	13
2-5	Monochromatic transmissivity of the $\text{SO}_2-\nu_1$ band between 1140 and 1180 cm^{-1} (showing band center and R-branch maximum). The conditions are the same as in Figure 2-6.	16
2-6	Degraded transmissivity (slit width is 1 cm^{-1}) from Fig. 2-5 for $u= .577$ cm atm $p_e=1.59$ atm and $T=298^\circ\text{K}$ (calculated spectrum solid, laboratory spectrum dashed).	16
2-7	Monochromatic transmissivity of R(5) and R(5) lines of fundamental band of NO between 1896 and 1898 cm^{-1} . The conditions are the same as in Figure 2-8.	19
2-8	Degraded transmissivity (slit width is 0.13 cm^{-1} from Figure 2-7 for $u=0.263$ cm-atm, $p=200$ torr and $T=300^\circ\text{K}$ (calculated spectrum solid, laboratory spectrum ⁽²¹⁾ dashed).	20
2-9	Monochromatic transmissivity of portions of the 10.5μ band system of NH_3 . A segment of the Q-branch between 900 and 950 cm^{-1} is shown on the left hand side and a segment of the R-branch between 1150 and 1200 cm^{-1} on the right hand side. The conditions are the same as in Figure 2-10.	21
2-10	Degraded transmissivity (slit width of 8 cm^{-1}) of a portion of the 10.5μ band system of NH_3 between 900 and 1260 cm^{-1} for $u=1.617$ cm atm _{STP} $p_e=4185$ torr and $T=299^\circ\text{K}$ (calculated spectrum solid, laboratory spectrum ⁽²³⁾ dashed).	23

2-11	Monochromatic transmissivity of NH_3 between 3100 and 3700 cm^{-1} for $u=6.23$ cm atm _{STP} , $p_e = 5090$ torr, and $T=299^\circ\text{K}$.	24
2-12	Degraded transmissivity (slit width of 50 cm^{-1}) from Figure 2-11. Calculated spectrum solid; laboratory spectrum ⁽²³⁾ dashed.	24
2-13	Monochromatic transmissivity of N_2O between 2204 and 2206 cm^{-1} for $u=0.31$ cm atm, $p=2$ torr, and $T=220^\circ\text{K}$.	27
2-14	Degraded transmissivity (slit width of 0.05 cm^{-1}) of spectrum from Figure 2-13 (calculated spectrum solid, laboratory spectrum ⁽²⁷⁾ Dashed).	27
2-15	Monochromatic transmissivity (calculated) of HCHO between 2880 and 2900 cm^{-1} (solid curve). Degraded transmissivity (measured by Hanst ⁽³⁰⁾ for $u=0.08$ cm atm, $p=0.0079$ atm and $T=300^\circ\text{K}$ (dashed curve).	29
3-1	Upwelling radiation at the top of atmosphere. Contributions from reflected sun radiation $E_R(\omega)$, atmospheric scattering $E_s(\omega)$, and thermal radiation $E_G(\omega)$. Ground temperature = 300°K , sun zenith angle $=45^\circ$, particulate matter according to Elterman 1968.	35
3-2	Transmissivity of atmosphere between 2135 and 2165 cm^{-1} . Upper trace calculated monochromatically, lower trace calculated with slit function (dashed), experimental curve solid line.	40
3-3	Flow diagram of SYMTOP/POLAYER logic.	43
3-4	Comparison of linear and quadratic interpolation for the line-by-line calculations.	45
3-5	Temperature, pressure and water vapor profiles used in the model calculations.	47
3-6	Signal difference vs. CO concentration in troposphere for different amounts of water vapor.	48
3-7	Signal difference vs. CO concentration with and without normal water vapor, indicating "negative correlation".	51
3-8	Water vapor distribution according to Gutnick.	52
3-9	Signal difference vs. CO in the presence of N_2O and H_2O .	54
3-10	Normalized signal difference and radiance vs. CO concentration with and without water vapor.	56
3-11	Radiance at the top of atmosphere vs. ground emissivity for different sun zenith angles at a ground temperature of 270K and CO concentration = 0.1 ppm.	57

3-12	Radiance at the top of atmosphere vs. ground emissivity for different sun zenith angles at a ground temperature of 300K and CO concentration = 0.1 ppm.	58
3-13	Radiance at the top of atmosphere vs. ground emissivity for different sun zenith angles at a ground temperature of 330K and CO concentration = 0.1 ppm.	59
3-14	Radiance vs. ground temperature for $\epsilon = 1.0$ and $\epsilon = 0.8$ for various sun zenith angles.	61
3-15	Signal difference vs. CO concentration for different sun zenith angles and $\epsilon = 0.8$ and $\epsilon = 1.0$ at ground temperature = 270K.	62
3-16	Signal difference vs. CO concentration for different sun zenith angles and $\epsilon = 0.8$ and $\epsilon = 1.0$ at ground temperature = 300K.	63
3-17	Signal difference vs. CO concentration for different sun zenith angles and $\epsilon = 0.8$ and $\epsilon = 1.0$ at ground temperature = 330K.	64
3-18	Signal difference vs. ground temperature at $\epsilon = 1.0$ and $\epsilon = 0.8$ for various sun angles and for CO concentration = 0.1 ppm.	65
3-19	Signal difference vs. CO ₂ concentration for sun zenith angle = 30°, ground reflectivity = 0.02, ground temperature = 300K.	68
4-1	Normalized upward radiance vs sun angle as function of wavelength.	75
4-2	Normalized upward radiance vs aerosol mass loading as function of sun angle.	77
4-3	Polarization vs aerosol content as function of nadir look angle.	79
4-4	Reflected radiance vs albedo for different aerosol contents.	82
4-5	Reflected radiance vs aerosol content as function of albedo.	84
4-6	Polarization vs albedo for different aerosol contents.	85
4-7	Polarization vs aerosol content as function of albedo.	86
4-8	Schematic of occultation experiment.	90
4-9	Transmission vs aerosol content as function of wavelength (grazing altitude 10 km).	93
4-10	Transmission vs aerosol content as function of wavelength (grazing altitude 15 km).	94
5-1	Normalized filter function used in the model calculations for CO, corresponding to OCLI filter 14-8806-760.	99

5-2	Optimization of instrument response as a function of CO concentration in instrument cell. Instrument parameters $l = 1$ cm, $p_T = 1$ atm, $T_G = 288.16^\circ\text{K}$, $c(\omega) = c'(\omega)$, given by Fig. 5-1. Atmospheric parameters: CO concentration in the troposphere = 0.1 ppm, ground temperature = 288.16°K , lapse rate = -6.5°C/km . Arrow points to maximum response, i.e., CO concentrations = 0.35, corresponding to a cell transmission of 0.83.	100
5-3	Sensitivity of instrument as a function of CO concentration in the troposphere with three CO concentrations in instrument cell as a parameter: 0.05, 0.35 and 1.00. Other instrument and atmospheric parameters same as in Fig. 5-2.	101
5-4	Sensitivity of instrument as a function of total pressure in instrument cell with nine CO concentrations in the troposphere. The figures on the curves refer to the multiplier, with which the concentration of 0.1 ppm in the troposphere is multiplied. Arrows refer to maximum sensitivity.	104
5-5	Sensitivity of instrument as a function of CO concentration in the troposphere for two different slit functions. The lower curve is for the slit function given in Fig. 5-1, the upper curve for a square slit function. If the upper curve is corrected to account for the larger area under the slit function, the points marked as (x) are obtained.	107
5-6	Sensitivity of instrument as a function of optical thickness in the instrument "sample" (calibration) cell.	109
5-7	Three normalized filter functions used in the computer simulation studies.	111
5-8	Sensitivity of the instrument to different ground temperatures and sun zenith angles as a function of ground emissivity at 4.6μ for zero concentration of CO in the troposphere.	117
5-9	Sensitivity of the instrument for the same conditions as in Fig. 5-8, but referenced to DV for 0.1 ppm CO concentration.	118
5-10	DV and DV/V as a function of CO concentration in the troposphere with and without water vapor.	119
5-11	DV/V as a function of CO concentration in the troposphere for different ground temperatures and variations of atmospheric temperatures and water vapor concentration.	121
5-12	DV/V as a function of ground temperature for various CO concentrations in the atmosphere.	122

5-13	DV as a function of V for different conditions of CO concentration, surface temperature, atmospheric temperature and water profile perturbations, surface emissivities, and sun zenith angles.	123
5-14	Perturbation of DV and V due to changes in the atmospheric temperature profile by $\pm 5^\circ\text{K}$ and in the water vapor profile by $\pm 50\%$ in mixing ratio.	125
5-15	Sensitivity of instrument as a function of total pressure in the instrument cell for different concentrations of CO in the troposphere, having a profile according to B37 (see Table 5-6).	127
5-16	Sensitivity of instrument as a function of total pressure in the instrument cell for different concentrations of CO in the troposphere, having a profile according to B36 (see Table 5-6).	128
5-17	Sensitivity of the instrument as a function of the total optical thickness of CO for the three profiles B20, B37 and B36, using cell pressures of 1 and 0.4 atm.	130
5-18	The ratio of DV as a function of total optical thickness for three CO concentration profiles (see Fig. 5-17, using two cell pairs with pressures of 1 and 0.4 atm.	131
6-1	Temperature and temperature gradient at 500 mb level for February 1971 in San Diego, California at 0000 and 1200 Z.	133
6-2	Temperature and temperature gradient at 500 mb level for February 1971 in Washington, D. C. at 0000 and 1200 Z.	134
6-3	Temperature and temperature gradient at 500 mb level for July 1970 in San Diego, California at 0000 and 1200 Z.	135
6-4	Constant pressure chart at 500 mb level for February 1, 1971 at 1200 Z.	138
6-5	Temperature spatial distribution for February 1, 1971.	139
6-6	Variability of relative humidity, temperature at 700 mb and thickness of 700-500 mb layer for 48 hours.	151
6-7	Variability of temperature and water vapor mixing ratio for selected days in February 1971 in San Diego, California.	152
6-8	Signal difference vs. fractional cloud cover for different amounts of CO concentration. Cloud altitude = 1 km.	155
6-9	Signal difference vs. cloud altitude for 100% cloud cover for different amounts of CO concentration.	156

6-10	Ratios of DV/V vs. CO concentration for A (ground temp. = 300K), B (0.6 cloud at 1 km, T = 291K), C (ground temp. = 285, cloud at 1 km, T = 284.9K), D (cloud at 2 km, T = 278.4K), E (cloud at 3 km, T = 271.8K), F (ground temp. = 270K, cloud at 4 km, T = 265.4K).	158
6-11	Details of pressure and temperature profile in the troposphere.	159
6-12	Signal difference vs. CO concentration for ground temperatures of 300 and 285K and atmospheric temperature variations.	160
6-13	Radiance vs. CO concentration for same conditions as Figure 6-12.	161
6-14	Signal difference vs. CO concentration for different water vapor concentrations and different ground temperatures.	162
6-15	Signal difference change per degree change per layer vs. altitude for no water and with water (Gutnick) for CO concentration of 0.2 ppm and ground temp. = 300K.	164

TABLES

1	Gases which are of Concern in the Troposphere and Stratosphere	xviii
2	Infrared Bands of Pollutants and Interfering Gases	xx
3	Line Parameters Generated by SYMTOP for Pollutants and Interfering Gases	xxii
4	Model Calculations Performed with POLAYER	vii
5	Channels Selected for the GFC Instrument	xxvi
6	Problem Areas which Need Further Investigation	xxvii
7	Supporting Data Requirements	xxix
2-1	Types of Molecules Considered in Atmosphere	5
3-1	Difference of Signal Changes Due to CO with and without Water Vapor in the Stratosphere	50
3-2	Signal Change for CO in the Presence of the Interfering Molecules H ₂ O and N ₂ O	53
3-3	Signal Change for CO for Varying and Constant Ground Emissivity	66
3-4	Signal Change for NO as a Function of Concentration	71
5-1	Effect of Instrument Cell Temperature Variations	102
5-2	Effects of Lab Calibration Applied to Real Atmosphere	110
5-3	Effects of Lab Calibration Applied to Real Atmosphere	113
5-4	Effects of Lab Calibration Applied to Real Atmosphere	114
5-5	Signal Change of CO for the Calibration Temperatures	115
5-6	CO Concentration for 3 Distributions	126
6-1	Verification of NMC Operational Temperature Analysis	145

LIST OF SYMBOLS

A_o	Area of entrance pupil
A	Rotational constant
B	Rotational constant
B_N	Ratio of self-broadening to nitrogen broadening efficiency
C	Rotational constant
$Ch(\theta)$	Chapman function describing the path of solar radiation through the atmosphere for sun zenith angles θ greater than 60° .
$C(\omega)$	Generalized instrument response function of the GFC channel containing gas cell.
$C'(\omega)$	Generalized instrument response function of the GFC channel containing reference cell.
c	Concentration
E	Upwelling radiance
E_G	Thermal radiation of ground and atmosphere
E_R	Solar radiation reflected from ground
E_ϕ	Solar radiation scattered by the atmosphere without having been reflected by the ground.
$E_{R\phi}$	Solar radiation reflected from ground outside the field of view and scattered by the atmosphere into the field of view.
F	Lower energy level for a given transition
$F_v(J, K)$	Rotational energy levels
$f(\theta)$	Equals $\sec \theta$ for $0 \leq \theta \leq 60^\circ$ and $Ch(\theta)$ for $\theta > 60^\circ$
H_s	Sun irradiance at the top of the atmosphere
h	Altitude of satellite
J	Rotational quantum number
K	Rotational quantum number

LIST OF SYMBOLS

$k(\omega)$	Monochromatic absorption coefficient in $\text{cm}^{-1} \text{atm}^{-1}$
l	Instrument cell length
n	Number of scatterers
N°	Blackbody radiance
p	Partial pressure of pollutant gas
p_N	Partial pressure of nitrogen gas
p_T	Total pressure
p_e	Equivalent pressure, defined by Eq. (5-5)
R_o	Instrument responsivity, wave number independent
S	Line strength
T	Temperature
T_C	Temperature of calibration source
T_G	Temperature of ground
u	Optical depth in cm atm
V	Signal voltage
$\Delta V, DV$	Signal voltage difference of gas and reference channels
z	Altitude
α	Line half width
γ	Function of sun zenith angle = $1 + f(\theta)$
ϵ	Emissivity
θ	Sun zenith angle
κ	Asymmetry parameter
κ_i	Extinction coefficient for species i
λ	Wavelength
μ	Micrometer = 10^{-4} cm
ν	Symbol for transition
σ	Scattering cross section

LIST OF SYMBOLS

τ	Transmissivity through atmosphere = $\tau_o \tau_p$
τ_o	Transmissivity through atmosphere due to normal constituents only.
τ_p	Transmissivity through atmosphere due to pollutant species only.
τ_G	Transmissivity through gas cell of GFC instrument
τ_A	Transmissivity through reference cell of GFC instrument
Ω	Solid angle in steradians
ω	Wavenumber in cm^{-1}

SUMMARY

The results of the first phase of the MAPS program entitled "Experiment Definition Phase" are summarized in seven Tables.

Table 1: Gases which are of concern in the troposphere and stratosphere.

The gases given in this table have been selected on the basis of our work conducted for NASA and reported in CR-1380 (July 1969) and in its sequel, "Air Pollution Detection by Satellites" (to be published soon) and also on the basis of the study conducted by the Norfolk Working Group whose results were reported in the

Table 1. Gases which are of Concern in the Troposphere and Stratosphere

	Troposphere	Stratosphere
C-compounds (Inorganic)	CO ₂ , CO	CO ₂ , CO
S-compounds	SO ₂ , H ₂ S	SO ₂
N-compounds	NO, NO ₂ , NH ₃	NO, NO ₂ , N ₂ O, HNO ₃ NH ₃
HC-compounds	HCHO, PAN, CH ₄	CH ₄ , <HC>
Oxidants	O ₃	O ₃
Halogens	I ₂ , HF, Br ₂	
Water Vapor		H ₂ O
Particulates	Total Aerosol Content	Layered Aerosol Content

NASA publication SP-285 (1971). The regions of the atmosphere in which the pollutants are of concern are the troposphere and stratosphere. Two distinct observational modes apply to these two regions. For the troposphere, only a nadir experiment appears to be practical, while for the stratosphere, only an occultation experiment appears to be applicable. Although the task description of Phase I of NAS1-11111 included the pollutant modeling of both the troposphere and stratosphere, time and funding limitations have made it impossible for us to include the stratospheric modeling. In addition, the sensor and mission requirements for a sun occultation experiment are so different that a separate development is warranted. (This subject will be pursued further in Phase II).

The following discussions are limited to the nadir observations. Of the 14 gases listed for the troposphere, the halogens, O_3 , PAN and H_2S have not been included in our model studies, because the concentrations and/or the band strengths of these pollutants (except O_3) are so low as to make a remote measurement from satellites extremely difficult. To observe O_3 in the troposphere in a nadir experiment is also nearly impossible because of the stratospheric ozone layer.

Table 2: List of infrared bands of pollutants and interfering gases.

Seven gaseous pollutants of importance in the troposphere were investigated. The active infrared rotation vibration bands of suitable intensity were selected and the transitions of the interfering species were identified and listed in matrix form. It is readily apparent that the normal atmospheric constituents CO_2 , N_2O , CH_4 and H_2O are present in almost every spectral region where pollutants are active. In addition, some isotopes and ozone are also interfering. The solar lines

Table 2. Infrared Bands of Pollutants and Interfering Gases

	λ	CO ₂	CO	SO ₂	NO ₂	NH ₃	NO	CH ₂ O	N ₂ O	CH ₄	H ₂ O	HDO	H ₂ O ¹⁸	O ₃	Solar Lines
CO ₂	1.6	$3\nu_1 + \nu_3$								$2\nu_3$	$2\nu_2 + \nu_3$				Fe, C, Ni, S, Si, Ti, Na, P, Mg
	2.1	$2\nu_1 + \nu_3$									$\nu_1 + \nu_2$ $\nu_2 + \nu_3$ $3\nu_2$				Fe, Ca, Ni, Si
CO	4.6	$\nu_1 + \nu_2$ $2\nu_1 - \nu_2$	0-1						ν_3		ν_2 $\nu_3 - \nu_2$ $\nu_1 - \nu_2$			$2\nu_1$	
	2.3		0-2							$\nu_3 + \nu_4 (?)$	ν_1, ν_3	$3\nu_2 (?)$ $\nu_1 + \nu_2$			Fe, Ti, Na, P, Mg, C, Ni, S, Si
SO ₂	8.6			ν_1					$2\nu_2$	(?)	ν_2	ν_2	ν_2	ν_3	
	4			$\nu_1 + \nu_3$					$\nu_1 + 2\nu_2$ $2\nu_1$	few lines					Si, Ca, Na
NO ₂	7.6				ν_1				ν_1	ν_4	ν_2	ν_2	ν_2		
	3.4				$\nu_1 + \nu_3$					ν_3	$2\nu_2$	$\nu_1, 2\nu_2$			Ca
NH ₃	10.5	$\nu_3 - 2\nu_2$ $\nu_3 - \nu_1$				ν_2			$2\nu_2, \nu_1$	(?)	ν_2	ν_2	ν_2	ν_3	
	3.0	$3\nu_2 + \nu_3$ $-\nu_2$				ν_1			$\nu_1 + \nu_3$ $2\nu_2 + \nu_3$	ν_3	ν_1, ν_3 $2\nu_2$				Si, Fe, Ca, Ti, C
NO	5.3	$3\nu_2^1$	0-1				0-1				ν_2				
HCHO	3.5							ν_4	$2\nu_2 + \nu_3$	$2\nu_4, \nu_3$	$2\nu_2$	$\nu_1, 2\nu_2$			Mg, Si, Ti, Fe

are of importance only at the shorter wavelengths. Their line position and strength are rather well known from the solar tables and they will be considered in the future data interpretation procedures. In the present modeling studies, they were not included.

Table 3: List of line parameters generated for pollutants and interfering gases.

All the transitions listed for the pollutants and interfering species in Table 2 are considered for the model input. The status of generating the line parameters is given in this table and the qualitative agreement with available experimental data is indicated in the last column. The line parameters of nearly 30,000 lines of nine molecules have been generated by the SYMTOPI program.

Table 4: List of model calculations performed.

The line parameters of the molecules listed in Table 3 were used as input to the POLAYER program. The POLAYER program calculates the upwelling radiation at the top of the atmosphere, including the sun reflected radiance, the thermal emission of the earth's surface and the thermal emission of the atmosphere. In addition, the POLAYER program calculates the signal difference at the detector after the radiance has passed through both the vacuum and specifying cells. The radiative transfer calculations through a non-homogeneous medium were made with the following assumptions:

1. The atmosphere is plane-parallel, with 8 layers in the troposphere and 12 layers in the stratosphere;
2. Atmospheric refraction can be neglected;
3. The only consideration of particulates is in the transmission losses;
4. The earth's surface is a "diffuse" reflector;
5. The absorbing gases are in local thermodynamic equilibrium.

Table 3. Line Parameters Generated by SYMTOP for Pollutants and Interfering Gases

Species	λ	Transition	# Lines	Source	Comparison
CO	4.6	0-1	145	Benedict et al.	Excellent
	2.3	0-2	160	SYMTOP	Excellent
CO ₂	1.6	$3\nu_1 + \nu_3$	1634	SYMTOP	Excellent
	2.1	$2\nu_1 + \nu_3$	924	SYMTOP	Excellent
	2.7	$3\nu_2^1 - \nu_2^1 + \nu_3$	130	SYMTOP	Excellent
		$2\nu_2 + \nu_3$			
	5.0	$2\nu_1 - \nu_2$	585	SYMTOP	Excellent
	$\nu_1 + \nu_2$				
10.5	$\nu_3 - \nu_1$	427	SYMTOP	Excellent	
	$\nu_3 - 2\nu_2$				
SO ₂	4.0	$\nu_1 + \nu_3$	3079	SYMTOP	Fair
	8.6	ν_1	6311	SYMTOP	Fair
NO ₂	3.3	$\nu_1 + \nu_3$	1420	SYMTOP	Not Available
	7.6	ν_1	2583	SYMTOP	Not Available
NO	5.3	0-1	484	SYMTOP	Excellent
N ₂ O	3.0	$\nu_1 + \nu_3$	303	SYMTOP	Excellent
		$2\nu_2 + \nu_3$			
	4.0	$2\nu_1$	688	SYMTOP	Excellent
		$\nu_1 + 2\nu_2$			
	4.5	ν_3	976	SYMTOP	Excellent
	7.8	ν_1	161	SYMTOP	Excellent
	8.6	$2\nu_2$	156	SYMTOP	Excellent
	NH ₃	2.3	$\nu_1 + \nu_2$	3007	SYMTOP
		$\nu_2 + \nu_3$			
3.0		ν_1	1015	SYMTOP	Good
CH ₄	10.5	ν_2	1015	SYMTOP	Very Good
	2.3	$\nu_3 + \nu_4$		SYMTOP	Fair
	3.3	ν_3			
	3.5	$\nu_2 + \nu_4$			
	3.8	$2\nu_4$			
	7.7	ν_4			
	ν_4				
HCHO	3.5	ν_4	1861	SYMTOP	Very Good
H ₂ O	2.7, 6.3	ν_3, ν_2	~1000	Gates et al.	Excellent
O ₃	4.7	$2\nu_1$			

Table 4. Model Calculations Performed with POLAYER

	λ (μ)	T _{Ground} (°K)	ϵ _{Ground}	θ	Atm. Temp. Prof.	Interf. Species Incl.	Interf. Species Not Incl.	Poll. Conc. ppm	Poll. Conc. Prof.	H ₂ O Conc. & Prof.	Time per Run(min)
CO	4.6	270 - 330	0.0-1.0	0°-90°	Sev- eral	H ₂ O N ₂ O	CO ₂ O ₃	0-0.4	3	4	16
CO ₂	1.6	300	.98	30°	1		H ₂ O CH ₄	320	1		50
	2.1	300	.98	30°	1	H ₂ O		300- 400	1	1	16
SO ₂	8.6	300	1.00	0°	1	H ₂ O	N ₂ O O ₃	.002	1	1	75
	4.0	300	.8	30°	1		N ₂ O CH ₄	.002	1		45
NO ₂	7.6	300	1.0	0°	1	H ₂ O N ₂ O	CH ₄	.002	1	1	61
	3.3	300	.8	30°	1		CH ₄ H ₂ O	.002	1		40
NO	5.3	300	.8	30°	1	H ₂ O CO ₂		.0002- .02	1	1	23
NH ₃	10.5	300	1.00	0°	1		H ₂ O O ₃ , CO ₂	.02	1		15
	3	300	.8	30°	1		CO ₂ , N ₂ O CH ₄ , H ₂ O	.02	1		15
HCHO	3.5	300	.8	30°	1		H ₂ O	.002	1		21

The table shows a list of conditions for which the model calculations were made. More extensive model calculations were made for CO than for the other gases. Nevertheless, the model calculations we did make for the other molecules were sufficient to establish the feasibility of their measurement and to determine the instrument cell parameters. Only one of the pollutants (NO) was found not feasible to be remotely measured by RGFC. The others were found to be either "firmly" or "conditionally" feasible (definition given in next paragraph). It is essential that more model calculations be performed in order to ascertain firmly the ability of the RGFC instrument to measure all pollutant concentrations within given error limits. However, it is necessary to select the variation of the parameters judiciously in order to limit the model calculations to a reasonable number. Although we have incorporated many short cuts into the calculational routines (simultaneous radiance calculations for all concentrations of a given pollutant, establishment of linear relationships, etc.), the number of model runs for each pollutant is still very large. Assuming it is desired to calculate the signal levels for three ground temperatures, three ground emissivities, three sun angles, three atmosphere temperature profiles, three pollutant concentration profiles and four water vapor distributions, the total number of model runs amounts to $3^5 \times 4 = 972$ for each of the nine spectral intervals. Since some of the calculations involve several thousand spectral lines, and require computing times of up to an hour, it has become mandatory to consider band modeling. The band modeling will be based upon the line-by-line parameters and can be checked for accuracy. Thus, we will have a higher confidence level in these calculations than we would have without these checks with the line-by-line calculations.

Table 5: List of channels selected for the GFC instrument.

Based on the results of the model calculations, decisions about the gases to be included, number of channels, spectral regions and cell parameters have been made. Because the model calculations were not sufficient for some of the pollutants, the decisions were not "firm" in all cases. This is indicated in the third column through the label "Cond", which means that the decision about the inclusion of the channel pair(s) is "conditional", subject to the outcome of further model calculations (see next paragraph).*

In order to proceed with the design phase without the benefit of further model calculations in the immediate future, we assume that the feasibility and utility of channel pairs in question can be "firmly" established through later model calculations. Therefore, the design concept will be based on 13 channel pairs with the cell lengths established at 1 cm, 2 channel pairs with the cell lengths established at 20 cm for the CO₂ measurement and two radiometer channels (indicated as one channel pair in Table 5), for the determination of the aerosol content in the atmosphere.

In case the planned model calculations should indicate that it is not practical to include one or more of these channel pairs in question, the design of the RGFC may be changed to eliminate the "superfluous" channel pairs or to retain them for use as additional channels for the pollutants established as "firm".

*Although no model calculations for methane have been made yet, the measurement of this molecule is believed to be feasible. Recent studies by B. Weinstock and H. Niki (Science 176, 290, 1972) indicate that this molecule plays an important role in the balance of carbon monoxide.

Table 5. Channels Selected for the GFC Instrument

Poll	λ μm	Level of Conf	No. of Channel Pairs	CELL PARAMETERS			
				l cm	c	P_T atm	u cm atm
CO ₂	2.1	Cond	2	20	1	2.5	50
CO	4.6	Firm	2	1	.35	1	.35
SO ₂	8.6	Firm	2	1	.1	1	.1
	4	Cond	1	1	.2	1	.2
NO ₂	7.6	Cond	2	1	.1	1	.1
	3.3	Cond	1	1	.2	1	.2
NH ₃	10.5	Firm	2	1	.2	1	.2
	3	Firm	1	1	.25	1	.25
HCHO	3.5	Cond	2	1	.2	1	.2
CH ₄	3.3	See Footnote p. xxv.	2	1	.4	1	.4
	7.7		1	1	.3	1	.3
Aerosol	Visi- ble	Firm	1	--	--	--	--

Table 6: Problem areas which need further investigations.

This table lists the problem areas which became apparent for certain pollutants through the model calculations and which placed these pollutants in the category "Cond" of Table 5. We believe that all of these problem areas can be satisfactorily solved through additional theoretical and experimental studies, conducted both in Phase II and in an independent program proposed for the ERTS-A Data Analysis.

Table 6. Problem Areas which Need Further Investigation

	λ (μm)	Statement of the Problem	Indicated Solution
CO_2	2.1	<ol style="list-style-type: none"> 1. The unknown dependency of the CO_2 transmissivity on the Mie scattering source term 2. The influence of the variation in ground reflectivity and atmospheric scattering on high accuracy reqmts 	<ol style="list-style-type: none"> 1. Perform Monte Carlo calculations of multiple Mie scattering with the inclusion of CO_2 absorption 2. Conduct model calculations with two cell pairs to minimize ground and atmospheric effects
SO_2	4	Present calculations indicate negative signals, even with no interfering gases, apparently due to difference in λ dependency between calibration blackbody and sun reflected radiance	Establish firmly the cause for the negative signal through additional computer modeling; investigate simulation of the λ dependency of sun reflected radiance during calibration.
NO_2	7.6	Present calculations indicate strong influence of water vapor absorption	Determine whether measurement uncertainty is within accuracy requirements for concentration determination
	3.3	See under $\text{SO}_2 - 4\mu\text{m}$	See under $\text{SO}_2 - 4\mu\text{m}$
HCHO	3.5	See under $\text{SO}_2 - 4\mu\text{m}$	See under $\text{SO}_2 - 4\mu\text{m}$
Aerosol	Visible	<ol style="list-style-type: none"> 1. Sun glitter from ocean surface 2. Aerosol Properties 3. Non-Lambertian land surface 4. Surface reflectance gradient 	<ol style="list-style-type: none"> 1. Establish utility of two wavelengths measurements 2. Establish theoretical and/or empirical relationships through a field test program (ERTS-A) 3. Assumption of small influence to be checked in proposed field test program 4. See under 3

This latter program would provide invaluable data, because theoretical results will be compared with field measurements taken at the ground, from aircraft and satellite.

The problem areas identified for the measurement of CO₂ arise mainly from the fact that the requirement of at least 1% accuracy in the determination of the concentration is much higher than for the other pollutants. More details are given in Section 3.4.2 of this report.

Table 7: Supporting data requirements.

This table gives a preliminary list of supporting data requirements. Most of these requirements are within the present state-of-the-art, such as ground brightness temperature, atmospheric temperature and pressure profiles, and cloud cover amount. Other supporting data such as water vapor profile and cloud top height are more uncertain at present.

The most significant result of the study conducted under Task 5 of Phase I is the conclusion that the accuracy of the temperature profiles available from existing objective analyses by the National Meteorological Center (NMC) is sufficient for satisfactory pollutant data analysis, thus eliminating the need for a separate sounder on the same spacecraft. Unfortunately, the same cannot be said about the measurement of the water vapor distribution. Only low altitude distributions (up to the 500 mb level) are available from the objective analysis of the observations (NMC) at synoptic times (0000Z and 1200Z time). Current weather forecasts do not include relative humidity, nor are observations made at altitudes higher than the 500 mb level. The planned synchronous meteorological satellites (SMS) are scheduled to provide water vapor data at the higher altitude.

The other constituents of the atmosphere, whose concentrations must be known

Table 7. Supporting Data Requirements

Parameter	Accuracy Requirement	Provided on Same Satellite Platform	Provided from Different Sensor Platform	Potential Technique
Ground brightness temp. at λ	$\pm 2^\circ \text{K}$	One GFC channel for each spectral interval. Accuracy better than $\pm 2^\circ \text{K}$		
Atmospheric Temp. Profile	$\pm 2^\circ \text{K}$		Objective analyses: 12 hour forecasts from NMC within an accuracy of $\pm 2^\circ \text{K}$ (RMS)	
Water Vapor Profile	Not fully established		Objective analyses: Mean RH in 1000-500 mb layer within an accuracy of $\pm 50\%$	Profile measurements extending to higher layers thru SMS-(OES)
Cloud Cover Amount	$\pm 10\%$	Vidicon, having the same fov		
Cloud Top Height	Not yet established	Estimate through temp. measurement		7615 Å oxygen line determination

for the pollutant data analysis, do not need to be measured. The assumption of the "standard atmosphere" is sufficient.

The knowledge of cloud top height is desirable when pollutant data are to be obtained above the cloud cover. The absolute temperature of the cloud top, and thus its height, may be inferred from a measurement of the brightness temperature and an assumed emissivity. This subject needs further study, together with the utility of obtaining pollutant data in the presence of partial cloud cover.

1

INTRODUCTION

Air pollution has long ceased to be only a local problem. The millions of tons of pollutants emitted into the atmosphere every year by industrial nations affect the entire atmosphere beyond the boundaries of local districts, states, and countries. The best-known examples of global pollution are the increase of carbon dioxide and of particulate matter, both of which have an influence on the global heat balance. But there are other lesser known phenomena, such as the formation of particulates from gaseous pollutants and the nature of removal mechanisms for some of the pollutants, which must be studied on a global basis.

Satellites can provide the global coverage. Instruments on-board unmanned or manned spacecraft can measure the vertical total burden of pollutants above an area on the surface. When these data are continuously obtained and augmented with data from monitoring stations located on or near the surface of the earth, the dynamics of contaminated air masses, the distribution and dissipation of air pollutants and the long-range effect on the global climatology can be studied.

Satellites can also provide the platform for sensing the upper atmosphere on a global scale which cannot be done as economically from other platforms, such as balloons. A knowledge of the chemical composition and reaction schemes of that atmospheric region is of great importance. Based on previous studies and the study by a Working Group of about 50 leading U. S. authorities in the field of remote sensing of pollution⁽⁴⁾, the pollutants which are of concern on a global basis are:

- CO₂ The global mean concentration of CO₂ is increasing and it has an effect on the global climate;
- CO The sources and sinks are not all known and the long range trends in global loading are not established;

SO ₂	Accumulation has toxic effects; in addition it contributes to particle formation, thus influencing the global heat balance;
H ₂ S	Contributes to the formation of SO ₂ through oxidation;
NO _x	Accumulation has toxic effects and is a vital ingredient in the formation of photochemical smog. It also contributes to the formation of particles; nitrous oxide may be important in the chemistry of the stratosphere;
NH ₃	Contributes to the formation of particles;
<HC>	Are ingredients of photochemical smog and contribute to particle formation; CH ₄ may contribute to the formation and decomposition of CO;
HNO ₃	Probably influences the chemistry and particle formation in the stratosphere;
O ₃	Changes in the stratospheric ozone layer have great effects in the amount of uv radiation reaching the earth's surface; ozone in the troposphere is an ingredient in photochemical smog;
H ₂ O	Is important in the chemistry of the stratosphere and particle size distribution;
Others	Fluorocarbons and halogens are toxic and are probably accumulating in the troposphere.

The measurement of some of the above pollutants by a satellite-borne infrared RGFC instrument can be ruled out on the basis of low concentrations and/or weak or non-existing infrared rotation-vibration bands. The pollutants which do not fall into these categories and which are the subject of the present study are CO₂, CO, CH₄, SO₂, NO₂, NH₃, HCHO and particulates. These pollutants are of concern in the troposphere and the measurements are made with nadir experiments. The pollutants

which are of concern in the stratosphere are O_3 , HNO_3 , NO , NO_2 , N_2O , CH_4 , SO_2 , NH_3 , H_2O and particulates. Their observation is made through limb or sun occultation experiments. Although line parameters for most of these molecules have been generated in the present program because they were needed also for the nadir experiment, model calculations for the sun occultation experiment have not been performed as yet.

REFERENCES

1. C. B. Ludwig, R. Bartle and M. Griggs, NASA-CR-1380 (1969).
2. Study of Critical Environmental Problems (SCEP) MIT Press (1970).
3. Study of Man's Impact on Climate (SMIC) MIT Press (1971).
4. Remote Measurement of Pollution, NASA SP-285 (1971).

2

MODEL INPUT (Task I)

2.1 THEORY OF SYMMETRIC AND NEARLY SYMMETRIC TOP MOLECULES

The molecules of interest to the present program are either symmetric top or nearly symmetric top molecules (with the exception of H_2O). A symmetric top molecule (i. e., a molecule for which at least two of the principal moments of inertia are equal) may be treated analytically much more readily than an asymmetric top molecule. An asymmetry parameter κ may be defined⁽¹⁾:

$$\kappa = \frac{2B - (A+C)}{A-C} \quad (2-1)$$

where the rotational constants A, B, and C are inversely proportional to the principal moments of inertia. The parameter κ equals -1 for a prolate symmetric top, 0 for a most asymmetric top, and +1 for an oblate symmetric top. A list of the types of molecules considered is given in Table 2-1.

The energy levels for a rigid symmetric top molecule are given by

$$F_v(J, K) = \omega_v + BJ(J+1) + (A-B)K^2 \quad (2-2)$$

where J and K are the rotational quantum numbers and v represents the set of vibrational quantum numbers. For a non-rigid top, (1) can be written more precisely as a multiple power series in $J(J+1)$ and K^2 , with coefficients different for each vibrational state. For a transition between any two states, the wavenumber of the transition can be expressed simply as the difference between the energy levels:

$$\omega(v', J', K' - v, J, K) = F_{v'}(J', K') - F_v(J, K) \quad (2-3)$$

Table 2-1 Types of Molecules Considered in Atmosphere

<u>Linear Molecules</u>
CO
NO
CO ₂
N ₂ O
<u>Spherical Top Molecules</u>
CH ₄
<u>Other Symmetric Top Molecules</u>
NH ₃
<u>Nearly Symmetric Top Molecules</u>
NO ₂ $\kappa = -.9939$
SO ₂ $\kappa = -.9416$
H ₂ CO $\kappa = -.9623$
<u>Asymmetric Top Molecules</u>
H ₂ O $\kappa = -.4377$

Selection rules for J and K are obeyed: for a perpendicular band (change of electric dipole moment perpendicular to the top axis, e.g., ν_4 band of NH₃ at 6.1 μm),

$$\Delta J = -1, 0, +1 ; \Delta K = -1, +1 \quad . \quad (2-4)$$

For a parallel band (change of electric dipole moment parallel to the top axis, e.g., ν_2 band of NH₃ at 10.5 μm),

$$\Delta J = -1, 0, +1 ; \Delta K = 0 \quad . \quad (2-5)$$

By starting with $J = 0$, $K = 0$, the wavenumbers of all rotational transitions may be calculated. Relative strengths of the lines are known from quantum mechanics: e.g., in a perpendicular band, when $\Delta J = +1$ and $\Delta K = +1$, the line strength is proportional to⁽¹⁾

$$A_{KJ} = \frac{(J+2+K)(J+1+K)}{(J+1)(2J+1)} \quad (2-6)$$

and the Boltzmann factor and statistical weight of the lower state.

Similar expressions exist for all combinations of $\Delta J = -1, 0, +1$ and $\Delta K = -1, +1$. For a parallel band, when $\Delta J = +1$ (and $\Delta K = 0$), the analogous expression is

$$A_{KJ} = \frac{(J+1)^2 - K^2}{(J+1)(2J+1)} .$$

Similar expressions exist for $\Delta J = -1, 0$ and $\Delta K = 0$.

Thus it is possible to generate a systematic list of transitions and relative line strengths for a symmetric top molecule. Certain molecules such as NH_3 and CH_4 , having particular symmetry properties, require special modifications to calculate the statistical weights.

Line parameters are outputted in a systematic pattern relative to the rotational quantum numbers, but are not sequenced by wavenumber. A separate sorting subroutine can be used to select the lines lying in specified wavenumber intervals and sort these by wavenumber for input to the POLAYER program.

Certain molecules (e.g., SO_2 and NO_2) are not symmetric tops, but are very nearly so. The first-order effect of asymmetry on the spectrum is to change the wavenumbers of the transitions slightly. In such a case, SYMTOP calculates the line parameters for the equivalent symmetric top, and makes first-order corrections for asymmetry to the wavenumbers of the transitions.

2.2 DESCRIPTION OF SYMTOP PROGRAM

Since many of the species of interest are symmetric top molecules or slightly asymmetric tops, we have developed a program which calculates the energy level structure of a symmetric top molecule, and from the selection rules and matrix elements for transitions between these energy levels, calculates the wavenumbers and (relative) strengths of the allowed vibration-rotation transitions. A value of the total band strength is required to produce dimensionalized line strengths. As the transitions are calculated, the spectral data are written on magnetic tape. This tape may be used directly as input for program POLAYER (to be described later) or it may be desirable to perform a presorting of the tape by wavenumber, possibly also merging one or more other tapes containing data for other molecular species.

In several instances, existing tabulations of line parameters were available from the literature. This was the case for three H_2O band systems, as well as for the CO fundamental band. The spectral data were transcribed to punched cards, which were acceptable as input data to the earlier forms of POLAYER or as input to the presorting routines used for the later versions of POLAYER.

The general form of SYMTOP which was developed required modifications for almost every different molecule to which it was applied. In general, intensity alternation results from statistical weight factors which depend on the symmetry of the molecule and the spins of identical nuclei. CO_2^{16} , for example, has missing alternate levels (i. e., the statistical weight factor = 0) for both the C^{12} and C^{13} species. However, $\text{CO}^{16}\text{O}^{18}$ lacks this symmetry, and does not have such intensity alteration. In the case of NH_3 , levels with $K=3N+1$ and $3N+2$ have statistical weight of 1, while it is 2 for $K=3N$.

2.3 RESULTS AND COMPARISON WITH LABORATORY DATA

2.3.1 Carbon Monoxide

CO-4.6 μ Line positions (ω), strength (S), half-width (α) and lower energy level (F) of 145 lines for the fundamental band of C¹²O and C¹³O have been taken from Benedict et al.⁽²⁾ Since the parameters S and α were derived from experimental data, the accuracy is given by the experimental uncertainty which is estimated as 5%. Good agreement was also obtained between our calculated and a measured sun spectrum (see Section 3.3).

CO - 2.3 μ Unfortunately no listing similar to that for the fundamental is available for the first overtone band (0 -2). A SYMTOP program was used to generate line locations, line strengths, and lower state energy levels for this band. The molecular constants were taken from the experimental data of Benedict et al. Data for 160 lines have been generated and stored on tape for both C¹²O and C¹³O species. A deck of punched cards with the same spectral data as that recorded on tape in addition to line half-width taken from data of James and Plyler⁽³⁾ was also produced. The generated line positions were compared with the observational data of Connes⁽⁴⁾. It was found that the value of ω_e of C¹³O presented by Benedict et al. was misprinted, which led to a discrepancy of 40 cm⁻¹. The discrepancy has been corrected in the program. Of 26 observed lines being compared, the worst discrepancy is .0038 cm⁻¹, which is within the measurement accuracy.

The generated data were further verified by comparing with a laboratory spectrum through the program POLAYER. The band strength of 2.06 (cm⁻² atm⁻¹ STP) was taken from experimental data of Korb et al.⁽⁵⁾ The spectrum chosen for comparison was taken from the experimental data of Plyler and Thibault⁽⁶⁾, whose experimental conditions are pathlength = 9.0 atm cm, temperature = 300° K and pressure = 1 atm. Figure 2-1 shows the monochromatic transmissivity and

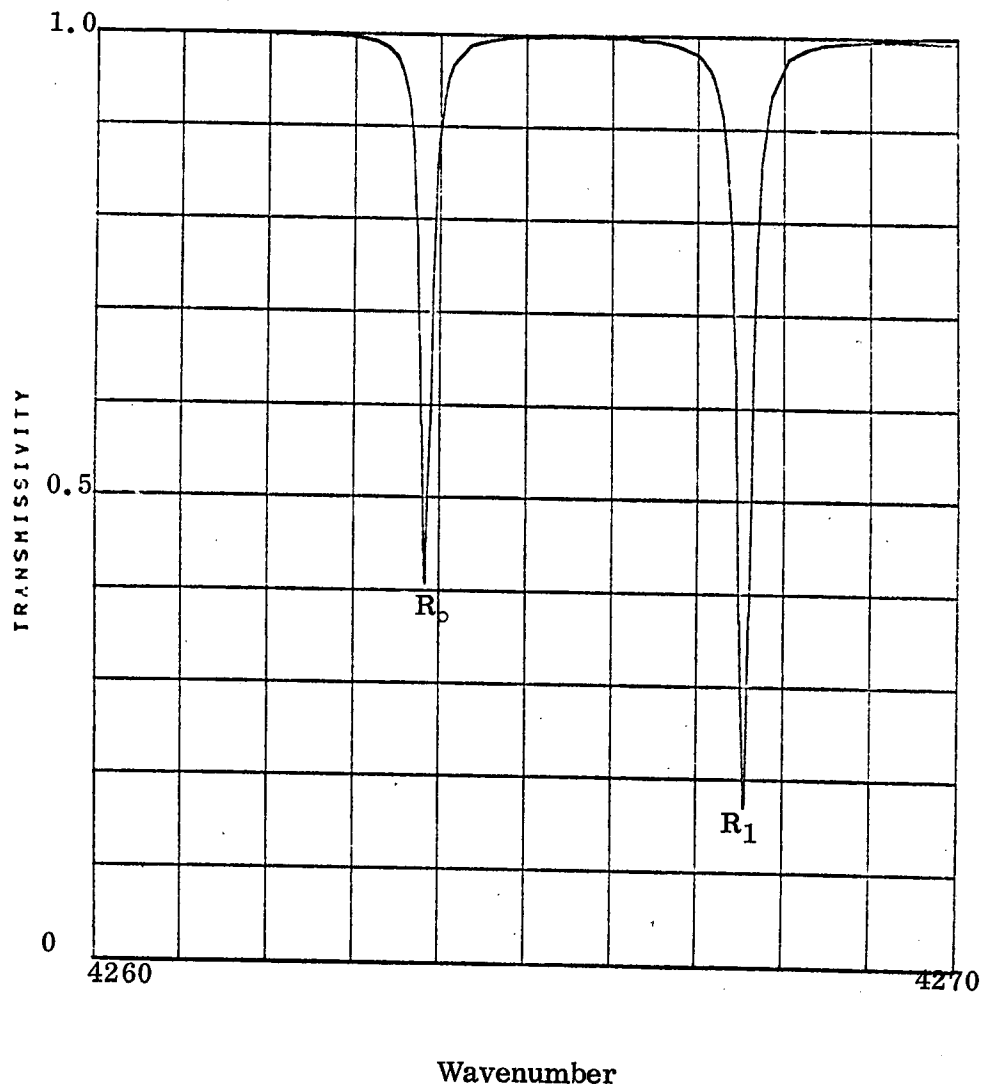


Figure 2-1. Monochromatic transmissivity of the R0 and R1 lines of the first overtone of CO for $u = 9.0$ cm-atm, $T = 300^\circ$ K and $p = 1$ atm.

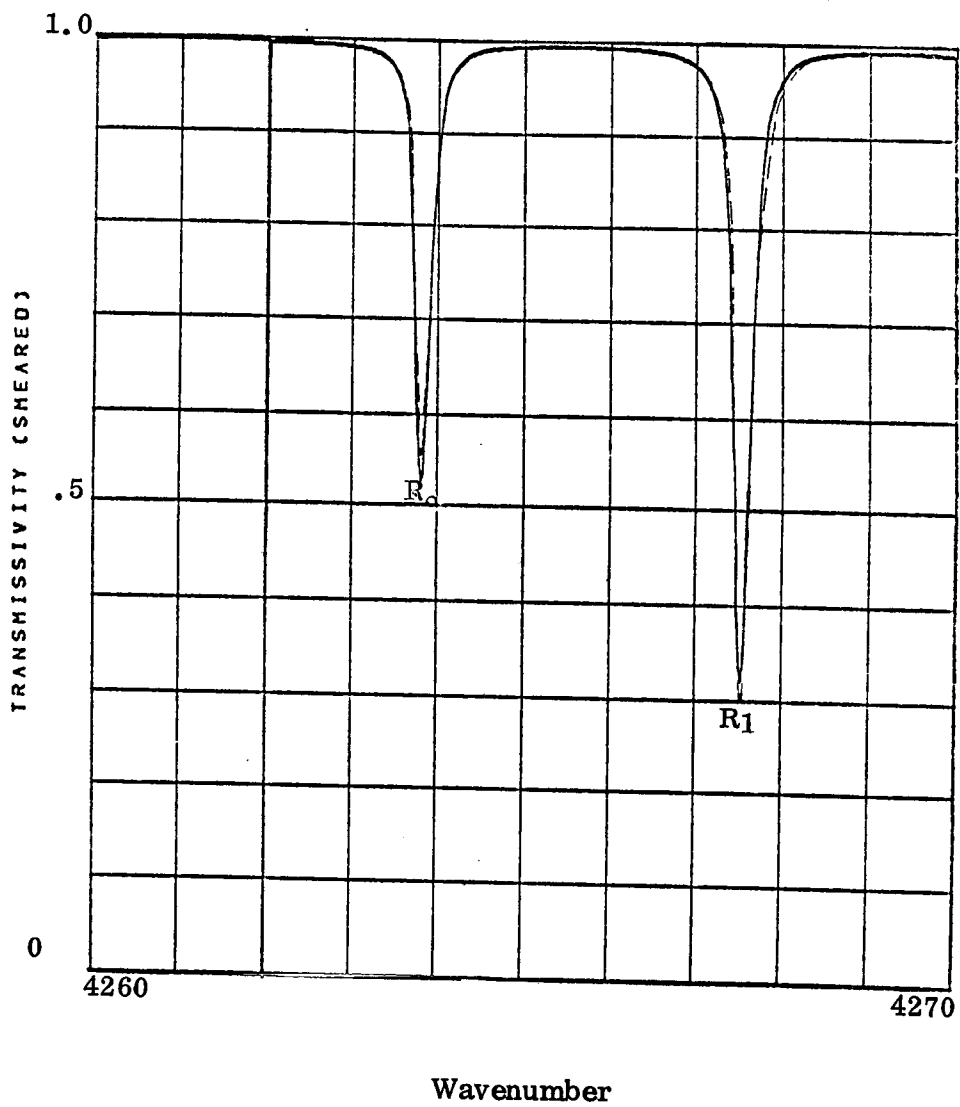


Figure 2-2. Degraded transmissivity (slit width of 0.11 cm^{-1} of the R0 and R1 lines of the first overtone of CO for $u = 9.0 \text{ cm-atm}$, $T = 300^\circ \text{K}$ and $p = 1 \text{ atm}$ (calculated spectrum solid, laboratory spectrum⁽⁶⁾ dashed).

Figure 2-2 shows a comparison of the generated spectrum (solid curve) assuming a slit width of 0.11 cm^{-1} and the laboratory spectrum (dashed curve). The agreement of these two curves is so close that they are nearly indistinguishable.

2.3.2 Carbon Dioxide

CO₂ - 1.6 μ The linear molecule version of the SYMTOP program can be applied to the molecule CO₂ with only minor changes. Because of its symmetric structure, alternate lines are missing from the spectrum. The 1.6 μ CO₂ band system, comprised of four fundamental transitions, has been calculated. Data for 1634 lines have been generated and stored on tape for the fundamental and first and second "hot" transitions of ¹²CO₂ and ¹³CO₂ (1.1% of CO₂ in the normal atmosphere) whose intensities are greater than one thousandth of the most intense line in this region. The parameters chosen to calculate the spectral data were taken from the literature; slight adjustments were made by a curve-fitting technique to improve the agreement with experimental line position measurements. We have compared the calculated locations with the wavenumbers measured by Courtoy⁽⁷⁾. Of 732 measured lines, 465 are found to be within 0.01 cm^{-1} , 722 within 0.05 cm^{-1} and all within 0.1 cm^{-1} . The most intense lines are found to be within 0.01 cm^{-1} . The line position fit is thus considered quite satisfactory.

A paper by Boese et al.⁽⁸⁾ provides the quantitative measurements of line intensities for the fundamental transitions. The total band intensity in the program was set equal to the observed value $2369 \times 10^{-5} (\text{cm}^{-2} \text{ atm}^{-1} \text{ STP})$ and the proper ratios 0.0536, 0.4432, 0.4517 and 0.0515 were assigned to the (30⁰1), (22⁰1), (14⁰1) and 06⁰1) bands respectively. Then a comparison was made with the intensities of individual lines. Of 149 measured lines being compared, 99 are found to be within the stated experimental error. A typical experimental error is about 5% of the observed value. The worst discrepancy from the mean measured value is $4.2 \times 10^{-5} (\text{cm}^{-2} \text{ atm}^{-1})_{296^\circ \text{K}}$ (15% of the line strength) compared with stated

experimental error of $\pm 2.0 \times 10^{-5} \text{ (cm}^{-2} \text{ atm}^{-1})_{296^\circ \text{K}}$ (8% of the line strength).

Boese et al. also present calculated line strengths to compare with their measured values, and for this line they show a similar discrepancy of 13% of the mean measured value.

The spectral data stored on the tape are further verified by comparing a spectrum generated by POLAYER with the laboratory spectrum of Boese et al. The laboratory conditions are pathlength = 800 atm cm, pressure = 380 mm Hg and temperature = 296° K. A triangular shaped slit function is assumed in the program with slit width chosen to be 0.08 cm^{-1} . Figure 2-3 shows the undegraded spectrum from 6330 to 6336 cm^{-1} . In Figure 2-4 the solid curve shows the calculated degraded spectrum while the dashed curve represents the measured spectrum. The hot lines are clearly shown in the spectrum and the magnitude of absorption is well reproduced. We believe that the slight discrepancies between the two curves are ascribable to the assumption of a triangular slit function in computation.

CO₂ - 2.1 μ The parameters ω , S and F of 1173 lines of the $2\nu_1 + \nu_3$ band systems have been generated through use of the linear molecule version of program SYMTOP. A half-width of $\alpha = 0.064 \text{ cm}^{-1}$ was assumed. The generation of data for this band system was necessary because of the negative results of the modeling studies for the 1.6 μ band. The molecular constants for the 2.1 μ band were taken from the work of Courtoy⁽⁷⁾. A curve-fitting technique was applied to improve the computed line positions. The resultant accuracy of the generated spectral lines is of the order of 0.02 cm^{-1} .

CO₂ - 5 μ The parameters ω , S, and F have been generated by SYMTOP for 585 lines of this perpendicular band system ($\nu_1 + \nu_2$) which overlaps both the carbon monoxide 4.6 μ band and the nitric oxide 5.3 μ band. This perpendicular band ($\nu_1 + \nu_2$) is different in structure from the 1.6 μ (parallel) band, most notably with the

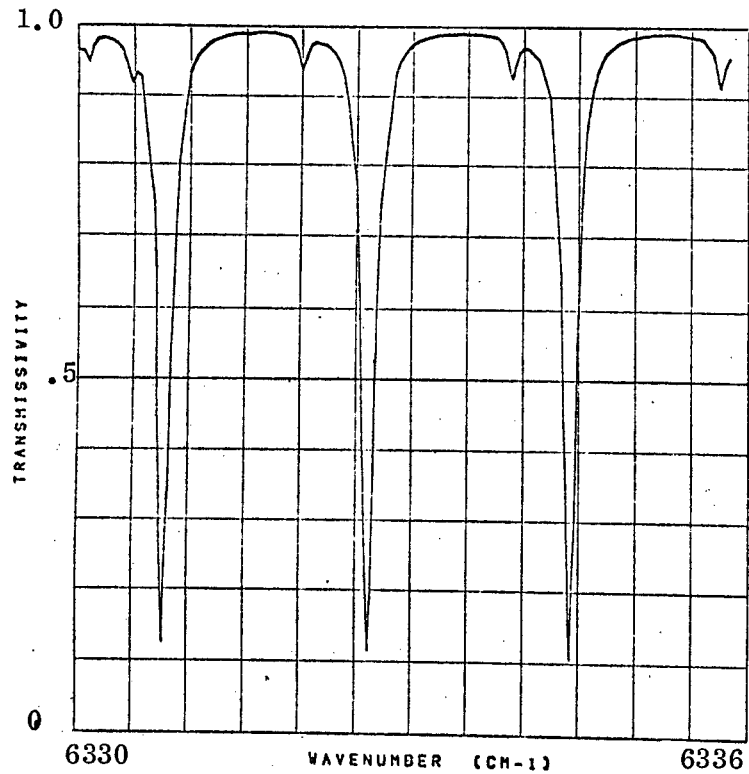


Figure 2-3. Monochromatic transmissivity of the band system at 1.6μ of CO_2 between 6330 and 6336 cm^{-1} for $u=800\text{ cm-atm}$, $p=0.5\text{ atm}$ and $T=296^\circ\text{ K}$.

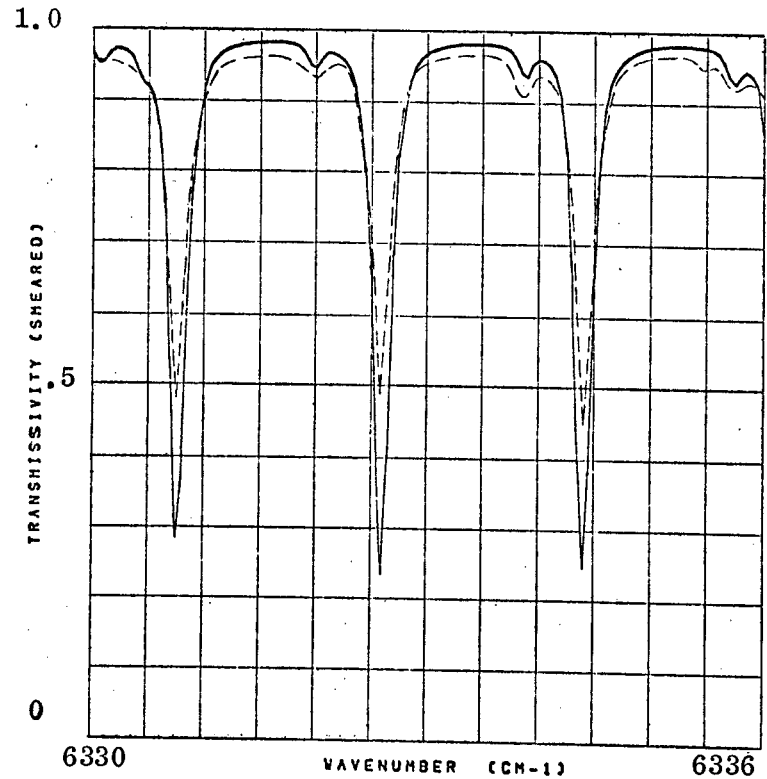


Figure 2-4. Degraded transmissivity (slit width of 0.08 cm^{-1}) of spectrum from Figure 2-3 (calculated spectrum solid, laboratory spectrum⁽⁸⁾ dashed).

appearance of a strong Q branch. The transitions included in the program ($00^0_0 - 30^1_0$, $00^0_0 - 11^1_0$, $01^1_0 - 12^2_0$ and $01^1_0 - 20^0_0$) are those which have been detected and identified in the solar spectrum. The molecular constants were taken from the data of Benedict published in "The Solar Spectrum from 2.8 to 23.7 Microns," by Migeotte et al.⁽⁹⁾ We have reproduced the calculated values (typically to about 0.03 cm^{-1}) listed in the solar spectrum except for the one transition ($01^1_0 - 12^2_0$) with the odd lower state quantum number J, apparently due to misprints of the molecular constants. For this transition, a different set of molecular constants was taken from the work of Courtoy⁽⁷⁾; the resultant accuracy of the generated spectral lines is comparable to the accuracy of the lines generated for the other transitions (typically about 0.03 cm^{-1}). The values of the band strengths were taken from Goody⁽¹⁰⁾.

CO₂ - 2.7 μ , 10 μ Line parameters of two more parallel bands of carbon dioxide have been generated using the same SYMTOPI program as that used to generate the 1.6 μ CO₂ band system. The 2.7 μ and the 10 μ band systems are required because they overlap the ammonia bands (3.0 μ and 10.5 μ). For these band systems, the molecular constants were taken from Migeotte et al.⁽⁹⁾ Only the portion of the 2.7 μ band system detected in the solar spectrum (i. e., wavenumber less than 3561 cm^{-1}) was generated and 150 lines were stored on tape. In the 10 μ region 427 lines were stored. For these two cases we are able to reproduce the calculated values listed in the solar spectrum which has a typical accuracy of about 0.01 cm^{-1} . The strengths of these three bands were taken from Goody⁽¹⁰⁾.

2.3.3 Sulfur Dioxide

SO₂ - 8.6 μ The parameters ω , S and F of 6311 lines of the ν_1 band of SO₂ have been generated based on the theory of slightly asymmetric top molecule. Values of the molecular constants were taken from Morino et al.⁽¹¹⁾

A half-width $\alpha = 0.08 \text{ cm}^{-1} \text{ atm}^{-1}$ was assumed. Considerable effort was made to improve the representation of the spectra of slightly asymmetric molecules, such as SO_2 . Perturbations of the energy levels for the lowest values of K have been included, with a resultant improvement in the representation of the spectrum.

A portion of the 8.6μ band including the band center and the R-branch maximum is shown in Figure 2-5, and the same spectrum viewed with a triangular slit of width 1 cm^{-1} is compared with the results of Burch⁽¹²⁾ in Figure 2-6.

Tables of SO_2 energy levels have been obtained from G. Steenbeckeliers⁽¹³⁾ of Belgium. Comparison of these tables shows that some of the perturbed energy levels are very accurately calculated by our program, while certain others are not. This discrepancy should be investigated, and should lead to a further improvement in the calculated spectrum.

We have been informed verbally that the SO_2 line parameters in preparation by R. F. Calfee may be soon available. Consequently, we have suspended further work on the refinement of our SO_2 line parameters, pending clarification of the availability of Calfee's data.

2.3.4 Nitrogen Dioxide

$\text{NO}_2-7.6\mu$ The SO_2 version of SYMTOP has been used to generate a set of parameters for 2583 lines of the ν_1 band of NO_2 . The molecular constants were taken from Abe et al.⁽¹⁴⁾ Because of the large numbers of lines (and consequent heavy overlapping) we have neglected the level-splitting effects of the unpaired electron, which were considered in the case of NO. We have found no good spectra for comparison. We are, however, planning on measuring our own laboratory spectra of NO_2 . Until better laboratory data do become available, we will not attempt further refinements in the calculation of the NO_2 line parameters.

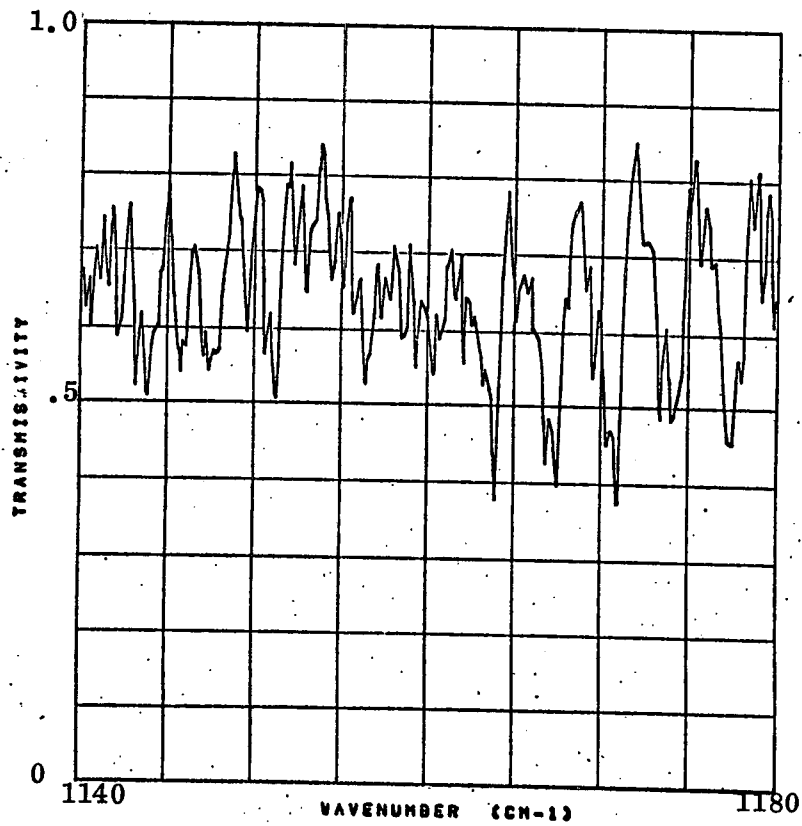


Figure 2-5. Monochromatic transmissivity of the SO_2 - ν_1 band between 1140 and 1180 cm^{-1} (showing band center and R-branch maximum). The conditions are the same as in Figure 2-6.

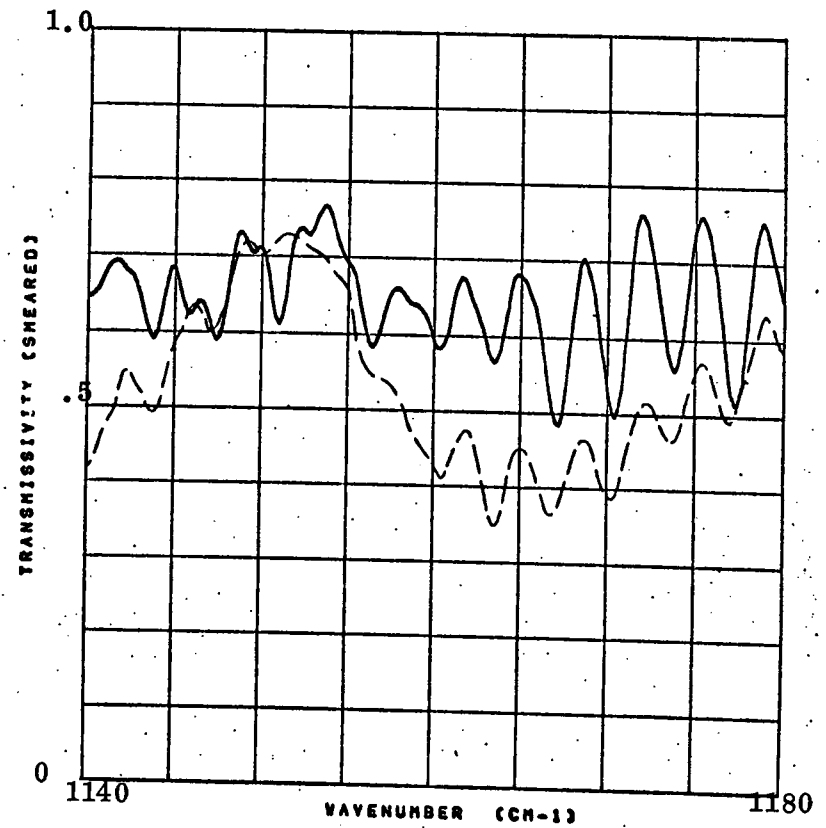


Figure 2-6. Degraded transmissivity (slit width is 1 cm^{-1}) from Fig. 2-5 for $u = .577 \text{ cm atm}$. $p_e = 1.59 \text{ atm}$ and $T = 298^\circ \text{K}$ (calculated ^{STP} spectrum solid, laboratory spectrum dashed).

The NO₂ molecule is very similar in structure to the SO₂ molecule, and the SO₂ version of SYMTOP was used directly for NO₂. A slight amount of line splitting resulting from the odd electron in the NO₂ molecule is of very minor importance because of the heavy line overlapping which occurs in the spectra of these molecules. A literature search indicated that insufficient data for NO₂ are available for our needs⁽¹⁸⁾.

2.3.5 Nitric Oxide

NO - 5.34 Parameters for 484 spectral lines in the NO fundamental band system have been generated by a modified version of the SYMTOP program for linear molecules. Because of the unpaired electron, the ground electronic state of NO is a ²Π state. The two levels ²Π_{1/2} and ²Π_{3/2} describe the state of the molecule, and divide the band into two subbands. Each line of the band is further split in two by Λ-doubling. Accordingly, the SYMTOP program had to be modified for this molecule. The molecular constants were taken from Herzberg⁽¹⁹⁾ to generate the spectral data. The line locations were compared with the experimental values of James⁽²⁰⁾. Of 98 measured lines, 35 lines are found to be within 0.05 cm⁻¹, 58 lines within .1 cm⁻¹, and the worst discrepancy is .192 cm⁻¹. Although the calculated values of James are in better agreement with the observed values, it is not clearly mentioned in the literature how the set of values was computed. However, the accuracy of the generated data is considered satisfactory to serve our purpose. The computed line strengths were also compared with the measured values of Abels and Shaw⁽²¹⁾. Of 73 measured lines, 47 lines are found to be within .05 (atm⁻¹ cm⁻²), 71 lines within .1 (atm⁻¹ cm⁻²)_{300° K}. The comparison shows excellent agreement.

The generated spectral data were used as an input to the program POLAYER to simulate a standard spectrum. Figure 2-7 shows part of the unsmearred transmissivity. The real spectrum to be compared was taken from the paper by Abels and Shaw with laboratory conditions: temperature = 300° K, pressure = 200 mm Hg and pathlength = .263 atm cm. By comparing the line locations obtained by James and the spectrum recorded by Abels and Shaw, it was found that the calibration of the Abels and Shaw spectrum was off by approximately 0.1 cm^{-1} . In Figure 2-8 the solid curve represents the generated spectrum from POLAYER and the dashed curve shows the laboratory spectrum with corrected calibration. Other portions of the spectrum were also compared and the evidence shows that they are in good agreement.

2.3.6 Ammonia

NH₃-10.5 μ An effective representation of the NH₃ 10.5 μ band system has been produced. SYMTOPI has generated a total of 1050 lines in this spectral region. We have compared the calculated locations with the wavenumbers measured by Garing et al.⁽²²⁾ Of 463 measured lines, 188 are found to be within 0.1 cm^{-1} , 351 within 0.5 cm^{-1} , and 415 within 1.0 cm^{-1} . The smallest discrepancies are quite strongly correlated with the most intense (hence, the most important) lines. It may be possible to refine these results even further; however, at the present, this is considered quite satisfactory.

Further verification of the spectral output from SYMTOPI is provided by comparing a spectrum generated by POLAYER with a laboratory spectrum. Quantitative measurements usually have limited spectral resolution, but a good check is provided on the gross features of the spectrum.

Graphs of segments of the calculated spectrum of NH₃ (portions of the Q and R branches) are shown in Figure 2-9. These graphs are output from POLAYER and represent the NH₃ spectrum as viewed with no instrumental distortion (i.e., monochromatically). The conditions of pathlength and pressure were chosen to simulate

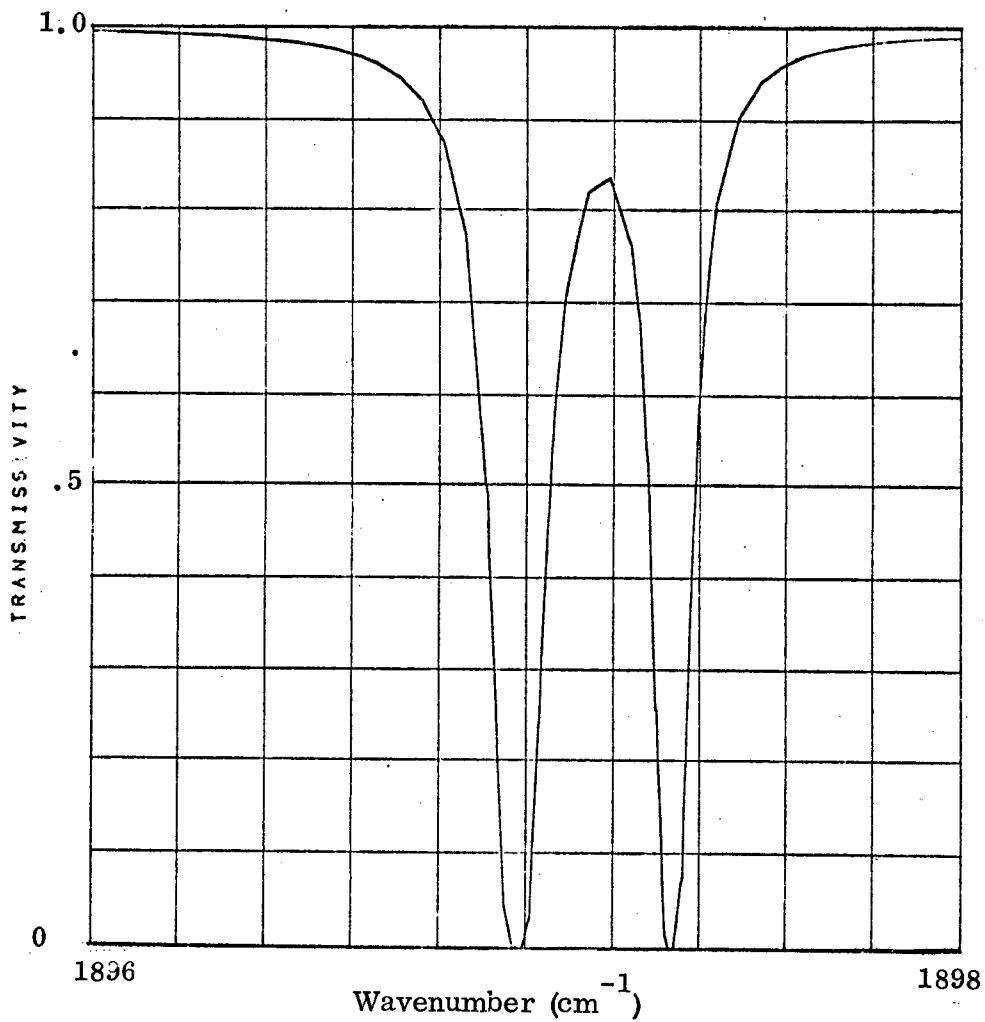


Figure 2-7. Monochromatic transmissivity of $R(5\frac{1}{2})_{\frac{1}{2}}$ and $R(5\frac{1}{2})_{\frac{3}{2}}$ lines of fundamental band of NO between 1896 and 1898 cm^{-1} . The conditions are the same as in Figure 2-8.

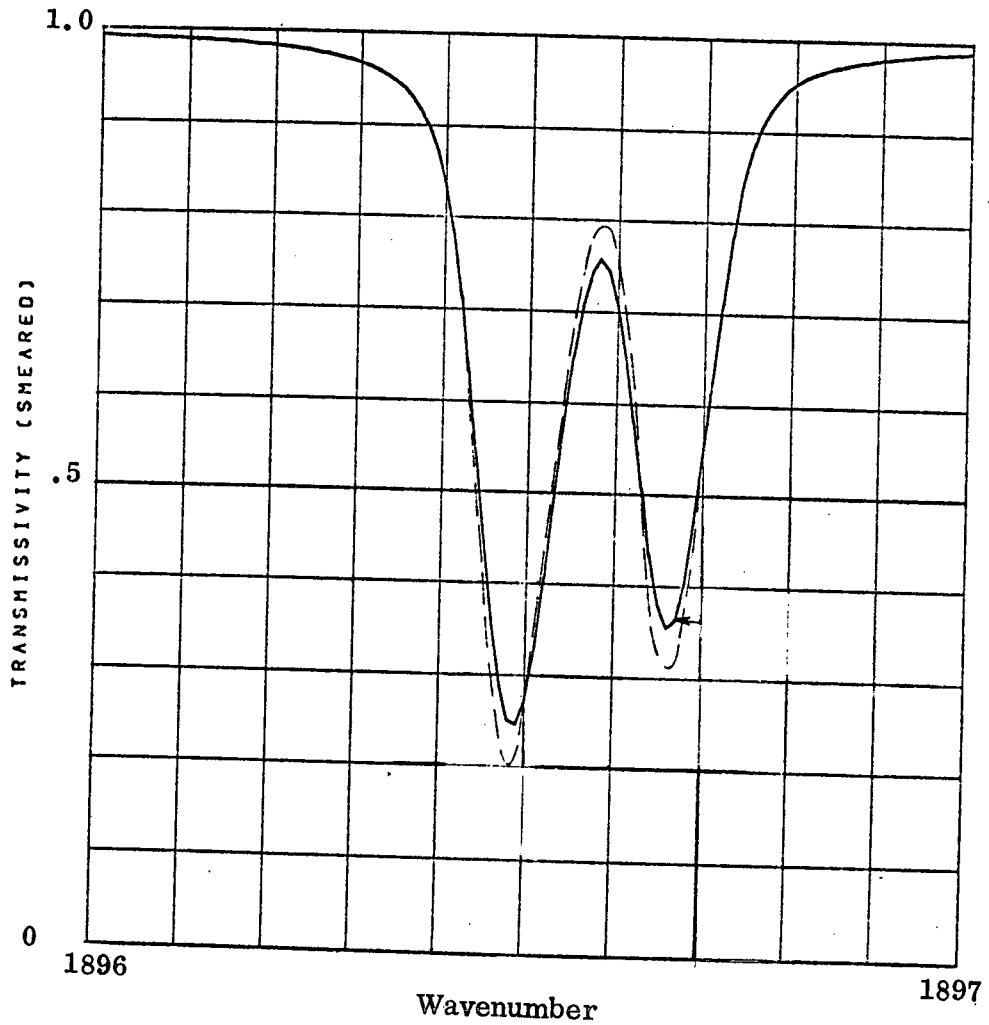


Figure 2-8. Degraded transmissivity (slit width is 0.13 cm^{-1} from Figure 2-7 for $u = 0.263 \text{ cm-atm}$, $p = 200 \text{ torr}$ and $T = 300^\circ \text{ K}$ (calculated spectrum solid, laboratory spectrum (21) dashed).

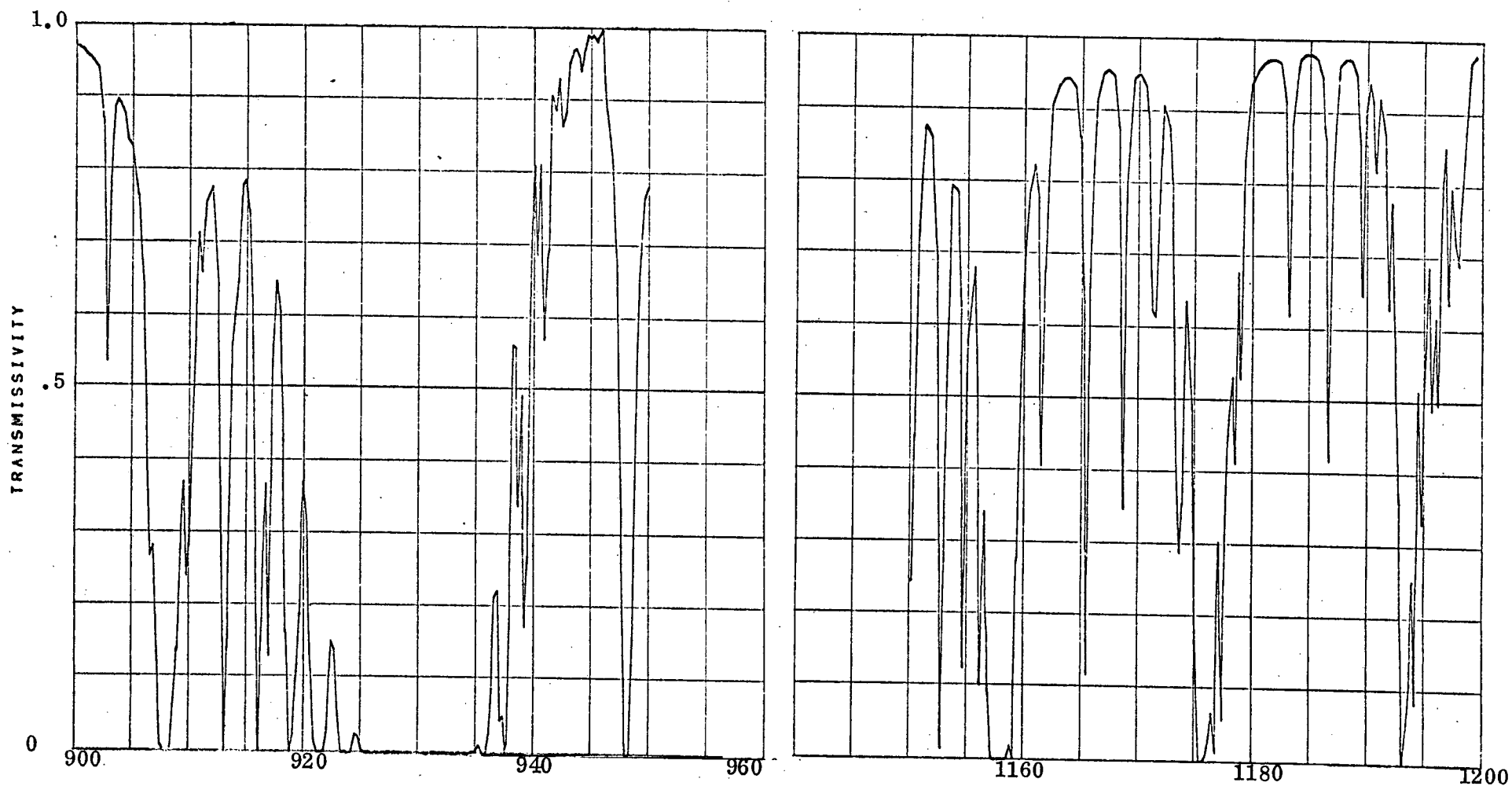


Figure 2.9 Monochromatic transmissivity of portions of the 10.5μ band system of NH_3 . A segment of the Q-branch between 900 and 950 cm^{-1} is shown on the left hand side and a segment of the R-branch between 1150 and 1200 cm^{-1} on the right hand side. The conditions are the same as in Figure 2-10.

one of the cell measurements of France and Williams⁽²³⁾. Unfortunately, the authors did not state the slit width that they used. Graphs of transmissivity for an assumed slit width of 8 cm^{-1} were generated by POLAYER and are shown in Figure 2-10.

The comparison is quite good as seen in Figure 2-10. The spectrum presented in France and Williams' paper is extremely small and their wavenumber scale cannot be read to an accuracy of better than 2 or 3 cm^{-1} . The comparison might be improved by assuming a slightly narrower slit width or a more realistic slit function than the assumed triangular shape.

$\text{NH}_3 - 3.0\mu$ The same version of the SYMTOPI program used to generate the spectral data for the 10μ (ν_2) ammonia band has been applied to generate data for the 3μ (ν_1) region. The molecular constants were taken from the experimental data of Benedict et al.⁽²⁴⁾, and the generated line positions were compared with their observations. 1015 lines were recorded on the magnetic tape. Of 257 observed lines being compared, 195 are found to be within 0.5 cm^{-1} , 225 within 1 cm^{-1} . The comparison shows the agreement being as good as that in the 10μ band.

A simulated spectrum was generated to match the experimental conditions of France and Williams⁽²³⁾ assuming a slit width of 50 cm^{-1} . It is unfortunate that no higher resolution spectrum such as that shown in the 10μ region is available for comparison. Figure 2-11 shows the unsmeared case while the comparison of the simulated spectrum (solid curve) is reasonably good as seen in Figure 2-12.

$\text{NH}_3 - 2.3\mu$ The ammonia 2.3μ region consists of a parallel band $\nu_1 + \nu_2$ ($\omega_0 = 4293.716$ and 4320.06 cm^{-1}) and a perpendicular band $\nu_2 + \nu_3$ ($\omega_0 = 4416.908$ and 4434.610 cm^{-1}). The band strengths of the parallel and perpendicular bands are 2.9 and 19.7 ($\text{cm}^{-2} \text{ atm}^{-1} \text{ STP}$), respectively, taken from a detailed study of these bands performed by Benedict et al.⁽²⁵⁾ The set of molecular constants presented by them has been used to reproduce the line parameters and 3007 lines were

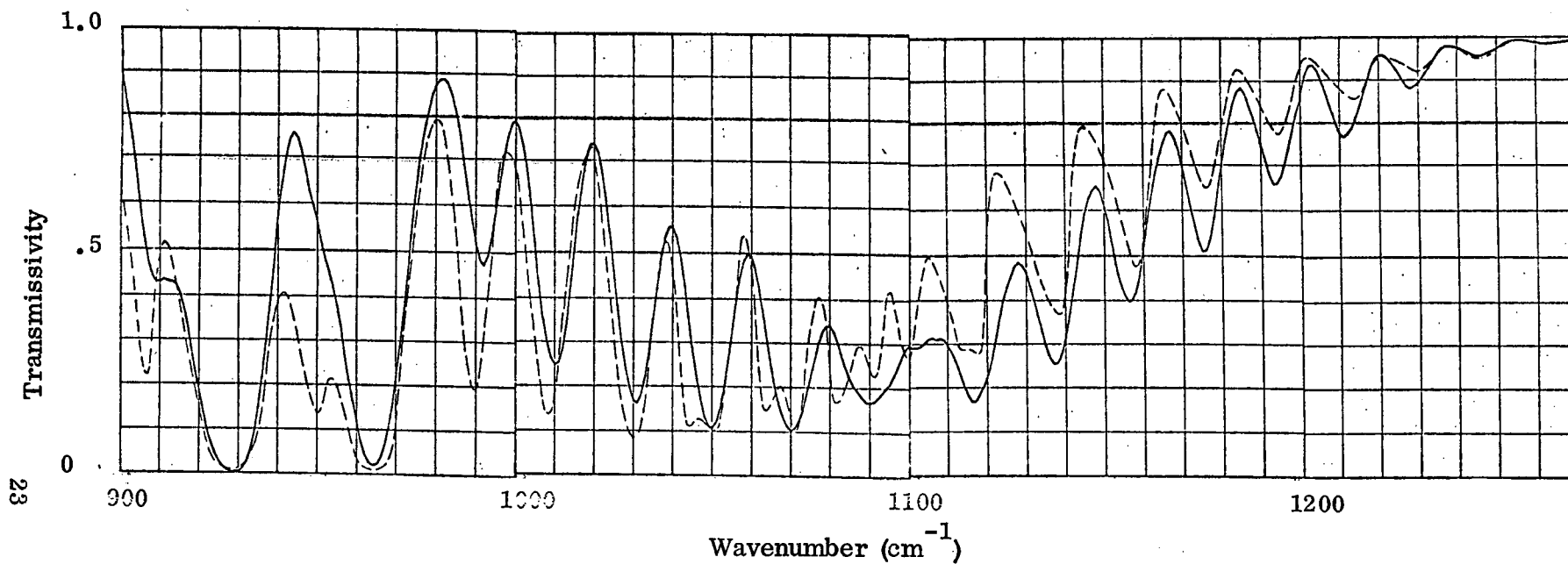


Figure 2-10. Degraded transmissivity (slit width of 8 cm^{-1}) of a portion of the 10.5μ band system of NH_3 between 900 and 1260 cm^{-1} for $u = 1.617 \text{ cm atm}_{\text{STP}}$, $p_e = 4185 \text{ torr}$ and $T = 299^\circ \text{K}$ (calculated spectrum solid, laboratory spectrum⁽²³⁾ dashed).

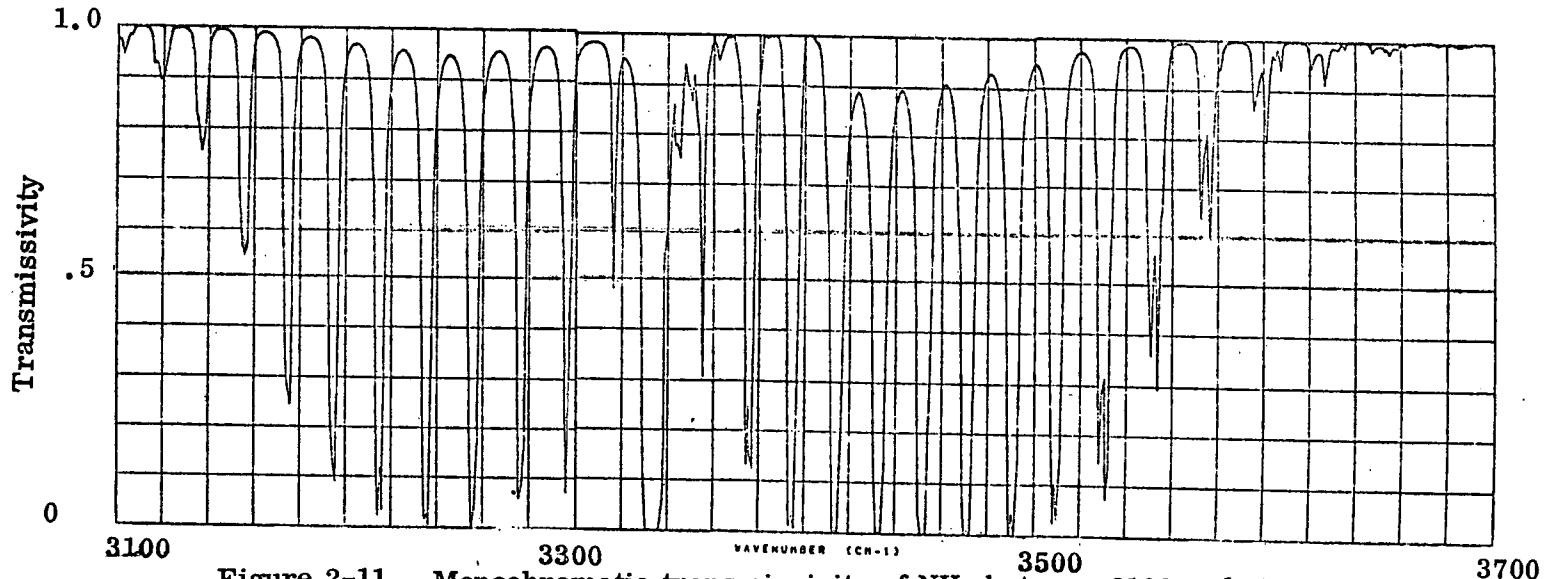


Figure 2-11. Monochromatic transmissivity of NH_3 between 3100 and 3700 cm^{-1} for $u = 6.23 \text{ cm atm}_{\text{STP}}$, $p_e = 5090 \text{ torr}$, and $T = 299^\circ \text{K}$.

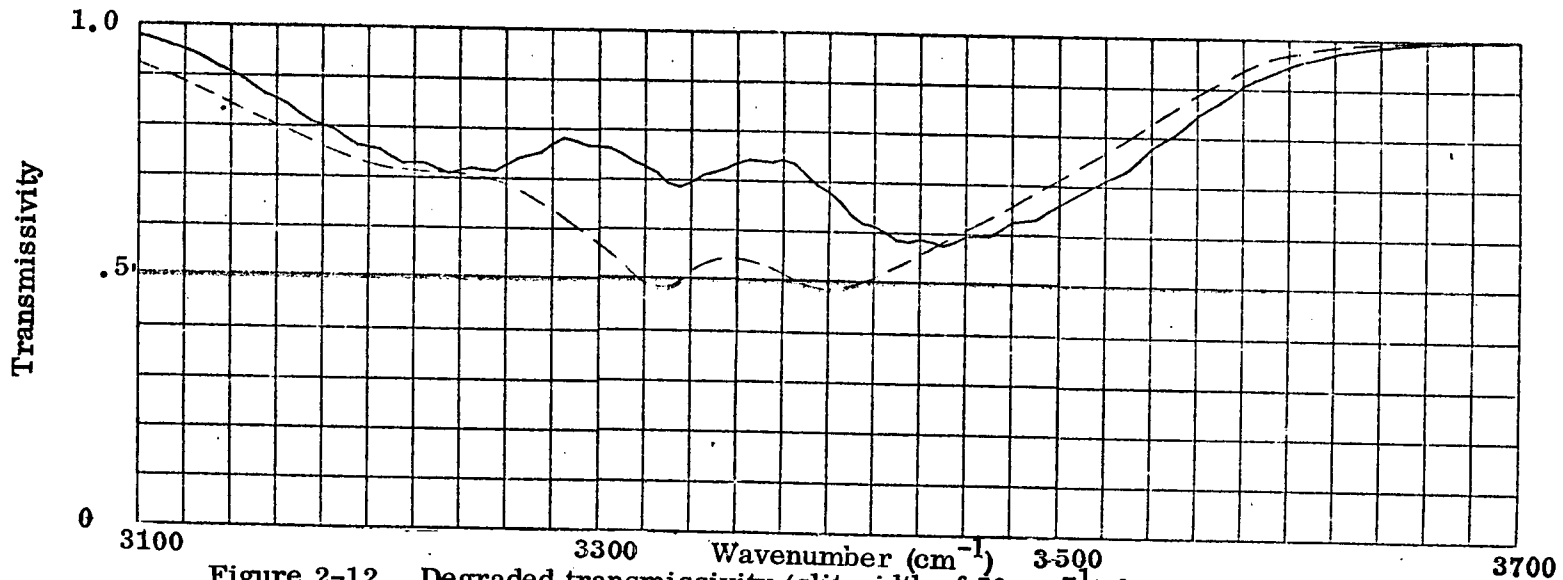


Figure 2-12. Degraded transmissivity (slit width of 50 cm^{-1}) from Figure 2-11. Calculated spectrum solid; laboratory spectrum (23) dashed.

recorded on tape. Unfortunately, the generated data do not reproduce their computed values to the same degree of accuracy achieved in the other NH_3 bands. The reason for these discrepancies is not clear at this moment. Comparison of the generated data with their observations has been made on the $\nu_1 + \nu_2$ parallel band. Of 336 measured lines, 311 are found to be within 0.5 cm^{-1} , all within 1 cm^{-1} . Although the generated data are not as good as the computed values presented by Benedict et al., the agreement is considered acceptable for this program.

No complete comparison has been made with the Benedict et al. observations of the $\nu_2 + \nu_3$ perpendicular band. Of about 100 lines being compared, the majority of the lines are found to be within 1 cm^{-1} . The line parameters could be further improved and an accuracy of less than 0.5 cm^{-1} could be expected, although the computed values by Benedict et al. show somewhat better agreement. However, since ammonia is only a possible interfering species in this region, the generated data are considered to be of acceptable accuracy.

2.3.7 Nitrous Oxide

N_2O - 4.5μ The wing of this band overlaps the CO fundamental band. The parameters for 976 lines in the 4.5μ band of N_2O (line strength, position, and energy level) were recorded on tape. For those lines whose wavenumbers are less than 2240 cm^{-1} , a deck of punched cards (868 cards) was also produced. The parameters chosen to generate the tape are taken from a paper by Tidwell et al.⁽²⁶⁾ The computed wavenumbers were compared with the solar spectrum of Migeotte et al.⁽⁹⁾ Of 201 measured lines being compared, 179 lines are found to be within 0.05 cm^{-1} , 199 within 0.1 cm^{-1} , and the worst discrepancy is 0.18 cm^{-1} .

A spectrum generated by POLAYER is compared with a laboratory spectrum produced by Plyler et al.⁽²⁷⁾ The band strength of $1920 \text{ (cm}^{-2} \text{ atm}^{-1} \text{ STP)}$ was adopted from Yale et al.⁽²⁸⁾ The laboratory conditions are: temperature = 220°K ,

pressure = 0.00263 atm and pathlength = 0.31 atm cm. Figure 2-13 shows the calculated spectrum in high resolution from 2204 to 2206 cm^{-1} . Comparison of the calculated smeared (solid curve) and the measured (dashed curve) spectrum is given in Figure 2-14. Absolute values of absorptivity were not given for the original laboratory spectrum, but the spectrum appears generally in good agreement. It appears that the experimental slit width (not specified) is slightly greater than the value of 0.05 cm^{-1} assumed in the computation. The apparent inconsistencies at 2204.2 cm^{-1} and 2205.8 cm^{-1} are believed to be due to measurement noise.

N_2O - Other Bands The nitrous oxide vibration-rotation bands which overlap bands of other species SO_2 (4.0 μ , 8.6 μ), NO_2 (7.6 μ), NH_3 (3.0 μ , 10.5 μ) include the following transitions: $\nu_1 + 2\nu_2$, $2\nu_1$, $2\nu_2 + \nu_3$, $\nu_1 + \nu_3$, and $2\nu_2$. All of the bands mentioned above are parallel bands. The SYMTOPI program used to generate the line parameters of 4.5 μ N_2O band was applied directly to generate the same line parameters of these bands. Of the ν_1 and $2\nu_2$ transitions, molecular constants are available from the solar spectrum of Migeotte et al.⁽⁹⁾ For the ν_1 transition, the computed values listed in the table were reproduced from the program to within the given accuracy ($\sim 0.01 \text{ cm}^{-1}$). However, for the $2\nu_2$ transition, the set of molecular constants shown in the table was unable to reproduce the same set of line parameters, apparently due to misprints of the molecular constants. A curve-fitting technique was applied to improve the computed values. The resultant accuracy in the positions of the generated spectral lines is comparable to the values listed in the table (typically about 0.01 cm^{-1}).

The molecular constants for the rest of transitions mentioned above are available from the data of Tidwell et al.⁽²⁶⁾ They also computed the line positions and compared with their observations. We are able to reproduce their computed values with a typical accuracy of about 0.01 cm^{-1} .

A total of 1308 lines were stored on a single tape for all transitions. The band strengths were taken from Goody⁽¹⁰⁾ except one transition $2\nu_2 + \nu_3$ whose value is not available and is estimated for this program.

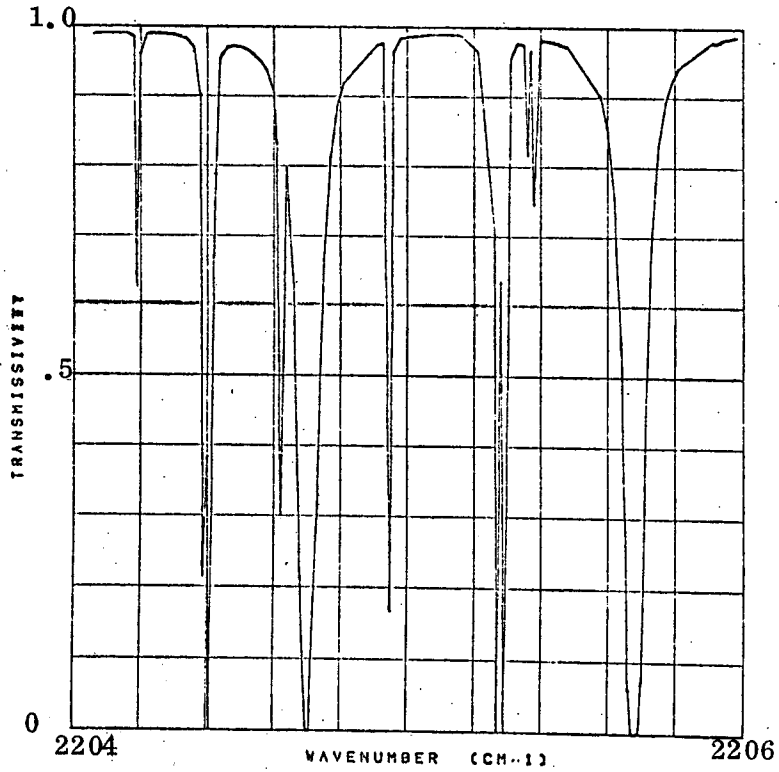


Figure 2-13. Monochromatic transmissivity of N_2O between 2204 and 2206 cm^{-1} for $u=2$, 0.31 cm atm , $p=2 \text{ torr}$, and $T=220^\circ \text{K}$.

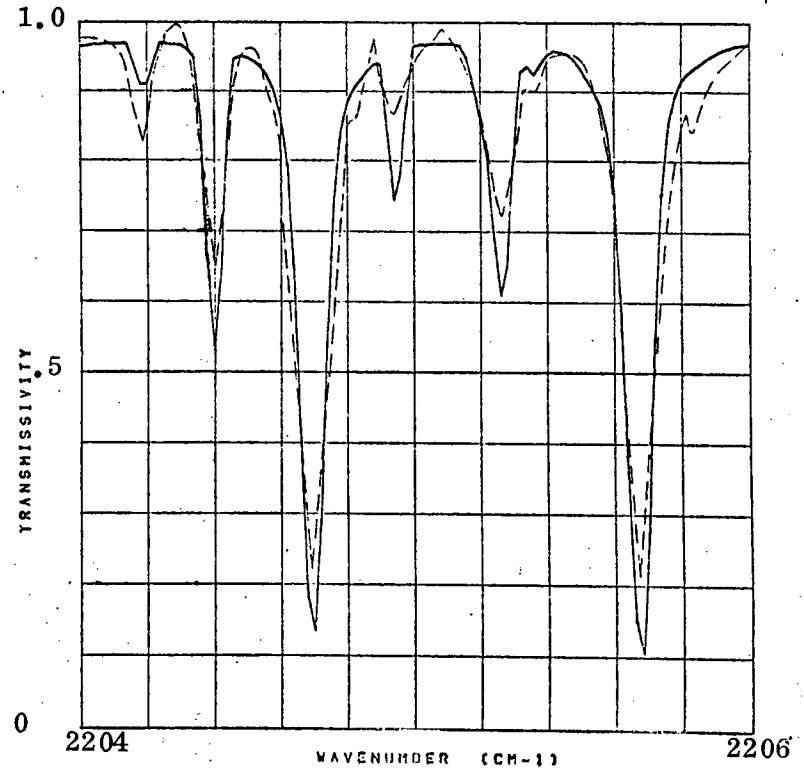


Figure 2-14. Degraded transmissivity (slit width of 0.05 cm^{-1}) of spectrum from Figure 2-13 (calculated spectrum solid, laboratory spectrum⁽²⁷⁾ dashed).

2.3.8 Formaldehyde

HCHO - 3.5 μ The formaldehyde molecule (HCHO), which is an asymmetric top, has been modeled by the SYMTOP program. The asymmetry parameter κ is nearly -1 (-.9623), so that HCHO does not deviate greatly from being a symmetric top.

There is a great lack of quantitative spectra for making comparisons. Herzberg⁽⁹⁾ shows a spectrum taken by H. H. Nielsen⁽²⁹⁾, but the experimental conditions specified are clearly incorrect. We have a spectrum taken by P. L. Hanst⁽³⁰⁾ with a resolution of apparently better than 1 cm⁻¹.

The Nielsen and Hanst spectra do not seem to be completely consistent, even allowing for difference in resolution.

A sample portion of the calculated high-resolution HCHO spectrum is shown in Figure 2-15. The large absorption peaks are Q-branches, which are well reproduced in wavenumber location. The finer R-branch structure in between the Q-branch peaks is also approximately reproduced. No attempt was made to match the resolution of the Hanst spectrum, which is shown in Figure 2-15 for comparison.

2.3.9 Methane

CH₄ Methane is a spherical top molecule, and it is this fact which results in considerable complication in calculating its spectrum. The symmetric top approximation (Eq. 2-2) predicts that all rotational levels of the same J value will have the same energy level. This increased degeneracy results in the appearance of higher-order perturbations which separate the energy levels in a manner difficult to treat analytically.

First-order corrections have been incorporated into SYMTOP and the program has generated the correct total strength and spectral location of the unsplit P- and R-branch lines from 2870 to 3170 cm⁻¹. The problem remaining is that of representing

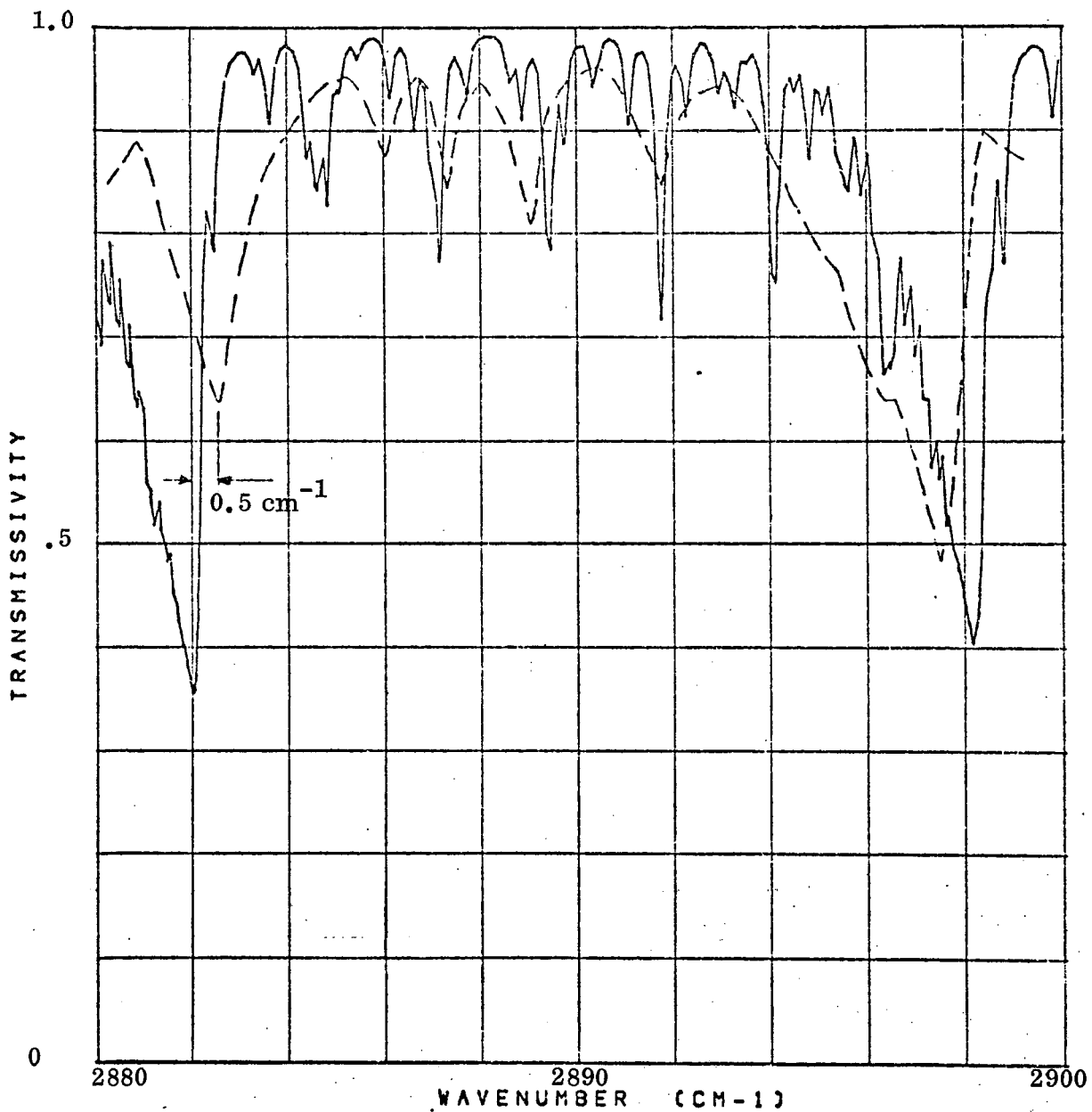


Figure 2-15. Monochromatic transmissivity (calculated) of HCHO between 2880 and 2900 cm^{-1} (solid curve). Degraded transmissivity (measured by Hanst⁽³⁰⁾) for $u = 0.08 \text{ cm atm}$, $p = 0.0079 \text{ atm}$ and $T = 300^\circ\text{K}$ (dashed curve).

the fine structure of these "lines" which are split into several components because of the molecular symmetry. Approximate expressions for the splitting will be developed.

2.3.10 Water Vapor

H_2O -1.6, 2.7 & 6.3 μ Extensive tabulations of water vapor lines have been published by NBS (31, 32). At present we have data on punched cards for nearly 1000 lines in the 2.7 μ and 6.3 μ bands.

REFERENCES

1. G. Herzberg, "Molecular Spectra and Molecular Structure: II. Infrared and Raman Spectra of Polyatomic Molecules," D. Van Nostrand Company, Inc., Princeton, New Jersey (1945).
2. W. S. Benedict, R. Herman, G. E. Moore, and S. Silverman, *Ap. J.* **135**, 277 (1962).
3. T. C. James and E. K. Plyler, *J. Chem. Phys.* **40**, 221 (1964).
4. P. Connes, J. Connes, and W. S. Benedict, *Ap. J.* **152**, 731 (1968).
5. C. L. Korb, R. H. Hunt, and E. K. Plyler, *J. Chem. Phys.* **48**, 4252 (1968).
6. E. K. Plyler and R. J. Thibault, *J. Res. NBS* **67A**, 229 (1963).
7. C. P. Courtoy, *Annales de la Societe Scientifique de Bruxelles* **73**, 5 (1959).
8. R. W. Boese, J. H. Miller, E. C. Y. Inn, and L. P. Giver, *J. Quant. Spectry. Radiative Transfer* **8**, 1001 (1968).
9. M. Migeotte, L. Neven, J. Swensson, "The Solar Spectrum from 2.8 to 23.7 Microns," Liege, Belgium (1956).
10. R. M. Goody, "Atmospheric Radiation. I. Theoretical Basis," Oxford University Press, London (1964).
11. Y. Morino, Y. Kikuchi, S. Saito, and E. Hirata, *J. Mol. Spectry.* **13**, 95 (1964).
12. D. E. Burch, J. D. Pembroke, and D. A. Gryvnak, *Aeronutronic Publ. No. U-4947* (July 1971).

13. G. Steenbeckeliers, private communication.
14. G. Abe, F. Myers, T. K. McCubbin and S. R. Polo, *J. Mol. Spectry.* 38, 552 (1971)
15. E. T. Arakawa and A. H. Nielsen, *J. Mol. Spectr.* 2, 413 (1958).
16. A. Guttman, *J. Quant. Spectry. Radiative Transfer* 2, 1 (1962).
17. G. E. Moore, *J. Opt. Soc. Am.* 43, 1045 (1953).
18. M. D. Olman and C. O. Hause, *J. Mol. Spectry.* 26, 241 (1968).
19. G. Herzberg, "Molecular Spectra and Molecular Structure, I. Spectra of Diatomic Molecules, D. Van Nostrand Company, Inc., Princeton, New Jersey (1950).
20. T. C. James, *J. Chem. Phys.* 41, 2806 (1964).
21. L. L. Abels and J. H. Shaw, *J. Mol. Spectry.* 20, 11 (1966).
22. J. S. Garing, H. H. Nielsen, and K. N. Rao, *J. Mol. Spectry.* 3, 496 (1959).
23. W. L. France and D. Williams, *J. Opt. Soc. Am.* 56, 70 (1966).
24. W. S. Benedict, E. K. Plyler, and E. D. Tidwell, *J. Chem. Phys.* 32, 32 (1960).
25. W. S. Benedict, E. K. Plyler, and E. D. Tidwell, *J. Res. NBS* 61, 123 (1958).
26. E. D. Tidwell, E. K. Plyler, and W. S. Benedict, *J. Opt. Soc. Am.* 50, 1243 (1960).
27. E. K. Plyler, E. D. Tidwell, and A. G. Maki, *J. Res. NBS* 68A, 79 (1964).
28. G. D. Yale, D. L. Ford, and J. H. Shaw, *Appl. Opt.* 7, 695 (1968).
29. H. H. Nielsen, *Phys. Rev.* 46, 117 (1934).
30. P. L. Hanst, private communication.
31. D. M. Gates, R. F. Calfee, D. W. Hansen, and W. S. Benedict, "Line Parameters and Computed Spectra for Water Vapor Bands at 2.7 microns," *NBS Monograph* 71 (1964).
32. W. S. Benedict and R. F. Calfee, "Line Parameters for the 1.9 and 6.3 Micron Water Vapor Bands," *ESSA Professional Paper* 2 (1967).

3

MODEL STUDIES FOR GASEOUS POLLUTANTS

(Task 2)

3.1 THEORY OF RADIATIVE TRANSFER

The radiation emergent from the atmosphere, designated here as $E(\omega)$, results from the operation of several different processes. The underlying surface emits thermal radiation; the atmosphere absorbs and emits radiation at a rate dependent on its local composition and temperature. The surface also reflects downwelling radiation, consisting mainly of solar radiation. Scattering of radiation by the atmosphere also takes place.

The actual calculation of $E(\omega)$ is an extremely formidable task. The major complexities arise from the presence of the scattering processes, which alter the direction of propagation of individual photons in a manner which can only be predicted statistically. It is thus desirable to separate $E(\omega)$ into its components as far as possible in order to make the problem more manageable. The quantity $E(\omega)$ may be written as a sum of component terms in the following form:

$$E(\omega) = E_G(\omega) + E_R(\omega) + E_\phi(\omega) + E_{R\phi}(\omega) \quad (3-1)$$

in which $E_G(\omega)$ represents the thermal radiation emitted by the underlying surface and the atmosphere, $E_R(\omega)$ represents the incident solar radiation reflected by the surface, $E_\phi(\omega)$ represents the radiation scattered by single and/or multiple-scattering processes in the atmosphere without having been reflected from the surface, and $E_{R\phi}(\omega)$, another atmospheric scattering term similar to $E_\phi(\omega)$, but for radiation which has undergone a reflection from the surface.

The functional dependence of these components of $E(\omega)$ is indicated below

$$\left. \begin{aligned}
 E_G(\omega) &= E_G(\epsilon, \tau, \omega, T_S, T_A) \\
 E_R(\omega) &= E_R(\rho, \theta, \tau, \omega) \\
 E_\phi(\omega) &= E_\phi(\theta, n\sigma, \tau, \omega) \\
 E_{R\phi}(\omega) &= E_{R\phi}(\rho, \theta, n\sigma, \tau, \omega)
 \end{aligned} \right\} \quad (3-2)$$

where T_S, T_A are the surface and atmospheric temperatures, ϵ, ρ are the surface emissivity and reflectivity, θ is the sun zenith angle, $(n\sigma)$ is the product of number of scattering centers (n) and scattering cross section (σ), τ is the transmissivity of atmosphere, referring generically to all sources of attenuation: molecular and particulate absorption and molecular and particulate scattering.

The equation of radiative transfer, without scattering and without solar radiation, for thermal radiation emerging from a plane-parallel atmosphere with an underlying surface of emissivity $\epsilon(\omega)$ can be written

$$\begin{aligned}
 E(\omega) &= E_G(\omega) \\
 &= \epsilon(\omega) N^0(\omega, T_S) \tau(\omega, 0) + \int_0^h N^0(\omega, T(z)) \frac{d\tau(\omega, z)}{dz} dz
 \end{aligned} \quad (3-3)$$

in which $N^0(\omega, T)$ is the Planck blackbody function, T_S is the surface temperature, h is altitude at top of atmosphere, $\tau(\omega, z)$ is the monochromatic transmissivity of the atmosphere at wavenumber ω between altitude z and top of atmosphere, $T(z)$ is the temperature of the atmosphere at altitude z .

The general expression for the transmissivity is given by

$$\tau(\omega, z) = \prod_i \tau_i(\omega, z) = \exp \left[- \int_0^z \sum_i \kappa_i(\omega, z') n_i(z') dz' \right] \quad (3-4)$$

where $\kappa_i(\omega, z')$ is the extinction coefficient for species i which is given by the sum of

the scattering and absorption coefficients, and n_i is the number density of contributing molecules of species i in the optical path.

The contribution from sunlight reflected from the surface becomes significant at shorter wavelengths. This contribution is given by the component $E_R(\omega)$:

$$E_R(\omega) = \frac{1}{\pi} [1 - \epsilon(\omega)] \cos \theta H_s(\omega) (\tau(\omega))^\gamma \quad (3-5)$$

where $[1 - \epsilon(\omega)]$ is the ground reflectance of a diffuse surface, θ is the sun zenith angle, $H_s(\omega)$ is the sun irradiance at the top of the atmosphere, $\tau(\omega) = \tau(\omega, 0)$ is the transmission vertically through the atmosphere, and $\gamma = 1 + f(\theta)$ with $f(\theta) = \sec \theta$ for $0 \leq \theta \leq 60^\circ$ and $\text{Ch } \theta$ for $\theta > 60^\circ$ ($\text{Ch } \theta$ is the Chapman function).

In order to gain some insight into the radiance levels which can be expected at the top of the atmosphere, we estimate the contributions of the different terms for some arbitrary but realistic conditions. For the first term in Eq. (3-1), E_G , we assume a surface temperature of 300°K , with an emissivity of 1 for oceans and 0.6 for land (see Figure 3-1). For simplicity in the figure, we have not included the effect of atmospheric absorption and emission. In general, this inclusion would lower the radiance level in the region of atmospheric absorption bands.

For the second term, E_R , we assume a sun zenith angle of 45° , a reflectivity of 0.02 for oceans and select 0.4 as an upper value of land surfaces, and we also assume that the transmission is given by the extinction due to Rayleigh and Mie scattering, and ozone absorption. The extinction is taken from the Elterman⁽¹⁾ model. For the third term, E_ϕ , we refer to the calculations of Plass and Kattawar⁽²⁾, who have calculated the reflected radiance for a zero albedo as a function of wavenumber, sun angle and different amounts of Rayleigh and Mie scatterers. However they did not include in their multiple scattering calculations the effect of molecular absorption (except for O_3). The fourth term, $E_{R\phi}$, has not been calculated explicitly for an atmosphere including particulates. However, it is contained in the

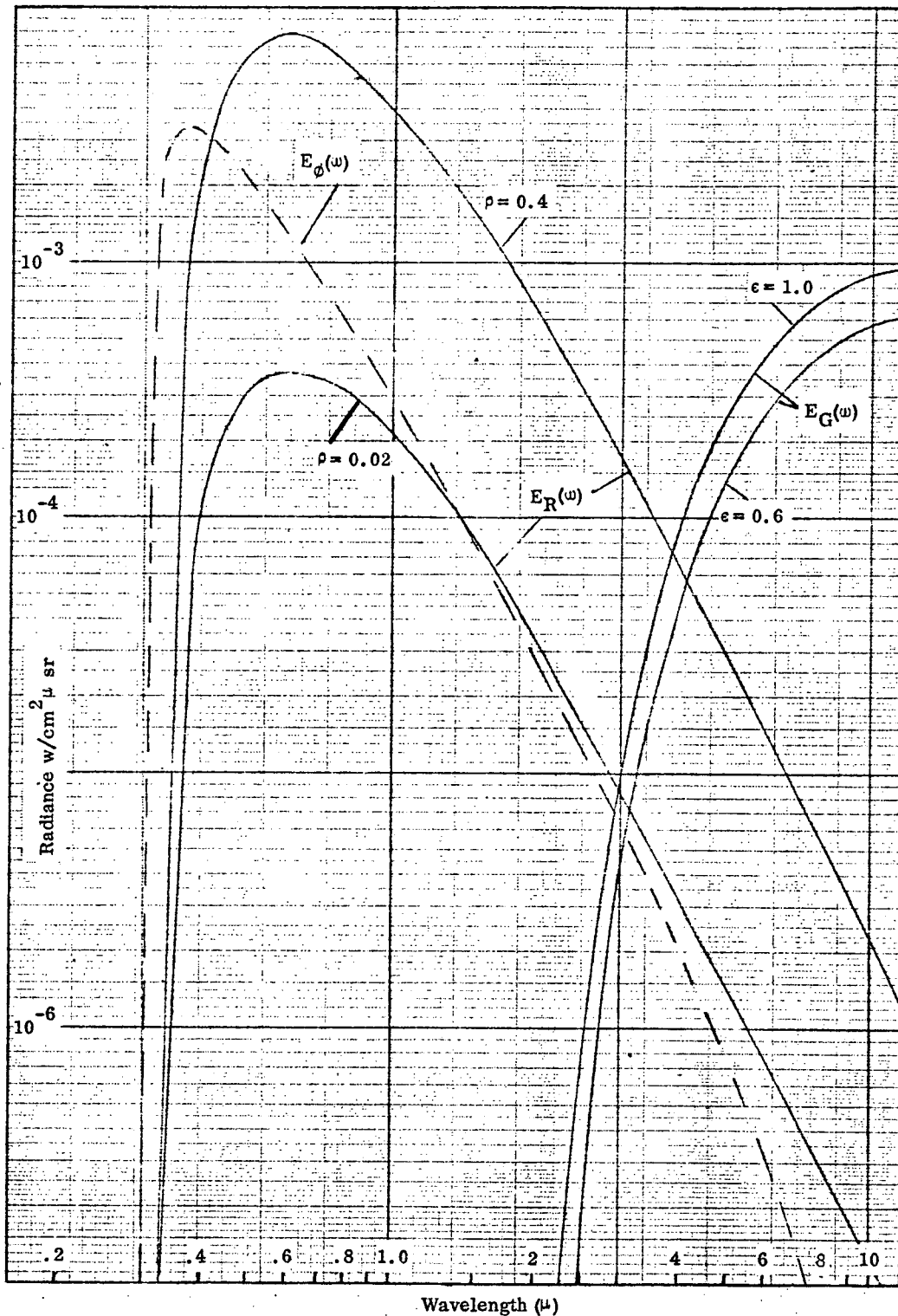


Figure 3-1. Upwelling radiation at the top of atmosphere. Contributions from reflected sun radiation $E_R(\omega)$, atmospheric scattering $E_{\phi}(\omega)$, and thermal radiation $E_G(\omega)$. Ground temperature = 300° K, sun zenith angle = 45°, particulate matter according to Elterman 1968.

calculations of Plass and Kattawar for surfaces with a given constant albedo, extending to infinity. The contribution of this term, especially from surfaces with an albedo different from the surface which is in the field-of-view, will be the subject of further investigation.

It is seen that the amount of sun radiation scattered from the atmosphere is comparable to the amount reflected from the ground. The relative magnitude depends upon the ground reflectivity and the number of scatterers. Thus, in a "clean" atmosphere with the standard Elterman distribution of aerosols and a high ground reflectivity of 0.4, the contribution of the atmospheric scattering (E_{ϕ}) is about 4 per cent of the amount reflected from the ground (E_R) for $\lambda > 2\mu$. (For $\lambda < 2\mu$, the contribution of E_{ϕ} increases rapidly and exceeds E_R for $\lambda < 0.4\mu$). On the other hand, when the atmospheric content of aerosols is larger and the surface reflectivity is low, such as for water, the contribution of E_{ϕ} becomes comparable to the amount of E_R . Thus, it becomes essential to know the term E_{ϕ} before the reflected sun radiation can be utilized for a measurement of a particular pollutant.

In the thermal region, the situation is analogous. The emission from the ground is dependent upon the ground brightness temperature. The species in the atmosphere absorb and emit depending upon the local temperatures and optical thickness. Thus, it becomes essential to know these ground and atmospheric parameters before the thermal region can be utilized for a measurement of pollutants.

3.2 DESCRIPTION OF GAS FILTER CORRELATION INSTRUMENT

The basic principle of operation of a gas filter correlation (GFC) instrument is to pass an undispersed beam alternately through one of two paths terminating on the

same detector: the first, through a cell containing a sample gas, and the second through a vacuum cell and an adjustable aperture which is used in zeroing the instrument. The output of the instrument is the difference of the signals from the two channels.

A detailed analysis of a characteristic GFC instrument was presented in Reference 3. The precise form of the equations depends on the particular geometry of the instrument, since each mirror reflectivity, window transmissivity, etc., must be considered. However, all these items, along with instrument responsivity may be lumped together into certain generalized instrument response functions.

The signal change ΔV is expressed by the equation

$$\Delta V = A \Omega R_0 \int E(\omega) \left[C(\omega) \tau_G(\omega) - C'(\omega) \tau_A \right] d\omega,$$

in which $A \Omega$ and R_0 represent the instrument throughput and responsivity. The quantities $C(\omega)$ and $C'(\omega)$ represent generalized filter functions and contain transmissivities and reflectivities of various components, as well as the transmissivities of filters which have been selected to restrict the operation to spectral regions where absorption bands of the species of interest exist.

The quantities $\tau_G(\omega)$ and τ_A represent the monochromatic transmissivity through the gas cell and the transmissivity of the adjustable aperture. This aperture is set by using a calibration blackbody source and adjusting the aperture until a zero signal is outputted by the instrument. The value of τ_A is given by

$$\tau_A = \frac{\int_{\Delta\omega} N^0(\omega, T_c) C(\omega) \tau_G(\omega) d\omega}{\int_{\Delta\omega} N^0(\omega, T_c) C'(\omega) d\omega}$$

where $N^0(\omega, T_c)$ is the Planck blackbody function at the calibration blackbody temperature T_c .

3.3 DESCRIPTION OF THE POLAYER PROGRAM

3.3.1 The Basic POLAYER Program

The designation POLAYER refers to a family of programs for calculating atmospheric radiance monochromatically. The calculational procedure is basically the same in all versions; the differences are primarily in the input/output format. The operation of the basic POLAYER program will be described first.

The atmosphere is divided into a number of layers (perhaps 10-20), each of which is assumed to be homogenous in temperature, pressure, species concentration, etc. The earth is described by a Lambert surface whose emissivity is inputted as a tabulated function of wavenumber. The reflectivity, assumed to be one minus the emissivity, is used to determine the reflected sunlight, but not (because of the computational difficulties) the reflected atmospheric radiance.

The program provides calculations over a specified wavenumber range. At the initial wavenumber, the equation of radiation transfer is evaluated at several points; at the top of the atmosphere (i.e., in front of the instrument), at the exit of a gas-filled instrument cell, and at the exit of a vacuum cell containing an adjustable aperture.

An increment of wavenumber is determined by the program; this increment is determined by the closeness of spectral lines. When lines are widely spaced, a coarser mesh is permitted; as a spectral line is approached, the mesh becomes finer in order to reproduce the spectral structure about the line center. This internal selection procedure can be over-ridden by specifying a minimum wavenumber increment; this procedure is useful, for example, in simulating cell measurements when some minimum pressure (e.g., of the order of one atmosphere) in the line of sight is known and thus rapid spectral changes will not occur within spectral intervals smaller than some specifiable minimum (e.g., 0.02 cm^{-1}).

As the program proceeds through the selected wavenumber interval, various integrals are calculated by the trapezoidal rule. These integrals include those of the radiances previously described as well as certain other useful integrals of cell transmissivities, atmospheric transmissivities, etc. Aside from these integrals, all other calculated quantities are erased from memory when a new wavenumber is selected.

At each wavenumber and in each atmospheric layer, the absorption coefficient of each spectral line is calculated and stored in memory. The lines are assumed to be of Voigt shape (i. e., a convoluted Doppler-Lorentz shape). A convenient approximate form developed by Whiting⁽⁴⁾ has been used. This form has been shown to reproduce the Voigt shape very closely under most conditions, and with an absolute maximum error of 5% occurring at near-zero pressures.

A major part of the calculational effort goes into the evaluation of these absorption coefficients. Since these are erased after they are used, we have made it possible to calculate a set of results for different pollutant concentrations, either in the atmosphere or in the instrument cell. Thus a set of several calculations may be made at only a very moderate increase in computing cost. This feature is very useful for conducting sensitivity studies.

The program also simulates the calibration of the instrument cell by an on-board blackbody of specified temperature and the setting of the vacuum cell aperture to the balance condition as described in Section 3.2.

The integrals are weighted by an instrument response factor which is read in as a tabulated function and incorporates the detector response and the transmission functions of the filters being used.

3.3.2 Test Calculation with POLAYER for the Solar Spectrum at 4.65 μ

The basic POLAYER program was tested through a calculation of the solar spectrum between 2136 and 2166 cm^{-1} . The line parameters of the fundamental band of $\text{C}^{12}\text{O}^{16}$, $\text{C}^{13}\text{O}^{16}$ and the ν_2 fundamental band of H_2O were inputted⁽⁵⁾⁽⁶⁾. The other

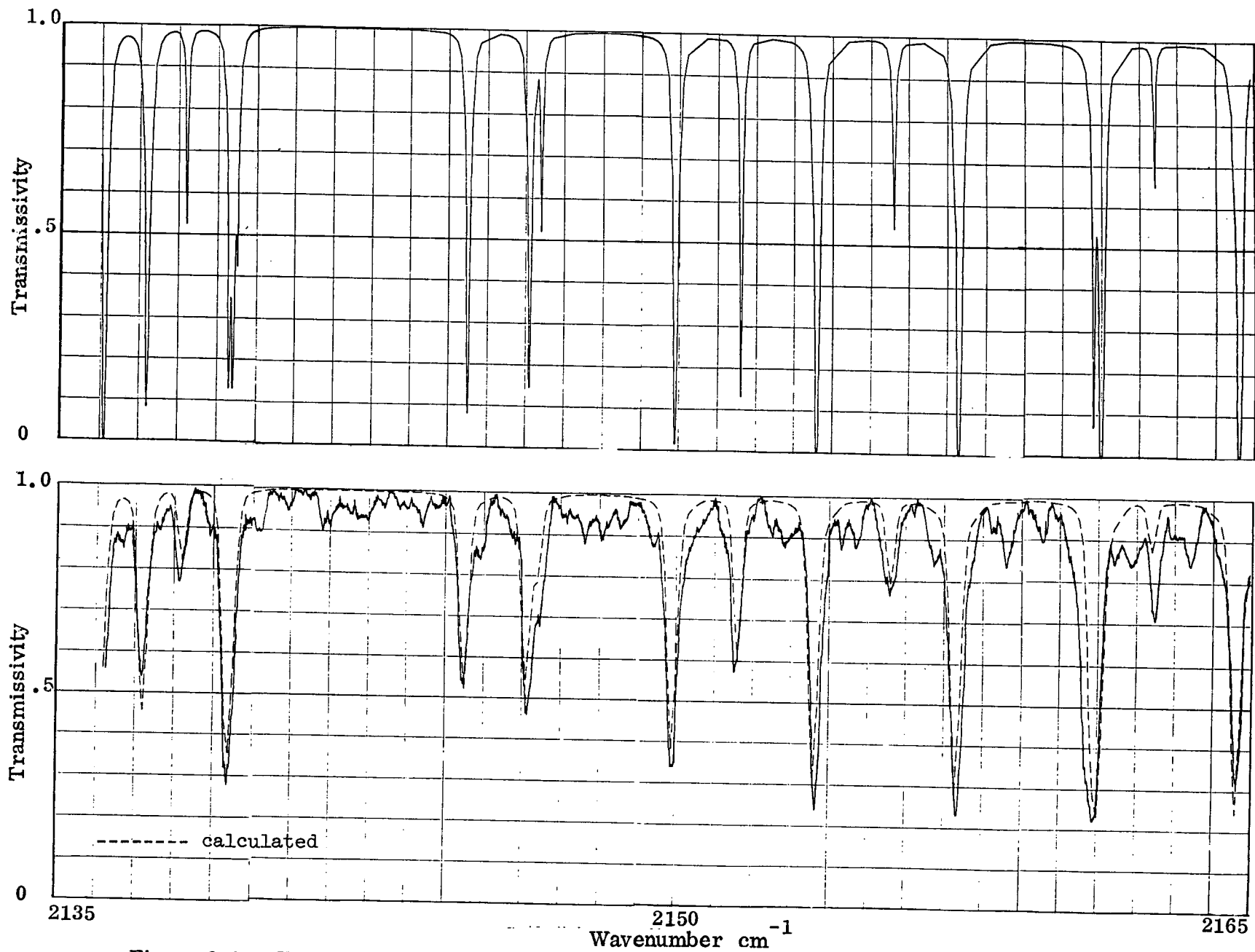


Figure 3-2. Transmissivity of atmosphere between 2135 and 2165 cm^{-1} . Upper trace calculated monochromatically, lower trace calculated with slit function (dashed), experimental curve solid line.

atmospheric constituents CO_2 and N_2O were not included in this calculation. The results of the calculations are compared with the measurements of the solar spectrum by Migeotte et al.⁽⁷⁾ The wavelength interval chosen involves the three plates 28, 29 and 30, for which the sun elevation was 25-32°, 19-25° and 24-30°, respectively. We have used a mean value of 25° for the calculation with POLAYER. In addition to the atmospheric absorption lines, the experimental spectrum contains the Fraunhofer lines of CO. The concentration of CO used in the calculation was 0.1 ppm in the troposphere and 0.001 ppm in the stratosphere. The water vapor concentration at the time of the measurements was listed as 58% relative humidity. In the first test calculations, the standard Gutnick concentration profile was used. However, the comparison between the calculated and experimental results showed that the Gutnick water vapor concentration was too high by a factor of 5. The slit width was listed as 0.2 cm⁻¹, which was also used in the calculations in conjunction with a triangular slit. The results of the calculations with and without a slit function are shown in Figure 3-2. The comparison of the calculated spectrum (degraded by the slit function) with the experimental spectrum shows good agreement, except for a number of weak lines, which are primarily N_2O absorption lines.

3.3.3 Versions of POLAYER

One version of POLAYER has been adapted specifically to the drawing of graphs (e.g., of transmissivity vs. wavenumber). Either (or both) the true monochromatic transmissivity or a transmissivity degraded by a slit function of triangular shape can be generated. This version is most useful for verifying the spectral data written on tape by comparing an experimental spectrum with the synthetic spectrum generated for the same set of experimental conditions.

Another version is designed to calculate the signal outputted by a GFC instrument without the plotting capability previously described (which requires significant core storage).

Different versions also exist to accept spectral line data in varying degrees of refinement. One version (the earliest stage of development) will accept randomly listed (tape or card) spectral line data, sort these by wavenumber, and store them in memory. On very large programs, since all the spectral data are stored in memory all the time, this results in excessive demands on core storage.

A modification was introduced to reduce memory usage. A separate program is used which merges the spectral data from a number of tapes, sorts them, and writes them on a new tape. This tape is then used with a modified version of POLAYER, which reads in and stores data for a limited number of lines at a time, then reads in new data as needed, while erasing the old from memory. In this way, the required field length is kept to a minimum. At the present time three operative versions of the POLAYER program are:

POLAYER I: Includes an automatic plotting routine used for the comparison of calculated and experimental data; and includes a sorting routine for input tapes.

POLAYER II: Automatic plotting routine removed; but includes the same sorting routine as POLAYER I.

POLAYER III: No plotting and sorting routine; accepts only one sorted input tape, which is the output of a separate sorting routine.

Sorting programs have been developed which accept several tapes, each containing spectral line parameters for only one molecule (unsorted as to wavenumber) from program SYMTOP and create a new tape used as input to POLAYER III. On this tape, all lines are sorted by wavenumber, and the line strengths are entered in absolute units.

Since it is no longer necessary to perform the line sorting in POLAYER, only a limited number of lines need to be stored in memory at one time, greatly decreasing the field length requirements, and, consequently, the cost of POLAYER runs. The present status of the logic schematic diagram is shown in Figure 3-3.

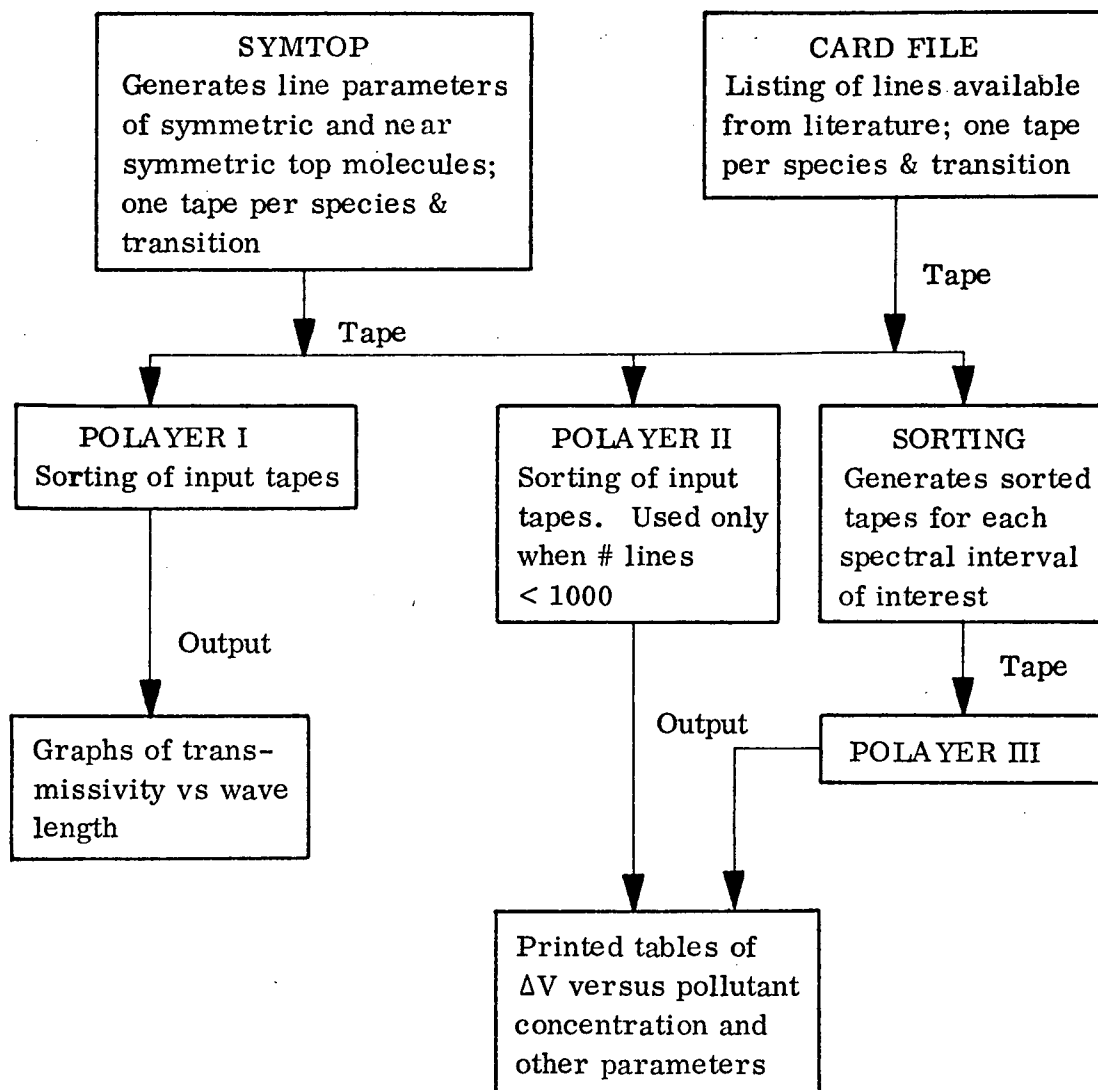


Figure 3-3. Flow diagram of SYMTOPI/POLAYER logic

3.3.4 Future Development of POLAYER

As stated in 3.3.3, the line-by-line calculations are very time-consuming when several thousand lines are involved. The central processor times become prohibitively long when many model calculations are required. Thus, it becomes imperative to investigate different approaches. Before we resort to the band-model

approach, different integration schemes are being investigated. In the present one, a linear interpolation between adjacent points on the spectral line contours is made, which requires very small steps when the radius of curvature is small, as it is near the line centers. An alternate method is to use a quadratic fit between three selected adjacent wavenumbers to achieve a better fit with coarser spacings. Different selection criteria for the points to determine the parabolae should be used for line centers, line wings in the presence and absence of neighboring lines, etc. As an example, computations for two neighboring lines, one from CO and the other one from H₂O, have been performed with the integration schemes. The results are shown in Figure 3-4. The results in terms of line contours are the same but the number of points considered is reduced from 49 in the linear interpolation scheme to 25 values in the quadratic fit.

In the present program, the number of contributing lines is fixed, e. g., at 20 or 40, depending on the spacings and strengths. It is realized that the selection of the number of contributing lines should be more flexible and should be based on the actual wing contribution. This procedure may not decrease the integration time in certain cases, but the calculations would be more precise.

3.4 RESULTS

In the following model calculations, using Eq. (3-1), the contribution of the scattering terms E_{ϕ} and $E_{\phi R}$ have not been considered, because the required Monte Carlo calculations, which include the absorption by the pollutant molecules, have not been performed yet.

3.4.1 Carbon Monoxide

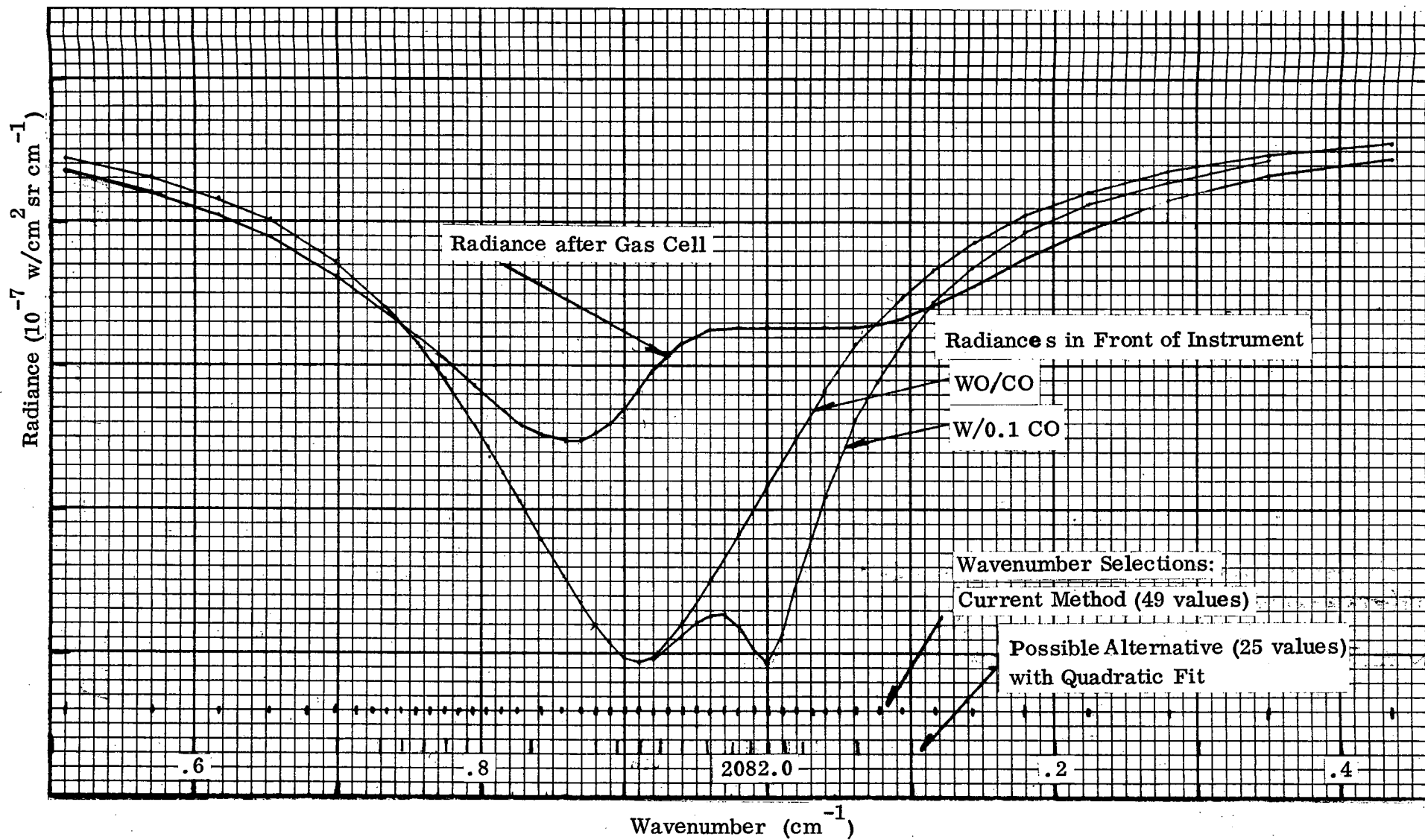


Figure 3-4. Comparison of linear and quadratic interpolation for the line-by-line calculations.

3.4.1.1 Comparison with Band Model Calculations. We have compared the line-by-line calculations with band model calculations. The signal change in radiance integrated over the band pass between clean and polluted atmospheres has been calculated in the line-by-line case to be about 5.75 per cent. The band model calculations are made in spectral intervals of about 0.1μ . If the band model results are averaged over the band pass, the mean signal change is about 20 per cent less than the mean signal change* of the line-by-line calculation. In this case, then, the band model calculations are conservative. More test cases, also with other molecules, have to be run to establish the utility of band model calculations in the majority of sensitivity calculations. Of course, to calculate the possible influence of other interfering gases and the degree of "randomness of correlation", only line-by-line calculations can be used.

3.4.1.2 Influence of Stratospheric CO. The total atmosphere is divided into 20 layers, 8 for the troposphere and 12 for the stratosphere. The distribution of CO was assumed to be 0.025 to 0.4 ppm in the troposphere and 0.001 ppm in the stratosphere.^(7a) By restricting the atmosphere to 8 layers (troposphere only), the signal difference is affected by less than 0.3 per cent for 0.1 ppm and less than 0.05 per cent for 0.4 ppm CO in the troposphere. Thus, it was decided to do the present calculations with only 8 layers since the computing time is cut down by more than a factor of 2. Of course, for a detailed investigation to be conducted later of the influence of the stratosphere (especially of stratospheric H_2O) and of different CO mixing ratios in the stratosphere, the program will be run with 20 layers.

3.4.1.3 Influence of Water Vapor. The atmospheric profile used in these runs together with the water vapor distribution is shown in Figure 3-5. The temperature and pressure profile is the Standard Atmosphere and the water distribution (fractional concentration) is taken from the Gutnick⁽⁸⁾ model called "standard wet" from here

*"Signal Difference" is denoted interchangeably as DV or ΔV .

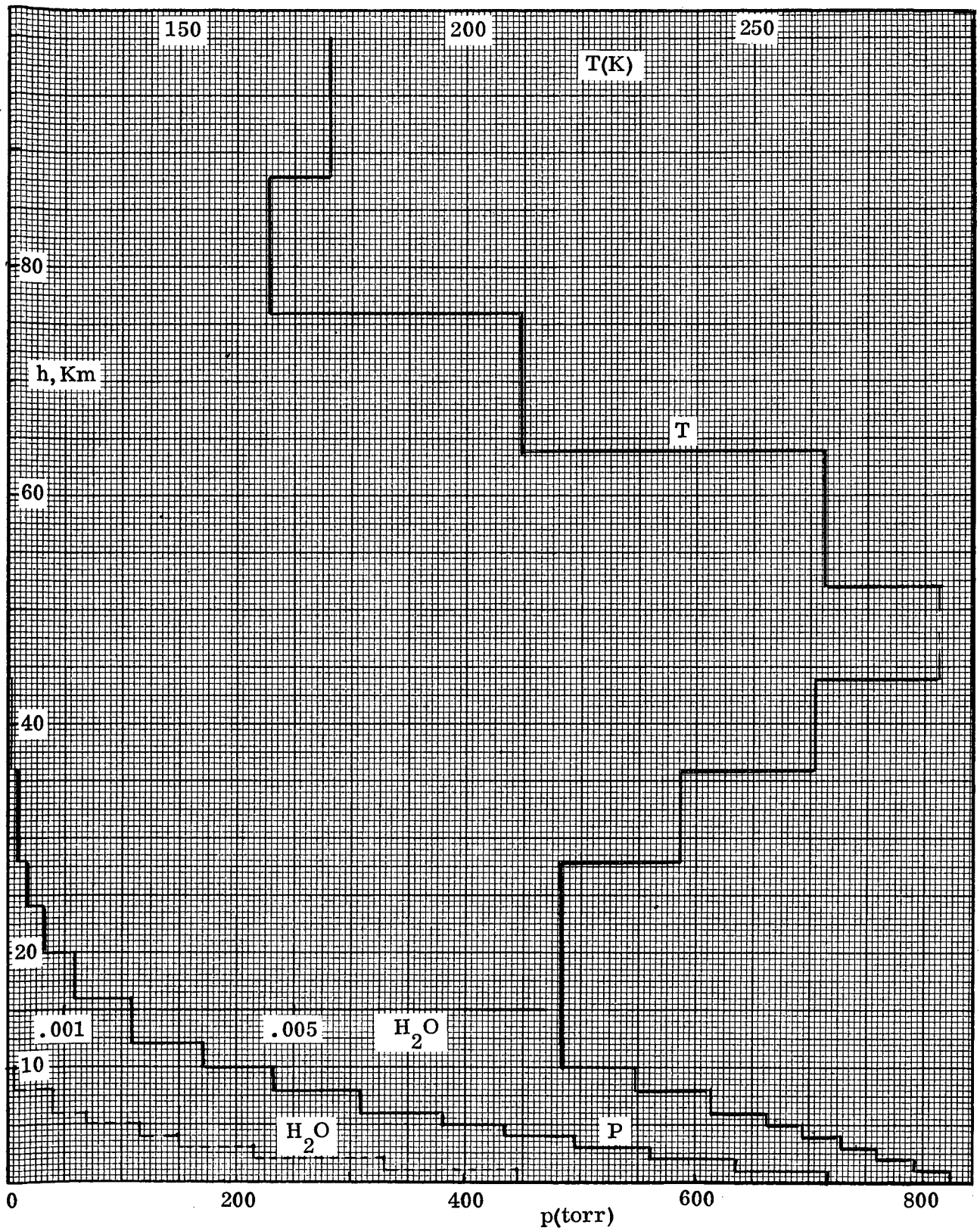


Figure 3-5. Temperature, pressure and water vapor profiles used in the model calculations.

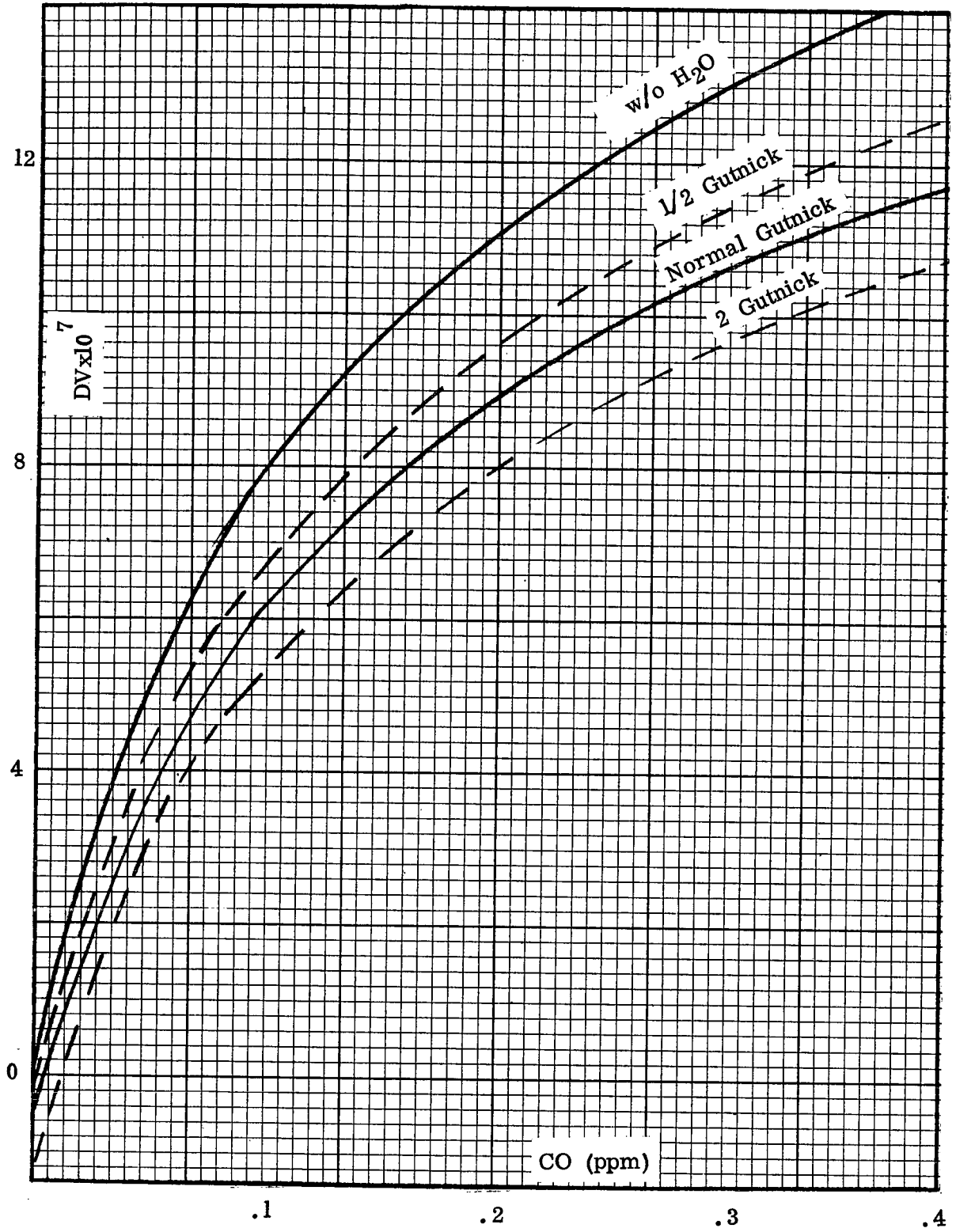


Figure 3-6. Signal difference vs. CO concentration in troposphere for different amounts of water vapor

on. The calibration temperature and ground temperature are 300° K and the ground emissivity is unity. A total of 90 CO lines and 108 H₂O lines were included. A comparison of the results between three different water concentrations and the dry atmosphere is shown in Figure 3-6. As expected, the ΔV is reduced by the presence of water vapor in the atmosphere. This reduction between dry and standard wet atmosphere amounts to about 23% for a CO concentration of .1 ppm. The reduction is caused firstly by the transmission loss due to H₂O and secondly by the "negative correlation," which can be studied when (CO) = 0. In that case, ΔV is negative as seen on Figure 3-6. It means that the water lines are not completely randomly distributed with respect to the CO lines, but correlate with the spacings between the lines of CO. The relative effect of both mechanisms on the reduction of ΔV is shown in Figure 3-7. If the ΔV originating from CO and the standard wet atmosphere is divided by τ_{H_2O} (as calculated by the program), the dashed line is obtained. One can see that the transmission loss is the predominant cause at the higher CO concentration and the "negative correlation" is the primary cause at the lower concentration.

3.4.1.4 Influence of Stratospheric H₂O on CO Measurements. Test runs were made to study the influence of stratospheric water vapor especially in view of neglecting the 12 stratospheric layers. The water distribution was taken from the Gutnick⁽⁸⁾ model up to 31 km and a constant mixing ratio above 31 km as shown in Figure 3-8. The results show that the influence of the stratospheric water vapor is negligible. In Table 3-1, the DV in 10^{-7} w/cm² sr are given for the 8 and 20 layered wet atmospheres and for five different CO concentrations in the troposphere and constant 0.01 ppm evenly distributed in the stratosphere.

Table 3-1. Difference of Signal Changes Due to CO with and without Water Vapor in the Stratosphere

<u>CO</u> <u>ppm</u>	<u>Troposphere</u> <u>Only</u>	<u>With Strato-</u> <u>sphere</u>	<u>Difference (%)</u>
.025	2.1400	2.1825	.2
.05	3.9028	3.9281	.6
.1	6.1361	6.1482	.2
.2	8.6514	8.6563	.05
.4	11.2950	11.2960	.01

It should be noted that these results are conservative since this model assumes relatively high mixing ratios for H₂O. The mixing ratio given by Mastenbrook⁽⁹⁾ is a factor of 10 smaller at 15 km altitude.

3.4.1.5 Model Calculations for CO with H₂O and N₂O. The standard atmospheric profile with a ground temperature of 300°K and a calibration temperature of 300°K was used to calculate the signal difference for different amounts of CO in the presence of H₂O and N₂O having a constant mixing ratio of 0.25 ppm. The value for zero concentration corresponds to a (negative) correlation of either H₂O or N₂O or both with the CO spectrum in the instrument cell. These values are shown for 10⁻⁷ DV in w/cm² sr in Table 3-2.

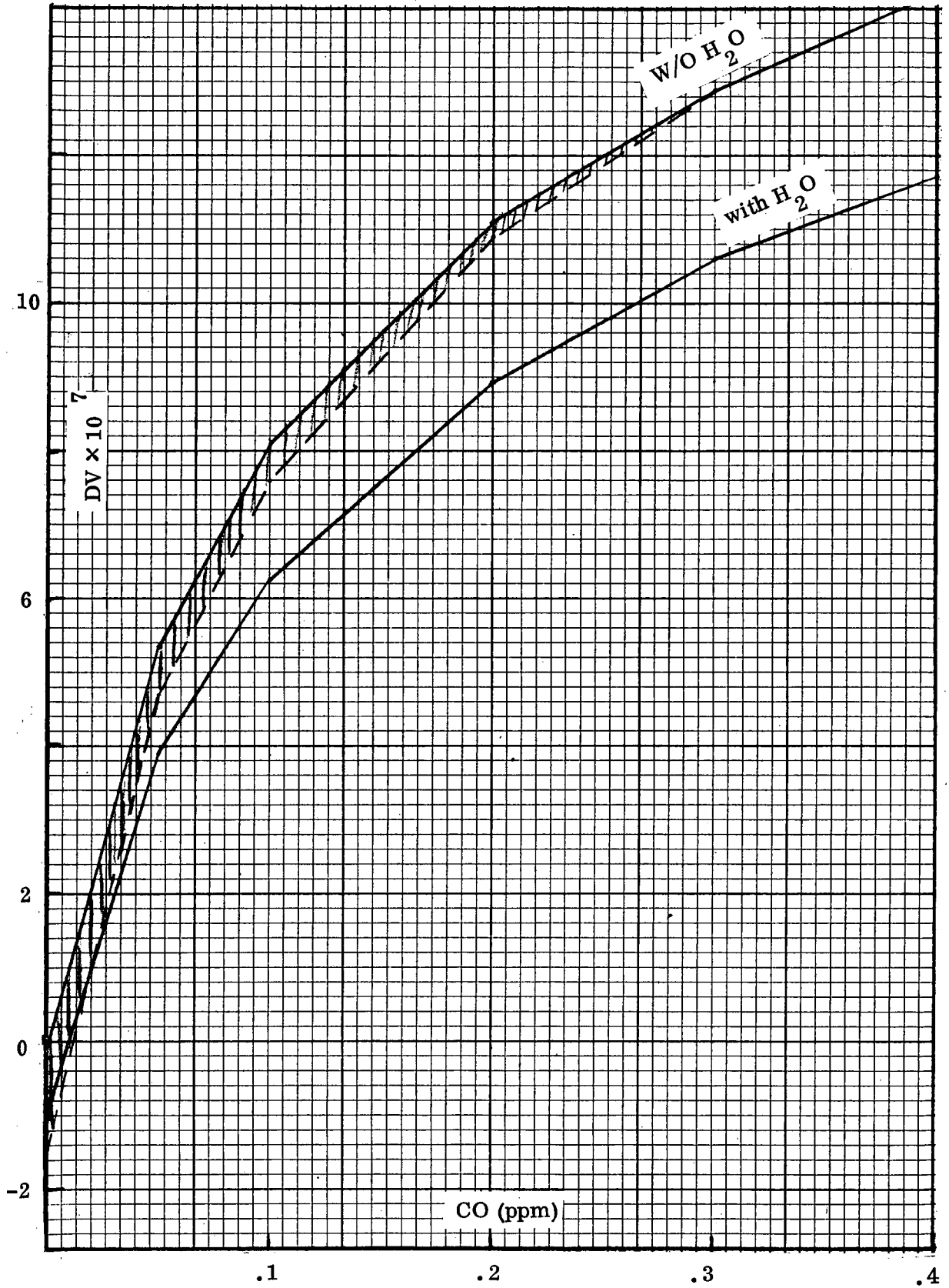


Figure 3-7. Signal difference vs. CO concentration with and without normal water vapor, indicating "negative correlation."

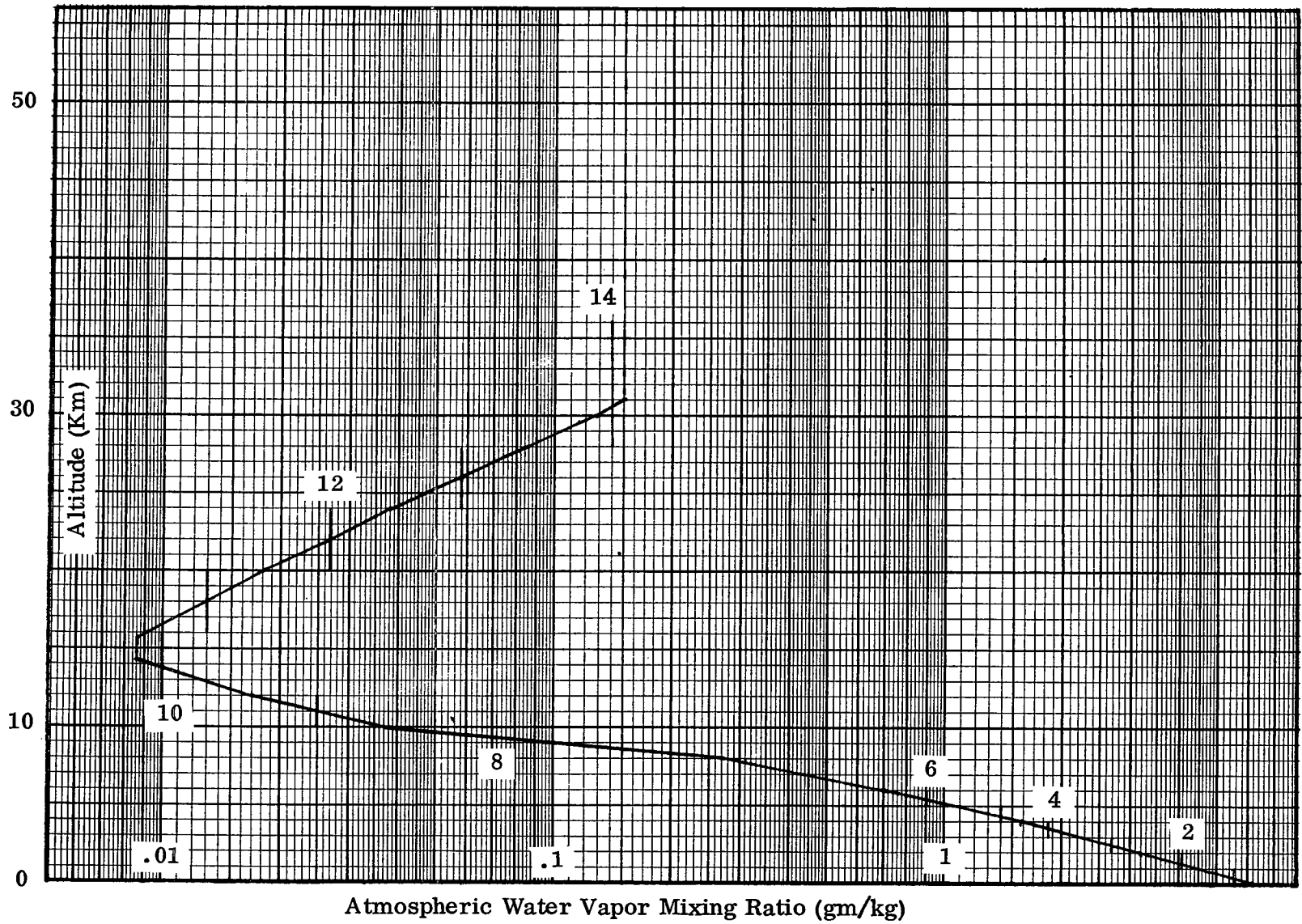


Figure 3-8. Water vapor distribution according to Gutnick

Table 3-2. Signal Change for CO in the Presence of the Interfering Molecules H₂O and N₂O

	CO Only	H ₂ O Only	N ₂ O Only	CO & H ₂ O & N ₂ O
For (CO) = 0	0	- .42	-.06	-.45
For (CO) = .1	8.06	6.19	7.15	5.88
%	0	-6.8	0.8	-7.6

The sensitivity curves for detecting CO in the presence of H₂O and N₂O are shown in Figure 3-9.

3.4.1.6 Model Calculations for CO with H₂O, N₂O, CO₂ and O₃. For the complete evaluation of the influence of interfering gases on the signal differences for CO, CO₂ and O₃ must be included. Although the line parameters for the $\nu_1 + \nu_2$ band of CO₂ have been generated, the model calculations have not been performed yet. The line parameters for the $2\nu_1$ band of O₃ must be generated yet. Although this band is quite weak, it will influence the signal difference for CO to some extent because of the stratospheric ozone layer. It should be noted that this band is of little significance when measurements are made from aircraft platforms.

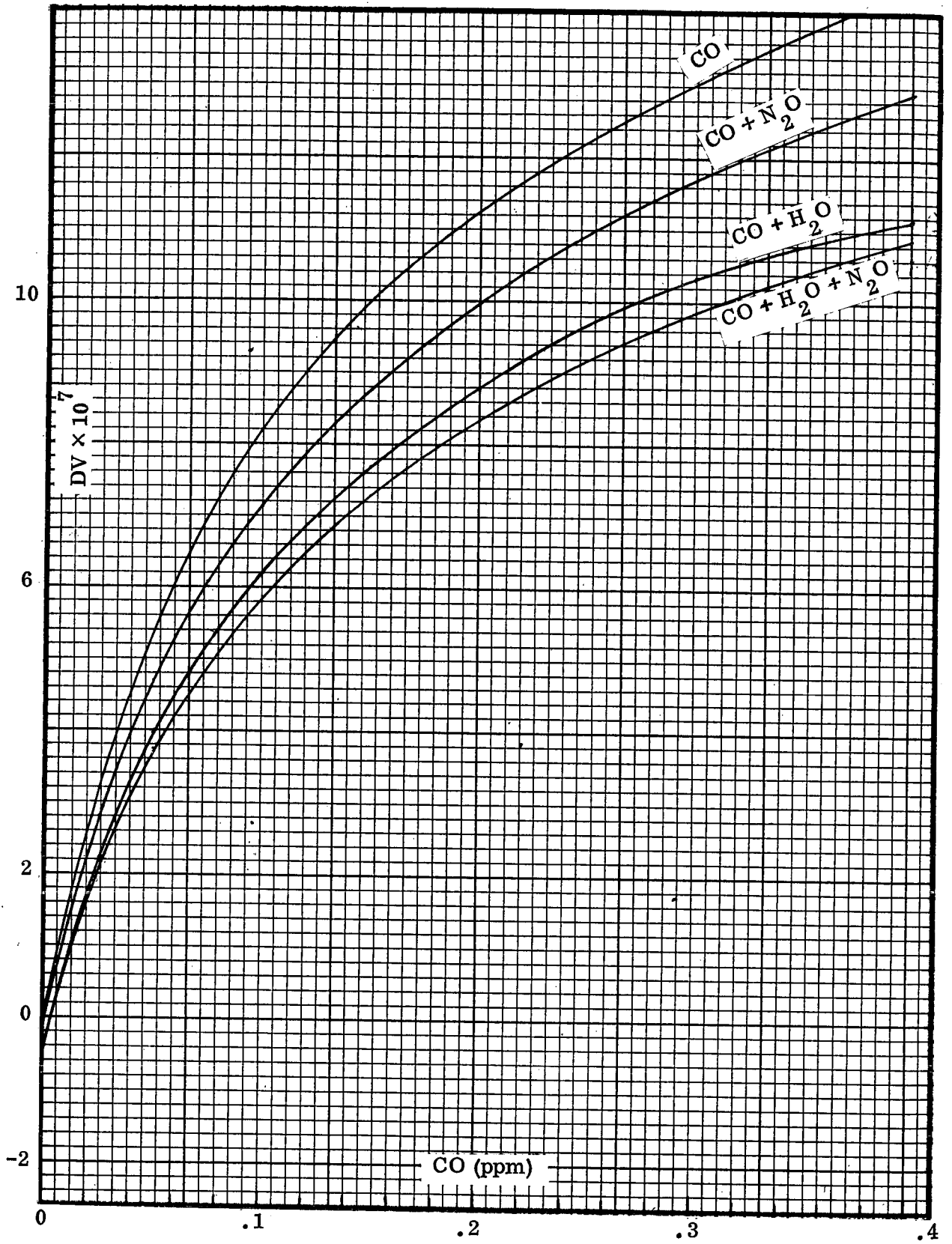


Figure 3-9. Signal difference vs. CO in the presence of N₂O and H₂O

3.4.1.7 Comparison Between DV and Radiance Measurements. For a concentration range from 0 to 0.4 ppm of CO in the dry troposphere, the DV normalized at the value for (CO) = 0.1 ppm is shown as the upper curve in Figure 3-10. The lower curve is the result for the standard wet atmosphere with N₂O, also normalized. As mentioned previously, the reduction in signal difference is partly due to transmission loss and partly due to "negative correlation." One can see that the signal is much more dependent upon the CO than the interfering gases H₂O and N₂O.

The solid line labeled "V" is the radiance integrated over the wave number interval (2070 to 2220 cm⁻¹) as calculated for the dry atmosphere, normalized at 0.1 ppm. The dashed line labeled "V" is the result for the standard wet atmosphere with N₂O. One can see that in this case the radiance is a slowly varying function of CO concentration, but that the radiance is strongly influenced by the interfering gases.

3.4.1.8 The Radiance as a Function of Sun Angle, Ground Emissivity and Temperature.

One of the outputs of the POLAYER program is the integral of the radiance at the entrance of the instrument, i. e., $\int_{\Delta\omega} E(\omega) d\omega$, where $E(\omega)$ is given by Eq. (3-3) and $\Delta\omega$ by the limit values of the spectral bandpass of interest. A square filter function is assumed. When $\epsilon = 1.0$ for all ω , there is no reflected sun energy. For any $\epsilon \neq 1.0$, the reflected sun energy is dependent upon the sun zenith angle θ , i. e., $\theta = 0$ when the sun is overhead, and $\theta = 90^\circ$ represents night time observation. Since $E(\omega)$ is a linear function of ϵ , only one calculation per sun zenith angle was performed. If the calculation is performed for $\epsilon = 0$, the dependency of the ground temperature is removed. Thus, a set of straight lines can be generated from calculations for $\epsilon = 1$ with the ground temperature as a parameter and for $\epsilon = 0$ with the sun zenith angle as a parameter.

Several runs with $\epsilon = 1, 0.9, 0.8, 0.6$ and 0.4 were performed and the linearity verified. Representative plots for $T_{GR} = 270, 300$ and $330^\circ K$ with a constant CO concentration of 0.1 ppm are shown in Figures 3-11 through 3-13.

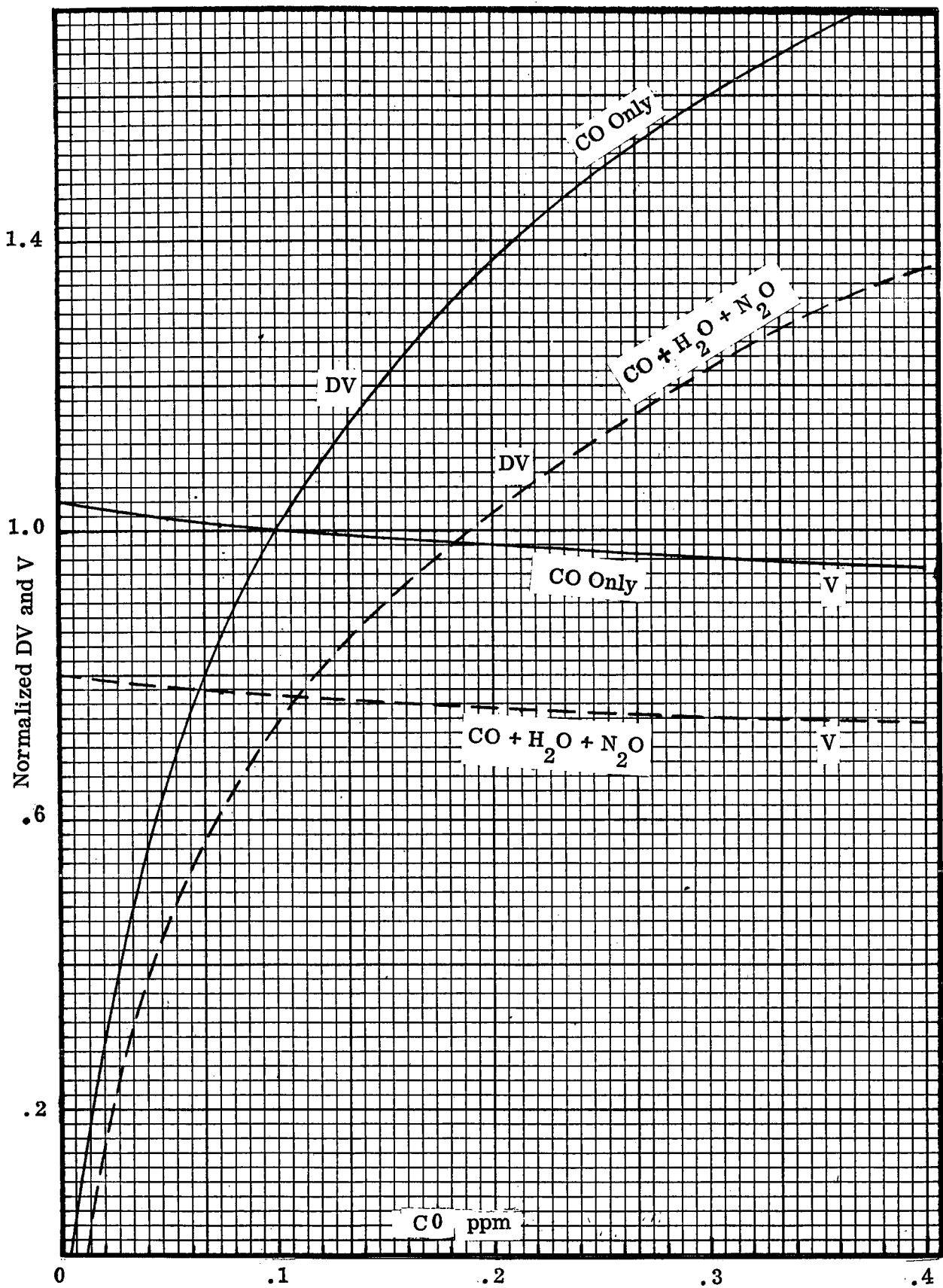


Figure 3-10. Normalized signal difference and radiance vs. CO concentration with and without water vapor.

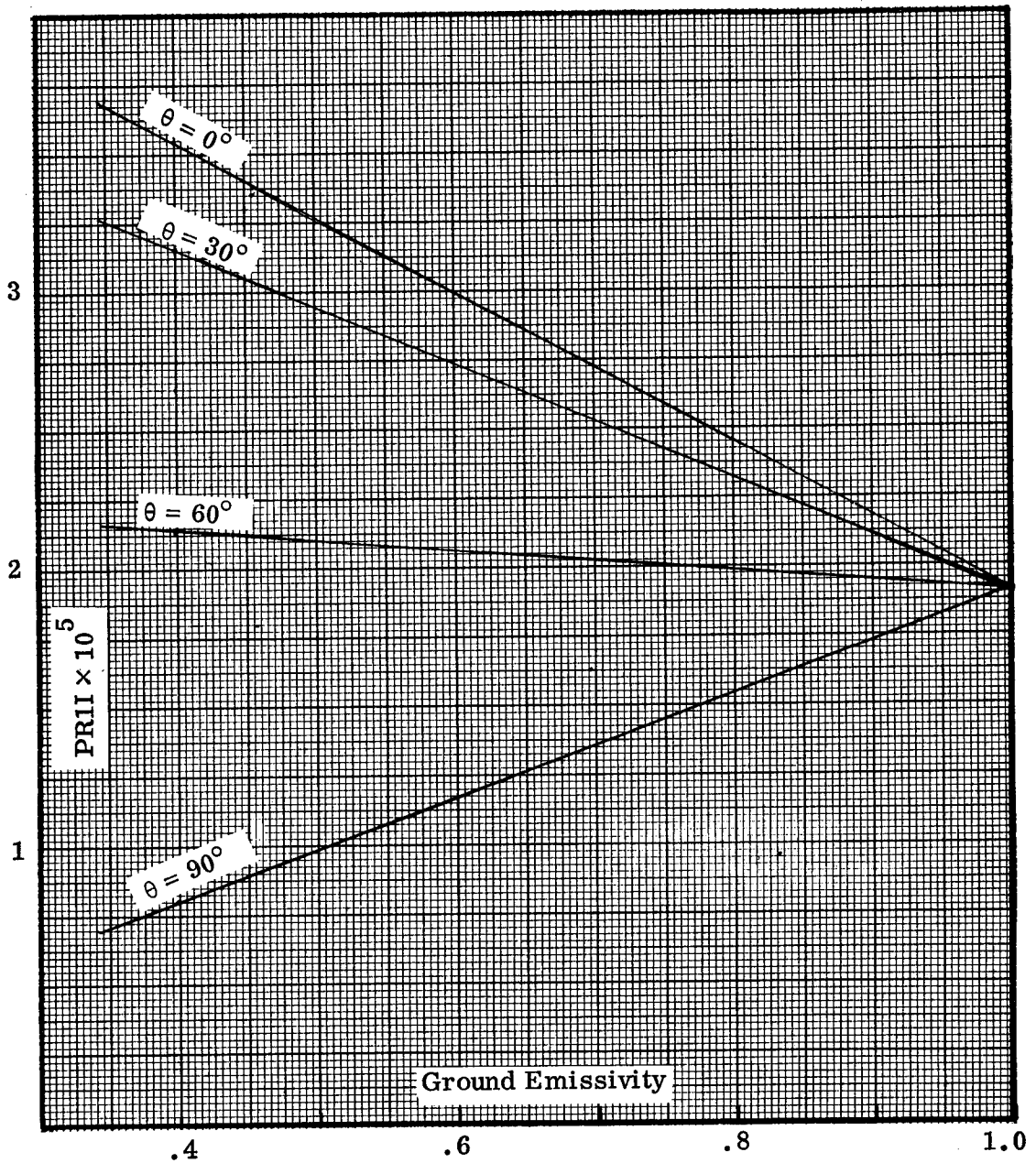


Figure 3-11. Radiance at the top of atmosphere vs. ground emissivity for different sun zenith angles at a ground temperature of 270K and CO concentration = 0.1 ppm

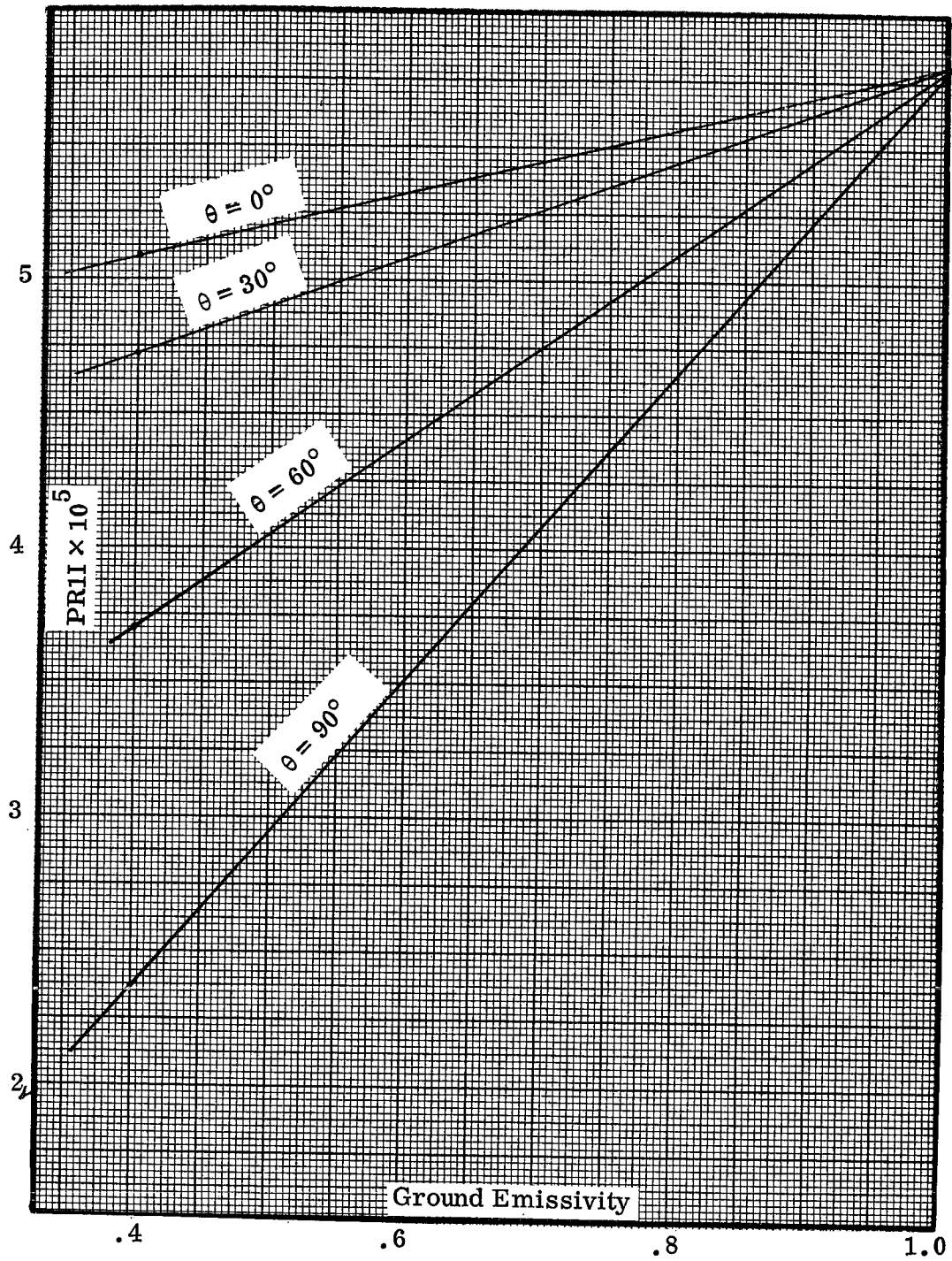


Figure 3-12. Radiance at the top of atmosphere vs. ground emissivity for different sun zenith angles at a ground temperature of 300K and CO concentration = 0.1 ppm

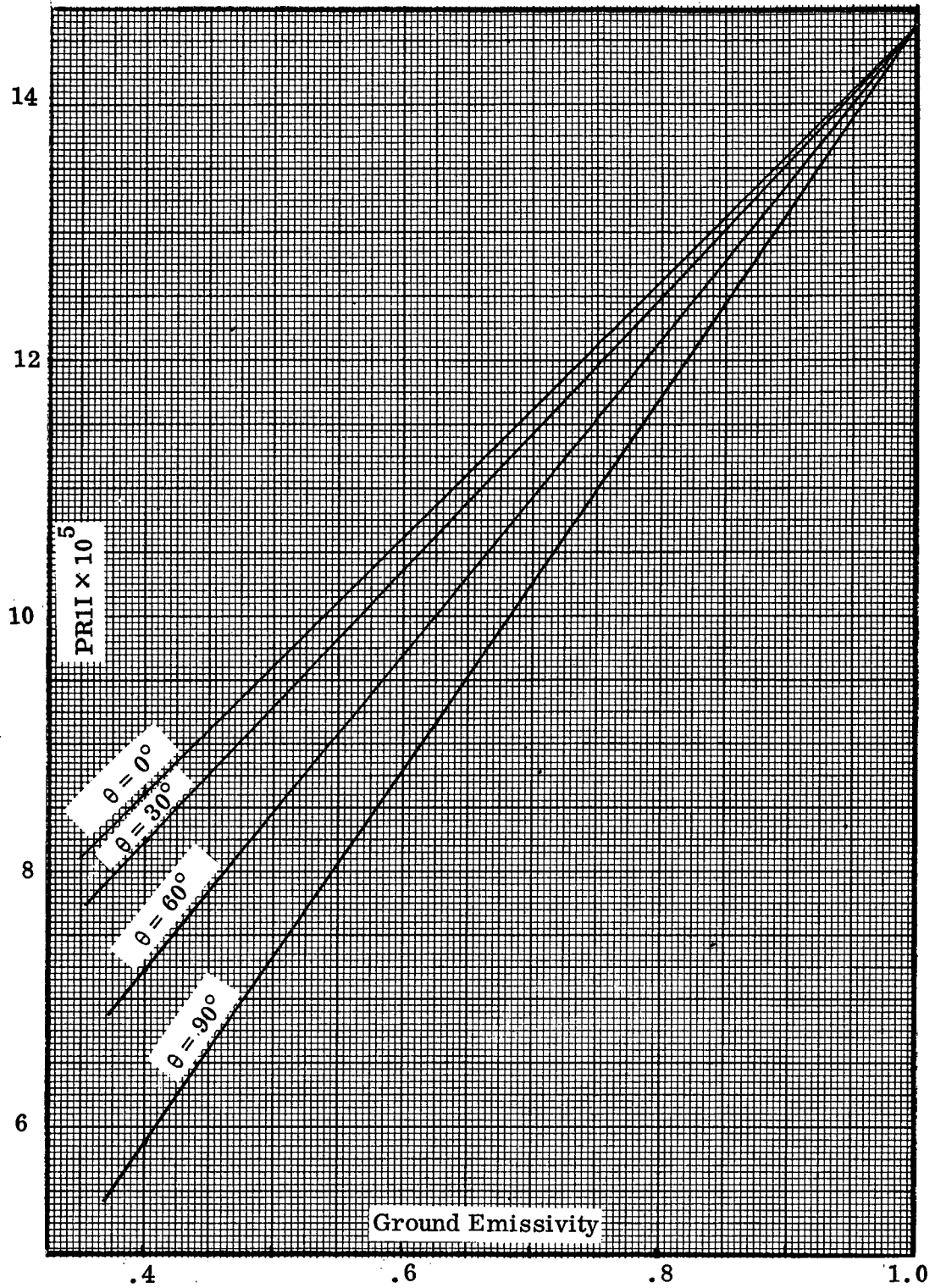


Figure 3-13. Radiance at the top of atmosphere vs. ground emissivity for different sun zenith angles at a ground temperature of 330K and CO concentration = 0.1 ppm

$\int_{\Delta\omega} E(\omega) d\omega$ w/cm² sr. The ordinates are labeled $RR11 \times 10^5$, which is the computer symbol for $\int_{\Delta\omega} E(\omega) d\omega$ w/cm² sr. The atmosphere profile was kept the same. As the temperature difference between ground and atmospheric temperature increases, the radiance becomes larger. Note that different scales in the figures are used. In Figure 3-14 a cross plot of the radiance versus the ground temperature for $\epsilon = 1$ and $\epsilon = 0.8$ and for four different sun zenith angles is presented. This plot illustrates the rapid increase for increasing temperature differences between ground and atmosphere.

3.4.1.9 ΔV as a Function of Sun Angle, Ground Emissivity and Temperature. Similar to the Figures 3-11 through 3-13 are the graphs for ΔV as a function of ϵ , T_G and θ . Straight lines are obtained which are cross plotted for ΔV as a function of CO concentration with ϵ and θ as parameters. In Figures 3-15 through 3-17 are shown the results for 270, 300 and 330° K and a ground emissivity of 1 and 0.8, representing typical values for water and land surfaces, respectively. One can see that for a low ground temperature the ΔV is increasing with decreasing sun zenith angle, but not so for high ground temperatures. This is illustrated in Figure 3-18, where ΔV is plotted as a function of T_{GR} with ϵ and θ as parameters. The line for $\epsilon = 1.0$ crosses over at the higher temperatures. The night time observations are represented by the $\theta = 90^\circ$ curves, which are always lower.

For the cases where the ground temperatures are different from the temperature of the calibration source, deviations in ΔV are observed. Since these deviations are related to the instrument performance, they are discussed in Section 5.

3.4.1.10 Influence of Variable Ground Emissivity on ΔV . The effect of a variable ground emissivity versus an averaged (ω independent) emissivity on ΔV was investigated. The emissivities were taken from the measurements by Hovis⁽¹⁰⁾ for two typical surfaces, silica sand and Pawnee Grassland soil. The spectral emissivity for the silica sand varies from 0.98 at 5μ to 0.78 at 4.6μ and the average emissivity is found to be 0.8426. In Table 3-3 we have tabulated the results (ΔV)

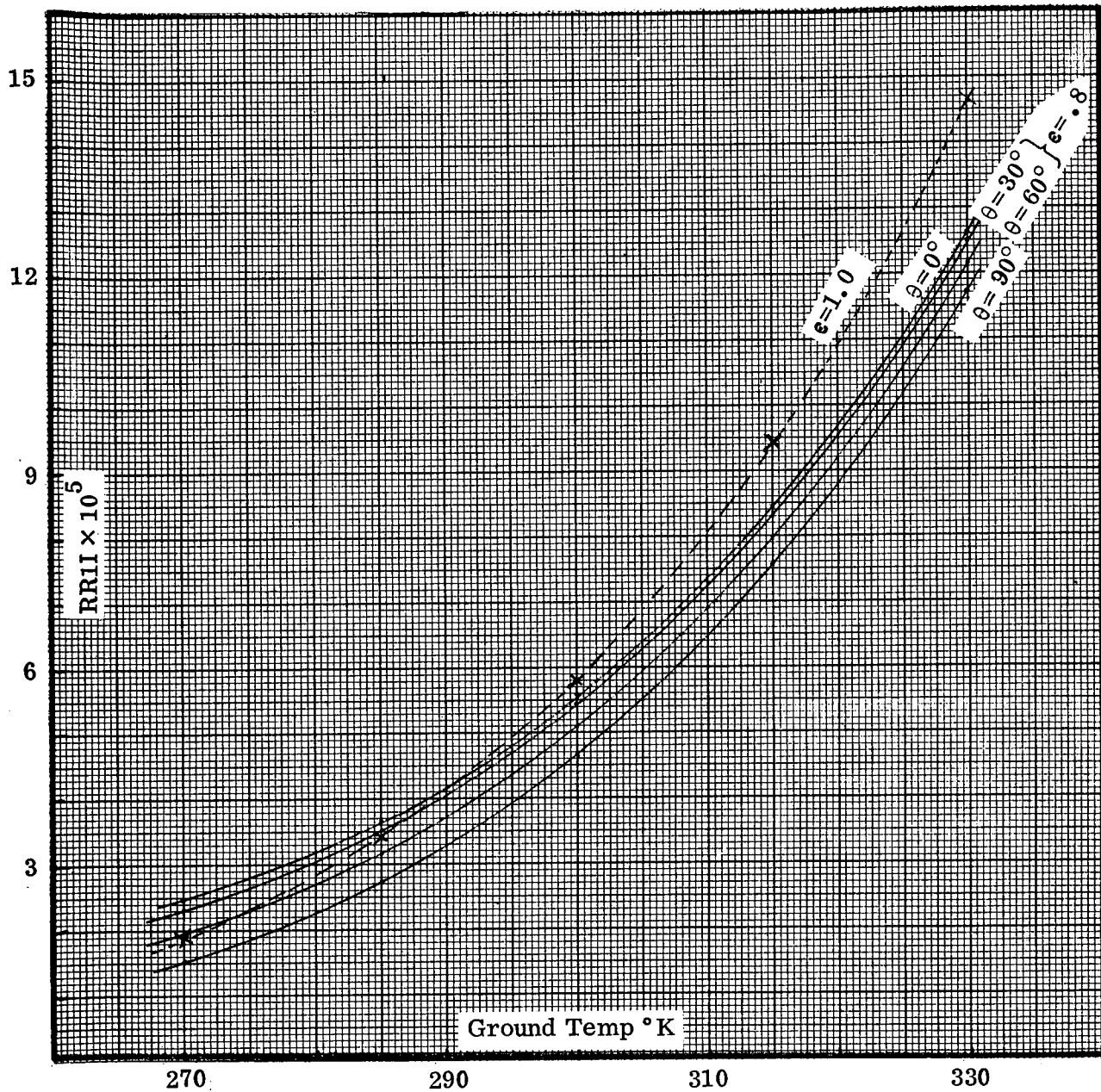


Figure 3-14. Radiance vs. ground temperature for $\epsilon = 1.0$ and $\epsilon = 0.8$ for various sun zenith angles

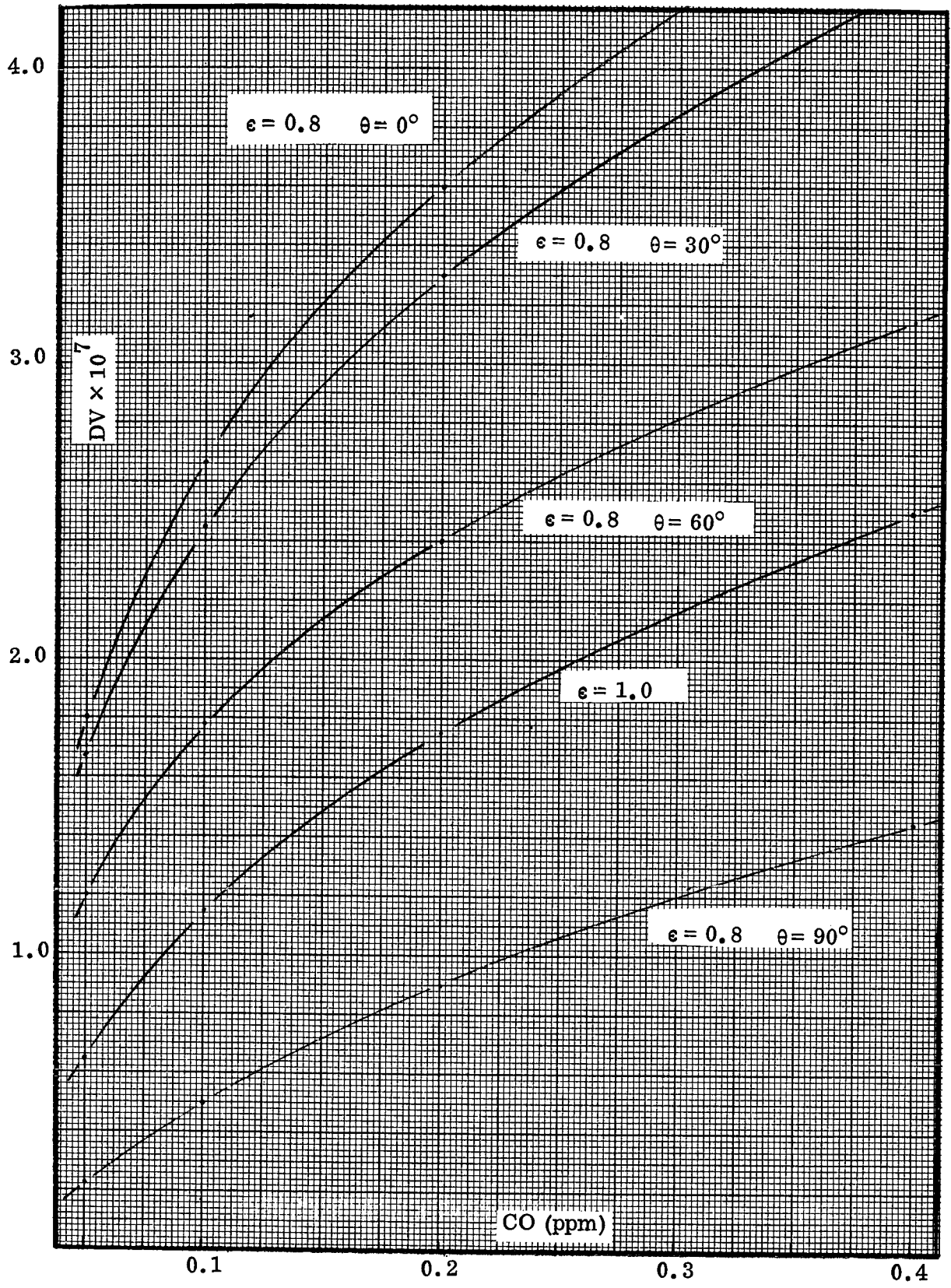


Figure 3-15. Signal difference vs. CO concentration for different sun zenith angles and $\epsilon = 0.8$ and $\epsilon = 1.0$ at ground temperature = 270K

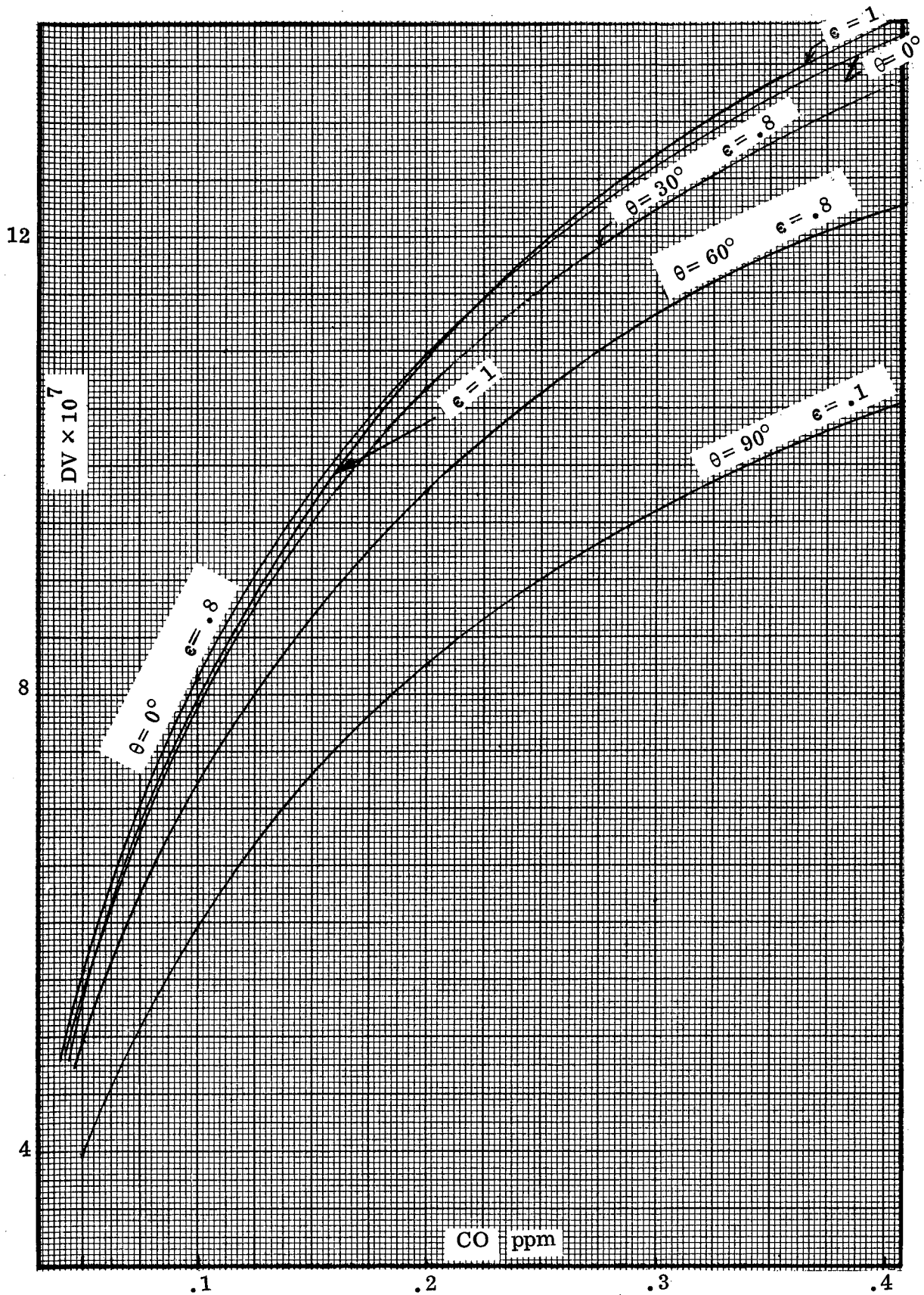


Figure 3-16. Signal difference vs. CO concentration for different sun zenith angles and $\epsilon = 0.8$ and $\epsilon = 1.0$ at ground temperature = 300K

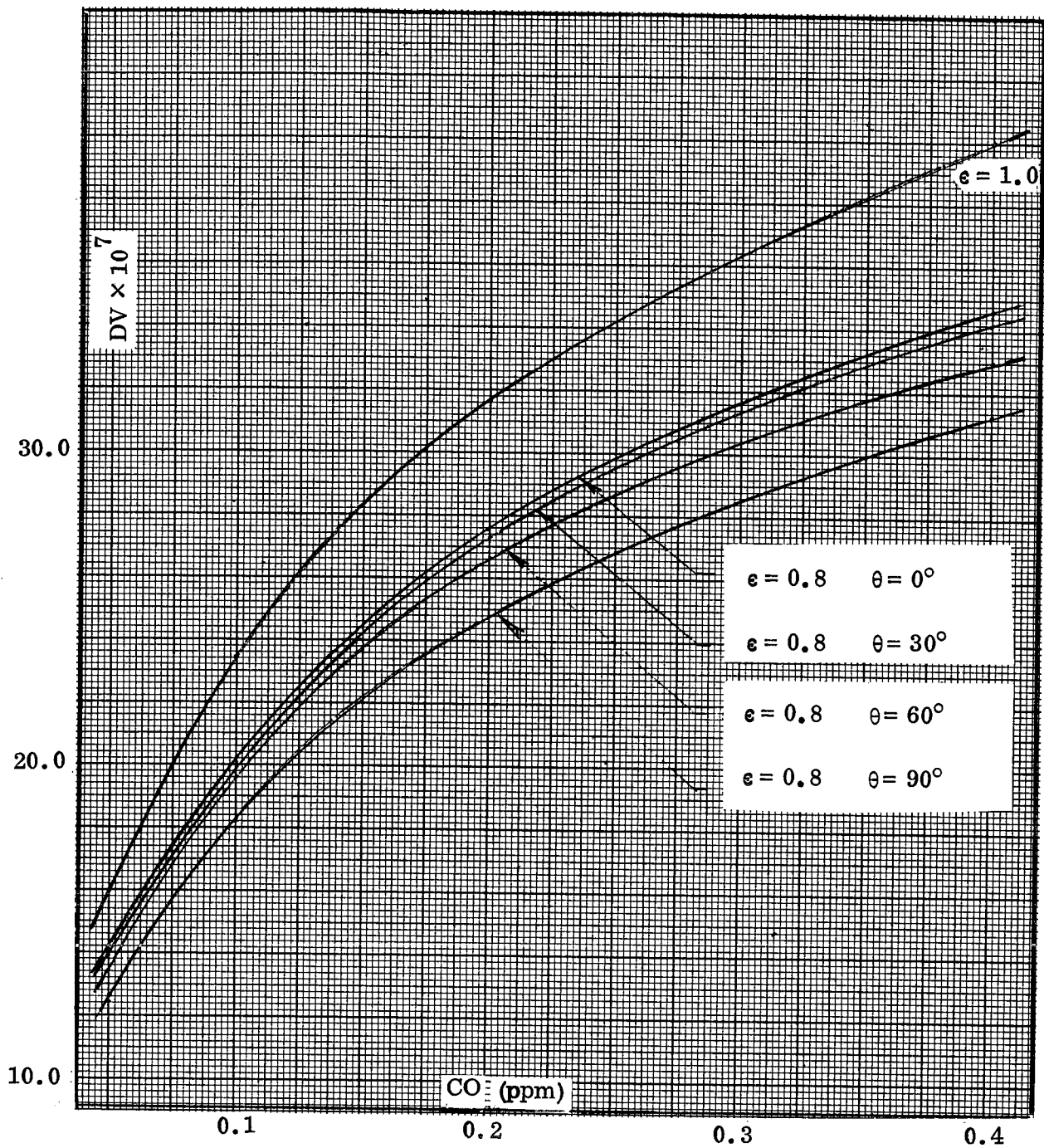


Figure 3-17. Signal difference vs. CO concentration for different sun zenith angles and $\epsilon = 0.8$ and $\epsilon = 1.0$ at ground temperature = 330K

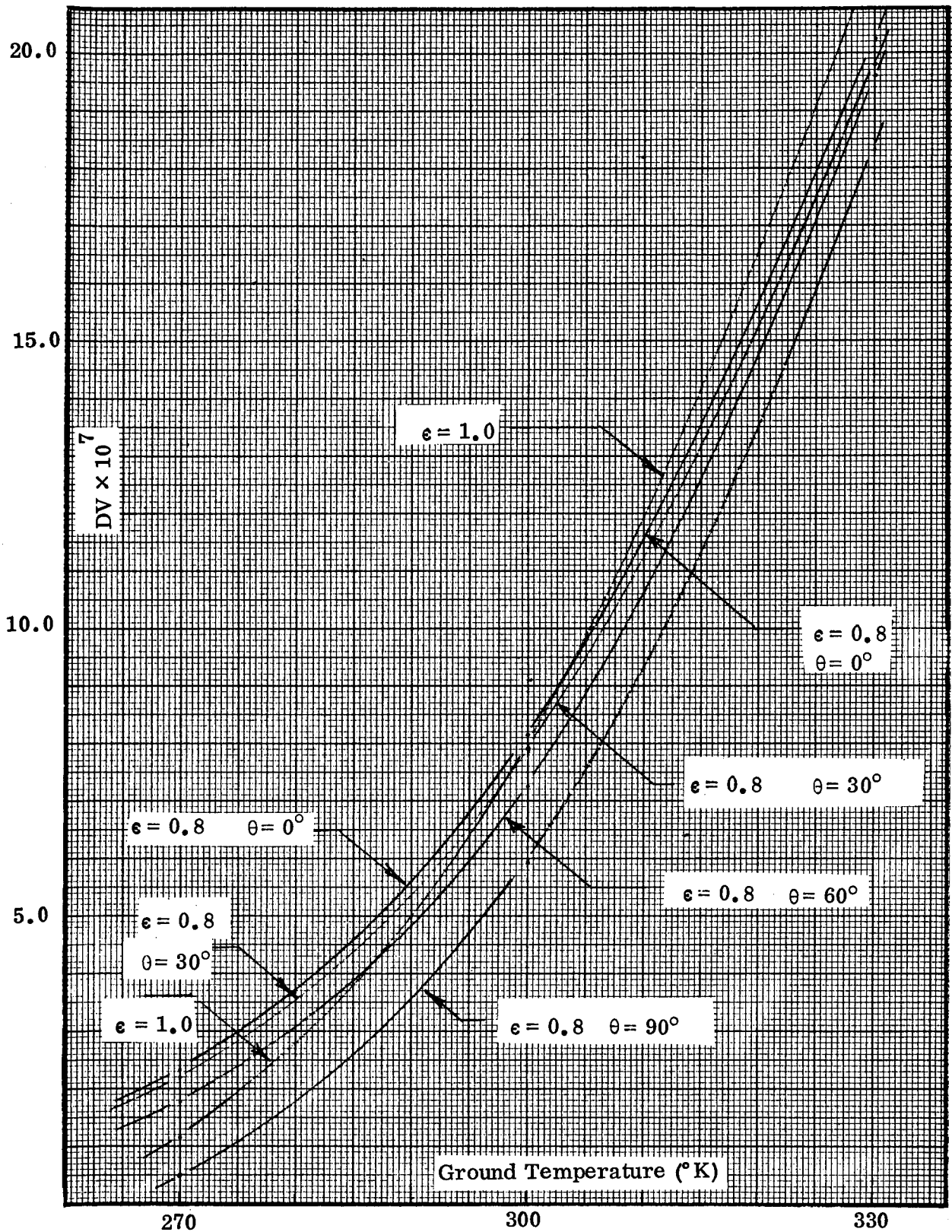


Figure 3-18. Signal difference vs. ground temperature at $\epsilon = 1.0$ and $\epsilon = 0.8$ for various sun angles and for CO concentration = 0.1 ppm

for the silica sand surface, using a dry atmosphere, and a ground temperature and calibration temperature of 300° K:

Table 3-3. Signal Change for CO for Varying and Constant Ground Emissivity

Sun Angle $\theta = 0^\circ$

<u>CO</u>	<u>$\epsilon(\omega)$</u>	<u>$\bar{\epsilon}$</u>	<u>Difference (%)</u>
.05	5.58×10^{-7}	5.53×10^{-7}	.9
.1	8.16×10^{-7}	8.11×10^{-7}	.6
.2	1.10×10^{-6}	1.10×10^{-6}	0
.3	1.27×10^{-6}	1.27×10^{-6}	0
.4	1.39×10^{-6}	1.39×10^{-6}	0

Sun Angle $\theta = 60^\circ$

.05	5.08×10^{-7}	5.03×10^{-7}	1
.1	7.41×10^{-7}	7.39×10^{-7}	.3
.2	9.99×10^{-7}	1.00×10^{-6}	.1
.3	1.16×10^{-6}	1.16×10^{-6}	0
.4	1.27×10^{-6}	1.27×10^{-6}	0

Similar results are obtained with the Pawnee Grassland soil, i. e., the difference between spectral emissivities and averaged emissivity input is insignificant.

3.4.2 Carbon Dioxide

3.4.2.1 Model Calculations for CO₂ at 1.6 μ . Calculations for the condition of a standard atmosphere with 320 ppm of CO₂ ocean surface with a reflectivity of 0.02 and a sun zenith angle of 30° show that the sensitivity of the GFC instrument for measuring a 1% concentration change in the 1.6 μ system (22⁰1) is too low. The band is weak so that the average transmission through the instrument cell for 1 atm CO₂ and an optical length of 10 cm and 100 cm is 0.9995 and 0.9897, respectively, which is too far removed from an optimized condition. To optimize the cell conditions, an optical thickness of 10³ cm atm would be required, which is impractical for space application. The signal change for 320 ppm CO₂ in the atmosphere is about 6×10^{-9} w/cm² sr using a cell transmission of 0.9897. This signal change is further reduced by about two orders of magnitude when changes of 1% in CO₂ concentration are to be measured.

3.4.2.2 Model Calculations for CO₂ at 2.1 μ . The model calculations with the 20⁰1 band system at 2 μ show the potential of measuring the CO₂ concentration to within one per cent. For this band the optical thickness needs to be only about 50 cm atm for an optimized condition, resulting in an average cell transmission of 0.76. However, a cell length of 50 cm would be impractically long. Thus, the present calculations are performed with a cell length of 20 cm and a total pressure of 2.5 atm. More model calculations have to be performed to investigate the influence of the higher than atmospheric pressure. The use of the isotope C¹³O₂¹⁶, which is established to have an abundance of 1.1 per cent of that of C¹²O₂¹⁶, was considered. A stronger band could be used and, thus, the cell length could be reduced. However, the two strong bands are located at 2.7 μ and 4.3 μ , which are heavily overlapped by water vapor and influenced by thermal emission, respectively. More work needs to be done in this area. The dependence of the signal change on the concentration is shown in Figure 3-19 normalized to the signal resulting from a concentration of 300 ppm. The signal level for 325 ppm of CO₂ is about 2×10^{-7} w/cm² sr.

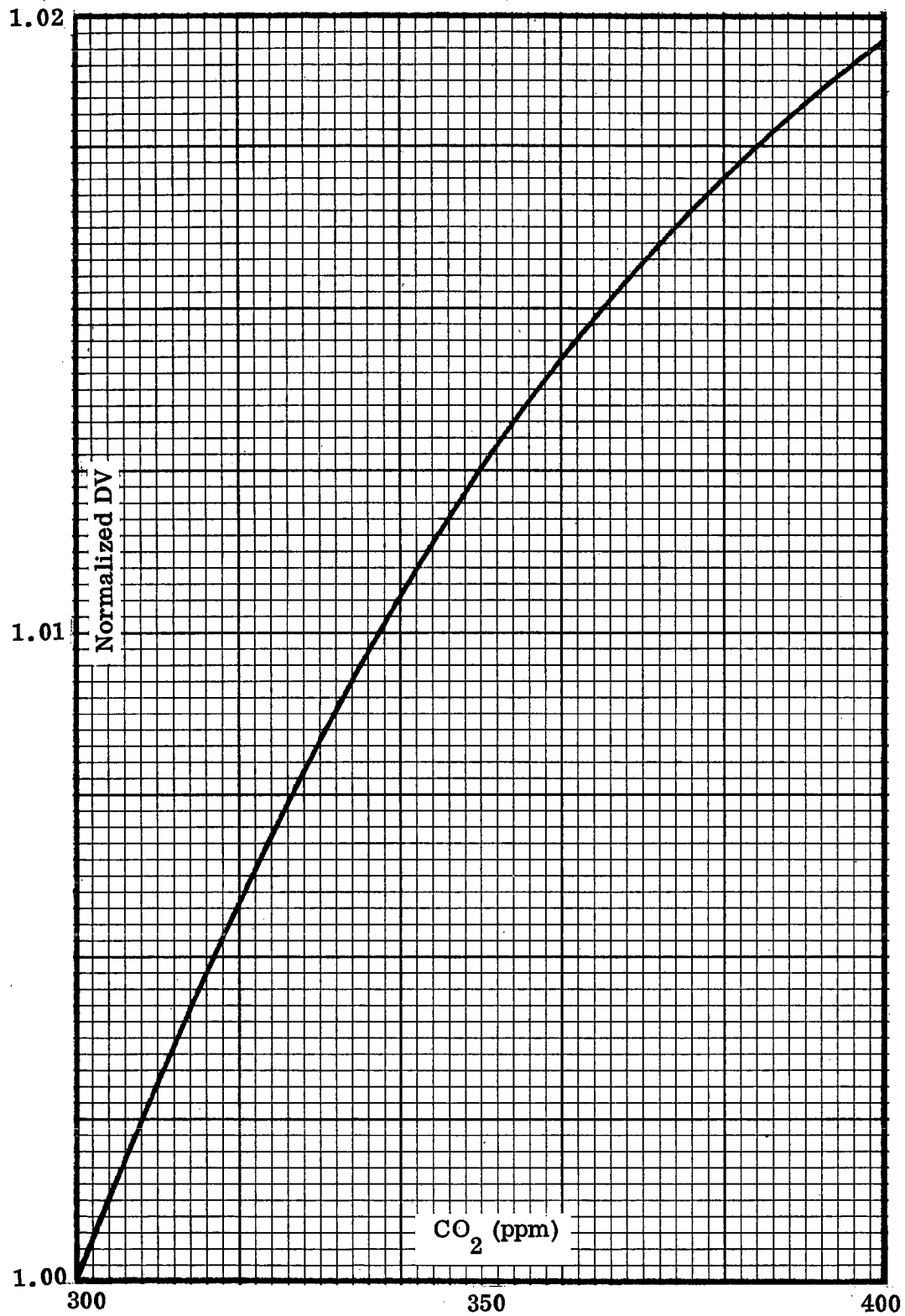


Figure 3-19. Signal difference vs. CO₂ concentration for sun zenith angle = 30°, ground reflectivity = 0.02, ground temperature = 300K

2

However, these results are obtained without introducing uncertainties in the ground and atmospheric variables. In addition, the atmospheric scattering term was not included in the calculations because the functional relationship of the absorption by CO₂ is not known at present and must be established through further Monte Carlo calculations.

3.4.3 Sulfur Dioxide

3.4.3.1 Model Calculations for SO₂ at 8.6μ. A normal U.S. wet atmosphere with a ground temperature of 300°K, and a SO₂ concentration of 2 ppb was assumed to determine the signal difference. A square filter from 8.4034μ (1190 cm⁻¹) to 9.1743μ (1090 cm⁻¹) was used in the instrument. In this region, about 4000 lines of SO₂ and 37 water lines are included. Additional interfering lines from N₂O and O₃ have not been considered yet. The calculations show that the signal difference is in the order of 1.1×10^{-6} w/cm²sr for a cell condition of 5 cm length, 100 per cent SO₂ concentration and 1 atm total pressure. However, these cell conditions are not yet optimized. We estimate that the product of cell length × concentration should be approximately .1 cm-atm for optimum cell conditions. More model calculations need to be performed to establish the final cell parameters and to determine the change of signal difference as a function of different SO₂ concentration profiles and the utility for using two cell pairs.

3.4.3.2 Model Calculations for SO₂ at 4μ. Using a ground temperature of 300°K, a ground emissivity of 0.8, a sun zenith angle of 30° and no interfering gases, a signal change of -1.3×10^{-8} w/cm²sr due to a SO₂ concentration of 2 ppb was calculated. The negative sign appears to be the result of the wavelength dependency of the reflected sun light (~6000°K), which is very much different from the one of the 300°K calibration source used for balancing the two channels. More analytical work needs to be done to understand clearly what that means in terms of data

interpretation. Also, the interfering gases N_2O , CH_4 and perhaps N_2 must be included in future calculations.

3.4.4 Nitrogen Dioxide

3.4.4.1 Model Calculations for NO_2 at 7.6μ . A normal U. S. wet atmosphere with a ground temperature of $300^\circ K$ and a NO_2 concentration of 2 ppb was used to determine the signal difference. A square filter from 7.1429μ (1400 cm^{-1}) to 7.6923μ (1300 cm^{-1}) was used in the instrument. In this region, about 1500 NO_2 lines are included, in addition to water and N_2O lines. Additional CH_4 lines have not been included yet. The calculations show that the signal difference is in the order of $4.5 \times 10^{-7}\text{ w/cm}^2\text{ sr}$ for a cell condition of 3 cm length, 1.66 atm total pressure and 50% NO_2 . As in the case for SO_2 , the cell conditions of 1 cm length with 10 percent of NO_2 at 1 atm total pressure will be near optimum. The difference between measuring NO_2 and SO_2 is in the interference of H_2O , which is much stronger in the case of NO_2 than for SO_2 . However, we believe that the effect of H_2O can be reduced significantly by the ratio technique. (See Section 5.4.) More model runs are required to firmly establish this.

3.4.4.2 Model Calculations for NO_2 at 3.3μ . The conditions used for the model calculations of SO_2 at 4μ have been used here. The calculated signal difference is $-2 \times 10^{-8}\text{ w/cm}^2\text{ sr}$, which is slightly more negative than the result obtained by for SO_2 . The apparent reason for the negative sign is the same as given for $SO_2 - 4\mu$. Further model calculations are needed, which must include the interfering molecules CH_4 and H_2O .

3.4.5 Nitric Oxide

This molecule is very heavily overlapped by H_2O and previous band model calculations had indicated that it will not be possible to observe NO in the atmosphere. The present line-by-line calculations tentatively confirm this conclusion. Using a U. S. wet standard atmosphere, a ground emissivity of .8 and ground temperature of $300^\circ K$

the signal differences for different amounts of NO are the following:

Table 3-4. Signal Change for NO as a Function of Concentration

NO(ppb)	0	0.1	1	10
DV $\times 10^{-7}$	-4.4807	-4.4699	-4.3733	-3.4677
Normalized	1	.9976	.9760	.7739

The negative sign arises from the presence of water vapor due to the negative correlation of its lines with the spacings between the NO lines. This effect may be reduced considerably by the ratio technique. However, the signal change due to a 10% concentration change at 1 ppb is less than 10^{-9} w/cm² sr, which appears to be insufficient.

3.4.6 Ammonia

3.4.6.1 Model Calculations for NH₃ at 10.5 μ . The calculations show that the measurement of NH₃ at 10.5 μ in concentrations of less than 1 ppb is feasible. Calculations were made assuming a ground temperature of 300° K and ground emissivity of 1.0 and the standard dry atmosphere. The signal difference for 20 ppb of NH₃ is 2.33×10^{-5} w/cm² sr. More detailed calculations have to be made in order to establish the sensitivity as a function of different concentration profiles, and ground conditions and the effect of the interfering gases N₂O, CO₂, H₂O and O₃.

3.4.6.2 Model Calculations for NH₃ at 3 μ . In the calculations, a ground temperature of 300° K and a ground emissivity of 0.8 was assumed. The sun zenith angle was assumed to be 30°. The signal difference for 20 ppb of NH₃ without interfering gases was calculated to be -2.1×10^{-7} w/cm² sr. More model calculations, which must include the interfering species CO₂, N₂O, CH₄ and H₂O, are needed to establish

the influence of the atmospheric and ground variables and the λ dependency of the reflected sun radiation on the balance condition.

3.4.7 Formaldehyde

The present calculations tentatively show that the measurement of 2 ppb of formaldehyde at 3.5μ appears to be feasible. The signal difference is about -2×10^{-7} w/cm² sr with optimized cell conditions but without the inclusion of interfering gases. More model calculations are needed to determine the influence of H₂O and HDO and the λ dependency of the reflected sun radiation.

REFERENCES

1. L. Elterman, AFCRL-68-0153, April 1968.
2. G. N. Plass, G. W. Kattawar, Appl. Opt. 9, 1122 (1970).
3. "Development of the Gas Filter Correlation Instrument for Air Pollution Detection," Final Report under contract NAS1-10466, March 1972.
4. E. E. Whiting, J. Quant. Spectry. Radiative Transfer 8, 1379 (1968).
5. Reference 2 of Section 2
6. References 31 and 32 from Section 2
7. Reference 9 from Section 2
- 7a. W. Seiler and C. Junge; J. Geoph. Res. 75, 2217 (1970).
8. M. Gutnick "Aids for Computing Stratospheric Moisture," GRD Research Notes No. 50. AFCRL 203 (1961).
9. H. J. Mastenbrook, J. Atmos. Sci. 25, 299 (1968).
10. W. A. Hovis, Jr. Appl. Optics 5, 245 (1966).

4

MODEL STUDIES FOR AEROSOL DETECTION (TASK 3)

The objective is to determine the feasibility of measuring the atmospheric aerosol content by one or more separate radiometer channels to be included in the GFC instrument.

4.1 EARTH-ORIENTED OBSERVATIONS

Previous work at Convair⁽¹⁾ had indicated that satellite measurements of (a) the intensity of backscattered radiance, and (b) the polarization of backscattered radiance, would yield information on the aerosol content of the atmosphere. Calculations of these parameters exist in the literature⁽²⁾ and further radiance intensity calculations were performed for us under another NASA contract, No. NAS1-10466, by Plass and Kattawar; these calculations were used to assist in determining the feasibility of measuring the atmospheric aerosol content with the GFC instrument.

4.1.1 Radiance Observations

The calculations by Plass and Kattawar made for Convair were designed to determine the dependency of the backscattered (reflected) radiance, as a function of wavelength, on the aerosol content of the atmosphere with an underlying ocean surface, assumed to be a specular reflector. The aerosol distribution and the total number of aerosols were varied. It was found that the upward radiance depends strongly on the total number of aerosols, but not on their vertical distribution. This is an important result. The total number of aerosols is a preferred parameter to measure since it is directly related to the mass loading of the atmosphere.

The previously published calculations of Plass showed that the upward radiance is much more sensitive to the aerosol content when the surface albedo is zero than when it is unity. Thus, the calculations performed for us by Plass and Kattawar were confined to an underlying ocean surface, which has a low albedo (.02) for high sun elevations. In addition to providing more sensitivity for an aerosol measurement the ocean surface has known reflectance properties (see discussion of this assumption in Section 4.1.5).

A detailed discussion of these calculations is given in our report "Air Pollution Measurements from Satellites" being prepared under NASA contract No. NAS1-1-466.

Figure 4-1 shows the variation of normalized upward radiance with μ_0 (cosine of solar zenith angle) as a function of wavelength for the normal aerosol content (1968 Elterman) and three times normal. The calculated points show some scatter about the smooth curves due to the statistical nature of the Monte Carlo method. The curves are not extended into the $\mu_0 = .95$ to 1.0 region where the specular reflection from the ocean surface would be seen by the observer.

*
The three wavelengths considered show comparable sensitivity to aerosol changes. However, the normalized radiance is less at the longer wavelengths, and since the incoming solar flux decreases at longer wavelengths, the absolute radiance level decreases rapidly with increasing wavelength (the absolute radiance at 1.67μ is about 6% of that at 0.7μ). Thus 0.7μ is the preferred wavelength of observation, and although there is some ozone absorption, the calculations show a negligible effect of ozone variations.

*These were selected because previous scattering calculations⁽²⁾ were made at these wavelengths and because the region $\lambda > 0.7\mu$ is little influenced by ozone absorption and Rayleigh scattering.

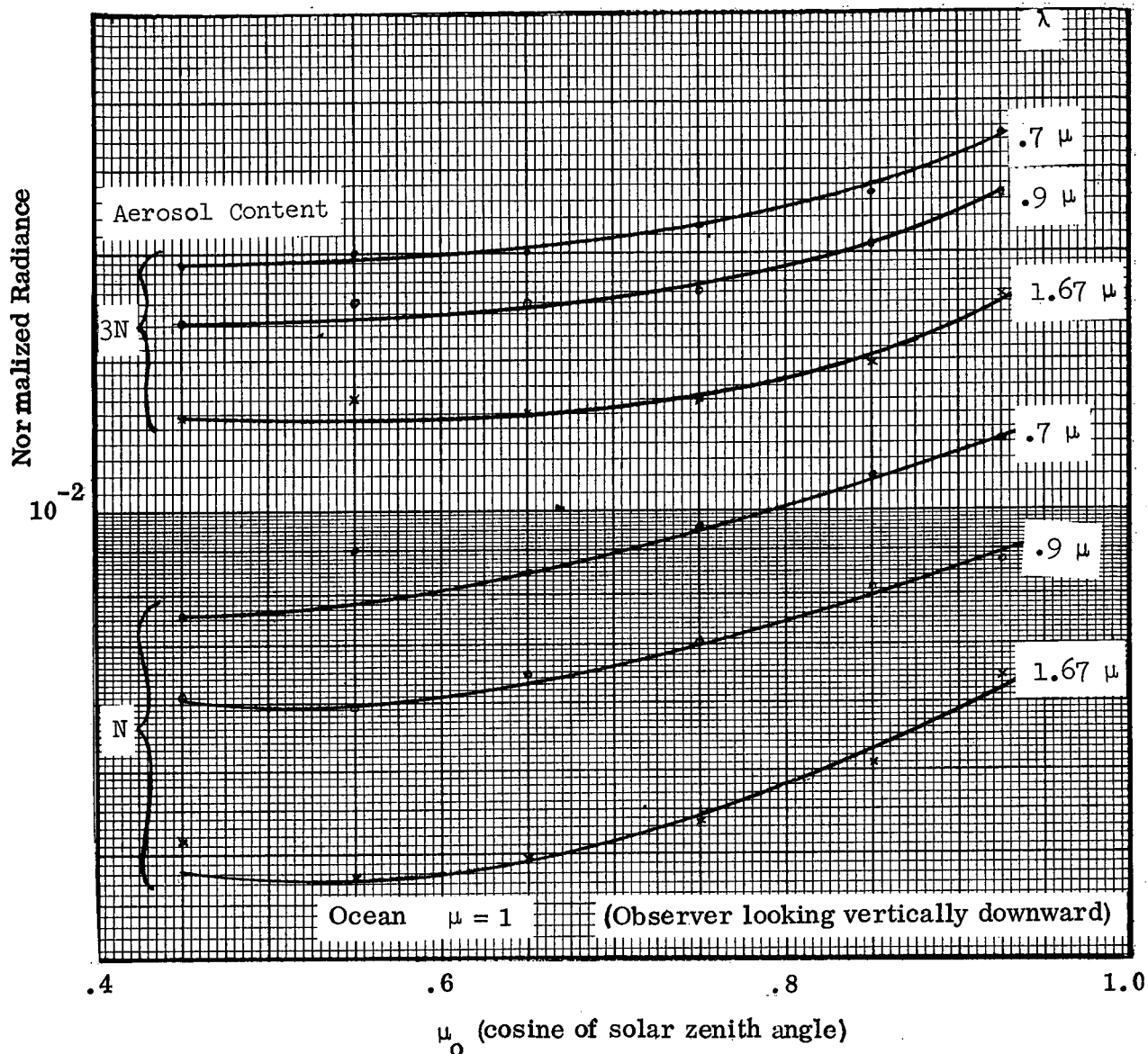


Figure 4-1. Normalized upward radiance vs sun angle as function of wavelength.

The angular distribution of the backscattered radiance is not a sensitive indicator of aerosol amounts, especially in the region $\mu = 0.5$ to 1.0 where observations from a typical polar orbit of 600 nmi altitude would be constrained due to the fact that a look angle of $\mu = 0.5$ is approximately tangent to the earth's surface. Also, non-vertical look angles would have a greater probability of having clouds in the field of view.

The smoothed data in Fig. 4-1 are replotted in Fig. 4-2 to show the relationship between the upward radiance, normalized to unit incident solar flux, and the aerosol content of the atmosphere for various sun angles. A simple linear relationship is shown to exist between radiance and the mass loading. These straight lines are based on only two values of mass loading, but a linear relationship may be established by considering the published data of Plass and Kattawar for zero albedo, which are shown in Fig. 4-2.

It is concluded then, for the ideal model conditions that the aerosol content of the atmosphere can be determined from radiance measurements from a satellite looking vertically down at the ocean at a wavelength of $0.7\ \mu$. For the real atmosphere and ocean certain problems arise, as discussed in Section 4.1.5 so that more than one wavelength of observation will be needed.

4.1.2 Polarization Observations

The polarization of radiation scattered by molecules is greater than that scattered by particles. Thus the polarization of radiation scattered by the atmosphere is reduced as particles are added to the atmosphere. It is this difference in polarization from that of the theoretical Rayleigh atmosphere which must be analyzed to determine the aerosol content. The aerosol content cannot be deduced directly due to the complexities of the coupling of Rayleigh and Mie multiple scattering and the presence of non-Lambertian surfaces, and must be determined by comparing the measurements with calculations for model aerosol atmospheres.

Sekera⁽³⁾ has discussed the theory of this type of observation, and Hariharan⁽⁴⁾ has performed aircraft measurements, making some deductions about the aerosol size distribution. However, the models used did not account for multiple scattering.

Plass and Kattawar⁽²⁾ have made Monte Carlo calculations, including multiple scattering, of the polarization of radiation scattered by realistic model atmospheres with various aerosol contents at wavelengths from $0.27\ \mu$ to $1.67\ \mu$. The wavelength most sensitive to aerosol changes is $0.7\ \mu$; at shorter wavelengths the Rayleigh

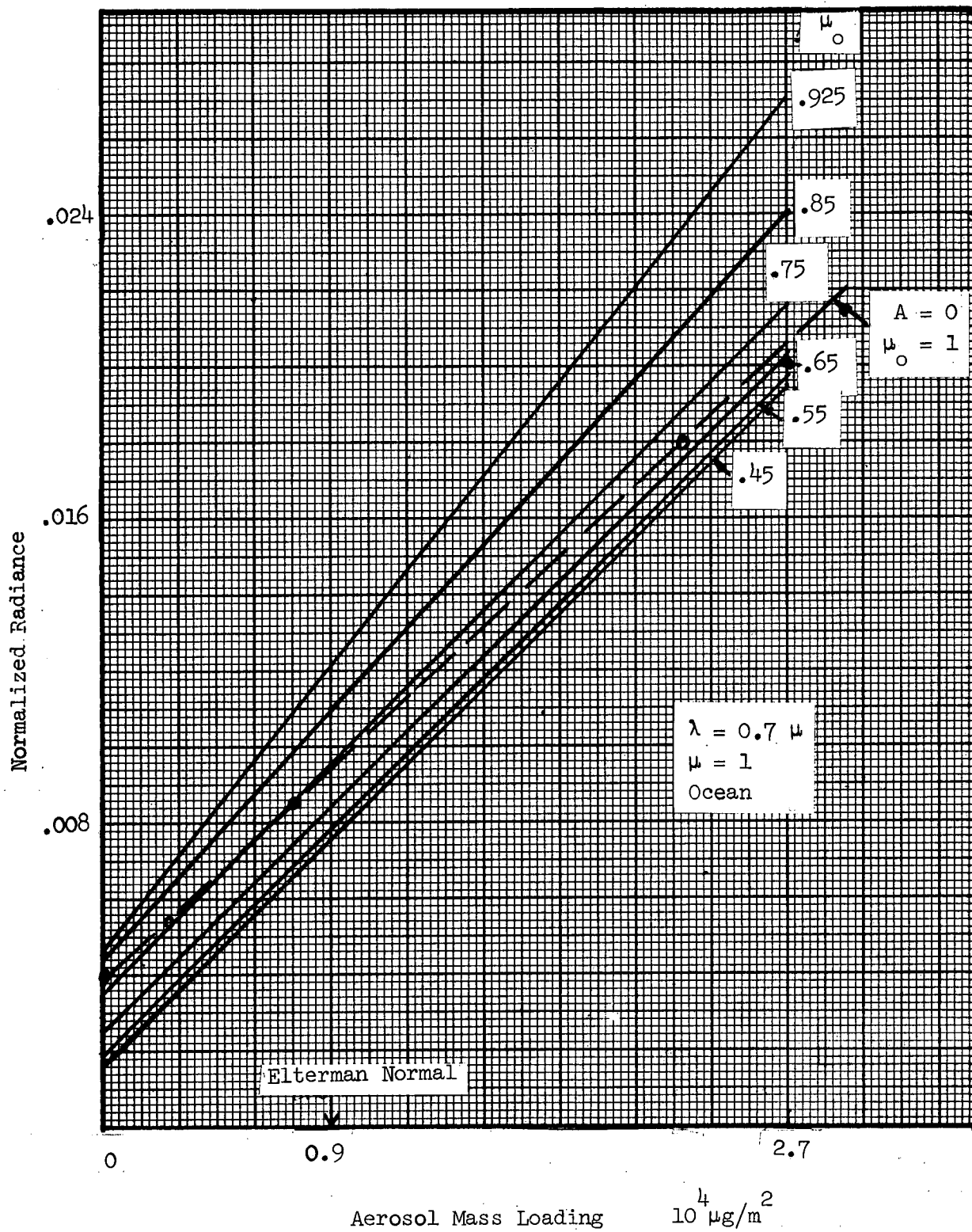


Figure 4-2. Normalized upward radiance vs aerosol mass loading as function of sun angle

optical thickness is much greater than the aerosol thickness and the molecular polarization dominates, and at longer wavelengths the polarization is small with corresponding small effects by aerosols.

As in the case of radiant intensity observations the effect of aerosols decreases as the albedo increases, so that measurements of polarization over low-albedo surfaces are desirable. Unfortunately, as found by Coulson et al.⁽⁵⁾ low reflectance surfaces are highly polarizing; this would make the modeling and data interpretation difficult.

For an overhead sun, the most sensitive look angle, from the calculations of Plass and Kattawar, is given by $\mu = 0.35$. However, as pointed out earlier, for NIMBUS-type orbital altitudes, observations are limited to $\mu = 0.5$ to 1. The sensitivity decreases as μ increases, i. e., looking towards the horizon is preferred. However this look angle will almost certainly include clouds in the field of view which would complicate the data interpretation.

The results of Plass and Kattawar for a wavelength of 0.7μ are presented in Fig. 4-3. The curves illustrate the decrease of sensitivity as the look angle approaches the vertical, although there is little difference between $\mu = .55$ and $\mu = .15$. It should be noted that these curves are for zero albedo; there are currently no calculations available on the polarization of the upward radiance over an ocean surface (since polarization calculations are considerably more complex than calculations of radiance only), so the discussions here are limited to calculations for zero albedo. Thus the values of polarization and their sensitivity to aerosol content are higher than are to be expected in the real atmosphere with an underlying non-zero albedo.

The calculations of Plass and Kattawar have been made mainly for an overhead sun, whereas for satellite observations it is of more interest to consider the observer looking vertically down with a variable sun angle. Unfortunately a simple

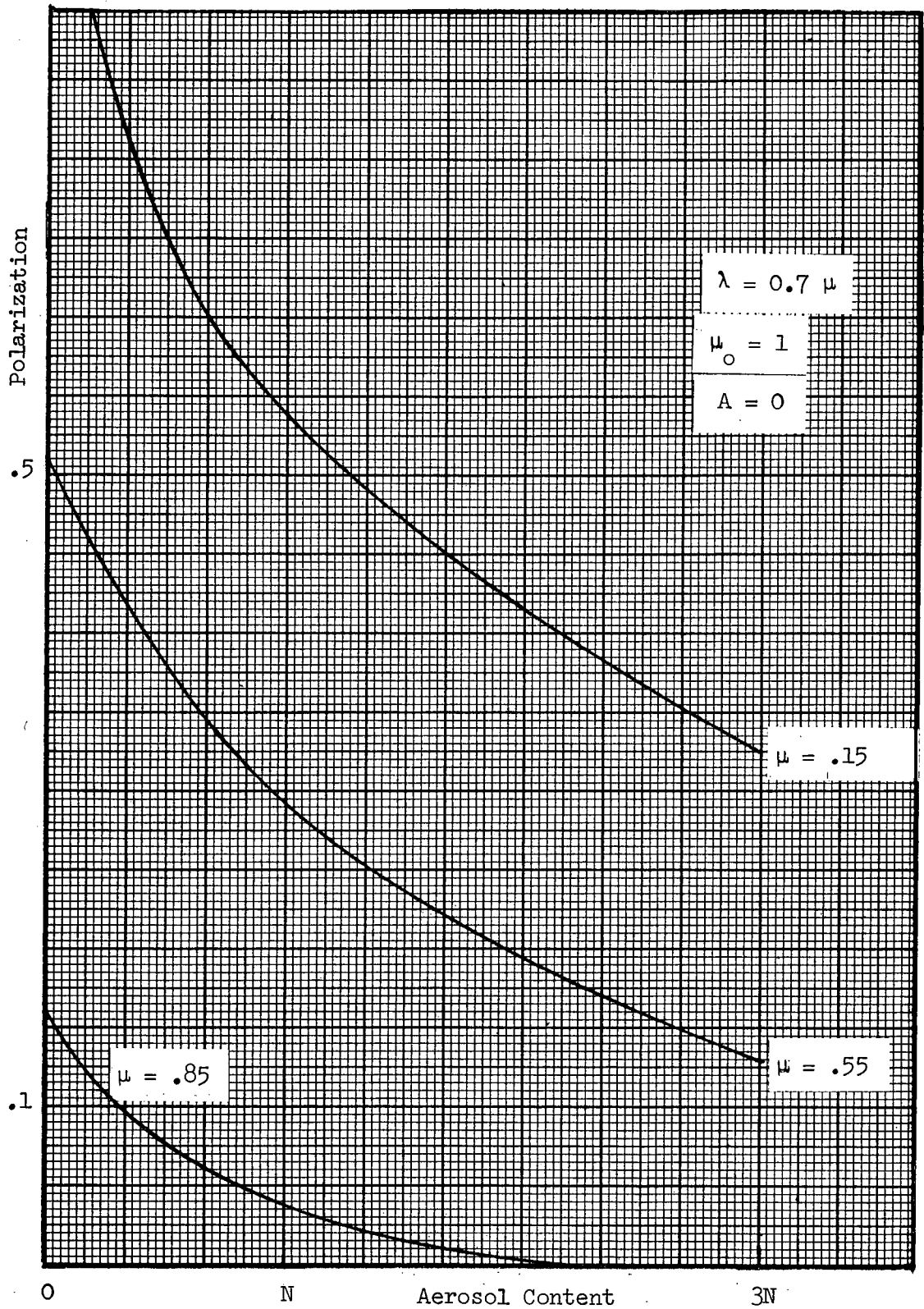


Figure 4-3. Polarization vs aerosol content as function of nadir look angle

reciprocity relationship does not exist for polarization⁽⁶⁾ ⁽⁷⁾.

However some inference may be made. If a relationship for polarization similar to that for intensity existed, viz.,

$$\mu I(0, \mu, \phi; \mu_o, \phi_o) = \mu_o I(0, \mu_o, \phi_o; \mu, \phi) \quad (4-1)$$

where $I(0, \mu, \phi; \mu_o, \phi_o)$ is the radiance at the observation angle specified by μ, ϕ due to an incoming solar beam specified by μ_o, ϕ_o , then the values of polarization and the sensitivity to aerosol content shown in Fig. 4-3 would be reduced; if the polarization were unchanged by interchanging the observer and source, then the sensitivity would be unchanged. Thus it appears that calculations for vertical observations will not indicate more sensitivity than that shown in Fig. 4-3.

4.1.3 Comparison of Radiance and Polarization Observations

A comparison of the accuracies of the radiance and polarization observations of aerosols for the model atmospheres may be made by considering the sensitivity curves shown in Figure 4-2 and Figure 4-3. It is reasonable to assume that the radiance can be measured to $\pm 1\%$, so that from Figure 4-2 it is found that the error in aerosol content is about $\pm 1.3\%$. The polarization of backscattered radiation can probably be measured to an accuracy of $\pm 1\%$ in the range 5-75%⁽⁸⁾ so that the error in near-normal values of aerosol content is about $\pm 7.5\%$ for a look angle of $\mu = .55$. It should be noted that this large error is somewhat underestimated, since it is for zero albedo; in addition, it will probably be even larger if the observer and sun are interchanged to consider more realistic conditions for satellite observations.

It should also be remembered that calculations of polarization for various vertical distributions of aerosols have not been performed, so it is not known whether polarization, like radiance, is independent of the distribution. Of course, the error estimates for both techniques assume that the relationships based on the calculations of Plass and Kattawar in Fig. 4-2 and 4-3 are correct.

It is concluded from the preceding discussions, based on model calculations, that satellite measurements of radiance are preferred to measurements of polarization to determine aerosol content. This is in contradiction to the often repeated statement that polarization measurements offer the best means of monitoring aerosol content. Such a conclusion may have been reached on the basis of ground-based observations of sky polarization. However, the results of Plass and Kattawar clearly show that the backscattered polarization is significantly less sensitive to aerosol changes, particularly at look angles close to the horizon. It is possible that polarization observations would provide information on the aerosol size distribution and vertical distribution; however this is not apparent from the published literature.

4.1.4 Observations over Land or Clouds

The previous discussions showed that the aerosol content may be determined with an underlying surface of known low albedo, such as the ocean. With higher albedos such as for land (~ 0.18) and clouds (~ 0.6) it is difficult to determine the aerosol content accurately without precise knowledge of the surface reflectivity.

Plass and Kattawar⁽⁹⁾ calculated the backscattered radiance (at 0.7μ) as a function of albedo for the Kondratiev et al. aerosol vertical distribution. (The aerosol optical thickness for this model is slightly less than that for the Elterman distribution). These results are shown in Fig. 4-4 together with curves for different aerosol contents based on later calculations by Plass and Kattawar⁽²⁾.

These latter calculations, based on the Elterman distribution, were made for albedos of $A=0$ and 1.0 , so that the curve-shapes were made to follow the 1968 calculations for intermediate values of albedo. The different aerosol contents are noted on the curves as N (the normal Elterman distribution), $3N$, $N/3$ and 0 (Rayleigh atmosphere). It is clear that as the albedo increases, the sensitivity of the radiance to aerosol content decreases.

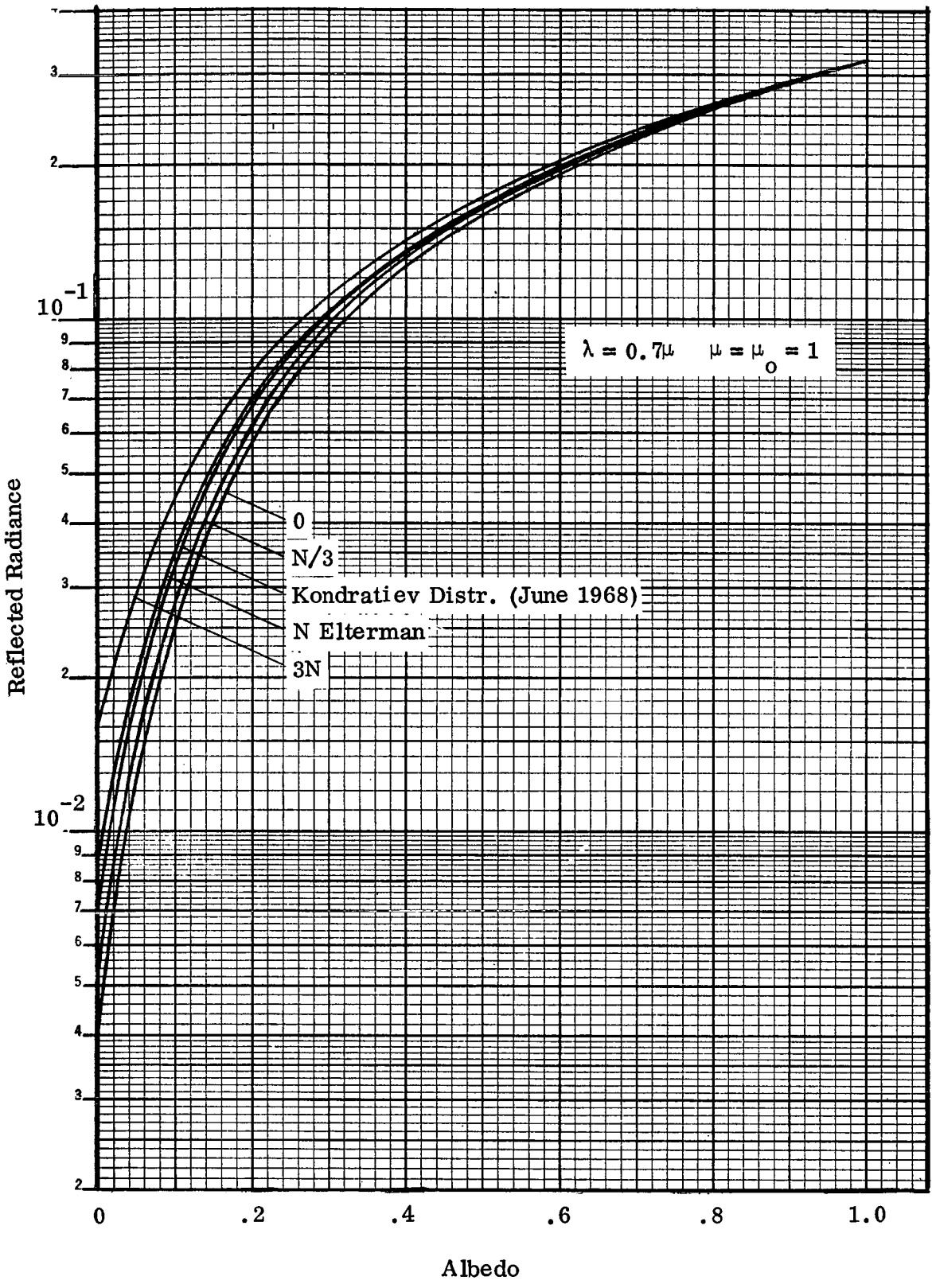


Figure 4-4. Reflected radiance vs albedo for different aerosol contents

A cross-plot of the data in Fig. 4-4 is given in Fig. 4-5., and shows that large errors are possible in measuring the aerosol content if the albedo is not known precisely. For example, over land, a normal aerosol content above a true albedo of 0.2 would be interpreted to be about 2.7 times greater if the albedo were incorrectly estimated to be only slightly lower at 0.18.

The polarization calculations of Plass and Kattawar (1970) are shown as a function of aerosol content and albedo in Figs. 4-6 and 4-7. In Fig. 4-6, only the data for the normal aerosol content were calculated for several values of albedo; the other curves are based on values at $A = 0$ and 1.0 and the shape of the curve N. It is seen that at albedos greater than 0.4 (e.g., clouds or snow) there is essentially no sensitivity to aerosol content. At the same time, the polarization does not change much with albedo so that no information is obtained on the albedo from a polarization measurement. Using the same example as above for the radiance measurement, it is seen that the estimated aerosol content would be only 1.3 times greater if the albedo were incorrectly estimated to be 0.18. Thus it appears that a polarization measurement would give a better estimate of the aerosol content. However, when the measurement errors in the polarization (± 0.01) and radiance ($\pm 1\%$) are considered in addition to the albedo error in the above examples, then the techniques are comparable, both giving the aerosol content within about a factor of 3.

From the above discussions, measurement of aerosol content above high albedo clouds will be difficult. However it is probably generally true that above clouds the aerosol content will be close to that of Elterman's clean air model. Over land, where the albedo is lower (~ 0.18), the measurement of absolute aerosol content is not accurate enough due to albedo errors; however, it will be possible to make accurate relative measurements over a period of time above any particular area. From such a series of measurements it will be possible to determine the surface albedo by assuming that the lowest radiance value corresponds to the Elterman clean air condition.

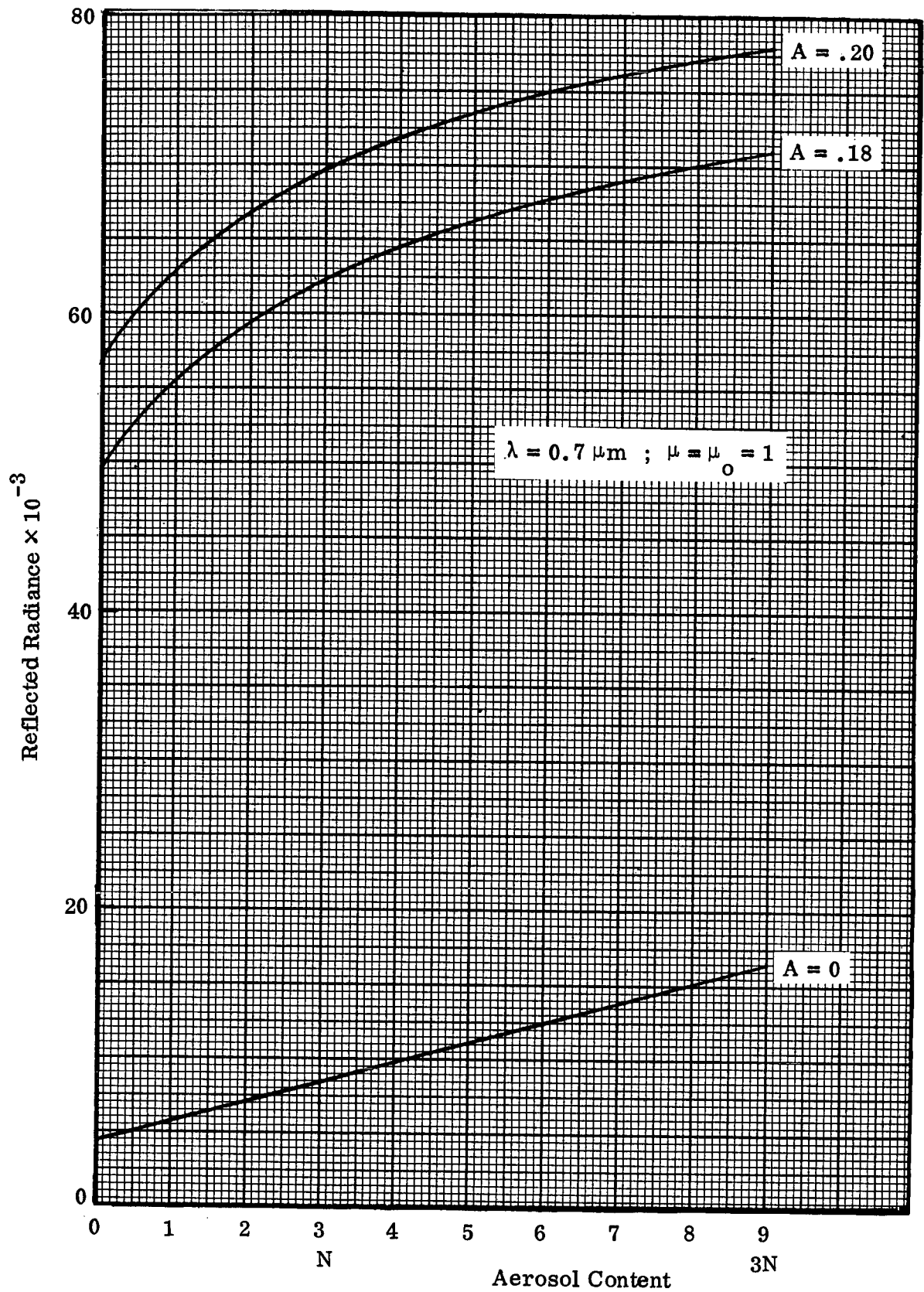


Figure 4-5. Reflected radiance vs aerosol content as function of albedo

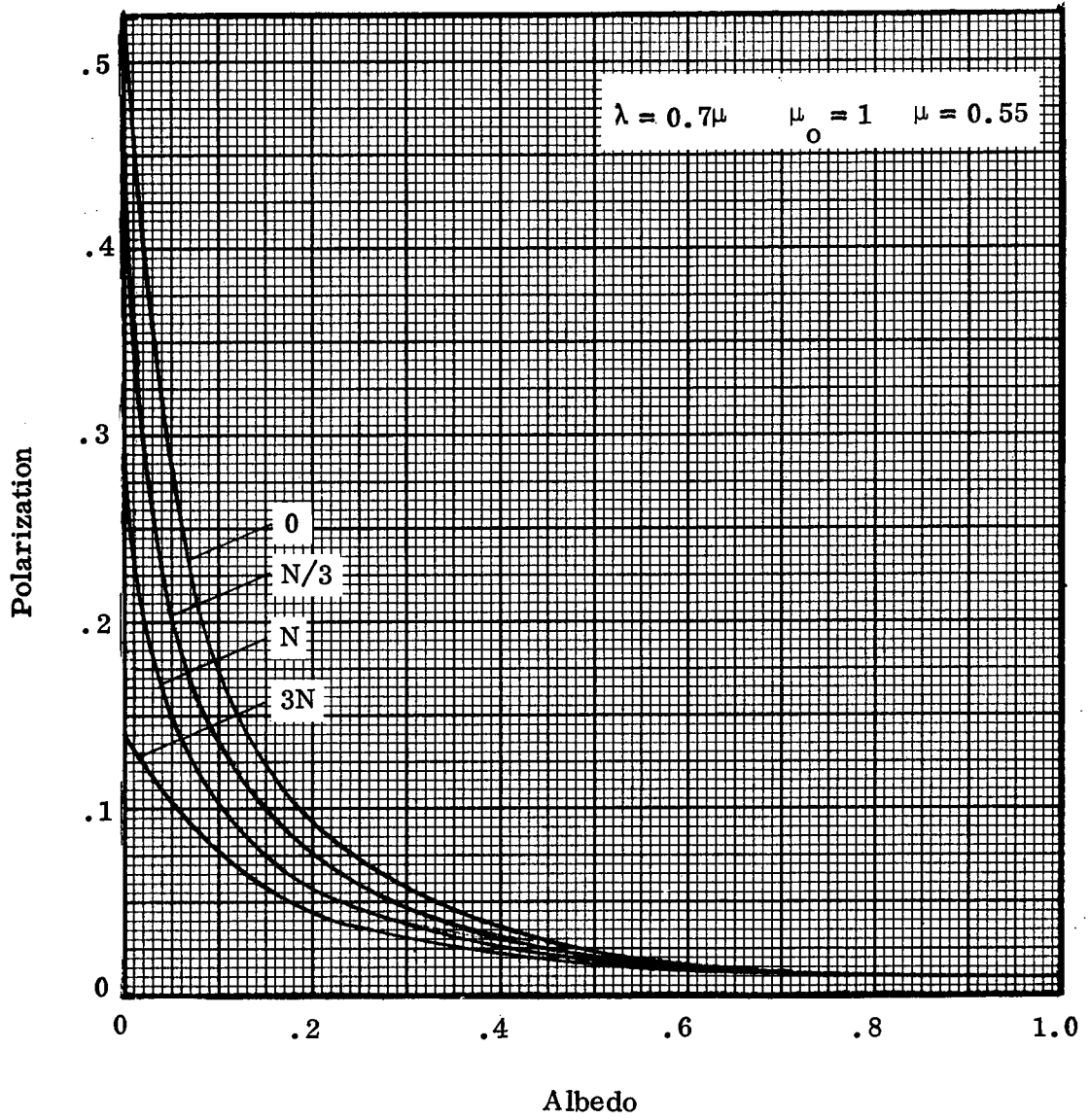


Figure 4-6. Polarization vs albedo for different aerosol contents

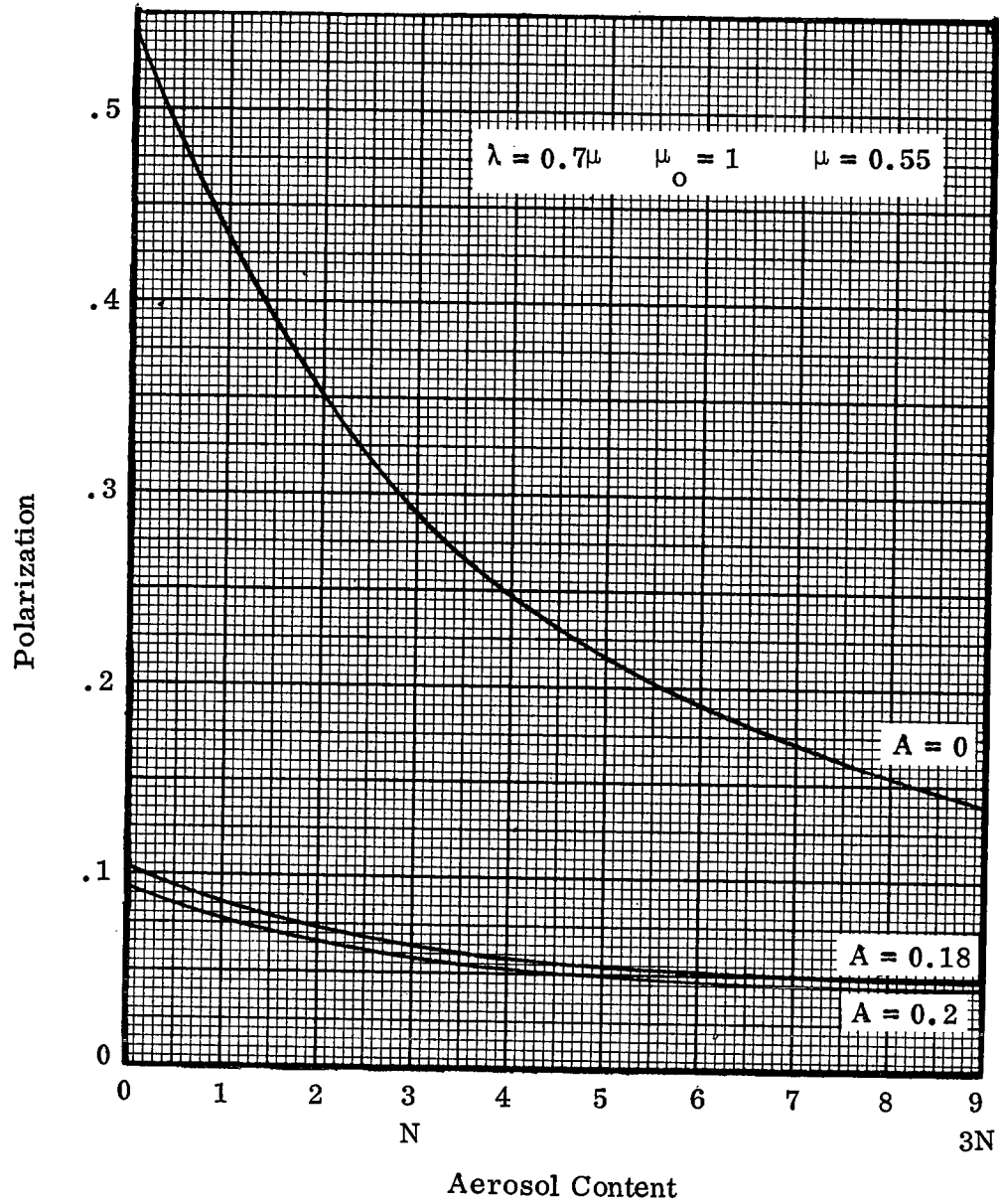


Figure 4-7. Polarization vs aerosol content as function of albedo

It may be possible to improve the aerosol determination over high albedo surfaces by making radiance measurements as a function of wavelength or by making simultaneous radiance and polarization measurements. The investigations⁽¹⁰⁾ using ERTS-A data and ground-truth data will be invaluable in resolving these problems.

4.1.5 Problem Areas

The proposed method of measuring aerosols from radiance observations is based on theoretical calculations which use a model atmosphere, a model aerosol distribution, and assume a smooth specular-reflecting water surface. In practice, of course, these model conditions are never realized so that deviations from the theoretical relationships are to be expected. We have proposed to investigate these deviations under an ERTS program⁽¹⁰⁾, which will include overflights by aircraft to obtain additional ground-truth data. We believe that only the combination of a theoretical study and field measurements will make a solution of some of the problems possible. The anticipated problems and their possible solutions are as follows:

4.1.5.1 Sun Glitter: If the ocean were perfectly smooth as assumed in the calculations an image of the sun would be seen at the specular reflection angle, and the only upwelling surface radiation observable at other look angles from space would be the diffuse sky radiation reflected from the ocean surface and the radiation scattered up from below the ocean surface. As the smooth ocean surface is increasingly disturbed, a glitter pattern becomes increasingly larger about the specular point. At sun zenith angles greater than about 30° the glitter effect has been considered negligible (except for very rough seas) at the nadir point. However, recent measurements by Hovis (private communication from R. S. Fraser, NASA, Goddard Space Flight Center), suggests that this assumption is not correct, so that the ocean surface radiance at the nadir is not known accurately.

This problem might be overcome by making observations at two wavelengths, assuming that the spectral variation of the surface radiance is known. The choice

of wavelengths must be made carefully since the spectral distribution of the radiance does vary due to ocean properties such as chlorophyll content, suspended matter and depth.

4.1.5.2 Aerosol Properties. In order to make model calculations, assumptions must be made about the aerosol properties, such as size distributions, vertical distribution, sphericity of the particles and the refractive index. All of these assumptions affect the phase function to be used in the multiple scattering calculations. The variability of each of these parameters in the real atmosphere should be investigated. Some work along these lines has been reported by Rosenberg⁽¹¹⁾ who suggests that the Junge aerosol model is not applicable to the atmosphere - in the case of humid atmospheres, due to condensation on the particles, and for dry atmospheres because the particles are non-spherical.

4.1.5.3 Non-Lambertian Surfaces. Most calculations of scattering properties of the atmosphere use an underlying Lambertian surface. However, the calculations for the ocean treat the surface correctly as a specular reflector for both the direct and sky radiation, and include the upwelling radiation scattered by the water from beneath the surface. Raschke⁽¹²⁾ uses a two-layer model of the atmosphere-ocean system, and a rough ocean surface (equivalent to a wind speed of about 1.4 m sec^{-1}) to calculate the radiance outside the atmosphere, but does not show a quantitative comparison with calculations for a smooth surface.

4.1.5.4 Surface Reflectance Gradient. The calculations of Plass and Kattawar assumed an underlying surface of constant reflectivity extending to infinity. However in the case of two adjacent surfaces with different reflectivities, radiation reflected from one surface will be scattered into the atmosphere above the other surface so that the apparent radiance above that surface is increased over the calculated theoretical value. This is probably a second order effect if the radiance is measured at points well removed from the boundary of the two surfaces. This will be verified

by comparing the theoretical calculations with aircraft measurements⁽¹⁰⁾.

4.2 SUN-ORIENTED OBSERVATIONS OF AEROSOLS

Satellite measurements of aerosols in the stratosphere are well suited to the occultation method, (illustrated in Figure 4-8), in which observations are made of the sun's radiation as the satellite enters or leaves the earth's shadow. From the observed attenuation along successive light paths, and allowing for refraction, the vertical distribution may be determined, if the aerosols are assumed to be uniformly distributed in the horizontal. These observations are generally restricted to the stratosphere and higher due to the presence of clouds and high attenuation (scattering and absorption) in the troposphere; these problems are discussed in some detail below.

The technique has not yet been applied to aerosol measurements, although Pepin⁽¹³⁾ has satellite measurements scheduled. The only satellite occultation measurement to date appears to be that of ozone by Rawcliffe et al.⁽¹⁴⁾ and Miller and Stewart⁽¹⁵⁾. Their measurements used the full disc of the sun (0.5° angular diameter), so that the vertical resolution in the deduced ozone was only about 16 km. Improvement of this height resolution would require the use of a sun-pointing device to observe a small area of the sun. To obtain a 2 km resolution, one-eighth of the disc's vertical diameter would be used, requiring extreme pointing accuracy, which will be very difficult to achieve on a satellite.

4.2.1 Cloud Interference

An obvious problem in using occultation methods to probe the lower atmosphere is the presence of clouds. Most clouds are confined to the troposphere, the height of which varies from about 17 km in the tropics to below 10 km in polar regions. If it is assumed that the clouds reach up to 10 km, it may be calculated that a cloud-free region nearly 700 km wide is required so that the line-of-sight from a 300 km orbit to the sun tangent to the earth's surface is unobstructed. Such a large clear area will

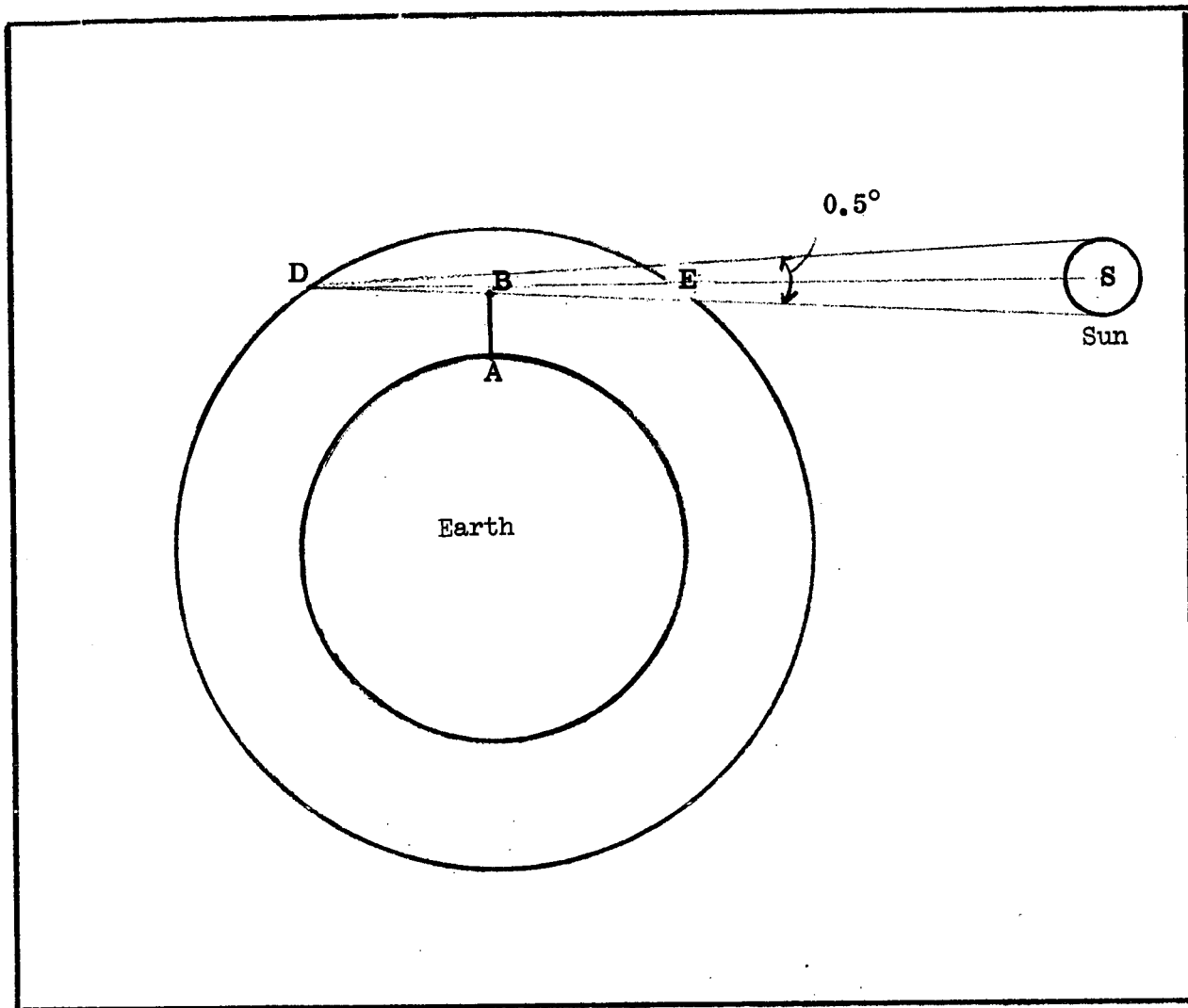


Figure 4-8. Schematic of occultation experiment

be very rare; even if the atmosphere were cloud-free, the strong attenuation (scattering and absorption) of the radiation through the lower atmosphere would preclude occultation probing at these low altitudes (see below).

Even if the observations are confined to the stratosphere, the problem of clouds is not entirely eliminated. Clouds do occur in the stratosphere. In addition to the occasional penetration of the tropopause by thunderheads, there are, at higher altitudes, nacreous (or mother-of-pearl) clouds and noctilucent clouds. Noctilucent clouds occur at about 80 km and are generally observed at high latitudes in the summer. The nacreous clouds are formed in the 20-30 km region and observed in middle latitudes in the winter. This latter altitude region is exactly where the SST (supersonic transport) commercial aircraft will be flying, so with the addition of particulates and water vapor from the SST exhaust products we might expect more observations of nacreous clouds in future years. These stratospheric clouds present a problem to occultation measurements since they will attenuate the sun's radiation by an unknown amount resulting in misinterpretation of the observations. However, if the interest is in the global loading of aerosols in the stratosphere, the data may be averaged over all latitudes to minimize errors due to stratospheric clouds.

4.2.2 Atmospheric Attenuation

The attenuation of the sun's radiation varies as a function of wavelength, and as a function of the grazing altitude of the radiation. Both gaseous absorption and molecular scattering must be considered. In the ultraviolet and visible region, ozone absorption is important, and in the infrared beyond about 0.8μ absorption by other atmospheric gases, particularly water vapor, is important. Rayleigh scattering is negligible in the infrared, but is a significant factor in considering shorter wavelengths for occultation. For aerosol observations an atmospheric "window" must be chosen.

Calculations of the sensitivity of various wavelengths to changes in aerosol content may be made based on the 1968 model atmosphere of Elterman. Fig. 4-9 and Fig. 4-10 show results of simplified calculations for occultation grazing heights of 10 km and 15 km respectively. The calculations are simplified to the extent that the sun is considered as a point source, so that the variation of transmission of the light rays from different parts of the sun is neglected. In addition, refraction of the light rays in the atmosphere is ignored.

Thus the transmission τ is given by

$$\tau = \exp(-2t(\omega) \text{Ch}(90^\circ))$$

where

$t(\omega)$ is the wave number-dependent vertical optical thickness above the grazing altitude and is the sum of contributions from Rayleigh scattering and aerosol scattering. Gaseous absorption is negligible in atmospheric windows at high altitudes.

$\text{Ch}(90^\circ) = 35$, is the Chapman function for zenith angle 90° .

$\text{Ch}(\theta)$ replaces the usual secant θ when θ is large.

The factor 2 accounts for the two equal optical paths BD and BE in Fig. 4-8.

The results show, as expected, that the shorter wavelengths are more sensitive to aerosol variations than the infrared region. Observations of attenuation at the shorter wavelengths would have to take into account the contribution of Rayleigh scattering, which is well known. In the infrared, the Rayleigh scattering is negligible, and, at the higher altitudes above about 12 km, the water vapor continuum absorption is negligible. Thus, no corrections to the observed data would be required at high altitudes in infrared window regions. However, the increased sensitivity, the well-established Rayleigh correction, the higher sun

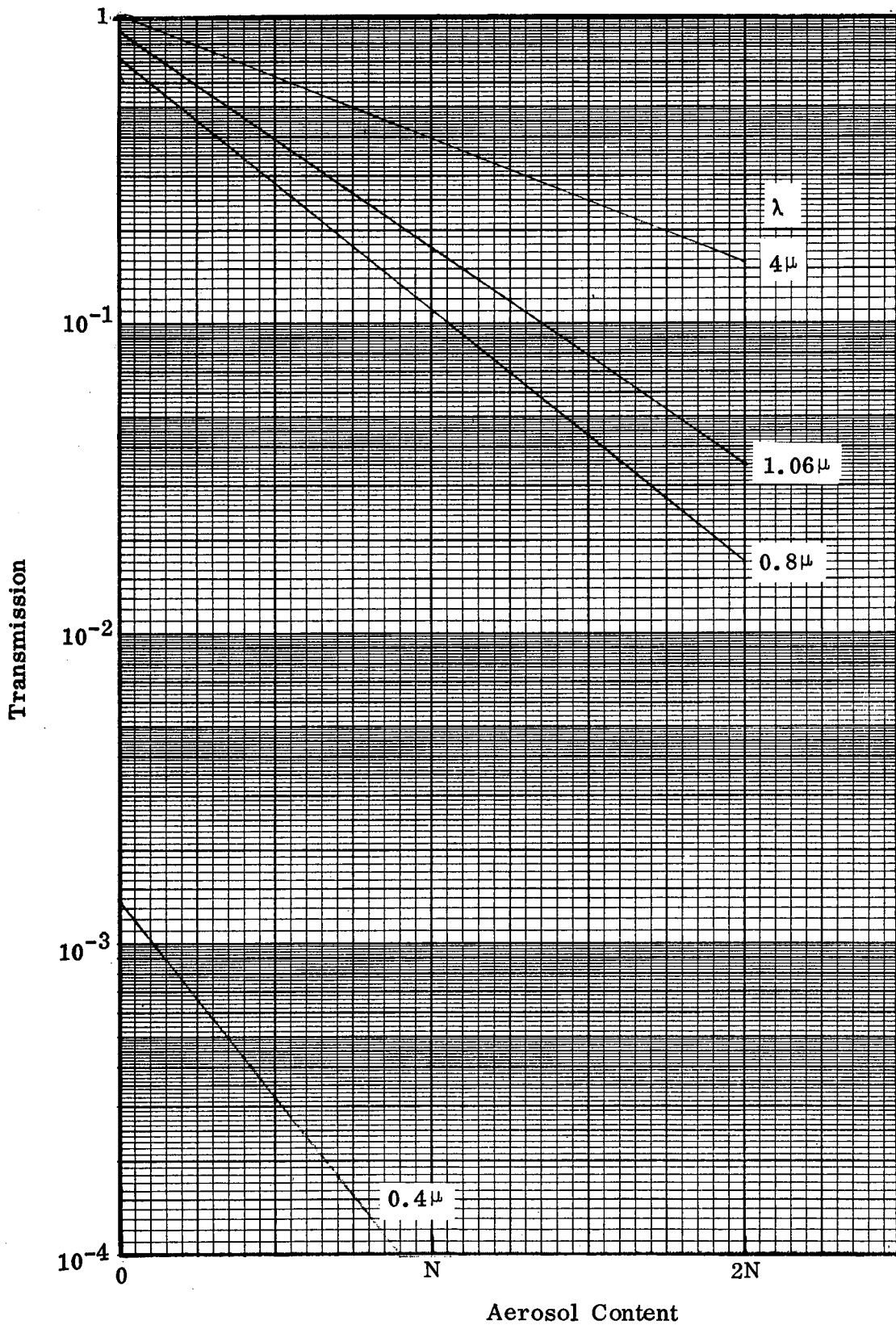


Figure 4-9 Transmission vs aerosol content as function of wavelength (grazing altitude 10 km)

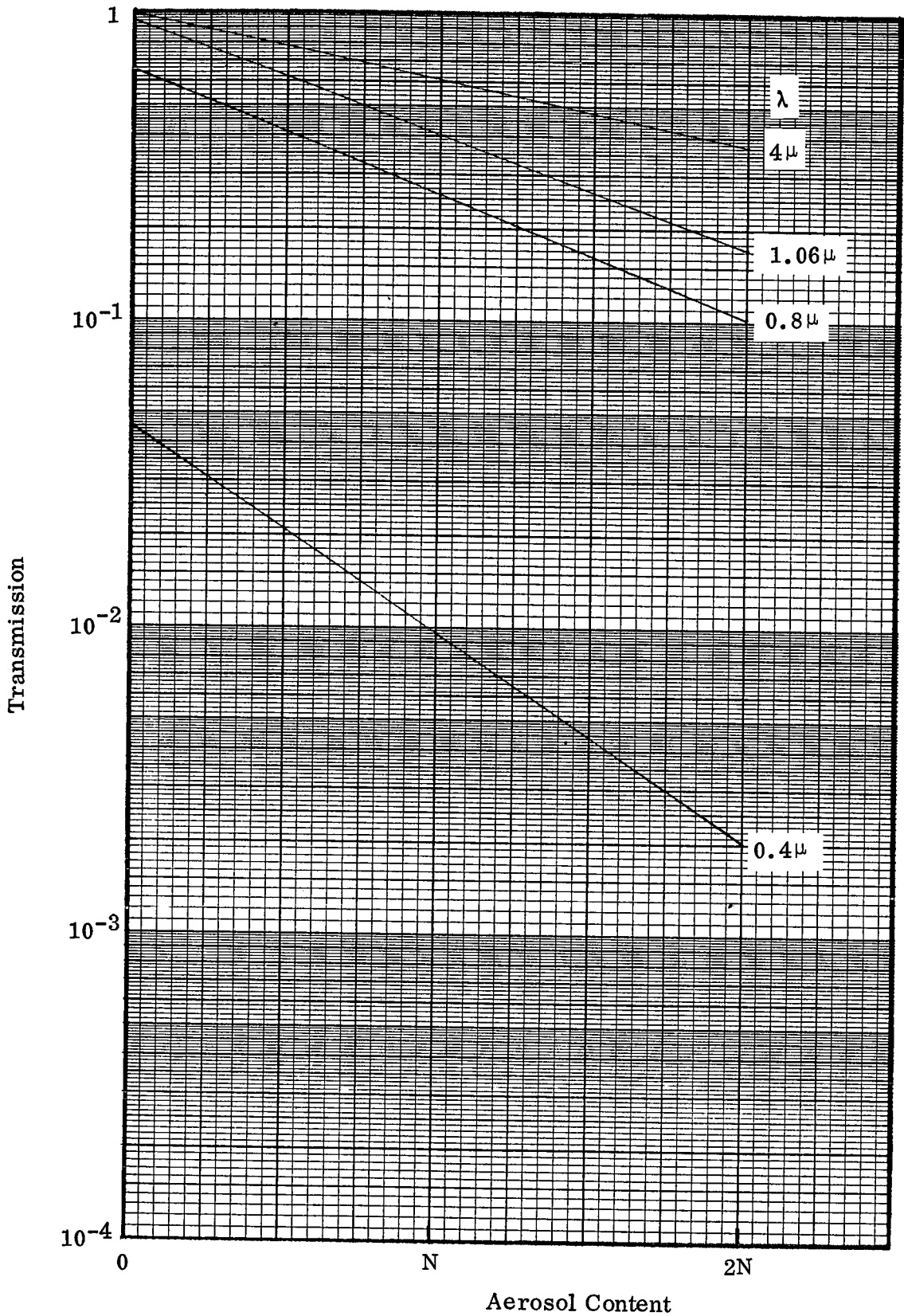


Figure 4-10 Transmission vs aerosol content as function of wavelength (grazing altitude 15 km)

radiance, and more sensitive detectors at shorter wavelengths would point to choosing the visible or ultraviolet region for aerosol observations by occultation.

It is seen from Fig. 4-9 and 4-10 that at shorter wavelengths the transmission changes by 10-20% for a 10% variation in the normal aerosol content. Thus the sun's spectral radiance with and without atmospheric attenuation must be measured very accurately to monitor stratospheric aerosol changes due to SST operation. It has been estimated⁽¹⁶⁾ that in the 1985-1990 period, assuming operation of 500 SST's, the aerosol concentration at SST altitudes will increase by about 10% on the average.

REFERENCES

1. C. B. Ludwig, R. Bartle and M. Griggs - Study of Air Pollutant Detection by Remote Sensors," NASA CR-1380, July 1969.
2. G. N. Plass and G. W. Kattawar, Appl. Opt. 9, 1122, 1970.
3. Z. Sekera, Icarus 6, 348, 1967.
4. T. A. Hariharan, Pure Appl. Geophys 77, 151, 1969.
5. K. L. Coulson, G. M. B. Bouricius and E. L. Gray, General Electric Report R65SD64, 1965.
6. S. Chandrasekhar, "Radiative Transfer," Oxford University Press, London, 1950.
7. Z. Sekera, Private Communication, 1972.
8. T. A. Hariharan, J. Sci. Instr. 2, 1135, 1969.
9. G. N. Plass and G. W. Kattawar, Appl. Opt. 7, 1129, 1968.
10. "The Determination of Aerosol Content in the Atmosphere using ERTS-A Data," Science Applications, Inc., Report No.SAI72-39-LJ, March 1972.
11. G. V. Rosenberg, Bull. (Izv.) Acad. Sci. USSR Atm. and Oceanic Phys. 3., No. 7 (1967).
12. E. Raschke, Beitr. Phys. Atmos. 45, 1, (1972).
13. T. J. Pepin, Private Communication, 1972.

14. R. D. Rawcliffe, G. E. Meloy, R. M. Friedman and E. M. Rogers, J. Geophys. Res. 68, 6419, 1963.
15. D. E. Miller and K. H. Stewart, Proc. Roy. Soc. A288, 540, 1965.
16. "Remote Measurement of Pollution," NASA SP-285, p 219, 1971.

5

INVESTIGATION OF RGFC INSTRUMENT PARAMETERS

(Task 4)

5.1 OPTIMIZATION PROCEDURE

The basic POLAYER program is used to optimize the instrument cell parameters of the RGFC instrument. For a given condition in the atmosphere, i.e., $E(\omega)$ at the entrance of the instrument, the parameters $c \ell$ (concentration of pollutant gas) \times cell length in cm), p_T (total pressure in atm, using nitrogen as foreign gas broadener) and T (temperature in degrees Kelvin of the gas in the cell) are varied until a maximum sensitivity is obtained. These parameters are related through the instrument cell transmission, $\tau_G(\omega)$, and the optical thickness, u , by

$$\tau_G(\omega) = \exp \left[-k(\omega) u \right], \quad (5-1)$$

where $k(\omega)$ is the monochromatic absorption coefficient in $\text{cm}^{-1} \text{atm}^{-1}$, and u is the optical thickness, given by

$$u = p_T c \ell \text{ cm atm} \quad (5-2)$$

The absorption coefficient for a spectral line with Lorentz shape

$$k(\omega) = \frac{S \alpha / \pi}{(\omega - \omega_0)^2 + \alpha^2} \quad (5-3)$$

where S is the line strength in $\text{atm}^{-1} \text{cm}^{-2}$, α is the line half-width at one-half of the line strength. The line half-width α is related to pressure, temperature and foreign gas and self broadening through

$$\alpha = \alpha_0 p_e \sqrt{\frac{T_0}{T}} \quad (5-4)$$

where α_0 is the line half-width at 1 atm and standard temperature T_0 for nitrogen broadening, T is the temperature and p_e is the equivalent pressure, given by

$$\left. \begin{aligned} p_e &= p_{B_N} + p_N \\ &= p_T [c (B-1) + 1] \end{aligned} \right\} \quad (5-5)$$

where p and p_N are the partial pressure of the pollutant gas and nitrogen gas, respectively, and B_N is the ratio of self-broadening to nitrogen-broadening efficiency.

For a given p_T and T , an optimum sensitivity of the instrument exists for a particular value of the product $c \ell$. Calculations of ΔV were performed by varying the CO concentration in the instrument cell and maintaining the other instrument parameters, $\ell = 1$ cm, $p_T = 1$ atm, and $T = 288.16^\circ$ K for 0.1 ppm CO uniformly distributed through the troposphere, the earth's surface temperature equal to 288.16° K and the standard US atmospheric temperature profile.* The instrument response function $C(\omega)$ and $C'(\omega)$ are assumed to be equal and are given by the curve shown in Figure 5-1. The results, shown in Figure 5-2 indicate a maximum sensitivity is obtained for $c_{CO} = 0.35$; the corresponding is $\bar{\tau}_G = 0.832$.

Additional calculations were made using the optimum value for c_{CO} ($=0.35$), cf. Figure 5-2, and the non-optimum values for $c_{CO} = 0.05$ and 1.0 . The calculation was made for CO concentrations ranging from 0 to 0.4 ppm uniformly distributed through the atmosphere. The remaining instrument parameters and earth surface temperature and atmospheric temperature profile were the same as those indicated in Figure 5-2. The results shown in Figure 5-3 indicate that a value of $c_{CO} = 0.35$ is an optimum value over the atmospheric CO concentration range from 0 to 0.4 ppm.

*This temperature was selected to be equal to the surface temperature of the U. S. standard atmosphere.

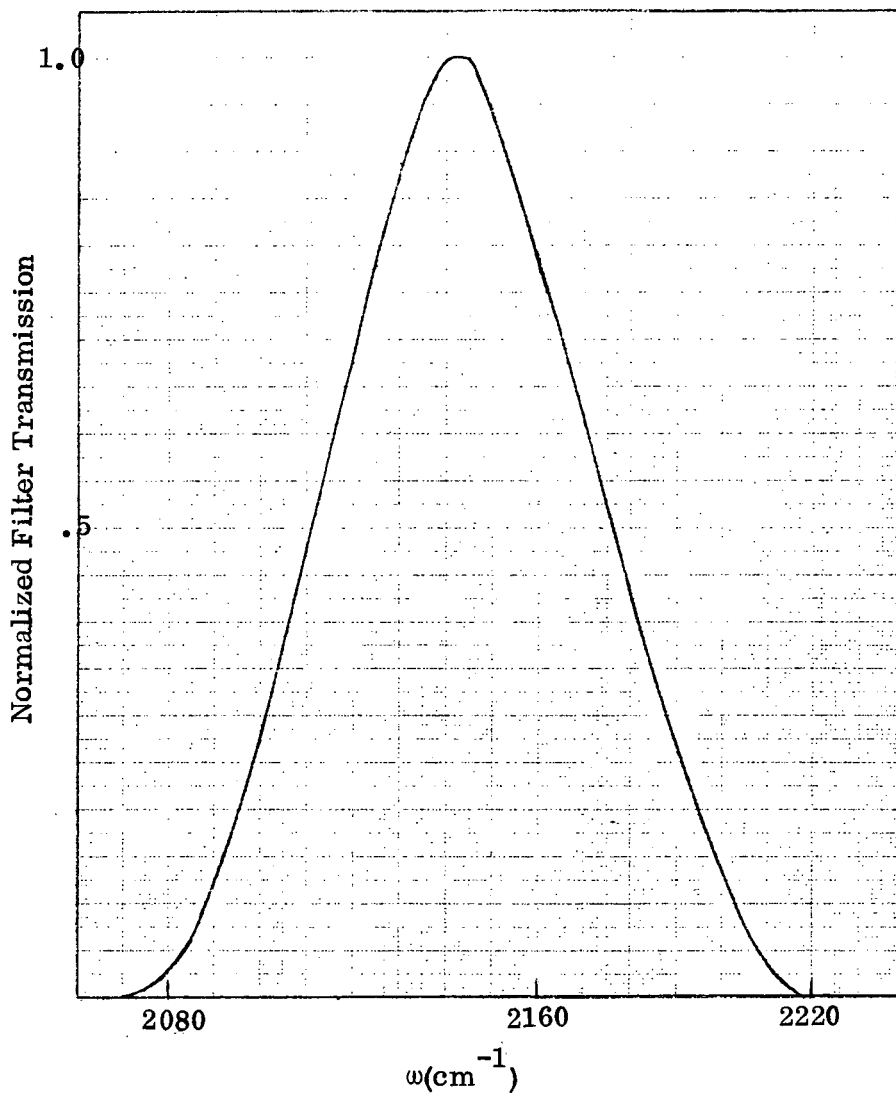


Figure 5-1. Normalized filter function used in the model calculations for CO, corresponding to OCLI filter 14-8806-760.

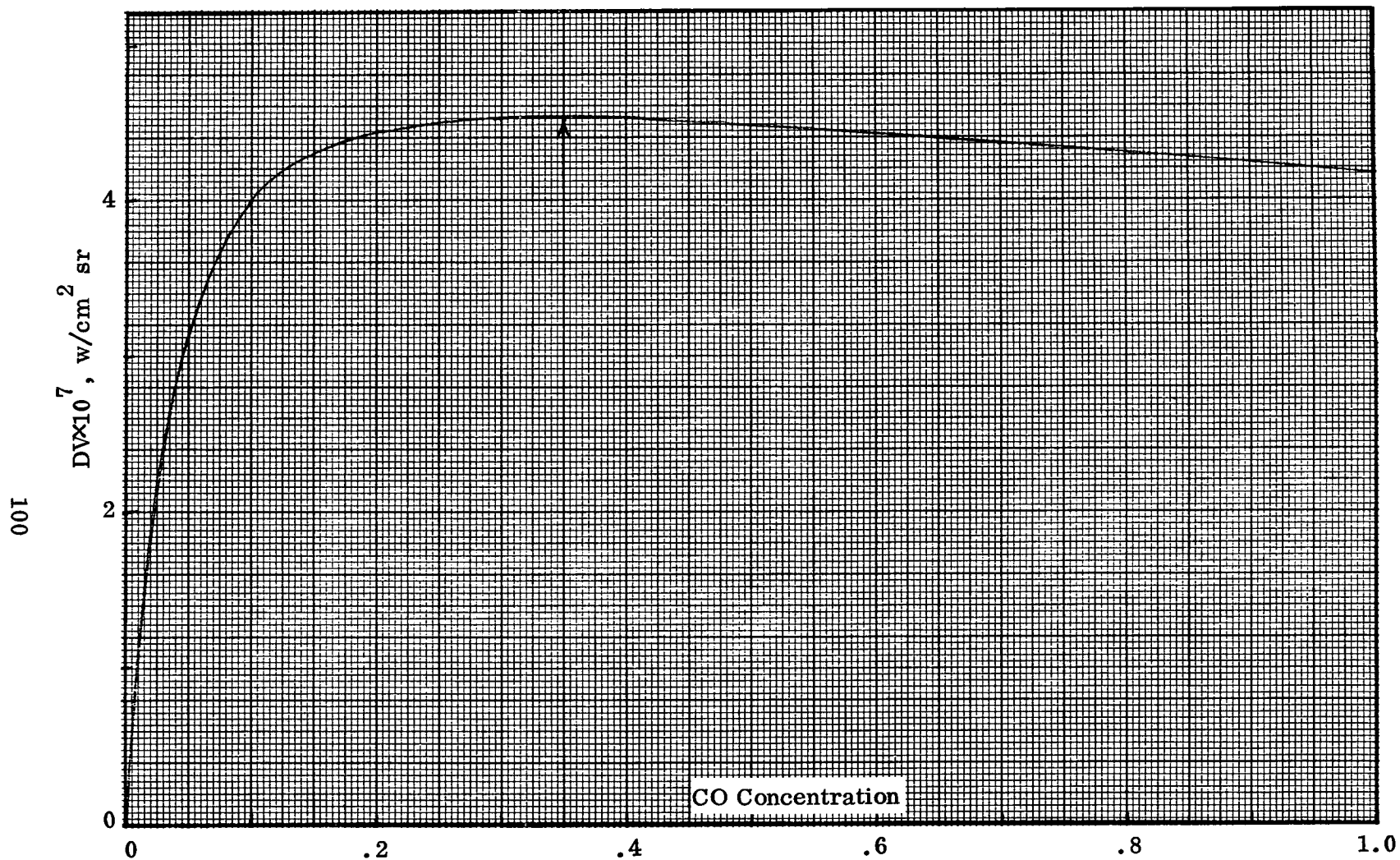


Figure 5-2. Optimization of instrument response as a function of CO concentration in instrument cell. Instrument parameters: $l = 1$ cm, $p_T = 1$ atm, $T_G = 288.16^\circ\text{K}$, $c(\omega) = c'(\omega)$, given by Fig. 5-1. Atmospheric parameters: CO concentration in the troposphere = 0.1 ppm, ground temperature = 288.16°K , lapse rate = $-6.5^\circ\text{C}/\text{km}$. Arrow points to maximum response, i.e., CO concentration = 0.35, corresponding to a cell transmission of 0.83.

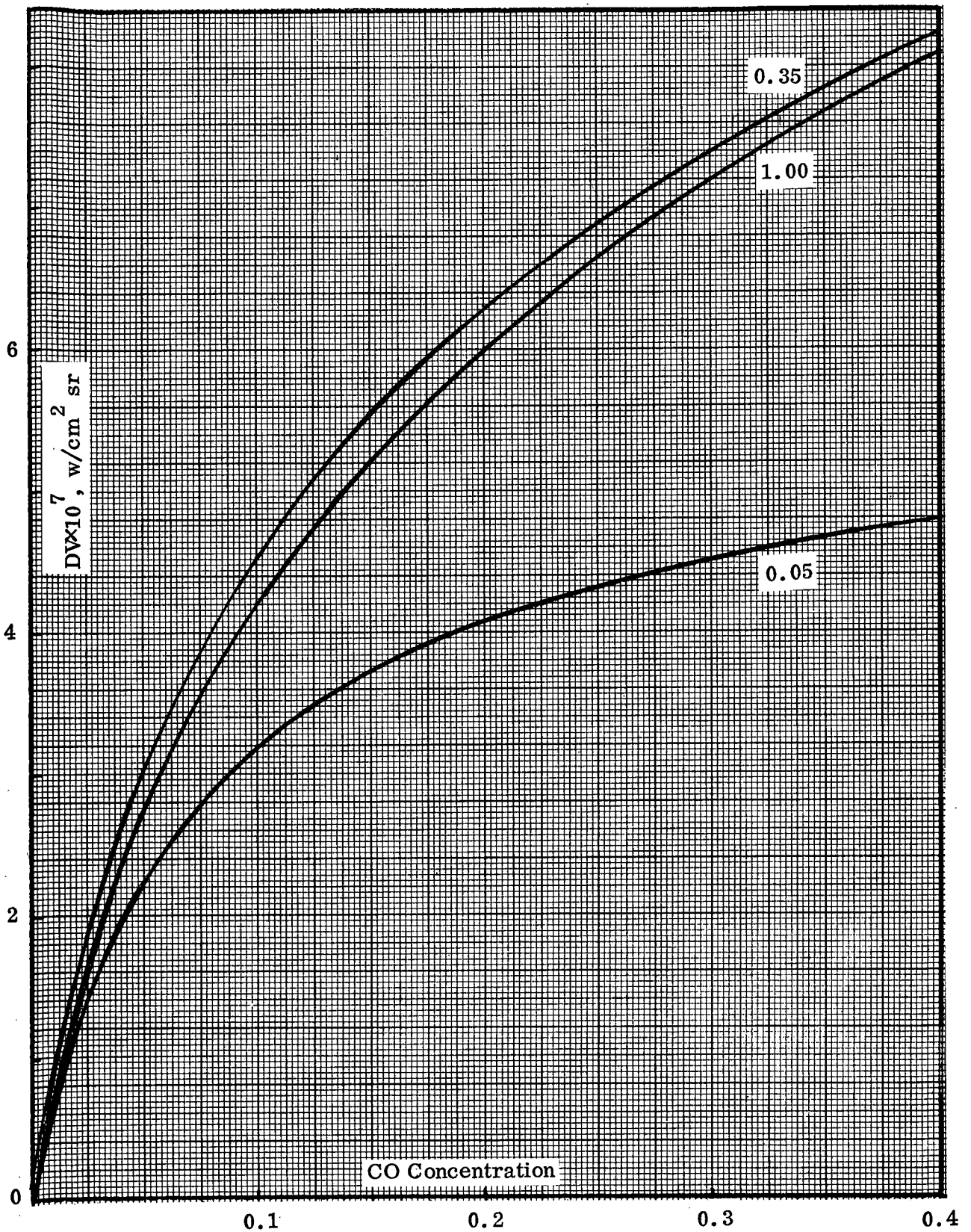


Figure 5-3. Sensitivity of instrument as a function of CO concentration in the troposphere with three CO concentrations in instrument cell as a parameter: 0.05, 0.35 and 1.00. Other instrument and atmospheric parameters same as in Fig. 5-2.

We have assumed that variations in the temperature of the correlating gas in the instrument cell, T , will have only small effects on the observed signal output. To verify this assumption Run B-09 was re-run but T was set at 270, 300 and 330° K. The results of these calculations are shown in Table 5-1 for three different atmospheric CO concentrations.

Table 5-1. Effect of Instrument Cell Temperature Variations

$T_G, ^\circ K$	$(CO)_{atm}, ppm$	$10^7 DV_c, W/cm^2-sr$	% Error
300	0.025	1.7510	--
	0.100	4.4431	--
	0.400	8.0675	--
330	0.025	1.7587	-0.44
	0.100	4.4319	0.25
	0.400	7.9179	0.19
270	0.025	1.7350	0.91
	0.100	4.4330	0.23
	0.400	8.1840	-1.44

The per cent error is calculated according to

$$\% \text{ error} = \left(\frac{DV(T = 300^\circ K) - DV(T)}{DV(300^\circ K)} \times 100 \right)$$

The calculated values of DV_c , where $DV_c = DV(\text{corrected}) = DV - DV \text{ for } (CO)_{\text{atm}} = 0$, indeed indicate that variations in T have only a small effect on DV_c . Since we anticipate controlling $T = 300^\circ\text{K}$ to within at least $\pm 1^\circ\text{C}$, the maximum effect due to variations in T will be about .05 per cent.

The influence of the total pressure in the instrument cell was studied in computer run B20, in which the optical thickness ($c \ell$) was kept constant. The results of DV as a function of total pressure in the cell with CO concentration in the atmosphere as a parameter are shown in Figure 5-4. The maximum sensitivity indicated by arrows is not very strongly dependent upon the total pressure in the cell.

5.2 LABORATORY CALIBRATION PROCEDURE

In this section, we investigate whether a laboratory calibration of the instrument response using a calibration cell which represents a one-slab atmosphere can be applied to pollutant measurements in the real, multi-slab atmosphere.

The signal difference is given by

$$\Delta V = A \Omega \int_{\Delta\omega} E(\omega) [R(\omega) \tau_G(\omega) - R'(\omega) \tau_A] d\omega \quad (5-6)$$

where ΔV is the signal output of the instrument (volts), $A \Omega$ is the étendue of the instrument ($\text{cm}^2\text{-sr}$), and $R(\omega)$ and $R'(\omega)$ are the responsivities of the two cells in the instrument (volts/watt). When the instrument is calibrated, $E(\omega)$ is replaced by $N^0(T, \omega)\tau$, where $N^0(T, \omega)$ is the radiance emitted by a calibration source and τ is the transmission through a calibration sample of the gas of interest.

Setting

$$\frac{R'(\omega)}{R(\omega)} \tau_A = \tau'_A(\omega) \approx \tau'_A \quad (5-7)$$

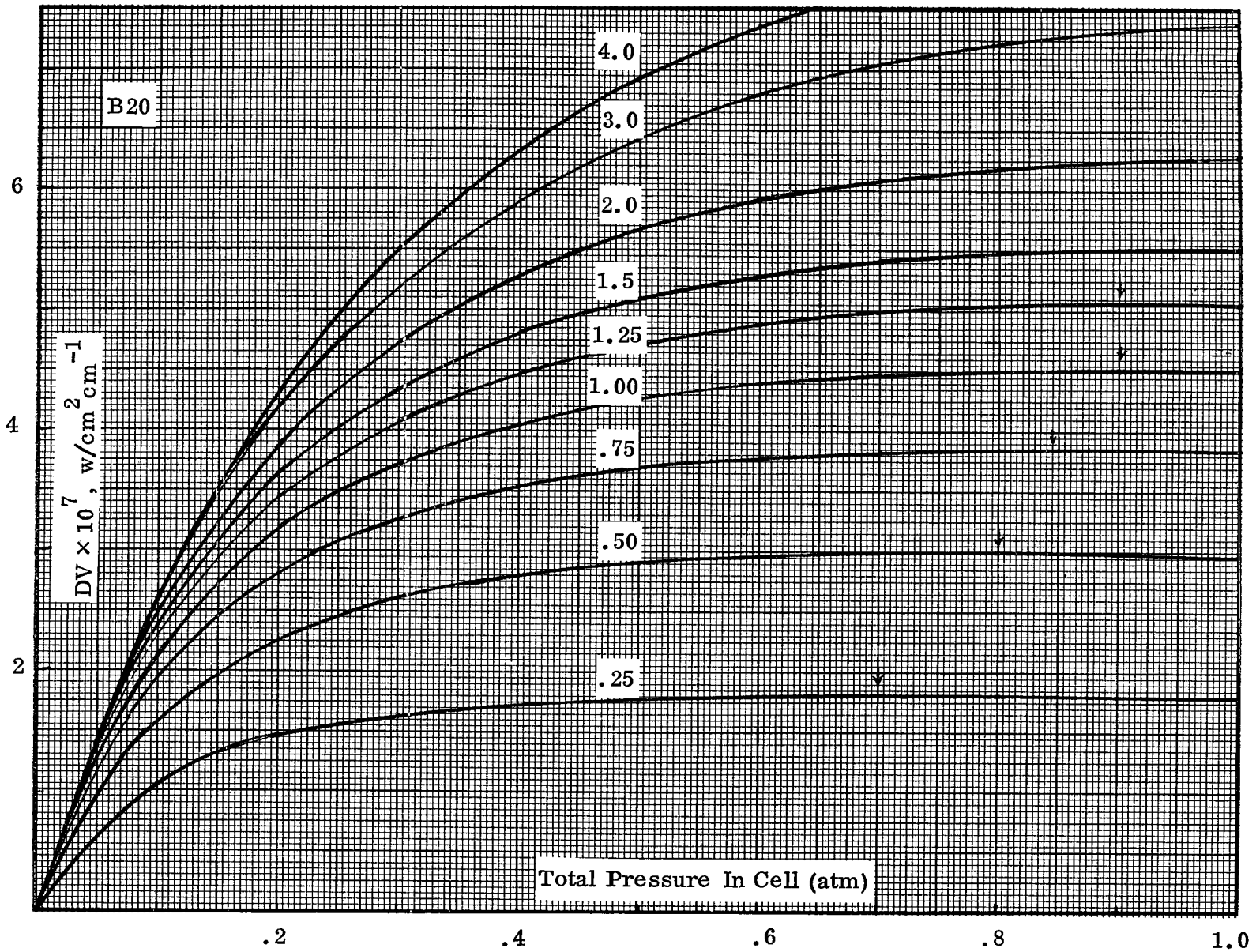


Figure 5-4. Sensitivity of instrument as a function of total pressure in instrument cell with nine CO concentrations in the troposphere. The figures on the curves refer to the multiplier, with which the concentration of 0.1 ppm in the troposphere is multiplied. Arrows refer to maximum sensitivity.

we have

$$\Delta V = \bar{R}_o \int_{\Delta\omega} E(\omega) [\tau_G(\omega) - \tau'_A] d\omega \quad (5-8)$$

where \bar{R}_o is the overall instrument responsivity over $\Delta\omega$. Thus, ΔV is proportional to \bar{R}_o .

Similarly, when the instrument is calibrated by placing known concentrations of CO in the sample cell having the transmission $\tau_c(\omega)$ and using a calibration source with a radiance, $N^o(T, \omega)$,

$$\Delta V_{cal} = A \Omega \int_{\Delta\omega} N^o(T, \omega) \tau_c(\omega) [R(\omega) \tau_G(\omega) - R'(\omega) \tau_A] d\omega \quad (5-9)$$

$$\approx \bar{R}_o \int_{\Delta\omega} N^o(T, \omega) \tau_c(\omega) [\tau_G(\omega) - \tau'_A] d\omega$$

Thus

$$\begin{aligned} \bar{R}_o &\approx \frac{\int_{\Delta\omega} E(\omega) [R(\omega) \tau_G(\omega) - R'(\omega) \tau_A] d\omega}{\int_{\Delta\omega} E(\omega) [\tau_G(\omega) - \tau'_A] d\omega} \\ &\approx \frac{\int_{\Delta\omega} N^o(T, \omega) \tau_c(\omega) [R(\omega) \tau_G(\omega) - R'(\omega) \tau_A] d\omega}{\int_{\Delta\omega} N^o(T, \omega) \tau_c(\omega) [\tau_G(\omega) - \tau'_A] d\omega} \end{aligned} \quad (5-10)$$

Computer calculations have been made in which the instrument is calibrated to obtain its overall responsivity and this responsivity applied to a signal from a real atmosphere. These results are then compared with the exact results that would be obtained if an overall responsivity were not used.

Before these results are shown, a brief discussion of the computer simulation is pertinent. From the equations presented, it is clear that if a laboratory

calibration is made for varying optical thicknesses of CO, as $u(\text{CO}) \rightarrow 0$

$$\left[\frac{d(\text{DV})}{d u} \right]_{u=0} = \bar{R}_o \int_{\Delta\omega} N^o (T_s^o, \omega) d\omega.$$

and, knowing the blackbody calibration source temperature, the overall responsivity \bar{R}_o may be determined. However, for the computer simulation, one of the problems is in selecting the "correct" value of $\Delta\omega$ over which to perform the calculations. Of course, in calibrating the real instrument this is automatically taken care of.

For the computer simulation, one choice is to perform the calculations over a spectral band-pass defined by the cut-off frequencies. Another choice is to select a band-pass defined by the values when the transmission through the two instrument channels is equal to one-half. Both of these choices have been used in the computer simulations, as will be shown, and the results obtained by using these two choices should be representative of the values that would result from a real calibration of the instrument.

The special case of

$$R(\omega) = R'(\omega) \equiv C(\omega) = C'(\omega)$$

was investigated initially; i. e., Run B-09 shown in Figure 5-3. The results of Run B-09 are re-presented in Figure 5-5. An identical computation except $C(\omega) = 1.0$ over $\Delta\omega$ is also plotted, Run B-18. These results are slightly different from those presented previously. The DV offset for $(\text{CO})_{\text{atm}} = 0$ caused by the difference between the ground and instrument reference temperature has been corrected by $\text{DV}(\text{corrected}) = \text{DV} - \text{DV for } (\text{CO})_{\text{atm}} = 0$. An effective \bar{R}_o (or C) is computed for $(\text{CO})_{\text{atm}} = 0.1$ ppm by

$$\bar{R}_o = \frac{\text{DV (Run B-09)}}{\text{DV (Run B-19)}} = 0.516$$

The DV for Run B-18 is multiplied by $\bar{R}_o (= 0.516)$ and plotted as (X) on Figure 5-5. The results indicate that using the mean responsivity, \bar{R}_o , creates an error of less than one per cent in determining the concentration of CO in the atmosphere up to a level of 0.3 ppm.

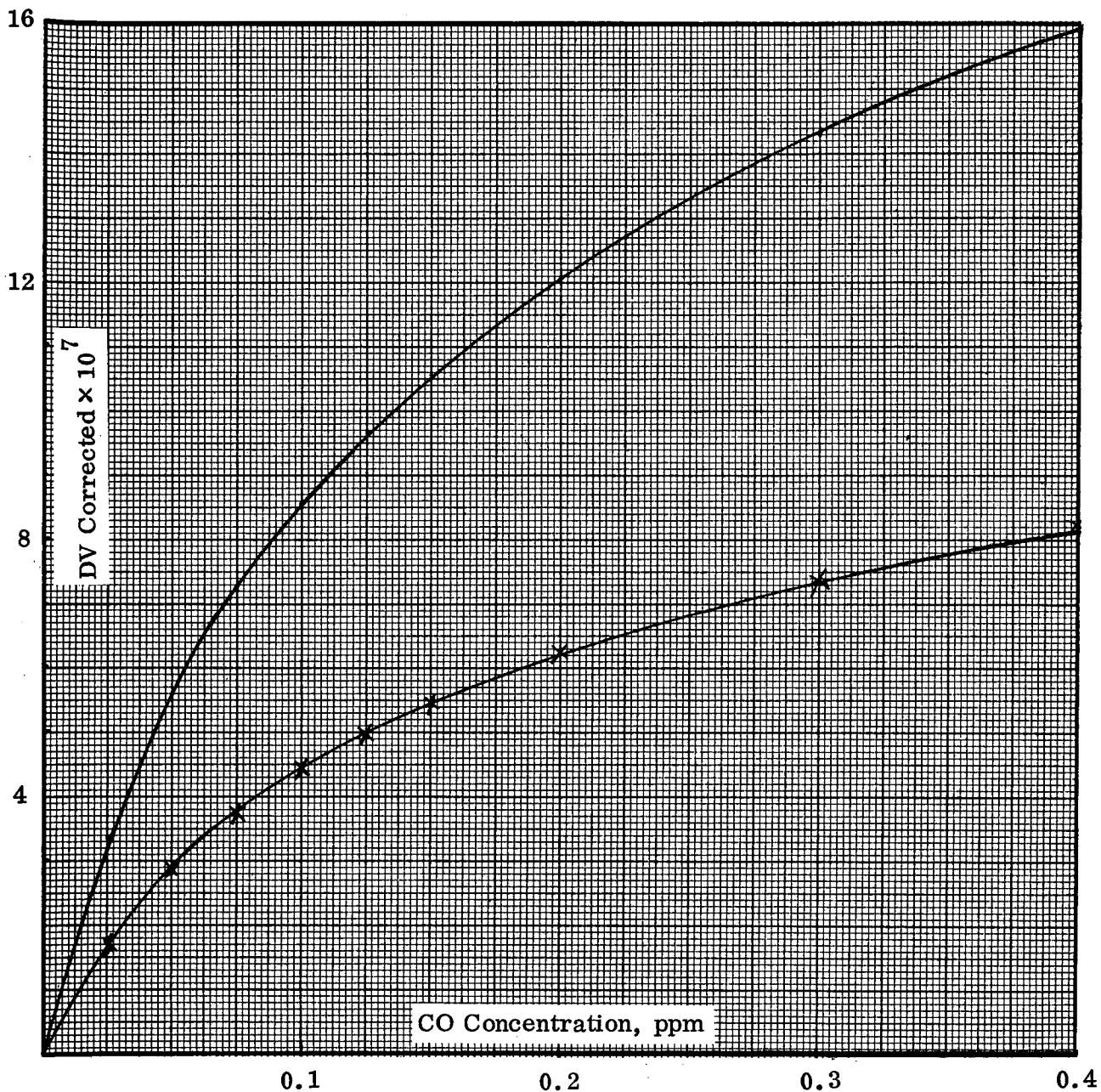


Figure 5-5. Sensitivity of instrument as a function of CO concentration in the troposphere for two different slit functions. The lower curve is for the slit function given in Fig. 5-1, the upper curve for a square slit function. If the upper curve is corrected to account for the larger area under the slit function, the points marked as (x) are obtained.

A calibration of the instrument has also been simulated with the identical instrument parameters used in Run B-09, but a calibration source temperature of 313.2° K and a sample gas temperature of 288.2° K were inputted. The results of these calculations are plotted in Figure 5-6. Run B-16 assumed the same instrument response function as Run B-09 and Run B-17 assumes $C(\omega) = 1.0$ over $\Delta\omega$. This mean responsivity, R_o , obtained by instrument calibration is $R_o = 0.500$; this differs from the atmospheric R_o by less than 2 per cent. Changing the calibration source temperature to 290° K and the sample gas temperature to 260° K resulted in a value of $R_o = 0.512$, which differs from the atmospheric R_o by less than one per cent; these temperatures more closely approximate the ground temperature and effective atmospheric temperature used in Run B-09. A series of calculations were made for the special case of $C(\omega) = C'(\omega)$ and the results are summarized in Table 5-2. Runs B-09, B-18 and B-43-2 give the values for DV_c computed through the real atmosphere. The other results are for a one-slab calibration. The spectral response function for both channels, $C(\omega) = C'(\omega)$, is shown in Figure 5-7.

As indicated previously, the overall responsivity (indicated by C in Table 5-2) is obtained by a computer simulation of a one-slab calibration. For example, DV_c for Run B-16 was computed using a blackbody calibration source temperature, $T_s^o = 313.2^\circ \text{K}$, and a temperature of the gas in the sample calibration cell, $T_{sc} = 288.2^\circ \text{K}$, and the spectral response functions, $C(\omega) = C'(\omega)$; DV_c for Run B-17 was computed using identical conditions except $C(\omega) = C'(\omega) = 1$ from $\omega_1 = 2070 \text{ cm}^{-1}$ to $\omega_2 = 2220 \text{ cm}^{-1}$. C_1 is computed as a function of CO concentration by

$$C_1 = \frac{DV_c \text{ (B-16)}}{DV_c \text{ (B-17)}} ,$$

which results in $C_1 \approx 0.5$. Defining the spectral bandpass by the values when the transmission is one-half, i.e., $\omega_1 = 2111 \text{ cm}^{-1}$ and $\omega_2 = 2176 \text{ cm}^{-1}$, gives values for $C_2 \approx 0.98$. Multiplying the responsivity, C, with the results of the atmospheric

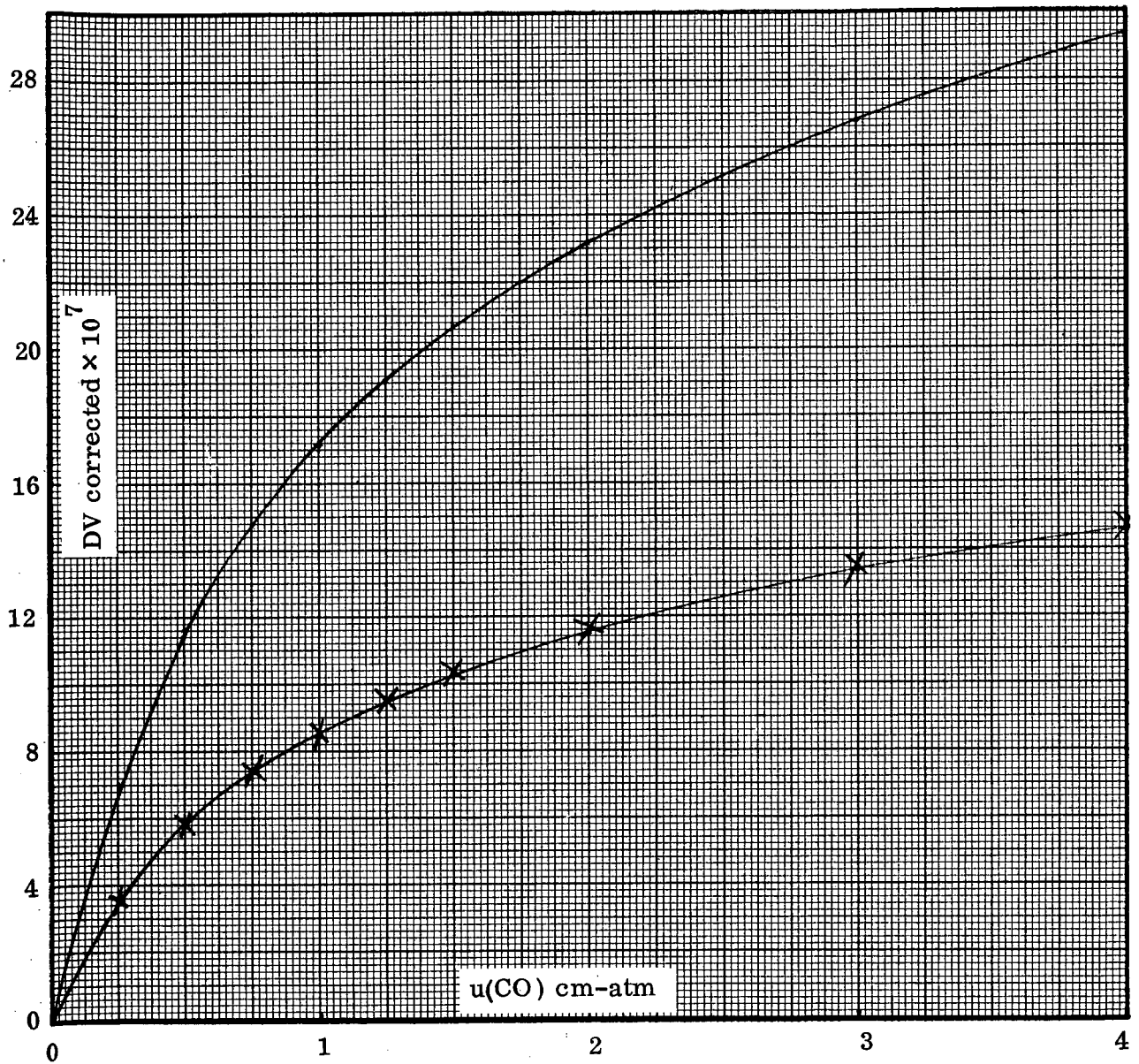
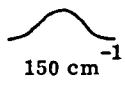
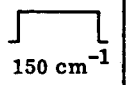
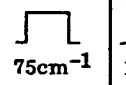
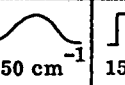
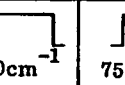
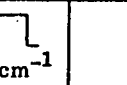
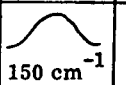
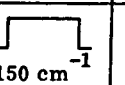


Figure 5-6. Sensitivity of instrument as a function of optical thickness in the instrument "sample" (calibration) cell.

Table 5-2. Effects of Lab Calibration Applied to Real Atmosphere

$DV_c \text{ w/cm}^{-2}\text{-sr} ; \tau_A = .8178 ; C(\omega) = C'(\omega) ; \omega_o = 2143 \text{ cm}^{-1}$														
$(CO)_{atm}$ PPM	B-09 $10^7 DV_c$	B-18 $10^7 DV_c$	B-43-2 $10^7 DV_c$	B-16 $10^7 DV_c$	B-17 $10^7 DV_c$	B-43-1 $10^7 DV_c$	\bar{C}_1	\bar{C}_2	B-32-1 $10^7 DV_c$	B-32-2 $10^7 DV_c$	\bar{C}_3	.500 × DV(B-18) × 10 ⁷	.981 × DV(B-43-2) × 10 ⁷	.512 DV(B-18) × 10 ⁷
0	0	0	0	0	0	0	--	--	0	0	--	0	0	0
.025	1.746	3.32	1.806	3.561	7.08	3.617	.5030	.9845	2.242	4.32	.5191	1.660	1.772	1.700
.050	2.915	5.58	3.006	5.802	11.58	5.903	.5026	.9829	3.599	6.97	.5164	2.790	2.949	2.857
.075	3.772	7.25	3.897	7.370	14.75	7.505	.4997	.9820	4.527	8.81	.5138	3.625	3.823	3.712
.100	4.442	8.57	4.584	8.556	17.13	8.718	<u>.4995</u>	<u>.9814</u>	5.220	10.20	<u>.5118</u>	4.285	4.497	4.388
.125	4.991	9.65	5.140	9.505	19.05	9.629	.4989	.9810	5.770	11.30	.5106	4.825	5.042	4.941
.150	5.455	10.57	5.616	10.294	20.66	10.502	.4983	.9802	6.224	12.22	.5093	5.285	5.509	5.412
.200	6.212	12.09	6.388	11.555	23.21	11.796	.4978	.9796	6.943	13.67	.5079	6.045	6.267	6.190
.300	7.318	14.31	7.524	13.337	26.81	13.620	.4975	.9792	7.941	15.71	.5055	7.155	7.381	7.327
.400	8.118	15.92	8.331	14.571	29.30	14.884	.4973	.9790	8.616	17.08	.5045	7.960	8.173	8.151
C(ω)	 150 cm ⁻¹	 150 cm ⁻¹	 75cm ⁻¹	 150 cm ⁻¹	 150cm ⁻¹	 75 cm ⁻¹			 150 cm ⁻¹	 150 cm ⁻¹				
	$T_G^o = 288.2^\circ K$ $\bar{T}_{atm} \sim 260^\circ K$			$T_S^o = 313.2^\circ K$ $T_{sc} = 288.2^\circ K$					$T_S^o = 290^\circ K$ $T_{sc} = 260^\circ K$			DV Error at 0.1 ppm		
	Atmosphere			Calibration					Calibration					

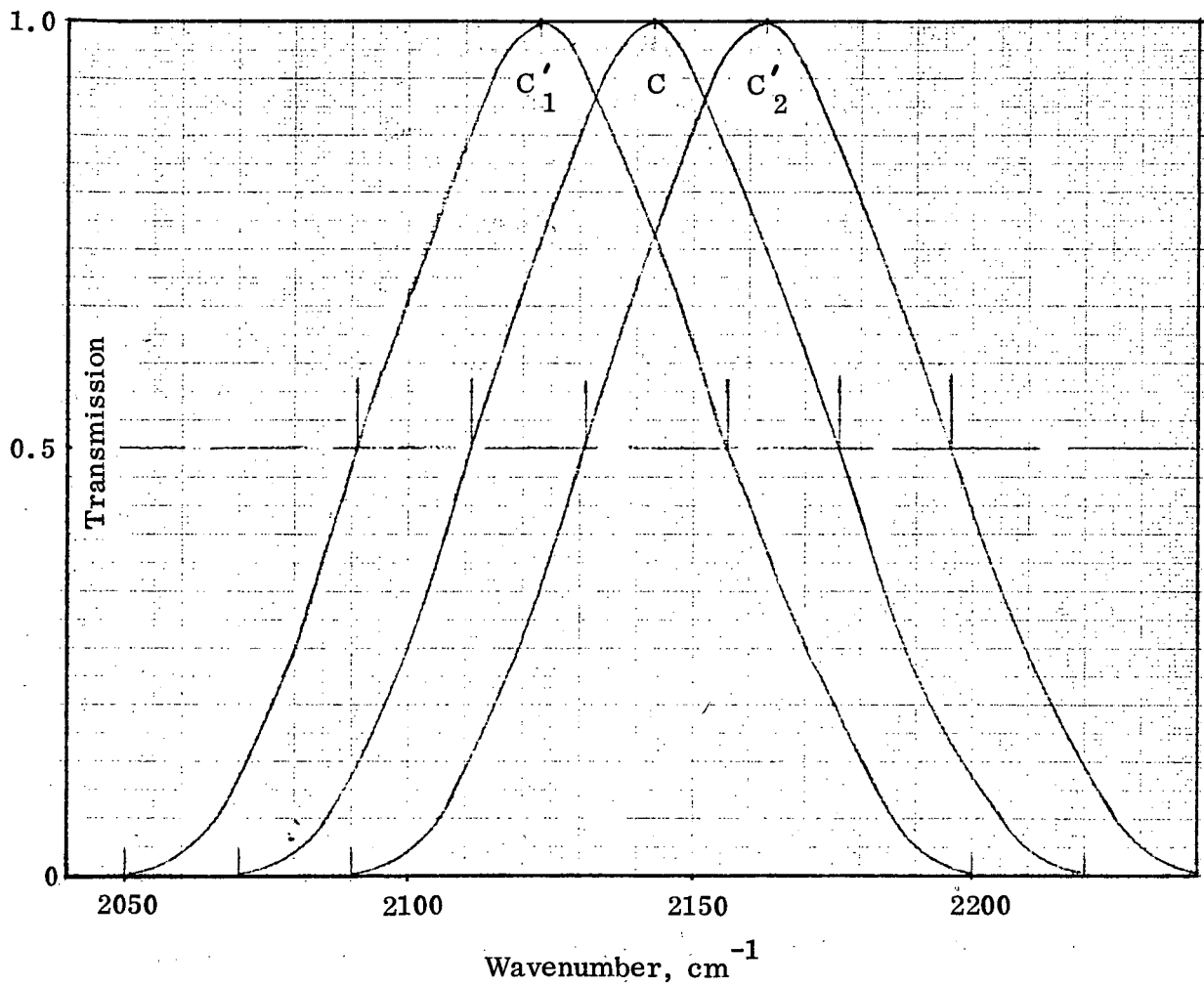


Figure 5-7. Three normalized filter functions used in the computer simulation studies.

computations, which were made using corresponding rectangular spectral response functions, simulates the application of the calibrated response to the case of a real atmosphere. The values thus obtained may be compared with the "true" values that would result if an overall responsivity had not been used. For example, at $C_{CO} = 0.1 \text{ ppm } C_1 (= 0.5) \times DV_c$ for Run B-18 ($= 8.57 \times 10^{-7}$) gives 4.285×10^{-7} which compares with DV_c for Run B-09 ($= 4.442 \times 10^{-7}$); or an error of 3.5% in DV_c would result from applying the calibrated instrument responsivity.

Also presented in Table 5-2 are the results obtained for the calibrated mean instrument responsivity when the calibration is simulated using temperatures more closely approximating the real atmospheric temperatures. These results indicate errors in DV_c will be less by about a factor of three. The results presented in Table 5-2 indicate better agreement between "true" values for DV_c and "one-slab calibration" values if the half-width of the spectral response function is selected for the computer simulation instead of the cutoff frequencies.

Computer simulations have also been performed for cases when $C(\omega) \neq C'(\omega)$. Two extreme cases were selected. In both cases $C(\omega)$ was maintained as indicated by Figure 5-6; but, $C'(\omega)$ was shifted with respect to $C(\omega)$ by plus 20 cm^{-1} in one case and by minus 20 cm^{-1} in a second case. The results are presented in Tables 5-3 and 5-4.

As in the case where $C(\omega) = C'(\omega)$, good agreement is obtained between the "true" values for DV_c and the values obtained when a calibrated mean instrument responsivity is applied. The best agreement results when the integrations are performed over the spectral intervals defined by the one-half transmission limits, namely, for Table 5-3, when $\omega_1 = 2091 \text{ cm}^{-1}$ and $\omega_2 = 2176 \text{ cm}^{-1}$ and for Table 5-4 when $\omega_1 = 2111 \text{ cm}^{-1}$ and $\omega_2 = 2196 \text{ cm}^{-1}$.

To summarize, the computer calculations indicate that a one-slab calibration of the instrument's responsivity may be applied to signals obtained by the instrument when observing a real atmosphere. This means that a detailed knowledge of the spectral responses of the two instrument channels is not necessary.

Table 5-3. Effects of Lab Calibration Applied to Real Atmosphere





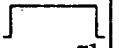





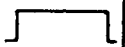

$DV_c, W/cm^2 - sr ; \tau_A = .7642 ; C(\omega) \neq C'(\omega); \omega_o(c) = 2143 cm^{-1} ; \omega_o(C') = 2123 cm^{-1}$											
(CO) atm PPM	B-10 $10^7 DV_c$	B-25 $10^7 DV_c$	B-45-2 $10^7 DV_v$	B-21 $10^7 DV_c$	B-22 $10^7 DV_c$	B-45-1 $10^7 DV_c$	\bar{C}_1	\bar{C}_2	$.485 \times DV(B-25) \times 10^7$	$.771 \times DV(B-45-2) \times 10^7$	
0	0	0	0			0	--	--	0	0	
.025	1.592	3.13	2.111	3.266	6.67	4.28	.4896	.7631	1.518	1.628	
.050	2.663	5.25	3.503	5.322	10.92	6.94	.4874	.7669	2.546	2.702	
.075	3.446	6.83	4.523	6.750	13.90	8.78	.4856	.7688	3.312	3.488	
.100	4.056	8.08	5.314	7.820	16.14	10.14	.4845	.7712	3.919	4.098	
.125	4.553	9.10	5.955	8.669	17.96	11.22	.4827	.7726	4.414	4.592	
.150	4.972	9.96	6.478	9.368	19.47	12.11	.4812	.7736	4.831	4.996	
.200	5.651	11.39	7.349	10.474	21.81	13.50	.4802	.7759	5.524	5.668	
.300	6.631	13.45	8.598	12.008	25.12	15.43	.4780	.7782	6.523	6.631	
.400	7.330	14.94	9.474	13.043	27.33	16.73	.4772	.7796	7.246	7.306	
$C_1'(\omega) C(\omega)$		 170 cm ⁻¹	 85 cm ⁻¹		 170cm ⁻¹	 85cm ⁻¹			3.4%	-1.0%	
								DV Error @ 0.1 ppm			
$T_G^o = 288.2^\circ K$ $\bar{T}_{atm} \sim 260^\circ K$ Atmosphere				$T_s^o = 313.2^\circ K$ $T_{sc} = 288.2^\circ K$ Calibration							

Table 5-4. Effects of Lab Calibration Applied to Real Atmosphere

$DV_c, w/cm^2-sr ; \tau_A = .8753 ; C(\omega) \neq C'(\omega) ; \omega_o(C) = 2143 cm^{-1} ; \omega_o(C') = 2163 cm^{-1}$										
$(CO)_{atm}$ PPM	B-11 $10^7 DV_c$	B-26 $10^7 DV_c$	B-45-4 $10^7 DV_c$	B-23 $10^7 DV_c$	B-24 $10^7 DV_c$	B-45-3 $10^7 DV_c$	\bar{C}_1	\bar{C}_2	.480 × DV(B-26) × 10 ⁷	.705 × DV(B-45-4) × 10 ⁷
0	0	0	0	0	0	0	--	--	0	0
.025	1.802	3.60	2.627	3.773	7.69	5.38	.4854	.7013	1.727	1.852
.050	2.997	6.05	4.343	6.124	12.62	8.71	.4852	.7031	2.903	3.062
.075	3.870	7.88	5.605	7.765	16.11	11.03	.4820	.7040	3.781	3.952
.100	4.553	9.33	6.588	9.010	18.78	12.78	<u>.4798</u>	<u>.7050</u>	4.477	4.645
.125	5.112	10.53	7.395	10.010	20.93	14.17	.4782	.7064	5.052	5.213
.150	5.586	11.56	8.072	10.843	22.74	15.36	.4748	.7059	5.546	5.691
.200	6.360	13.25	9.200	12.181	25.67	17.28	.4745	.7050	6.357	6.486
.300	7.491	15.79	10.857	14.082	29.88	20.00	.4713	.7041	7.576	7.654
.400	8.309	17.66	12.084	15.405	32.88	21.97	.4685	.7012	8.473	8.519
$C(\omega), C'_2(\omega)$										
		180 cm ⁻¹	85 cm ⁻¹		180 cm ⁻¹	85cm ⁻¹			1.7%	2.0%
	$T_G^o = 288.2^\circ K$ $\bar{T}_{atm} \sim 260^\circ K$			$T_S^o = 313.2^\circ K$ $T_{SC} = 288.2^\circ K$					DV Error @ 0.1 ppm	
	Atmosphere			Calibration						

5.3 IN-FLIGHT CALIBRATION

In this section we show the results of the investigation about the influence of different calibration temperatures on ΔV . The ground temperature was kept at 270°K, but in one case $T_C = 270^\circ\text{K}$, in another case $T_C = 300^\circ\text{K}$. The results for four different CO concentrations are as follows:

Table 5-5. Signal Change of CO for the Calibration Temperatures

T_C	300°K	270°K	Difference
ϵ_{GR}	1	1	
$\Delta V @ 0 \text{ ppm}$	1.363×10^{-9}	0	1.363×10^{-9}
.05	6.7216×10^{-8}	6.5865×10^{-8}	1.351×10^{-9}
.1	1.1515×10^{-7}	1.1381×10^{-7}	1.34×10^{-9}
.2	1.7772×10^{-7}	1.7639×10^{-7}	1.33×10^{-9}
.3	2.2054×10^{-7}	2.1922×10^{-7}	1.32×10^{-9}
.4	2.5390×10^{-7}	2.5259×10^{-7}	1.31×10^{-9}

As expected, in the case for which the ground and calibration temperatures are the same, $\Delta V = 0$ for $c_{CO} = 0$. But for a temperature difference of 30°K, $\Delta V^\circ = 1.363 \times 10^{-9} \text{ W/cm}^2 \text{ sr}$. This offset is only about 1.4% of the signal for $c_{CO} = 0.1 \text{ ppm}$. It is further found that the offset remains nearly constant for all CO concentrations, as shown in the last column.

The offset ΔV° as a function of ground temperature, emissivity and sun angles was further investigated. In Figure 5-8 we have plotted ΔV° for the three temperatures 270, 300 and 330°K, whereby $T_C = 300^\circ\text{K}$. The different lines are for the sun zenith angles 0, 30, 60 and 90°. One can see that for low angles, ΔV° increases due to the fact that the wavelength dependency of the reflected sun energy is that of a 6000°K blackbody and thus quite different from the 300°K calibration blackbody. The offset ΔV° also increases with decreasing ϵ , since then the reflectivity increases. In all cases, maximum ΔV° is obtained for $\epsilon = 0$. The exception is the night time ($\theta = 90^\circ$) and $\Delta V^\circ = 0$ for $\epsilon = 0$. Since for $\epsilon = 0$ only sun reflected energy is observed, the lines for a given θ , but different T_{GR} , must have the same value for $\epsilon = 0$. These points are convenient check values for the computer program as well as the hand plots.

For the higher ground temperatures, the absolute magnitude of ΔV° appears to be large. However, when ΔV° is related to the signal obtained for 0.1 ppm CO, it is found that for the present case ΔV° is never more than 3% of $\Delta V_{0.1}$. These results are shown in Figure 5-9, where $\delta_1 = \Delta V^\circ \times 100 / \Delta V_{0.1}$ is plotted versus the ground temperature for $\epsilon = 0.8$ and 0.4 and θ as a parameter.

5.4 INVESTIGATION OF RATIO TECHNIQUES

5.4.1 Ratio of Signal Difference of One Cell Pair to Signal

It was found that the ratio DV/V reduces atmospheric effects on the measurements of CO. As an example, this ratio has been plotted for different concentrations of CO and water in the atmosphere (see Figure 5-10). The four upper curves are the signal differences as a function of CO concentration for a dry and three different wet atmospheres. If the water concentration of the wet atmosphere is uncertain to within 1/2 and 2 times the normal Gutnick model, the determination of the CO concentration is uncertain to within 42%. The lower four curves are the values of

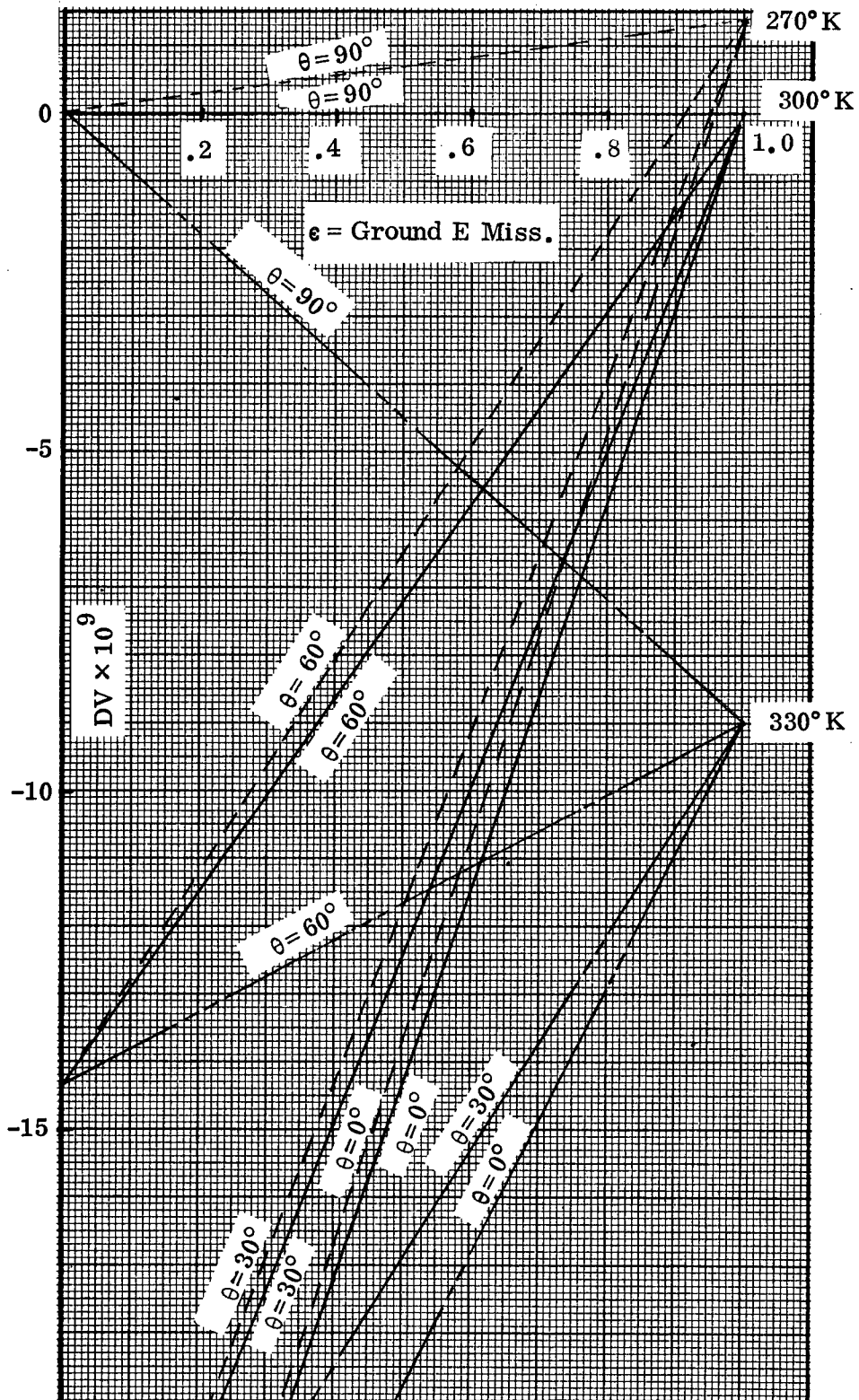


Figure 5-8. Sensitivity of the instrument to different ground temperatures and sun zenith angles as a function of ground emissivity at 4.6μ for zero concentration of CO in the troposphere.

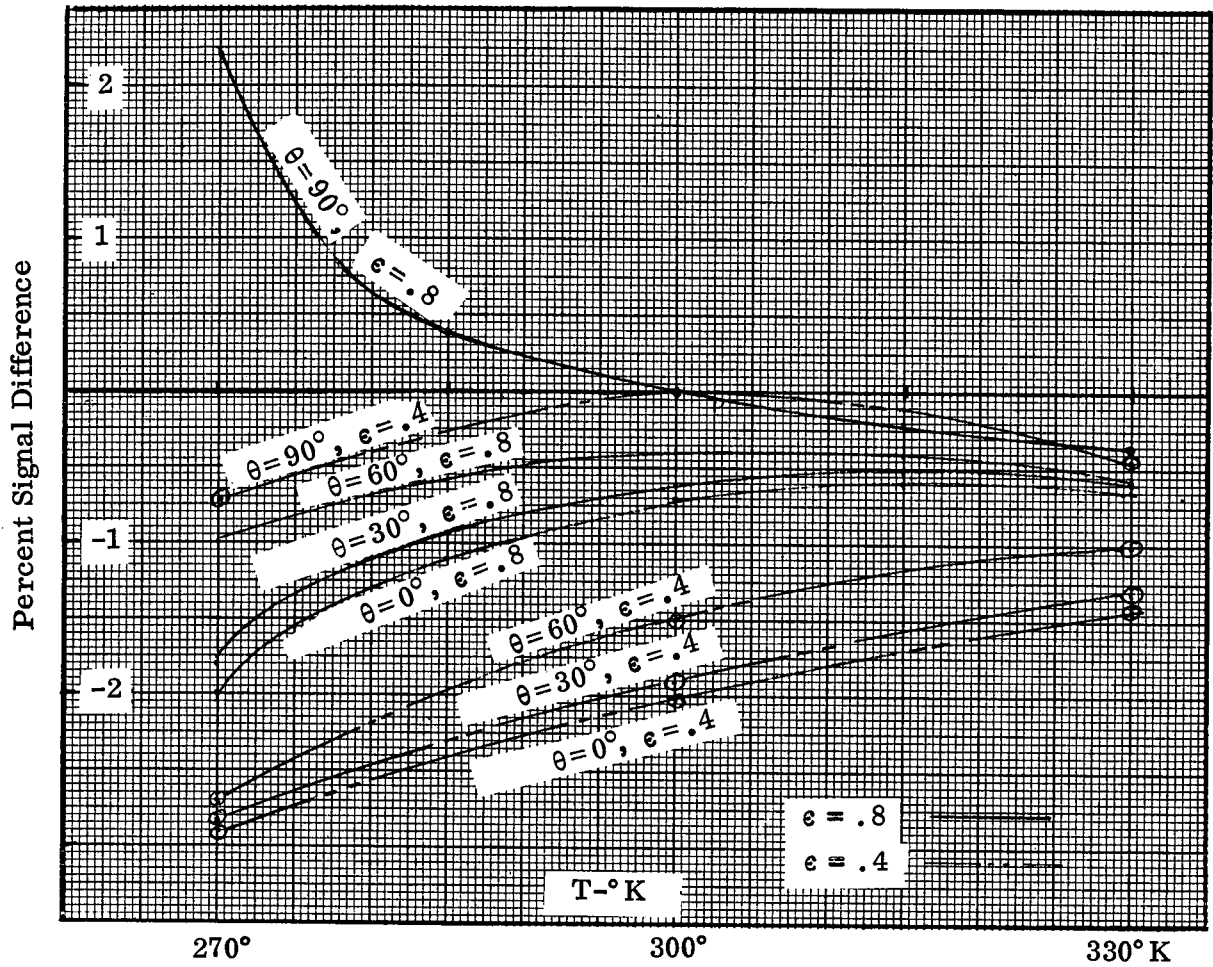


Figure 5-9. Sensitivity of the instrument for the same conditions as in Fig. 5-8, but referenced to DV for 0.1 ppm CO concentration.

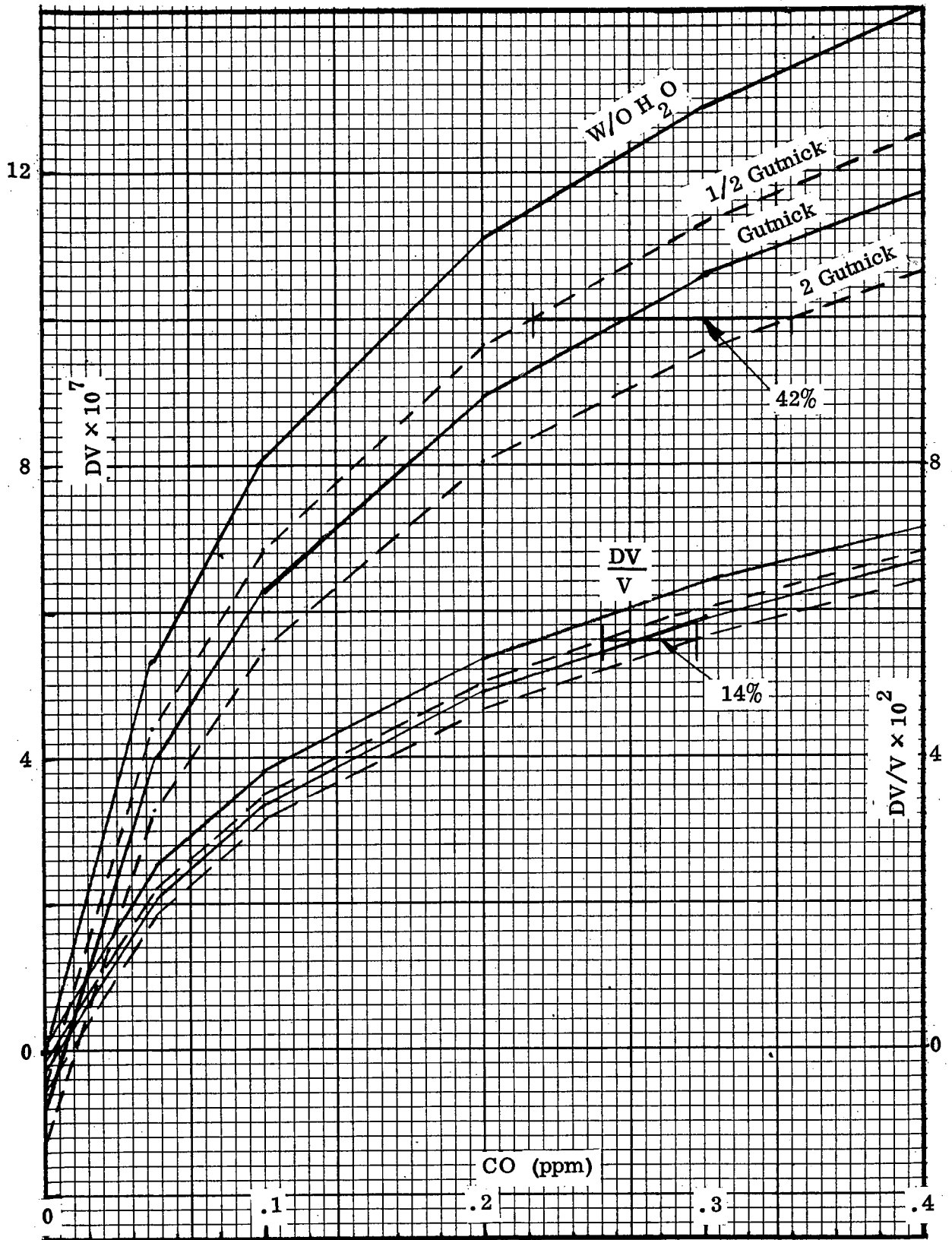


Figure 5-10. DV and DV/V as a function of CO concentration in the troposphere with and without water vapor.

DV/V for the same atmospheres. As can be seen, the uncertainties in the determination of the CO concentrations are reduced to about 14%. The influence of varying ground temperature is also reduced when the ratio is used instead of ΔV alone.

Figure 5-11 shows the ratio versus c_{CO} for T_G from 315 to 260°. At $c_{CO} = .1$ the difference in the ratio for $T_G = 300^\circ$ and 285° is 5×10^{-3} out of 30.3×10^{-3} , or 16.7%, whereas the difference in ΔV for $T_G = 300$ and 285° is $3 \times 10^{-7} \text{ W/cm}^2$ ster out of 6.13×10^{-7} , or $\sim 50\%$, a considerably larger difference. The value of the ratio will decrease as T_G approaches the average atmospheric temperature. This is seen in Figure 5-12, a plot of $\Delta V/V$ versus T_G for different CO concentrations. The sensitivity of $\Delta V/V$ for changes in T and water vapor are indicated in Figure 5-11 by line lengths.

From these calculations the changes in $\Delta V/V$ were converted to changes in CO concentration. Interpreting these as independent error sensitivities, and assuming the expected uncertainties in T_G , T, and water vapor to be $\pm 2\text{K}$, $\pm 2\text{K}$, and 20% respectively, the expected errors in CO concentration at $c_{CO} = .1 \text{ ppm}$ are

- $\pm 3.3\%$ for $\Delta T_G = \pm 2\text{K}$
- $\pm 4.4\%$ for $\Delta T = 2\text{K}$
- $\pm 2.4\%$ for $\Delta WV = \pm 20\%$
- $\pm 6.02\%$ for all three error sources.

The relationship between ΔV and V was further examined for different conditions of CO concentration, surface temperatures, atmospheric temperature and water vapor profile perturbations, and for different surface emissivities and sun zenith angles. Figure 5-13 shows the plot of ΔV and V for the temperature and water vapor. Several interesting observations can be made. For instance, the

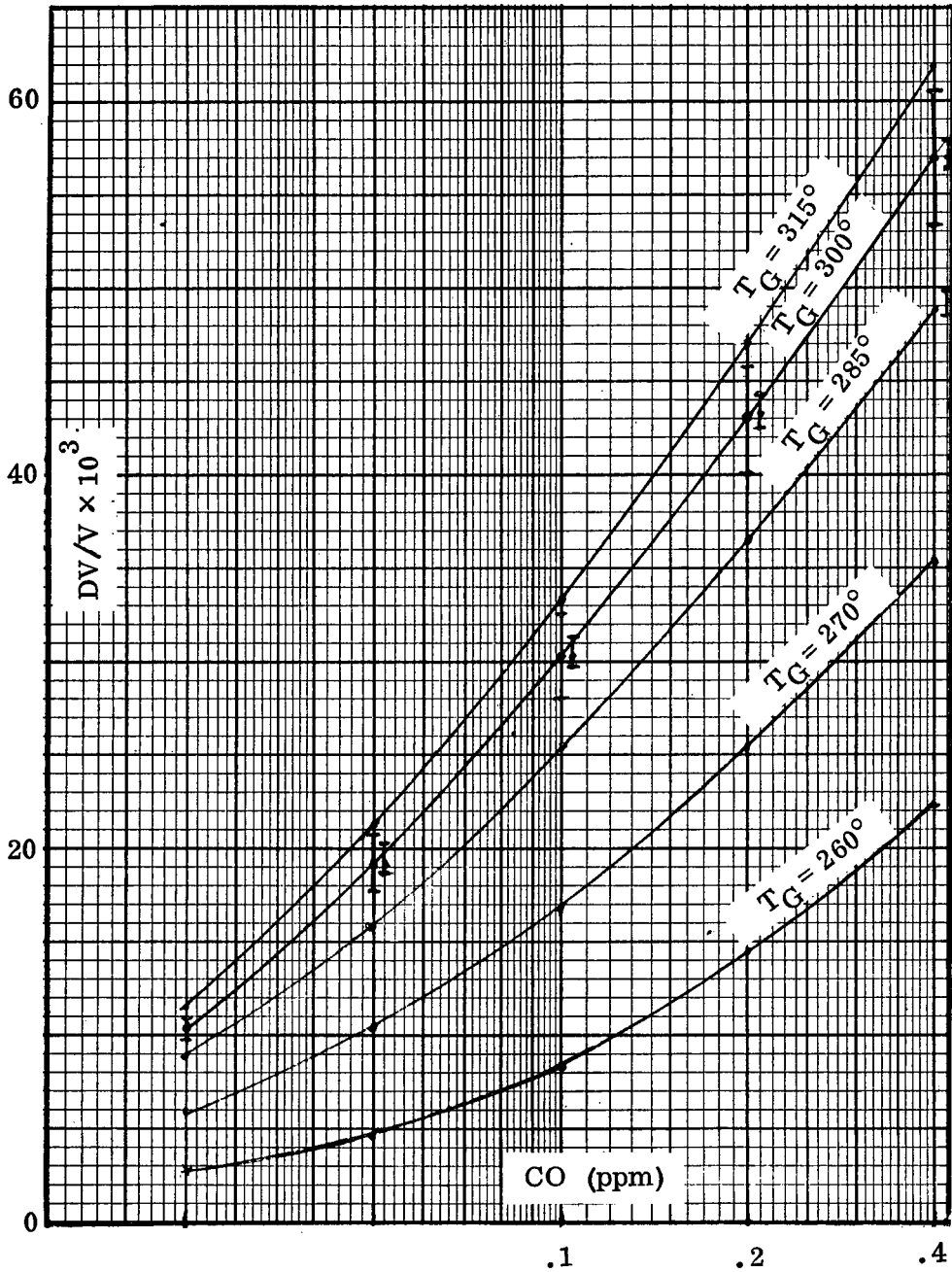


Figure 5-11. DV/V as a function of CO concentration in the troposphere for different ground temperatures and variations of atmospheric temperatures and water vapor concentration.

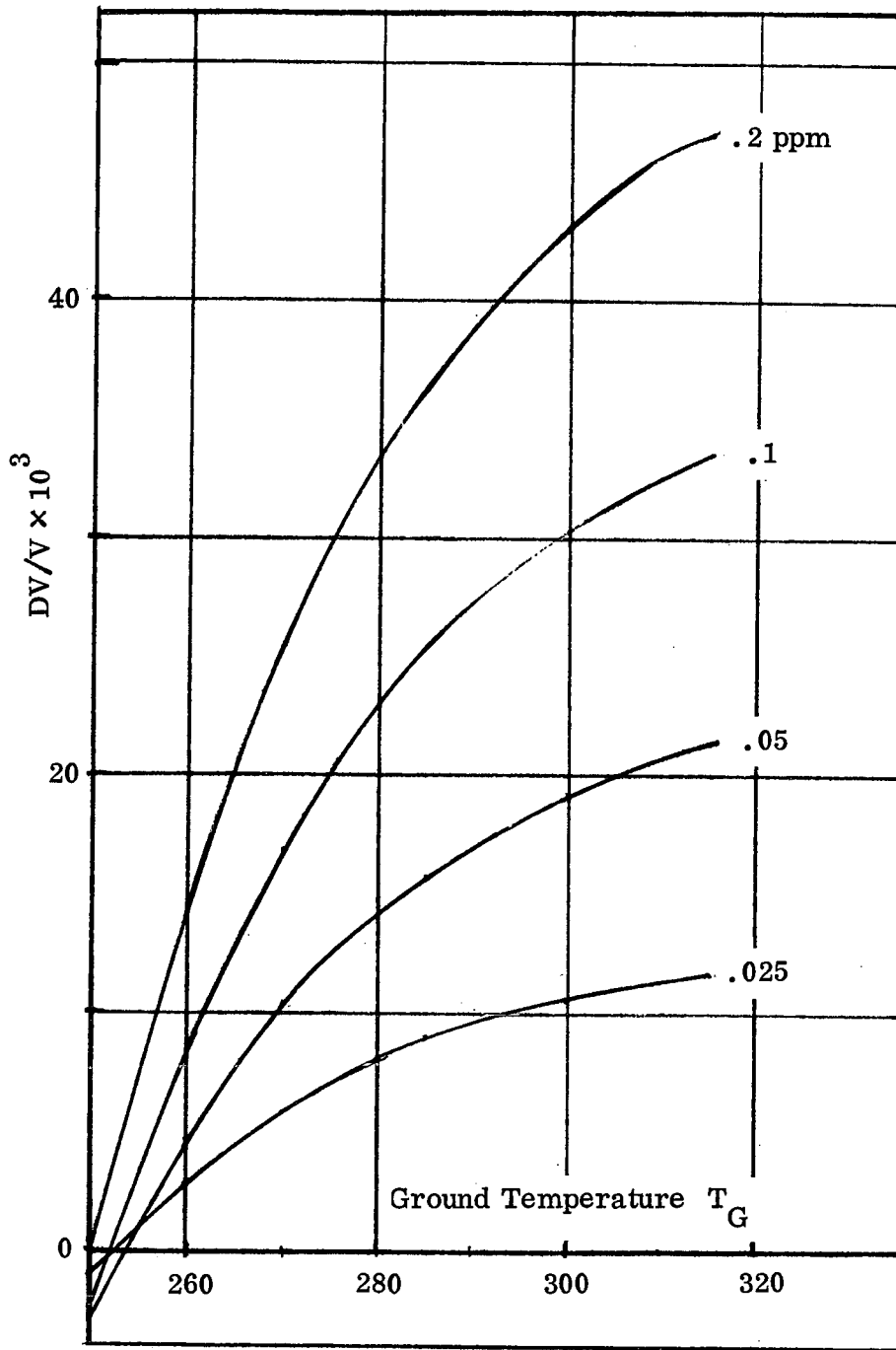


Figure 5-12. DV/V as a function of ground temperature for various CO concentrations in the atmosphere.

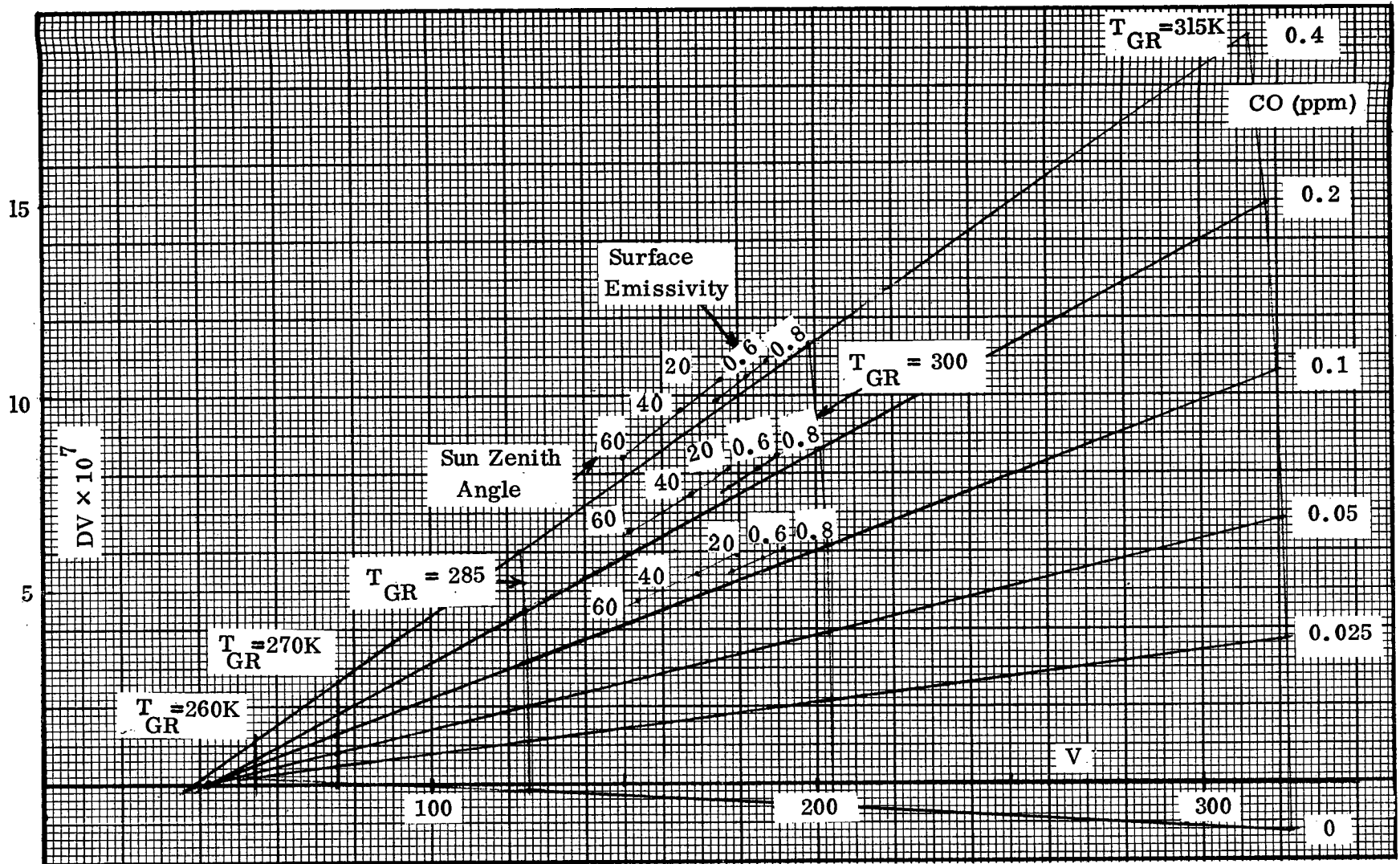


Figure 5-13. DV as a function of V for different conditions of CO concentration, surface temperature, atmospheric temperature and water profile perturbations, surface emissivities, and sun zenith angles.

quantity $Q = \Delta V / (V - 42)$, which is the approximate slope of ΔV vs. V at different CO concentrations, appears to be independent of surface temperature. It is likely that the term with value 42 in the indicated case depends in value on the average atmosphere emission, and could be expected to differ for different atmospheres. Removal of the surface temperature dependence from the $\Delta V/V$ relation could result also in less sensitivity of the CO concentration to other uncertainties, beside the surface temperature dependence. It might even be possible to combine the gas cell radiance values from several instrument channels in order to better estimate the observed surface temperature. Figure 5-13 also shows the effect of different values of surface emissivities. The slopes of ΔV versus V as the sun zenith angle is changed appear to be the same as the slope for the standard case, implying independence. A translation of the curves with surface emissivity, however, is in evidence. It may be possible that different term values in the denominator for Q could be found to reduce the effect of surface emissivity uncertainties on the Q function.

Figure 5-14 shows superimposed on the standard cases the curves of ΔV versus V for CO of 0.4 and 0.1 ppm, the perturbation on ΔV and V due to changes in the atmospheric temperature profile by $\pm 5K$ and in the water vapor profile by $\pm 50\%$ in mixing ratio. The perturbations are shown for ground temperature of 300 and 285K. The indicators at 300K and 0.4 ppm CO equally hold for the other cases.

The uncertainties of Q due to water vapor changes appear to be largely removed, because they line up with the ΔV vs. V slope. Changes in atmospheric temperature affect the Q values for different amounts of CO. The uncertainties in temperature are expected to be small, therefore Q will likewise have small uncertainties.

This approach has to be further explored, especially with respect to uncertainties in the atmospheric scattered sunlight, important at the shorter wave-

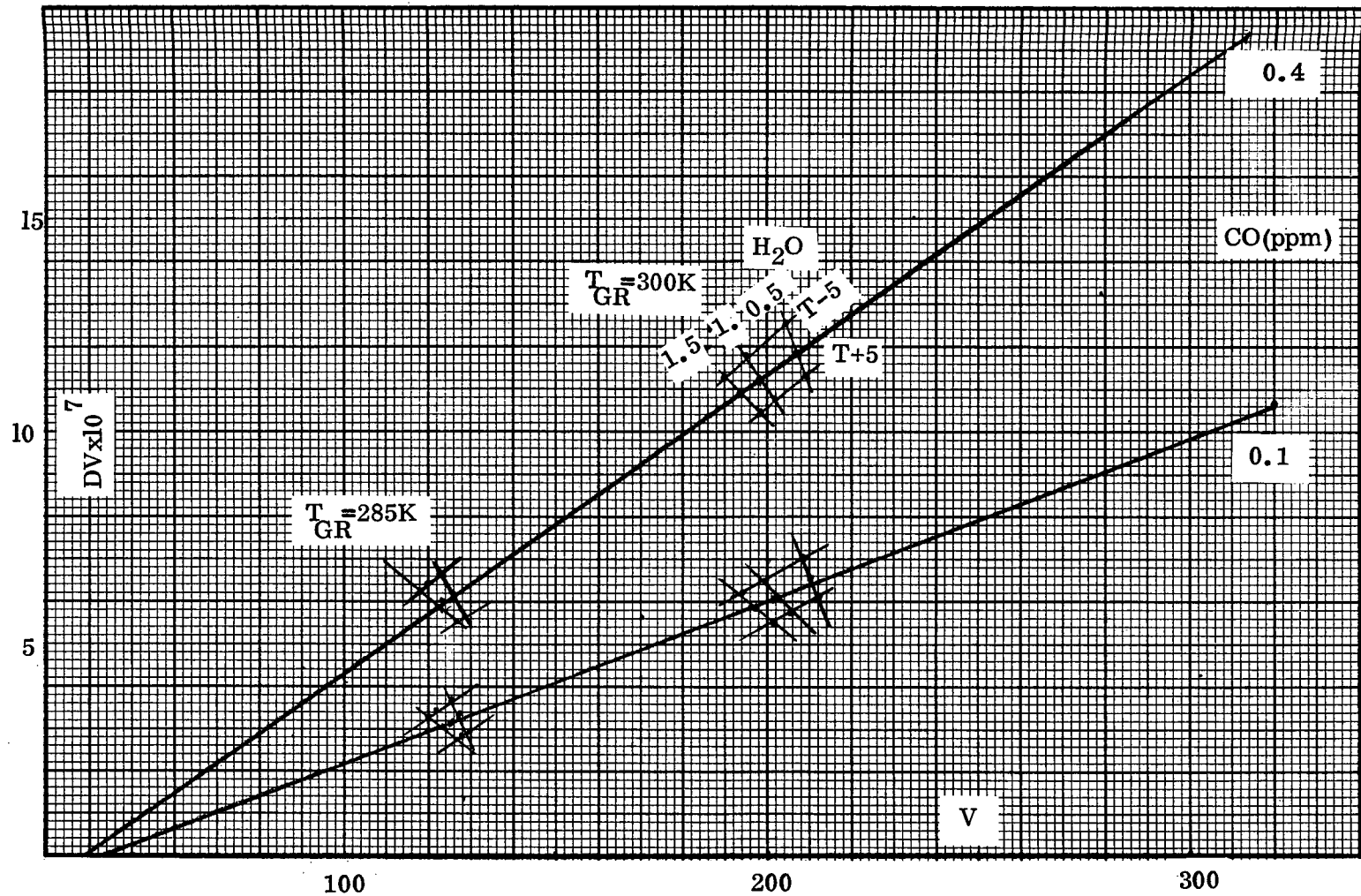


Figure 5-14. Perturbation of DV and V due to changes in the atmospheric temperature profile by $\pm 5^\circ K$ and in the water vapor profile by $\pm 50\%$ in mixing ratio.

lengths, and the effects due to the atmospheric emission. This may lead to a viable method of reducing the uncertainties due to some of the parameters affecting the instrument performance.

5.4.2 Ratio of Signal Difference of Two-Cell Pairs

Calculations were made for different cell conditions, in which the total pressure was changed from zero to 1 atm, keeping the CO concentration constant. The signal difference ΔV as a function of total cell pressure is plotted parametrically with 27 different CO concentrations in Figures 5-4, 5-15 and 5-16. The distribution of CO in the 8 layers is given in Table 5-6. The numbers on the curves refer to the factor with which every layer is multiplied.

Table 5-6. CO Concentration for 3 Distributions

<u>Layer</u>	<u>B20</u>	<u>B 37</u>	<u>B36</u>
1	10^{-7}	10^{-7}	10^{-5}
2	10^{-7}	10^{-7}	10^{-6}
3	10^{-7}	10^{-7}	10^{-7}
4	10^{-7}	10^{-7}	10^{-7}
5	10^{-7}	10^{-7}	10^{-7}
6	10^{-7}	10^{-6}	10^{-7}
7	10^{-7}	10^{-6}	10^{-7}
8	10^{-7}	10^{-7}	10^{-7}
Total Path Length	56.6×10^{-3} cm atm	174.9×10^{-3} cm atm	1065.9×10^{-3} cm atm

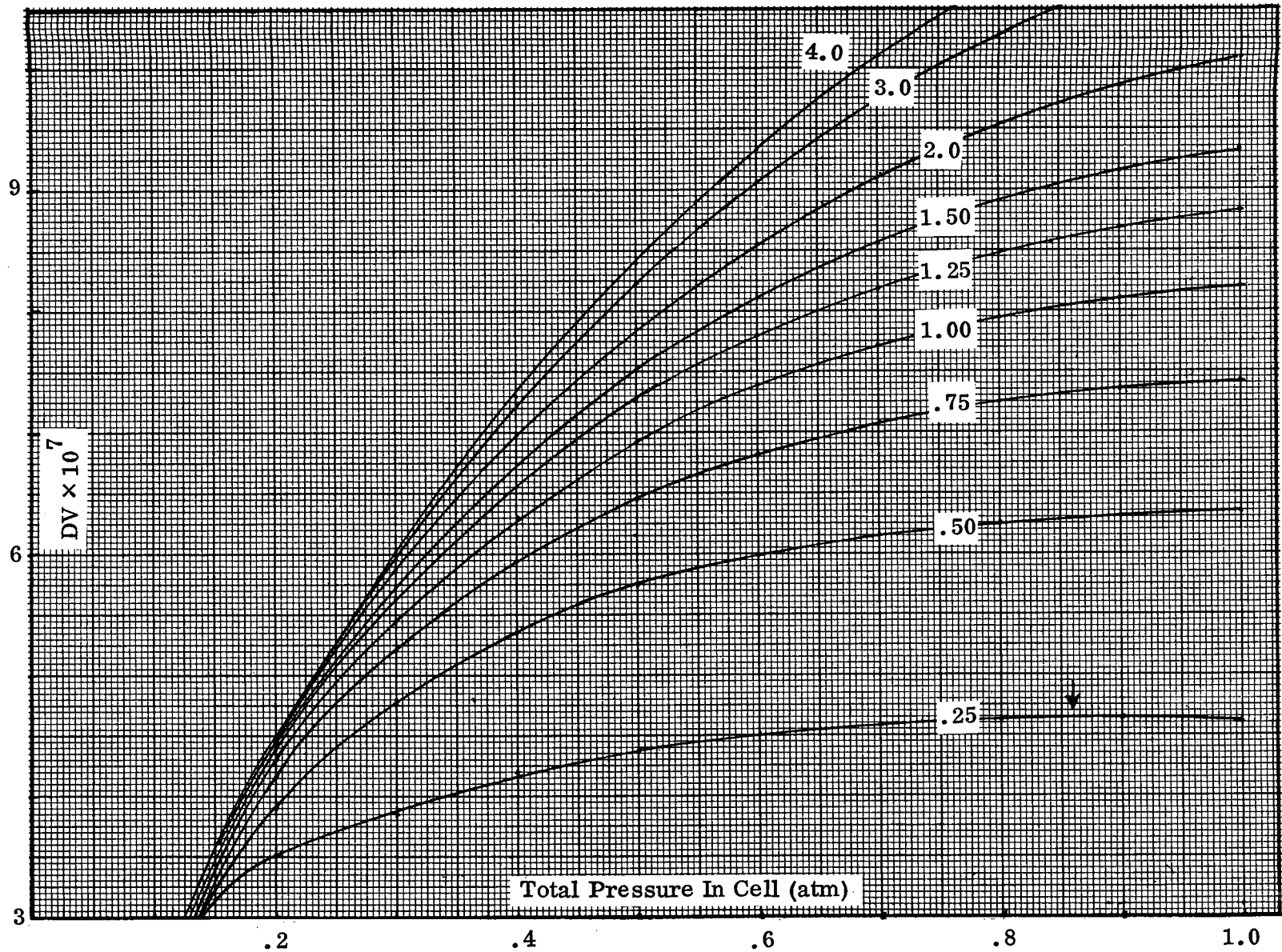


Figure 5-15. Sensitivity of instrument as a function of total pressure in the instrument cell for different concentrations of CO in the troposphere, having a profile according to B37 (see Table 5-6).

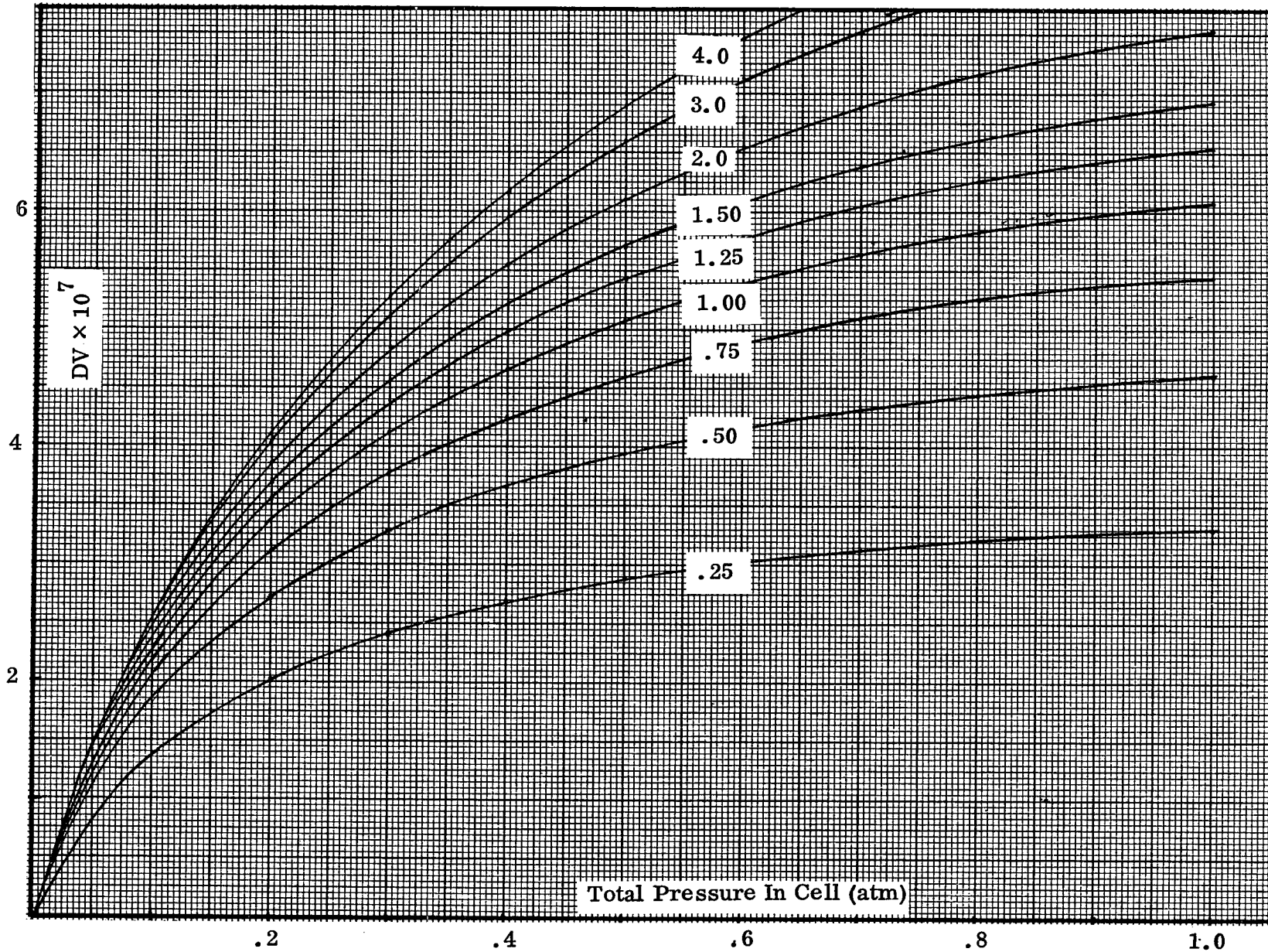


Figure 5-16. Sensitivity of instrument as a function of total pressure in the instrument cell for different concentrations of CO in the troposphere, having a profile according to B36 (see Table 5-6).

The results of DV versus the optical path (cm-atm) are plotted in Figure 5-17 for the three distributions and two cell pressures. The shapes of the curves and ratios appear to be sufficiently different to give some information about the distribution. This is shown in Figure 5-18, where the ratio of the DV for the channels at different pressures versus optical path is plotted. The two distributions B-37 and B-20 are very similar, but B-36 (build-up of CO near the surface) shows a different behavior.

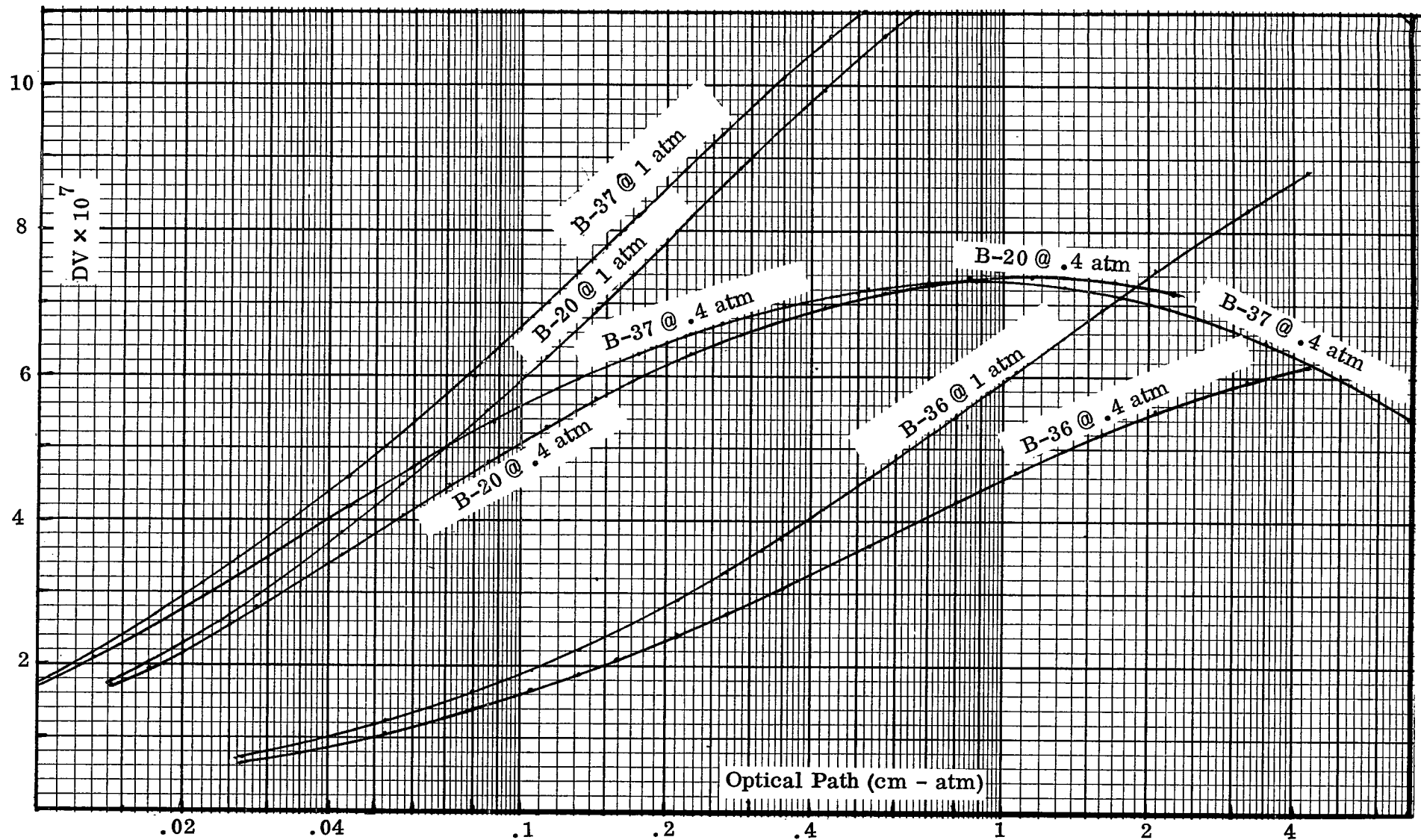


Figure 5-17. Sensitivity of the instrument as a function of the total optical thickness of CO for the three profiles B20, B37 and B36, using cell pressures of 1 and 0.4 atm.

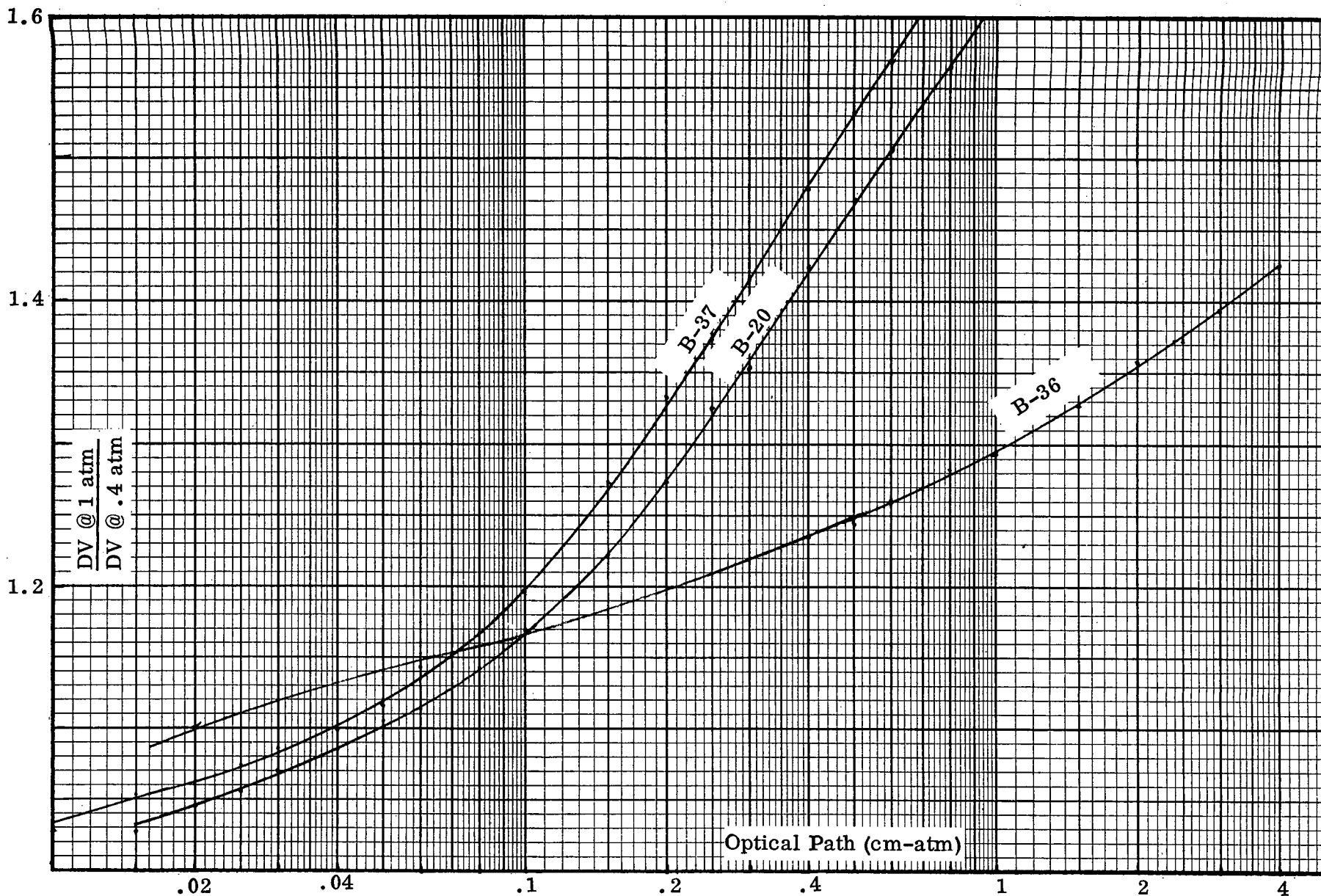


Figure 5-18. The ratio of DV as a function of total optical thickness for three CO concentration profiles (see Fig. 5-17), using two cell pairs with pressures of 1 and 0.4 atm.

6

STUDY OF MISSION REQUIREMENTS

(Task 5)

In this section, the supporting data requirements are investigated. These are atmospheric temperature and pressure profile, the water vapor profile, and the extent of cloud cover and cloud top height. The effect of the uncertainties in these atmospheric parameters on the signal difference of the RGFC instrument are investigated for the measurement of CO.

6.1 ATMOSPHERIC TEMPERATURE AND PRESSURE PROFILE

6.1.1 Temporal and Spatial Variations of Temperature Profiles in the Real Atmosphere

In order to gain some insight into the spatial and temporal variations of the vertical atmospheric temperature profiles, meteorological data for two different climatological regions were analyzed. Archival data from the National Climatic Center in Asheville, N.C. of the Northern Hemisphere and U.S. for July 1970 and February 1971 were utilized.

(a) Temporal Changes

The temperature and spatial temperature gradients at the 500 mb level were plotted from 12 hours data for a month's interval. Figure 6-1 shows this data for San Diego, February 1971; Figure 6-2 is for Washington, D.C., February 1971; and Figure 6-3 is for San Diego, July 1970. Temperature data was from station reports for Figure 6-1 and from the upper level charts for Figures 6-2 and 6-3. The temperature gradient was obtained from the upper level chart by estimating the distance between isotherms in the vicinity of the station and then converting to degrees centigrade per 100 nautical miles. It should be noted that the isotherms on the upper level charts are spatially smoothed data and therefore, do not represent the exact

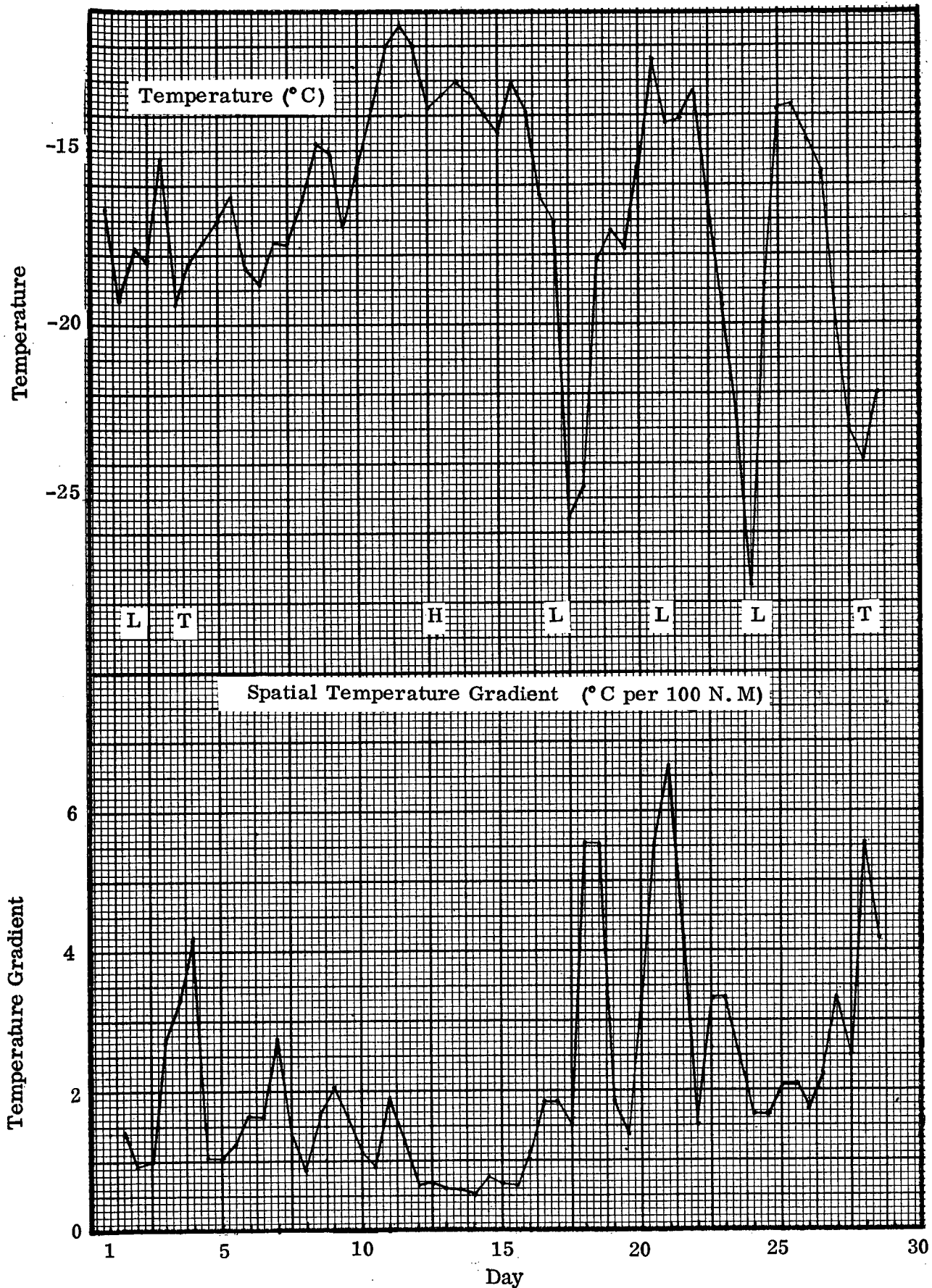


Figure 6-1. Temperature and temperature gradient at 500 mb level for February 1971 in San Diego, California at 0000 and 1200 Z.

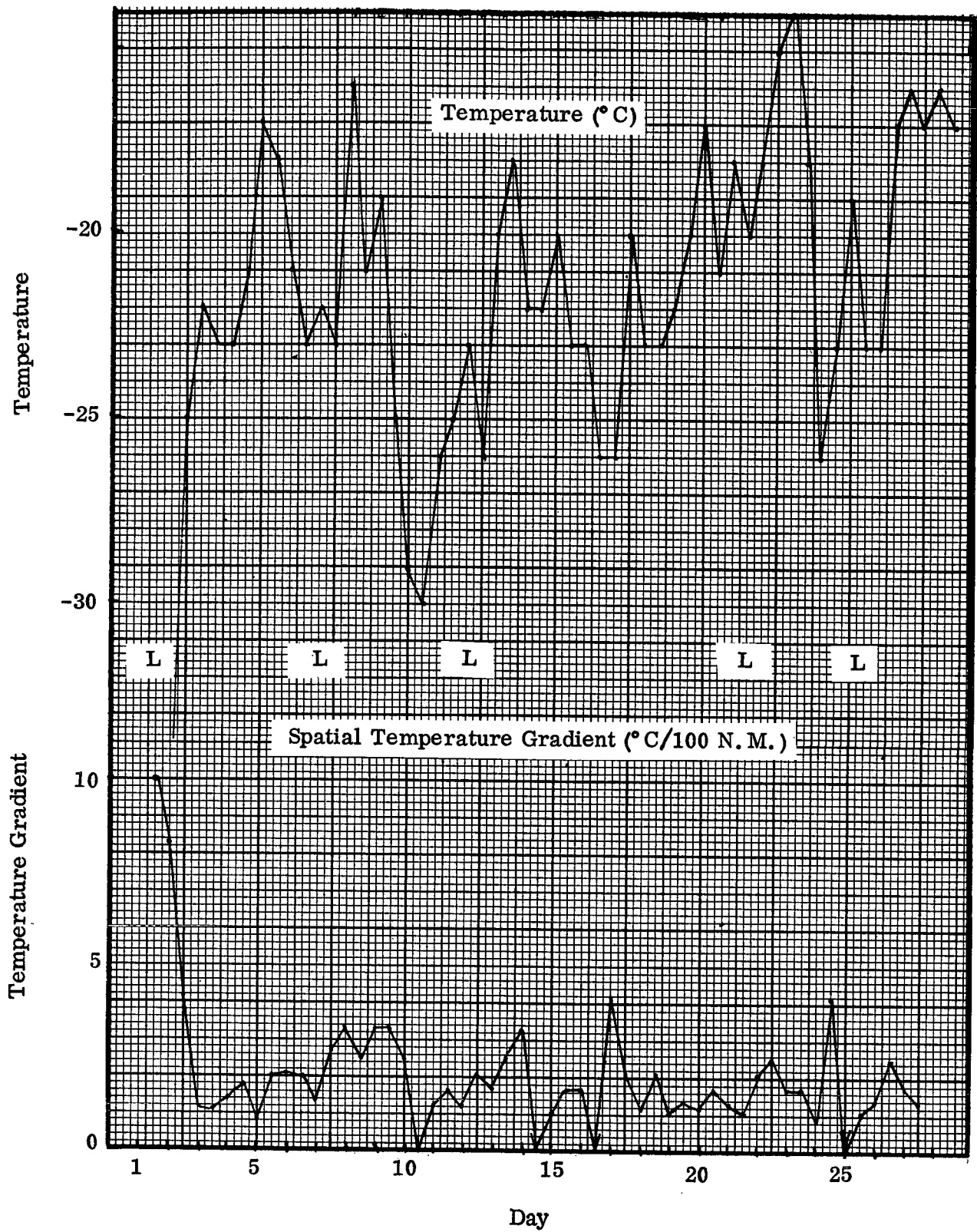


Figure 6-2. Temperature and temperature gradient at 500 mb level for February 1971 in Washington, D.C. at 0000 and 1200 Z.

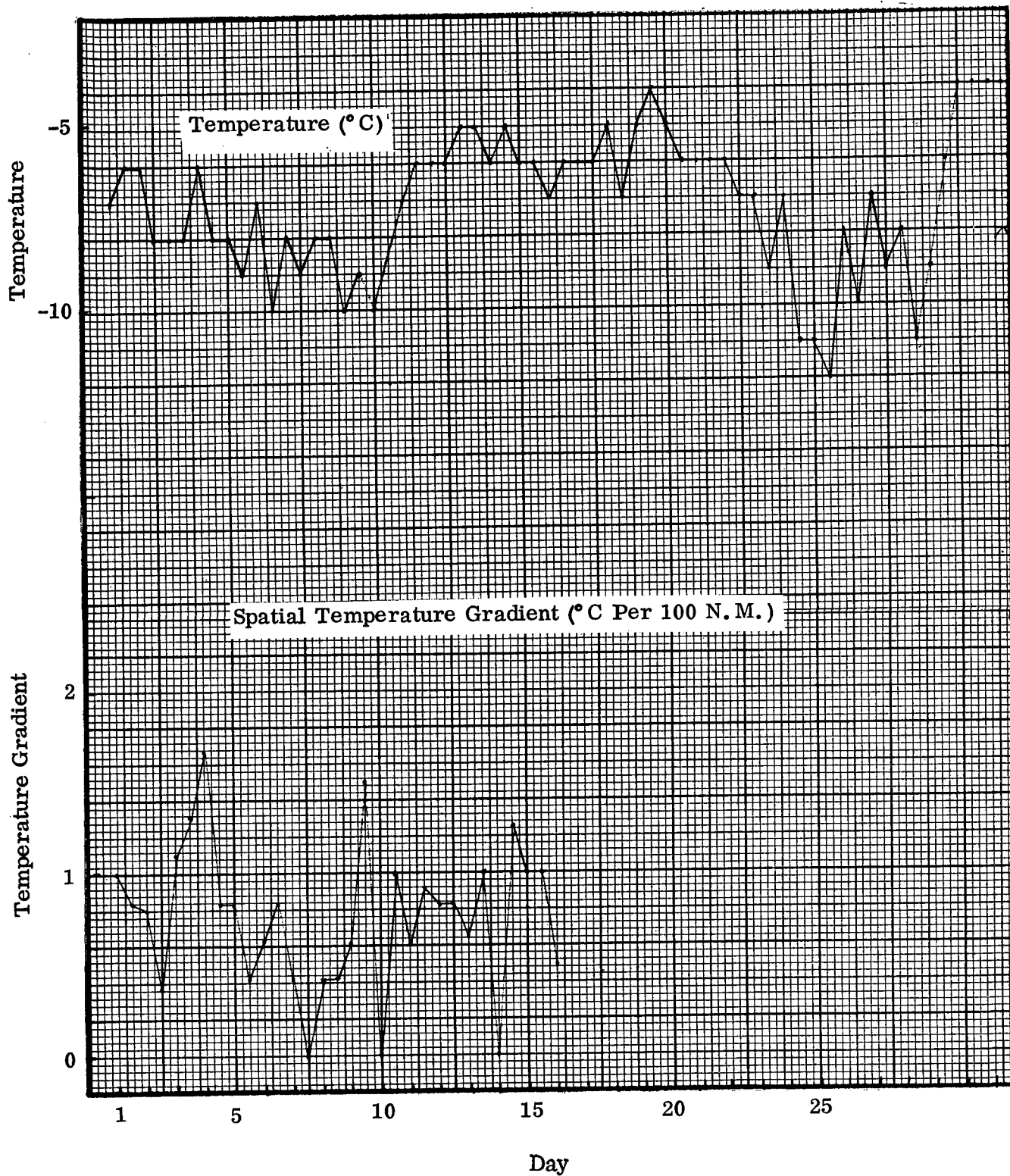


Figure 6-3. Temperature and temperature gradient at 500 mb level for July 1970 in San Diego, California at 0000 and 1200 Z.

values that may have existed at the time. The temporal variations of the spatial temperature gradient may give a clue to the error in the spatial temperature gradient estimate. Several observations were made from this limited data:

1. From the data no apparent diurnal cycles were in evidence - at least not with significantly large values. Some diurnal variation is seen in the monthly averages. For 12 hours data there are variations from other causes masking the diurnal variation. The station data for San Diego show a 0.3° C difference between 00 hour and 1200 hour monthly averages.
2. The 12 hour sampling interval is inadequate to show variations with finer time resolution. This could lead to errors due to under-sampling. Something to watch out for.
3. Changes in temperature and spatial temperature gradient appear to be associated with the passage of fronts and cyclones in a somewhat systematic manner, and with thermal activity and errors in a more random manner. For instance, February in San Diego is predominantly under the influence of the Pacific High with stable conditions, both in temperature and spatial gradient. Changes in temperature occur near times when lows are moving in with cold air. Spatial temperature gradients are higher also when lows or troughs are approaching. During July in San Diego the situation appears to be more stable with fewer large temperature spikes, but with increased fluctuations which may be due to the strong thermal effects in the Southwest. Data for Washington D. C., in February show fluctuating temperature between warm and cold as lows are approaching. The spatial temperature gradients are fairly well behaved, except near the first of the month, when a very deep low existed.
4. It appears from these data, assuming that the upper chart data represent a low error from the actual situation, and that no temporal under-sampling error exists, that the spatial temperature gradient is stable and low

enough to allow interpolation with little error over relatively short distances (100 n.mi.) most of the time. The monthly average of spatial temperature gradient at Washington in February was 1.67° C per 100 n.mi., with maxima of 3-10° C per 100 n.mi occurring near lows.

5. The spatial temperature gradients appear greatest when lows are approaching. These events are relatively rare events, considering all time and space, and occur near storms when GFC instrument data may also be less efficient for other environmental reasons such as clouds.

(b) Spatial Changes

The spatial distribution of temperature over the USA is shown in Figure 6-4 for February 1, 1971. The (5 degree) isotherms are widely spaced (for low spatial temperature gradients) most everywhere. They are very closely spaced near the large low pressure area over eastern Canada implying large spatial temperature gradients. To illustrate the temperature gradients and changes in gradients, the upper level chart data was used to plot temperature against degrees latitude for every 5 degrees in longitude from 90° W to 120° W. These plots are shown in Figure 6-5.

1. From these data it appears quite feasible to interpolate over relatively long distances, even for large spatial temperature gradient areas using methods similar to those used operationally by NMC. Changes in temperature gradient are generally small with larger changes occurring more rarely at air mass boundaries. The larger values of finite differences lead to interpolation in errors, especially for larger spatial intervals.
2. For February 1, 1971 the largest spatial temperature difference is about 9.82° C per 100 n.mi. with an average of about 2° C per 100 n.mi. The maximum value of the second temperature difference is estimated at about 5° per (100 n.mi.)² with an average value of zero.

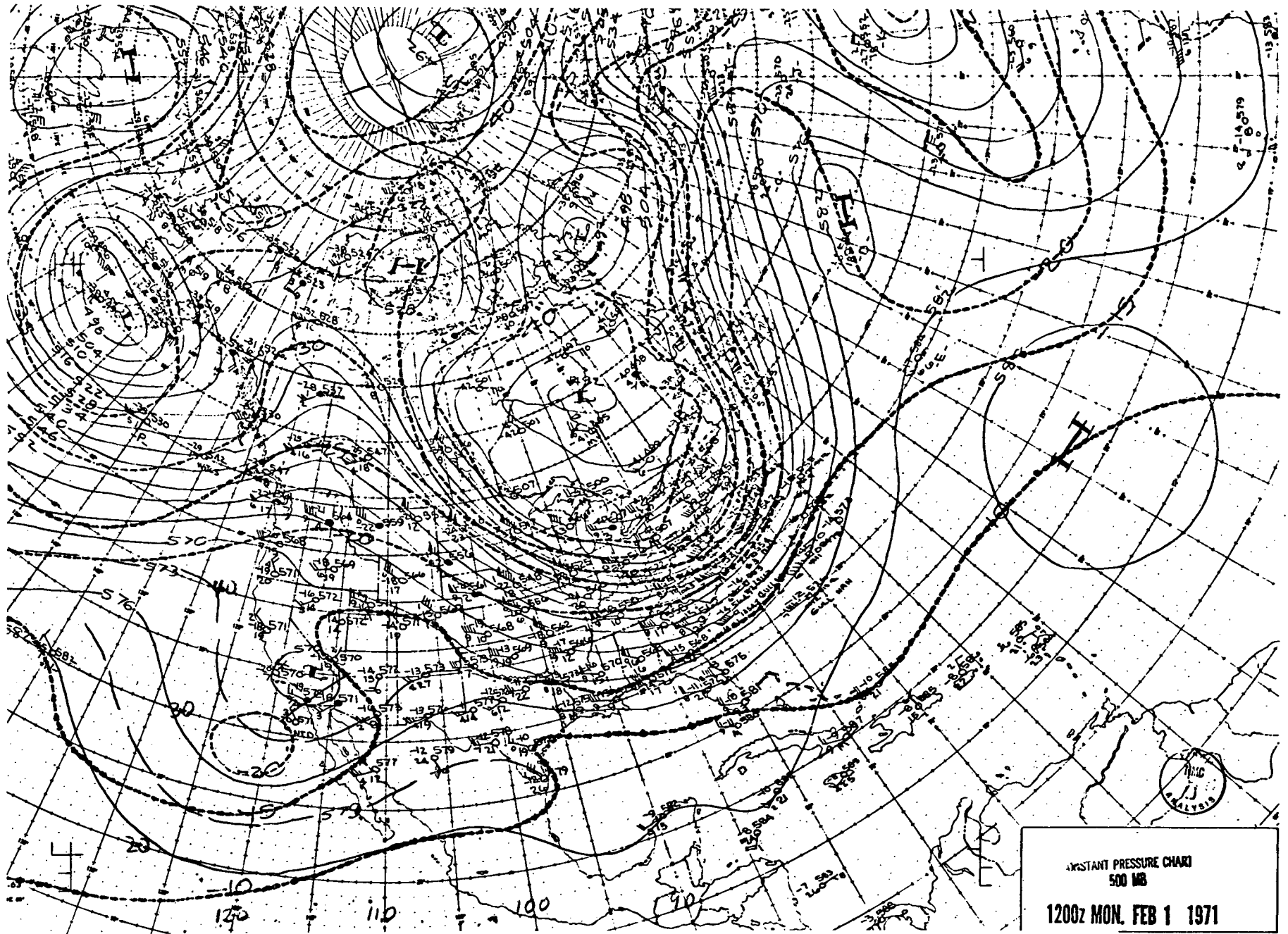


Figure 6-4. Constant pressure chart at 500 mb level for February 1, 1971 at 1200 Z

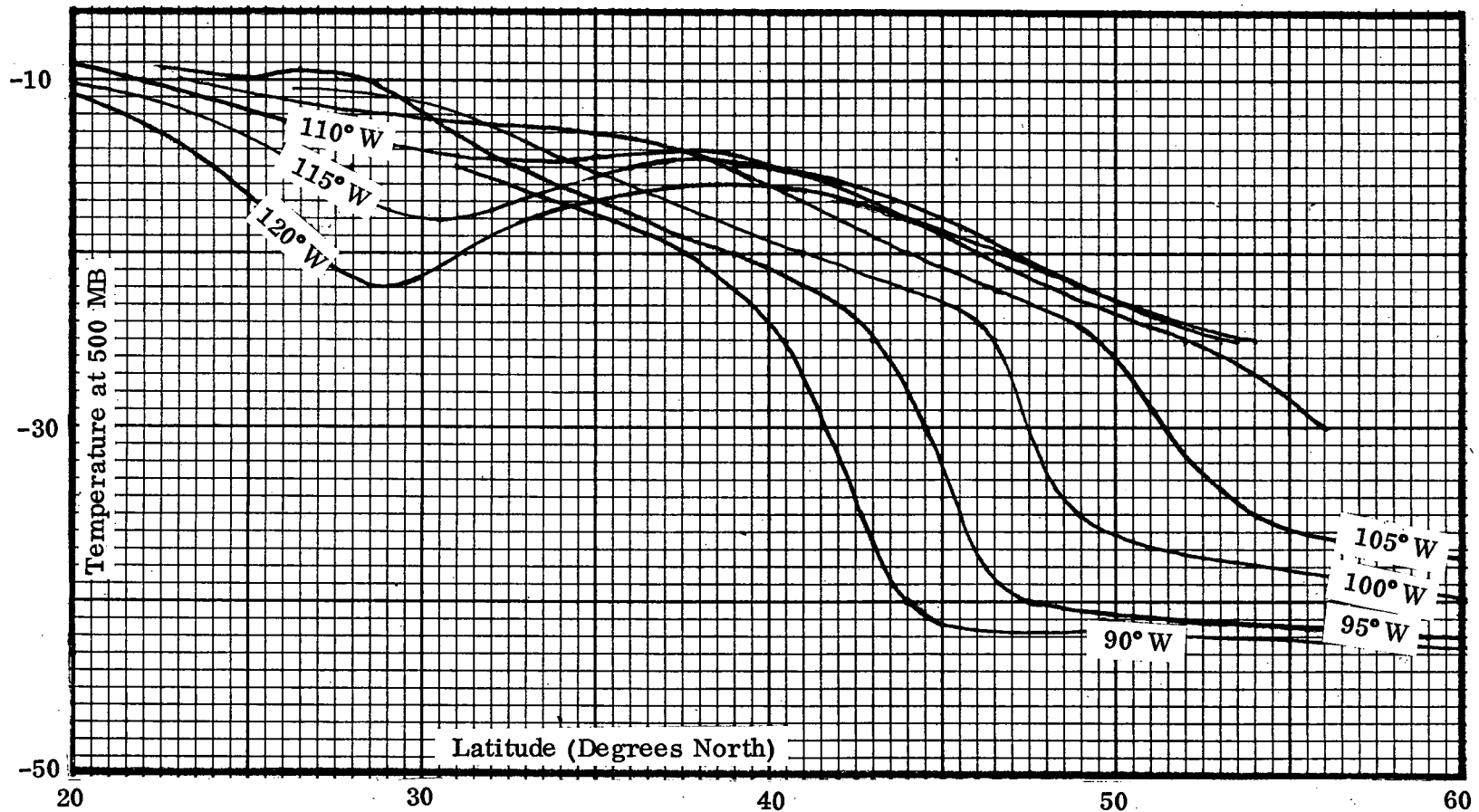


Figure 6-5. Temperature spatial distribution for February 1, 1971.

3. The error can be estimated for linearly interpolated data with finite values for second differences and zero higher order differences. This error is given by the values of the truncated Gregory-Newton interpolation formula. The error varies within the interval and, hence, the average error is obtained by integration of the error over the interval. This leads to an interpolation error of $\Delta^2 T/12$, where $\Delta^2 T$ is the second order finite difference. The maximum average error for a maximum $\Delta^2 T$ of 5° per $(100 \text{ n.mi.})^2$ is then $5/12^\circ \text{C}$ over 100 n.mi. intervals. This is small compared to the expected value of 2°C measurement error. Smaller errors can be expected for the interpolation method used by NMC, because it is quadratic in two dimensions.

6.1.2 The Accuracy of Temperature Data

Existing verification procedures compare objective analysis of temperature to actual observations. Verification statistics grouped by geographical regions and by altitude were assembled for us by NMC. It appears that the existing meteorological observation system produces objective analyses and forecasts which are sufficiently accurate for the measurements of trace contaminants. Current operational inclusion of data from satellite atmospheric soundings has improved the objective analysis and forecast in conventional data sparse areas (over oceans) as well. This has been verified experimentally with SIRS data. Temperature and water vapor profile soundings will be available from satellites, such as the NOAA series (ITOS-D 1972, ITOS-E 1973, ITOS-F 1974, ITOS-N 1975), the NIMBUS series (NIMBUS V 1972, NIMBUS VI 1974) and on geosynchronous satellites GOES (SMS-B 1973), and ATS-G(1974). The low altitude satellite soundings will take place at asynoptic times so that forecasting techniques must be used to incorporate these into the objective analysis and forecasts. The profiles from synchronous altitude satellites will be capable of giving soundings every three hours over the entire visible disc.

Objective analysis produces a best estimate of the state of the atmosphere at synoptic times (every 12 hours) using all available observational sources, including ship report, aircraft and SIRS soundings. These analyses are produced twice daily by the NMC analysis-forecast operation. The objective analysis is performed using corrections to a first guess field derived from actual data entered twice daily. The corrections are determined from a comparison of the data with the interpolated values of the given field at the observation points. For analysis of pressure heights the reported wind is taken into account in determining the lateral gradient of the correction. Several scans are made with successively smaller interpolation scales⁽³⁾. Forecasts are produced from the objective analyses. The methods used in objective analysis and forecasting are suitable for temporal and spatial interpolation to areas of air pollution observation from satellites.

(a) Radiosonde Accuracy

Analysis of paired radiosonde flights showed the RMS temperature error of the temperature sensor to be between 0.3° C and 0.4° C. This error and an assumed RMS pressure error of 3 mb combine to give RMS height and density errors at specified pressure levels. At 100 mb pressure level, the RMS height error was reported at 105 ft (32 m)⁽¹⁾.

(b) Temporal and Spatial Temperature Changes

Project Stormy Spring⁽²⁾ used a mesoscale rawinsonde network with ascents every 1.5 hours during the passage of five storms in April 1965.

Empirical study of the data confirmed the implication of the thermal wind relation that the mean temperature in a deep layer will not change rapidly in space or time and that windshears can be used as predictors of the changes. The thermal wind relation implies for each one degree change in mean temperature per 100 km a wind change of 39 m/sec (78kt) across the 7-16 km layer (similar for other layers). The observed extreme geostrophic wind of less than 200m/sec from 400 to 100 mb gives a horizontal temperature gradient of $5.1^{\circ}/100$ km. The Stormy Spring data showed that the temperature at a given level is considerably more variable than the average temperature between pressure levels. Changes in layer mean temperature were computed for intervals of 1.5 to 12 hours and space changes of 100 to 350 km (4.1°C for 6 hours and 3.5°C for 300 km). Large temperature changes over short time and space intervals were not found. This is an important characteristic of the atmosphere, and much smaller changes could be expected for clear air, non-storm situations which are of most interest to air pollution measurement.

(c) Relative Accuracy of SIRS and Radiosonde Data

The relative accuracy and utility of SIRS data relative to radiosonde data for objective analysis was determined using tropospheric height and thickness values derived from NIMBUS 3 SIRS soundings (thickness of pressure layers is related to layer temperature)⁽⁴⁾. Relative accuracy and utility depends strongly on cloud condition, pressure level and instrument status. The SIRS thickness in the upper troposphere compares well to radiosonde thickness in the absence of high clouds. Both data gave thickness rms errors of between 20 to 30 meters with the SIRS thickness error slightly greater.

(d) Temperature Errors from SIRS

The standard error of temperature was found to be between 1°C and 2°C for pressure levels from 850 to 30 mb from NIMBUS 3 SIRS data from May-June and October-November 1969⁽⁵⁾.

Correction for cloudiness and high terrain is necessary in the derived regression equations. A comparison with radiosondes with known surface temperature shows good agreement at all levels up to the tropopause. In the Southern hemisphere profiles are degraded by lack of surface temperature, and inversions aloft cannot be retrieved.

A comparison of geopotential heights from SIRS and objective analysis show reasonable agreements.

A comparison of 500 mb analysis with and without SIRS soundings gave deeper lows over mid-Pacific with a maximum difference in height of 120 meters. Twenty-four, forty-eight hour and 3-day forecasts were made from the two analyses and compared to later analyses. The forecast made from the analyses which incorporated the SIRS data showed marked improvement.

(e) SIRS Sounding for Operational Use

Temperature profiles can be retrieved from satellite radiance measurements with an algorithm to find the solution which differs least from the initial guess in order to satisfy the observed radiance observations⁽⁶⁾. The initial guess is from the dynamic forecast. SIRS-B data have been used for NMC analysis-forecast operations. Verification statistics indicate SIRS derived temperatures are, in most cases, better than the 12-hour forecast. Partial cloudiness is a major problem source.

(f) Sea Surface Temperature

Data from HRIR on ITOS1 were used to determine global sea surface temperature to an accuracy of between 2-3K (3.5 - 4.1 μ) (standard deviation) as compared to ship reports⁽⁷⁾.

6.1.3 Summary of Requirements for Atmospheric Temperature and Pressure Profile Data

The measurements in the thermal region depend upon the temperature and pressure distribution along the optical paths within the field of view existing at the time

data is taken. Subsequent processing of the RGFC data for data interpretation will require an estimate of the average temperature and pressure profile with height within the field of view. It appears from an examination of methods and techniques used that the existing meteorological observation system will be able to provide the required estimate of the atmospheric state.

The National Meteorological Center (NMC) routinely produces objective analyses as a best estimate of the state of the atmosphere from all available observations. Forecasts are produced from the objective analyses. The methods employed in objective analysis and forecasting can be used for the estimation of the atmospheric temperature and pressure profiles for the locations and times applicable to the RGFC data. The NMC verifies objective analyses and forecasts by comparing these products with observations. The resulting verification statistics give the average error between the temperature observations at different pressure levels and the smoothed best estimate of the state of the atmosphere which was produced from the observations. Table 6-1 gives the mean absolute temperature error at different pressure levels for four months of 1970. The errors are less than 1K with no essential difference between the statistics obtained from the 70 radiosondes in the northern hemisphere or the 19 radiosondes in the USA.

The operational analysis and forecast operation includes all available operationally useful data from satellite temperature sounders. Reported experiments have shown that SIRS data has significantly improved the objective analysis in data sparse areas (judged from forecast performance with and without inclusion of SIRS data). However, it appears that a SIRS sounding does not give an independent observation of temperature as a radiosonde would, but relies on the operational objective analysis and short term forecasts (up to 12 hours) to provide an initialization for SIRS analysis. The temperature profile from the objective analysis is changed if the SIRS radiances are inconsistent with it, until the computed and measured radiances agree within the expected errors of the instrument. This can

Table 6-1. Verification of NMC Operational Temperature Analysis

Pressure Level (mb)	MEAN ABSOLUTE TEMPERATURE ERROR (K)							
	1970							
	Jan		April		July		Oct	
	a	b	a	b	a	b	a	b
200	.8	.9	.7	.8	.7	.7	.7	.7
250	.7	.7	.6	.7	.6	.5	.6	.7
300	.7	.6	.7	.7	.5	.5	.6	.6
500	.6	.7	.6	.7	.5	.5	.5	.6
700	.7	.7	.6	.6	.5	.6	.6	.7
850	.8	1.0	.7	.9	.6	.7	.7	.9

a 70 radiosonde stations in Northern Hemisphere

b 19 radiosonde stations in U.S.A.

be interpreted to mean that SIRS type data can be expected to improve the analysis in data sparse regions, but that the objective analysis will remain the best estimate of the atmospheric state.

Calculations have been made using the COLAYER program to obtain an understanding of the instrument sensitivity to changes in the atmospheric temperature profile. The atmosphere was approximated by eight layers with average temperatures and pressures in each layer. The instrument sensitivity was determined by making different computer runs with the temperature in each layer changed by +5K, -5K from the standard average temperature. These runs were made for different CO concentrations, for an assumed surface temperature of 300K and for an assumed water vapor distribution according to Gutnick. The sensitivity to temperature changes can be interpreted in terms of an error in CO concentration for assumed uncertainty in atmospheric temperature. In Section 5, the expected relative error in

CO concentration (0.1 ppm) was reported as $\pm 4.4\%$ for temperature uncertainties of $\pm 2\text{K}$.

It seems reasonable from the foregoing to draw the preliminary conclusion that sufficiently accurate atmospheric temperature profiles can be obtained from operational objective analyses. An average error (from verification statistics) of $\pm 1\text{K}$ could lead to an average error in estimated CO concentration of $\pm 2.2\%$ at 0.1 ppm. The instrument sensitivities and expected errors would, of course, be different at other values of ground temperature, atmospheric relative humidity, other atmospheric pressure distributions, and for other species and concentrations. The effect of these have to be further examined. Additionally more detail examinations of the uncertainties of atmospheric temperature determinations are warranted.

The following subsections present more detail discussions of atmospheric temperature uncertainties, and objective analysis and verification methods.

(a) Objective Analysis

The following was extracted in part from documents received from the NMC. Objective analysis of meteorological parameters are produced twice a day. "The height, temperature, and wind analyses are made for the 1977-point octagonal grid for the Northern hemispheres for each of nine mandatory pressure levels from 850 to 100 mb. On the same grid, analyses are also made of the following parameters: height and temperature of the 70-, 50-, 30-, and 10 mb levels; sea level pressure; surface air temperature; temperature of four selected isentropic (potential temperature) surfaces (for tropopause modeling); and the mean relative humidity of the surface to 500-mb layer. The sea level pressure and surface air temperature analyses are used to compute the 1000 mb height field. These analyses serve as input to the primitive equation (PE) forecast model."

Tropical analyses of wind and temperature at different pressure levels are also produced on a grid extending between 48S to 48N. Current plans are to extend the analyses and subsequent forecasts on a global basis. Work is in advanced stages

of testing and verification. "The analysis techniques essentially apply corrections to a first-guess field. These corrections are determined from a comparison of the data with the interpolated value of the guess field at the observation point. For the analysis of the height of a pressure surface, the reported wind is taken into account in determining the lateral gradient of the correction to be applied.

The analysis is performed in a series of cycles, usually 2 to 4 in number. The first-guess value at each grid point is adjusted by examining the reports in the vicinity. Once each point has been adjusted on a given cycle the newly assigned values are used in a succeeding cycle. For the first two cycles, the number of reports in the vicinity of a grid point is used to determine how far away an observation may be and still exert some influence on a grid point. For dense data regions, like the United States, this distance is less than for a sparse data region, like the Atlantic Ocean."

(b) Verification of Temperatures

The first paragraph is from NMC descriptions of verification procedures. "Seventy radiosonde stations have been chosen as the locations at which the verification results are computed. Analyses and forecasts based on 1200 Z data are verified. Values of wind and temperature at 850, 700, 500, 300, 250 and 200 mb are interpolated biquadratically to each of the verification stations from the grid point values of the operational analyses at those six levels. An identical interpolation procedure is applied to the grid point values of the operational forecasts at initial time and at 12, 24, 36 and 48 hours after initial time. Both the 0000Z and 1200Z radiosonde reports are examined and the wind and temperature values at the verification levels are saved for each of the seventy stations."

The verification statistics are computed monthly. Similar errors could be computed on a daily basis, but is not currently available. The average error from 19 verification stations from the U.S. for a given objective analysis can be expected to be somewhat more variable than the monthly average errors because the error is

synoptic, i. e., depends on the presence of storm systems. The average errors from 70 verification stations, because they are distributed over the Northern hemisphere, can be expected to be closer to the monthly average errors.

(c) Uncertainty in Atmospheric Temperature Measurement

The temperature measurements with a radiosonde appear to be quite accurate. This was determined by R. W. Lenhard at AFCRL from analysis of data obtained from paired simultaneous radiosonde flights released about 10 miles apart. These paired ascents show differences in heights of pressure surface which implies that the radiosonde system delivers temperature information accurate to 0.3K (RMS). The radiosonde measures temperature and pressure. The average temperature between two pressure levels is related to the thickness of the layer between the pressure levels by the hydrostatic equation:

$$z_t - z_b = - \frac{R}{g} \int_b^t T d(\ln P) \approx \frac{R}{g} \bar{T} \ln \frac{P_b}{P_t}$$

where z_t , z_b are geopotential height of the pressure levels P_t and P_b , respectively, \bar{T} is the average virtual temperature, R is the dry gas constant for air, and g is acceleration of gravity. This gives the height differential between pressure levels and hence the temperature and pressure profiles with height.

An additional property of the atmosphere is that the spatial gradient of the layer thickness determines the wind velocity within the layer. A radiosonde, when tracked by radar, can yield the instantaneous wind vectors. These are smoothed to determine the wind velocity at pressure levels. The thermal wind equation is

$$\frac{\nabla V}{\Delta z} = - \frac{g}{f T} \nabla_P T \times k$$

where ∇V_g is the geostrophic wind vector in the layer with thickness Δz and average temperature \bar{T} , $\nabla_p T$ is the horizontal gradient of the mean temperature in the layer, f is the coriolis parameter and k is a unit vector in the local vertical direction.

Spatial gradients of temperature tend to be high near the boundary of airmasses. At these boundaries large changes of temperature and pressure occur and are accompanied by high wind velocities. Geographic regions with spatial temperature gradients which are different from pressure level to pressure level then must have spatial gradients of layer thickness.

Project Stormy Spring used a mesoscale rawinsonde network with ascents every 1.5 hours. Data was taken during the passage of five storms in April 1965 by C. Kreitzberg at AFCRL. Empirical study of the data confirmed the implication of the thermal wind relation that the mean temperature in a deep layer will not change rapidly in space or time and that windshears can be used as predictors of the changes. The thermal wind relation implies for each one degree change in mean temperature per 100 km a wind change of 39 m/sec (78kt) across the 7-16 km layer (similar for other layers). The observed extreme geostrophic wind of less than 200 m/sec from 400 to 100 mb gives a horizontal temperature gradient of $5.1^\circ/100$ km. The Stormy Spring data and other data show that the temperature at a given level is considerably more variable than the average temperature between pressure levels. Large temperature changes over short time and space intervals were not found. This is an important characteristic of the atmosphere, and much smaller changes could be expected for clear air, non-storm situations which are of most interest to air pollution measurement.

The variability of temperature at different pressure levels was examined from hourly radiosonde data collected by AFCRL and available in GRD Research Note No. 60.

Figure 6-6 shows the variability of the 700 mb temperature and the thickness of the 700-500 mb layer from hourly radiosondes. The effect due to 12 hour soundings is illustrated in the figure by the straight lines joining 12 hourly soundings. The mean error and standard deviation was evaluated from the soundings as the deviation from the straight line. This was done for the two 12-hour segments and for the total. The relative temperature error σ_T/T is $1.34/(273 \pm 8.5)$ or 0.5%, the relative thickness error $\sigma_{\Delta z}/\Delta z$ is $6.03/2580$ or 0.233%.

This indicates that indeed there is less variability in the average temperature within a layer than the temperature at a level. In the example a ratio of two was found.

6.2 WATER VAPOR PROFILE

6.2.1 Temporal and Spatial Variations of Water Vapor Profiles in the Real Atmosphere

Atmospheric relative humidity profiles are not normally included in objective analysis, instead an average relative humidity within the 1000 to 500 mb layer is included. No verification statistics for this are available. Water vapor soundings from satellites, however, have been found to give relative humidity to within 20% of radiosonde relative humidity.

The station data obtained from the National Climatic Center was examined in order to gain a feel for the variability of water vapor profiles with time and in comparison with the standard atmosphere. In Figure 6-7 the constant pressure data for three groups of three days during February 1971 for San Diego are shown. The temperature and the mixing ratio (MR) are shown for the 850 and 500 mb pressure levels. The mixing ratio was derived from the relative humidity, which was given in the station data using the relationship

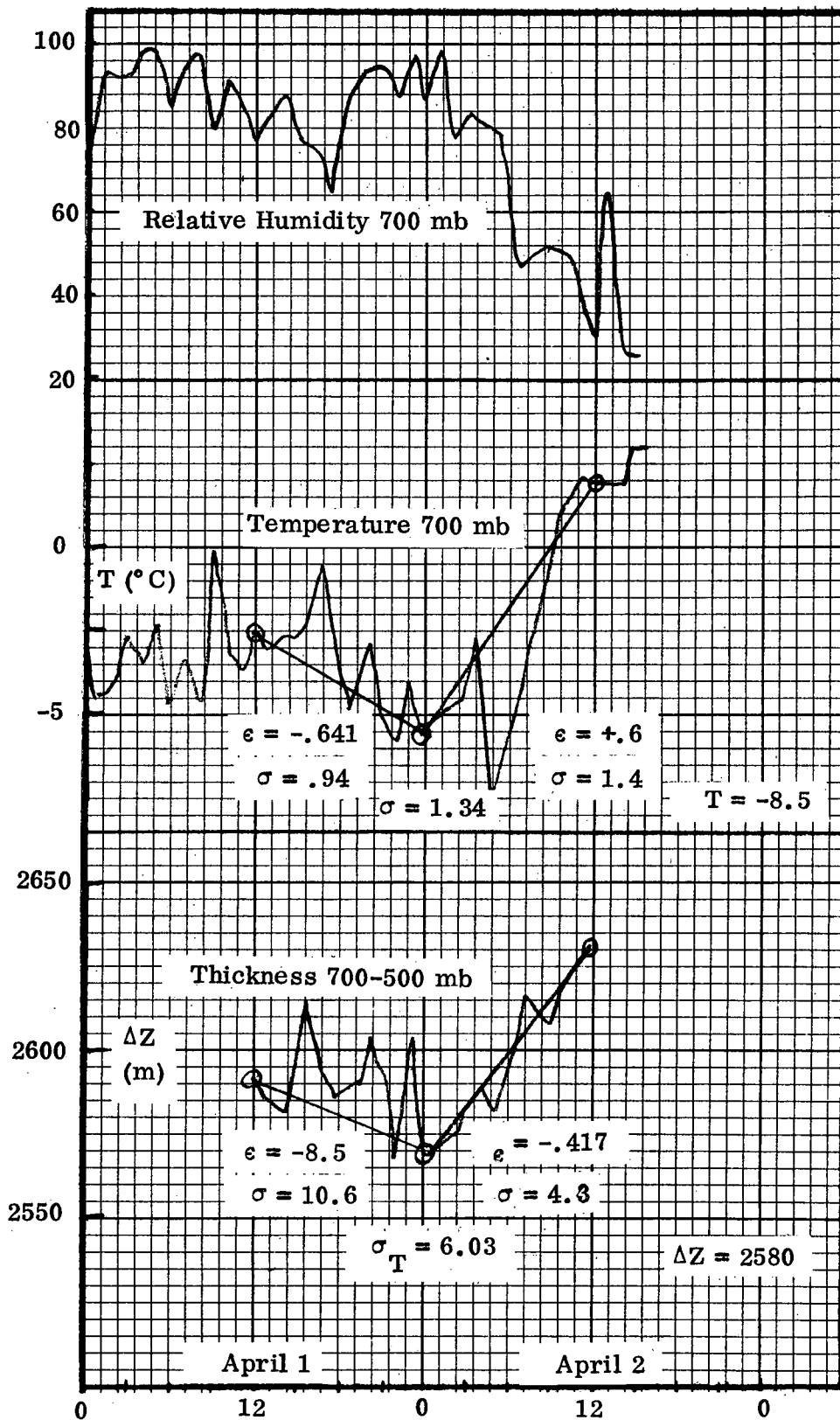


Figure 6-6. Variability of relative humidity, temperature at 700 mb and thickness of 700-500 mb layer for 48 hours.

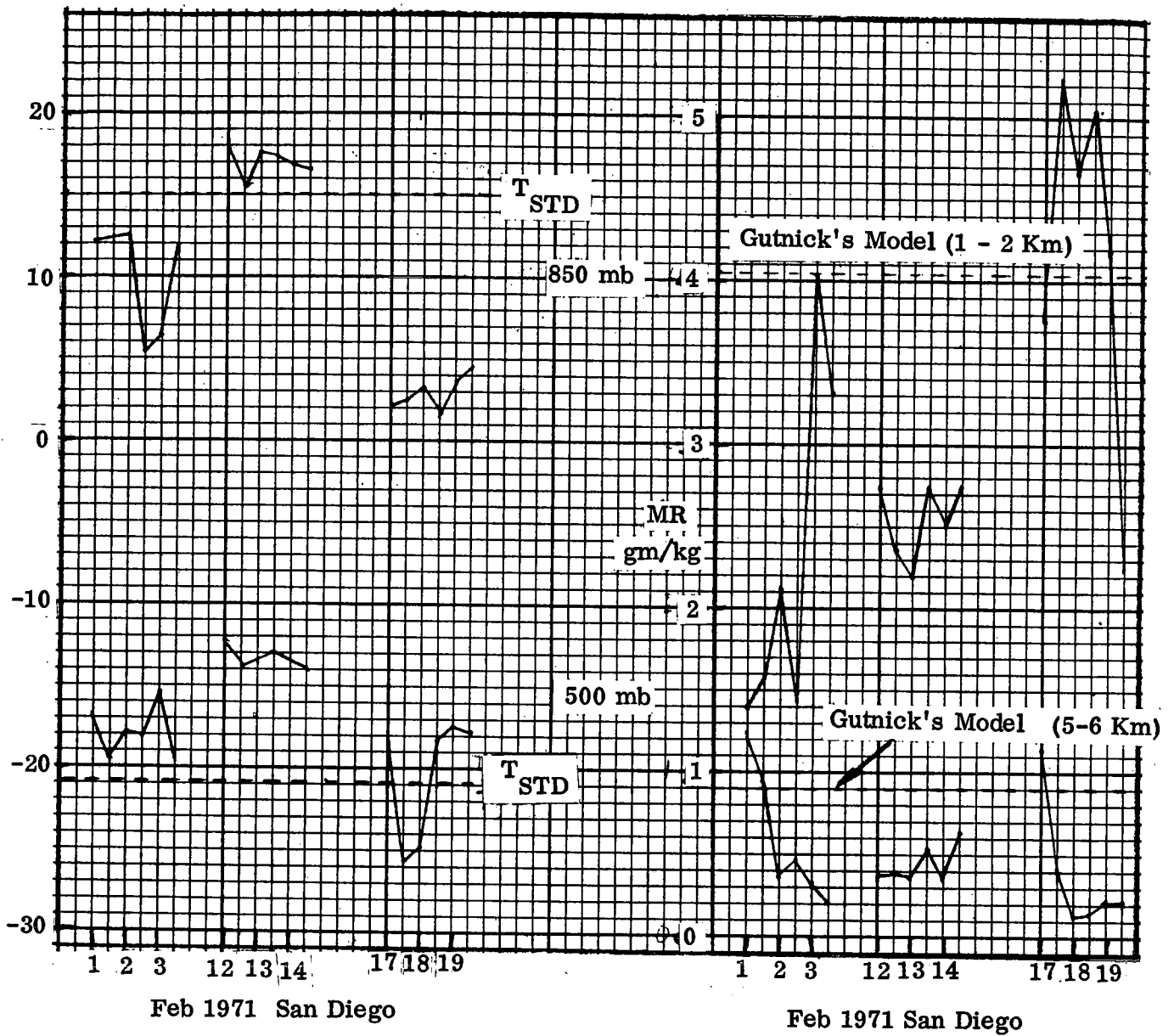


Figure 6-7. Variability of temperature and water vapor mixing ratio for selected days in February 1971 in San Diego, California.

$$\text{MR (gm/kg)} = \frac{828}{P(\text{mb})} * e_s (\text{mmHg}) * \text{RH}$$

The value of e_s , the saturation vapor pressure, is tabulated as a function of temperature. The dashed lines indicate the respective values for the standard atmosphere and Gutnick's model.

The actual data compared with the standard values of temperature and mixing ratio show the effect of shifting air masses. From February 1 to 3 a weak low appeared (visible on the upper air charts and not included in this report) with a drop of temperature at the 850 mb level and a rise of water content. The 500 mb level became drier with no significant change in temperature. A different air mass existed between February 12 to 14. It was recognized that the Pacific High was dominating the situation with warm temperatures and low values of spatial temperature gradients. Now in Figure 6-7 this influence of the Pacific High is seen, because both levels show warmer temperatures than both the atmospheric model and the situation on February 1 to 3. The water vapor content is also considerably lower than the Gutnick's model (but not anywhere near zero). During February 17 to 19 a low pressure system developed offshore, and rapidly passed eastward. The 850 mb temperature was much reduced with a high water vapor content at this level. However the 500 mb temperature showed a 2-day transient with a marked decrease of mixing ratio after the passing of the low.

It appears reasonable to speculate that the temperature and water vapor content at any given time and location depend primarily on the characteristics of the prevailing airmass. Since airmasses tend to be conservative, the temperature and water vapor profiles tend to be conservative until the airmass changes or moves on, or except for localized heating effects. This implies considerable stability both temporal and spatial, which will help the temperature and water content interpolation problem.

6.2.2 Water Vapor from SIRS (NIMBUS IV)

Comparisons of satellite derived and radiosonde observed water vapor profiles indicate that the error of SIRS-derived relative humidity in the mid-troposphere (400-600 mb) is less than 20%. Relative humidity error in the lower troposphere (1000 to 600 mb) is less than 30%. This RAOB-SIRS comparison was for coincident data (within 3° latitude and longitude and 6 hours) for 21 November 1970⁽⁸⁾.

6.3 CLOUD COVER

A partial cloud cover produces a temperature drop sensed from HRIR which depends on the cloud altitude and percentage cloud cover. A method is derived to compute a cloud temperature difference correction, from per cent cloud cover and cloud altitude guesses. Theory was compared to data processed from NIMBUS 3 and BOMEX showing a rather good correlation (within 1K) in the respective temperature differences⁽⁹⁾.

The COLAYER program was modified so that a thin cloud layer of varying amounts of cloud cover could be inserted between each atmospheric layer. The cloud was assumed to have a spatially uniform emissivity. Although different cloud emissivities could have been used, only clouds with unity emissivity were used. The program computes the radiance at the top of each atmospheric layer and the transmission through each layer in the same way as before. However, at the assumed cloud layer the radiance is the average radiance of the cloud and the radiance from below the cloud, according to the cloud amount. Runs were made with fractional cloud amounts of 0, .3, .6 and 1.0 at 1 km cloud altitude and at 1, 2, 3, 4, 5 and 6 km for full cloud cover.

It was found that the instrument response, ΔV , is linear with cloud amount, Figure 6-8. The values of ΔV for solid cloud cover depend on the cloud surface temperature and hence give increasingly smaller values of ΔV for higher clouds as shown in Figure 6-9. The ratio $\Delta V/V$ is less sensitive than ΔV to the surface

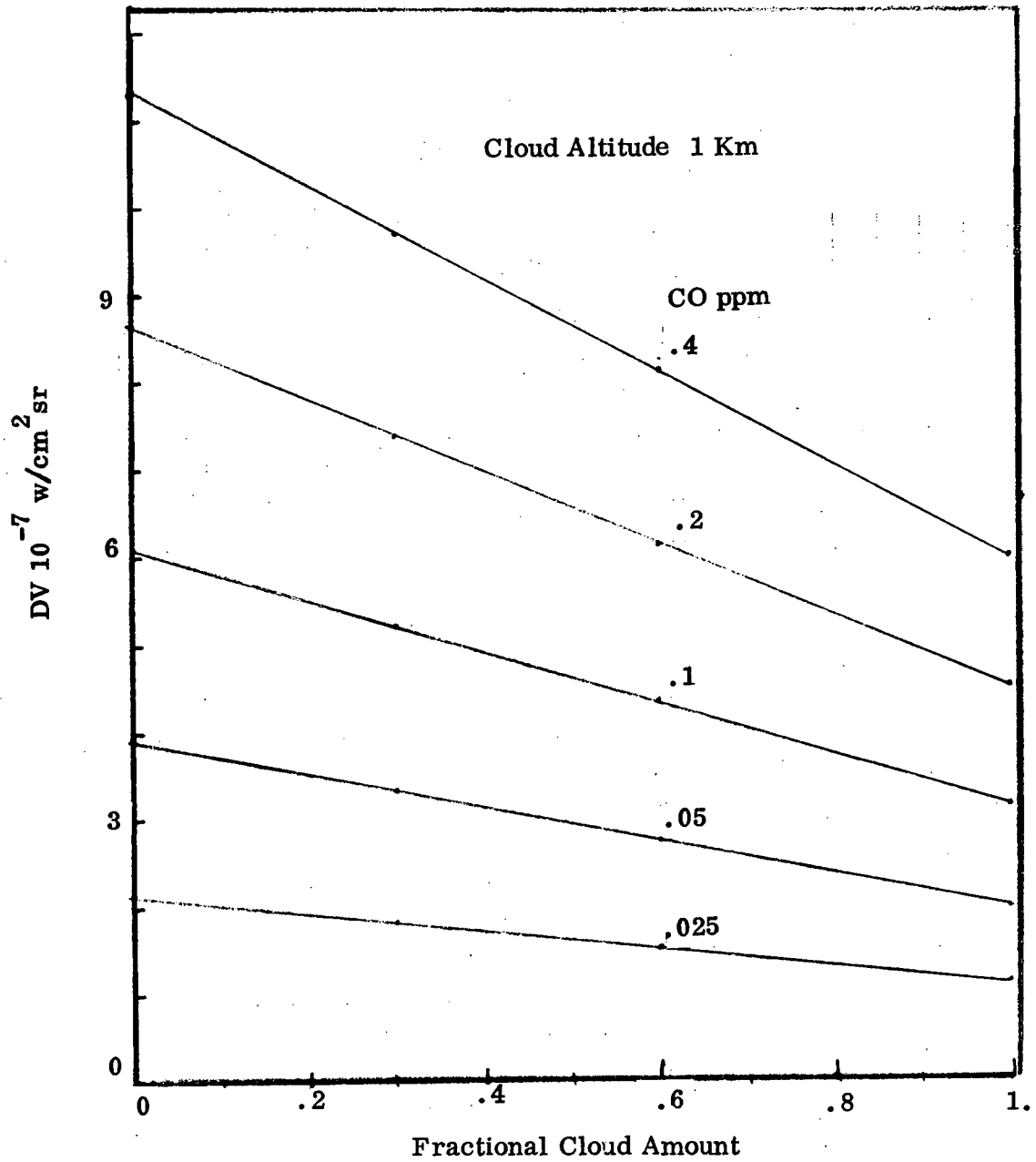


Figure 6-8. Signal difference vs. fractional cloud cover for different amounts of CO concentration. Cloud altitude = 1 km.

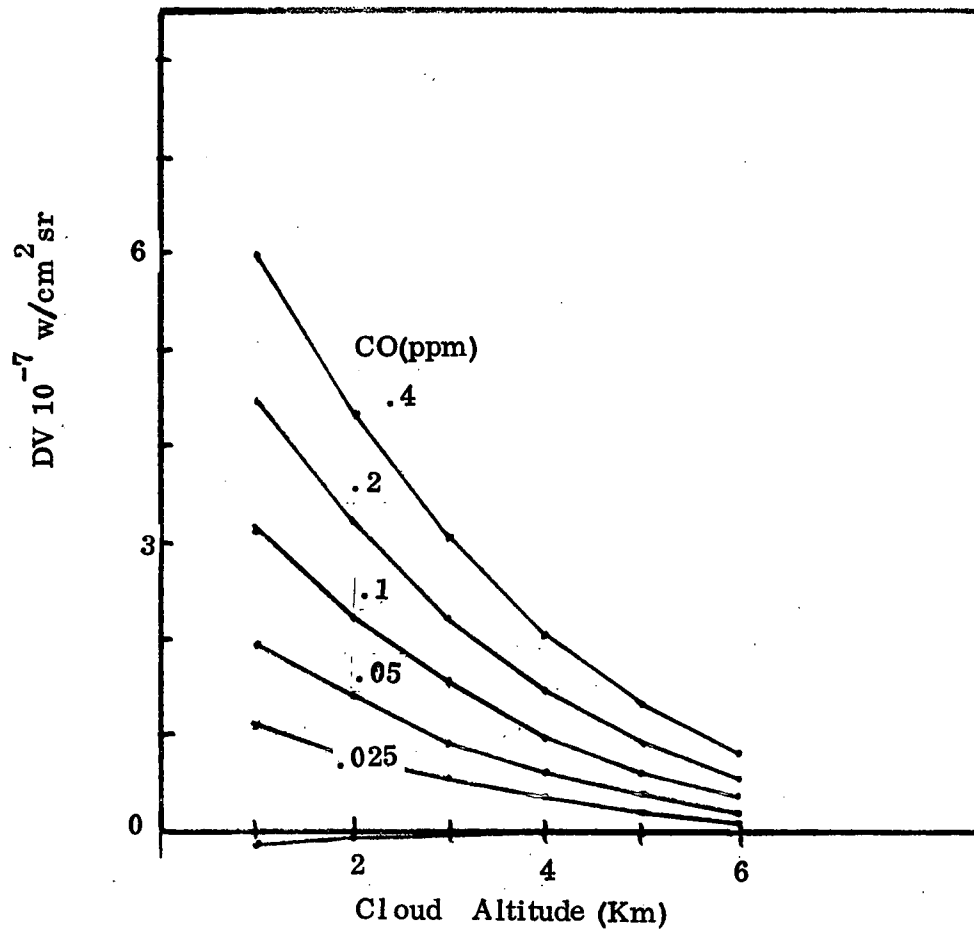


Figure 6-9. Signal difference vs. cloud altitude for 100% cloud cover for different amounts of CO concentration.

temperature. In Figure 6-10 the ratio $\Delta V/V$ plotted against CO concentration is seen to closely compare to the shape of the curves for ground temperatures of 300, 285 and 270K.

6.4 THEORETICAL SENSITIVITY OF GFC INSTRUMENT TO UNCERTAINTIES IN ATMOSPHERIC PARAMETERS

Calculations were made with the COLAYER program to determine the changes in instrument signal output with changes in atmospheric temperature and water vapor concentration profiles. The optimum gas cell conditions and an eight layer atmosphere (to 10 km) were used. The standard atmosphere temperature, pressure and water vapor profiles which were used for the calculations during the last month are shown in Figure 6-11. The temperature and pressure profiles are for the U.S. Standard Atmosphere 1966. The water vapor profile is Gutnick's model.

The temperature profile was changed from the standard profile by +5 and -5 degrees at all layers simultaneously for an atmosphere with four different water vapor concentrations: zero, standard, 50% and 150% standard. Furthermore, different amounts of ground temperature were assumed. The instrument signal ΔV and the radiometer value of the vacuum channel RR6 (RR6 is the symbol for $\int E(\omega) C'(\omega) \tau_A d\omega$) are plotted as a function of CO concentration in Figures 6-12 and 6-13 for no water vapor. The $\pm 5^\circ$ temperature profile changes are also plotted. At $c_{CO} = .1$ ppm and $T_G = 300^\circ$ K, an increase of 5° everywhere gives a decrease in signal ΔV of $\frac{.53}{7.94} 100\%$ (or 1.33% per degree) for a corresponding uncertainty in CO concentration of 12% (or 2.6% per degree). The instrument radiometer output (RR6) in Figure 6-13 is a weak function of atmospheric temperature. It is seen however that both ΔV and RR6 are strongly affected by the surface temperature. The effect of different amounts of water vapor on the instrument signal is shown in Figure 6-14. A 50% reduction in water vapor gives a 7% increase in signal at $c_{CO} = .1$ for a corresponding uncertainty in CO concentration of 14%.

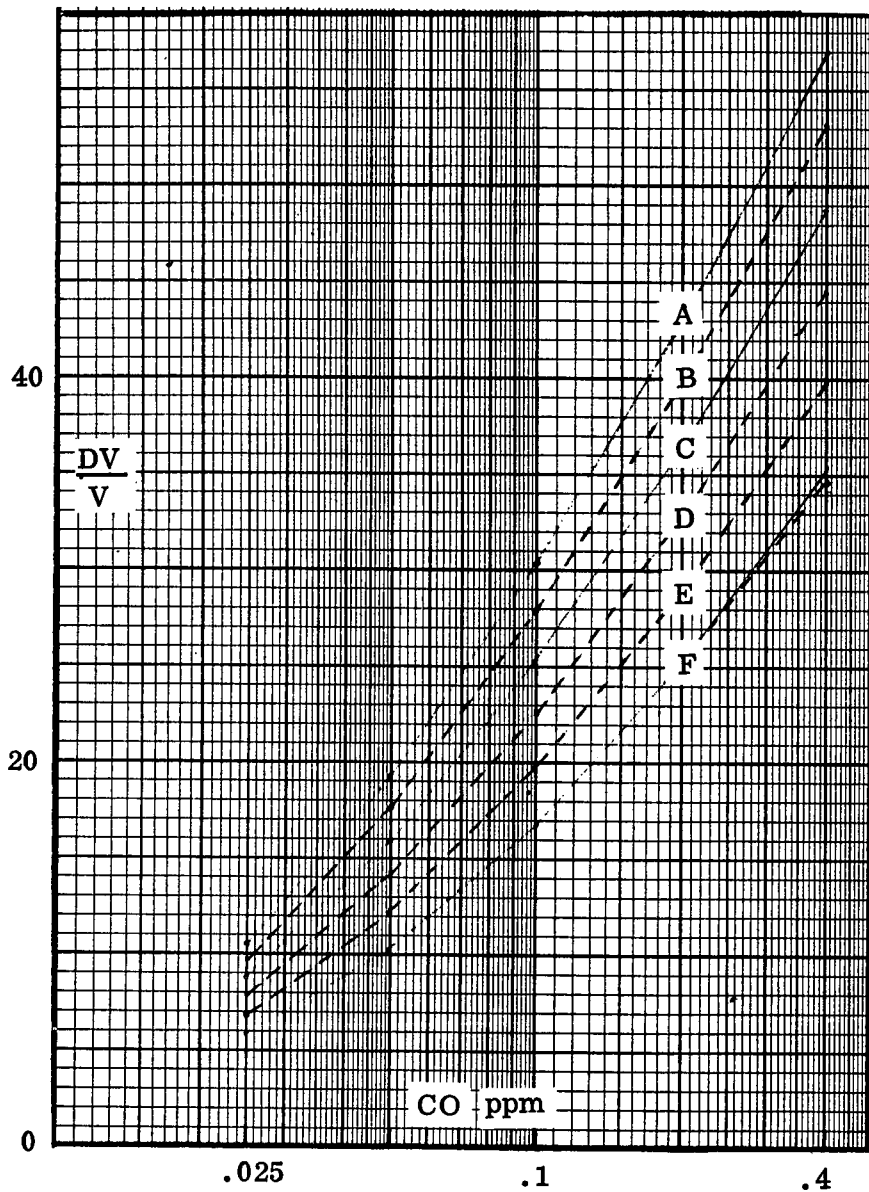


Figure 6-10. Ratios of DV/V vs. CO concentration for A (ground temp. = 300K), B (0.6 cloud at 1 km, $T = 291K$), C (ground temp. = 285, cloud at 1 km, $T = 284.9K$), D (cloud at 2 km, $T = 278.4K$), E (cloud at 3 km, $T = 271.9K$), F (ground temp = 270K, cloud at 4 km, $T = 265.4K$).

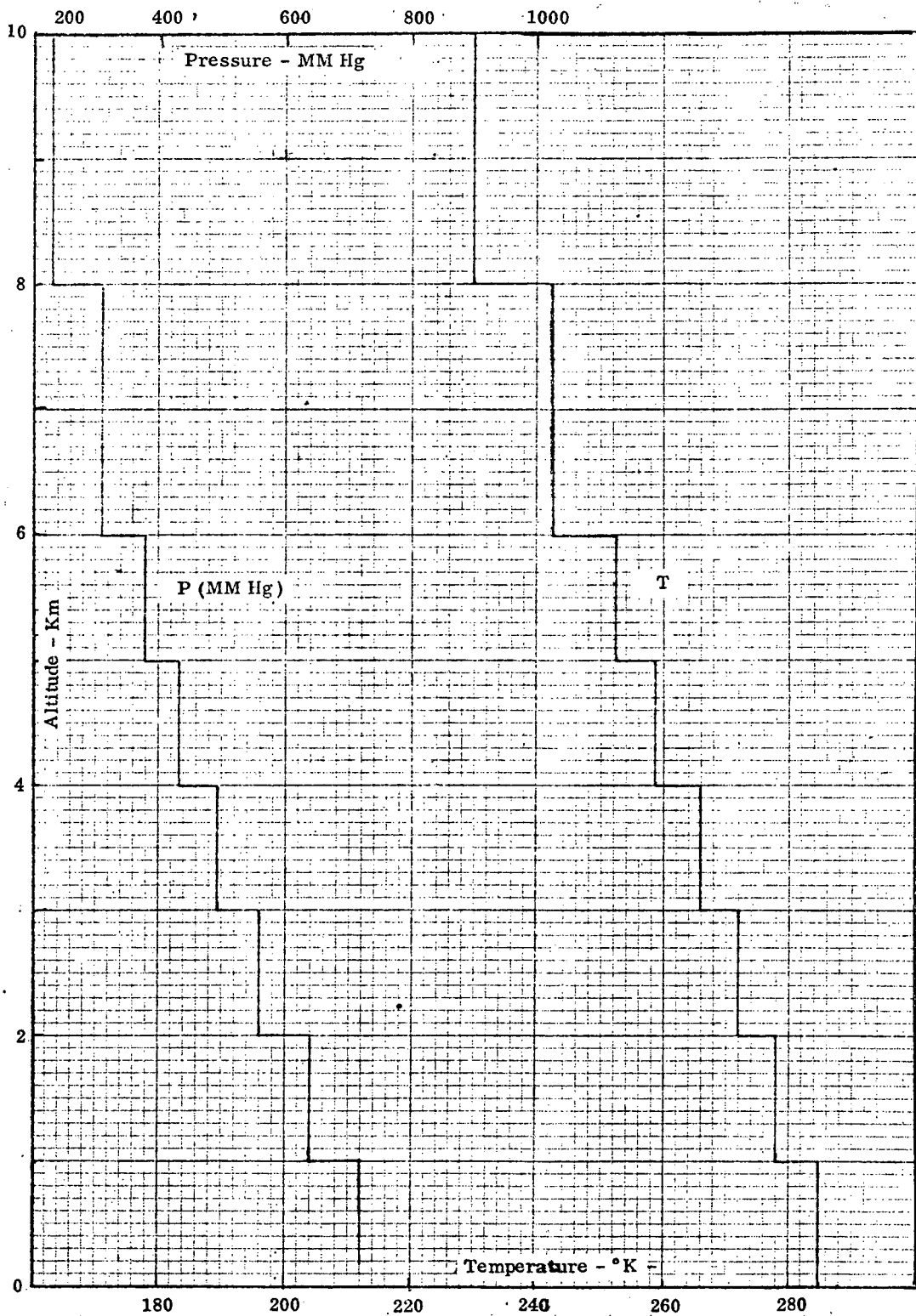


Figure 6-11. Details of pressure and temperature profile in the troposphere

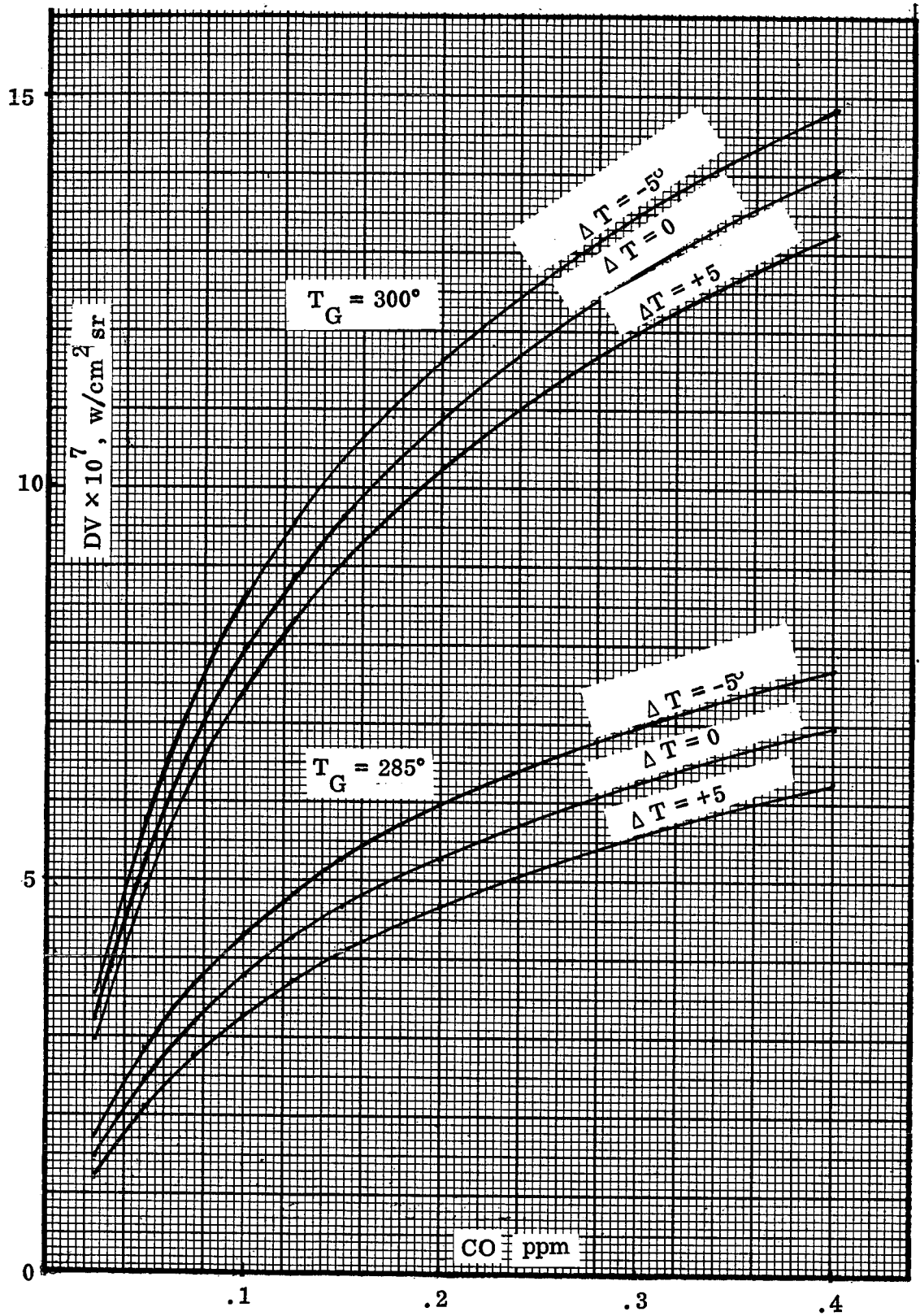


Figure 6-12. Signal difference vs. CO concentration for ground temperatures of 300 and 285K and atmospheric temperature variations.

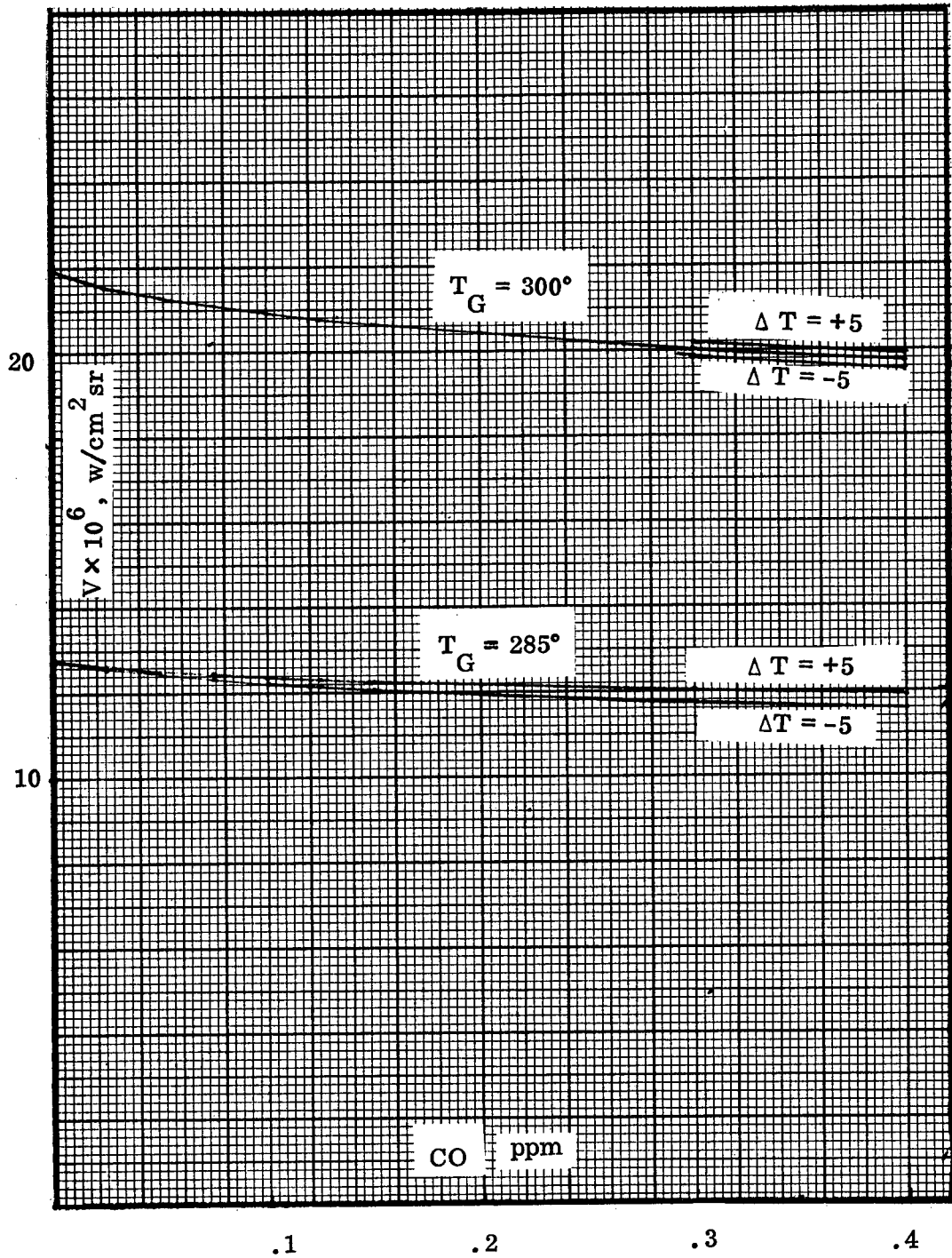


Figure 6-13. Radiance vs. CO concentration for same conditions as Figure 6-12.

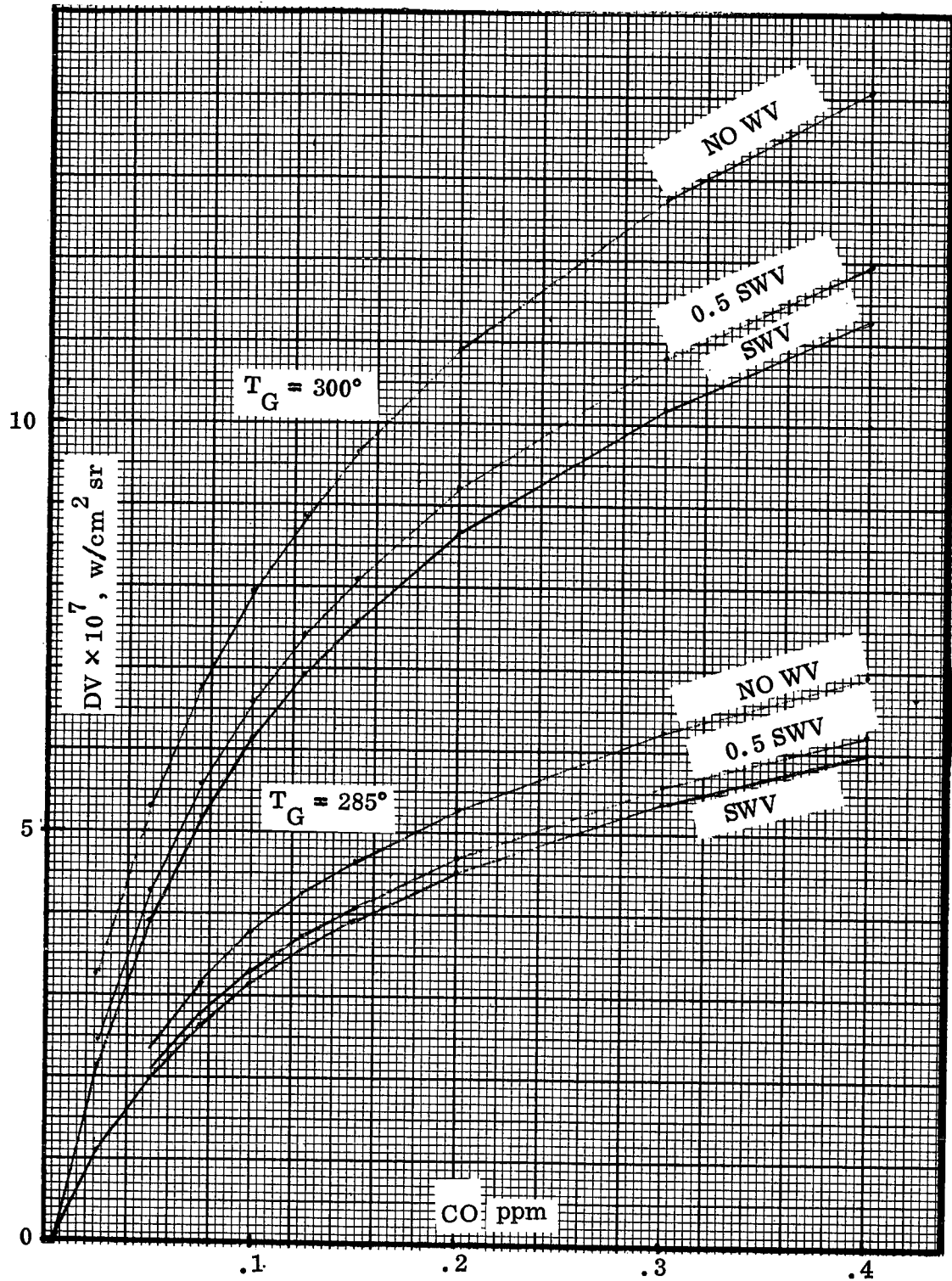


Figure 6-14. Signal difference vs. CO concentration for different water vapor concentrations and different ground temperatures.

The signal uncertainties due to independent layer temperature uncertainties were determined for each atmospheric layer. These signal changes per temperature change are not statistically independent. Therefore, it was not possible to simply combine them to obtain meaningful estimates of signal uncertainty due to random distributions of layer temperature errors. Figure 6-16 shows the rate of change of signal with temperature for the dry and the standard water vapor model. The temperature uncertainties at low atmospheric layers appear weakened by the presence of water vapor. The altitude of greatest signal sensitivity to temperature errors appears to be about 3 km. However the shape of the curve shown in Figure 6-15 could change for other temperatures and water vapor distributions and temperature errors in other layers.

It was found similarly unprofitable to perturb the water vapor concentration at each atmospheric layer in order to be able to statistically combine errors and to obtain an estimate of the expected signal uncertainty. This approach was abandoned in favor of changing the entire profile, whether temperature or water vapor, so that the instrument signal uncertainties can be maximally bounded. It appears reasonable that the uncertainties determined in this manner are maximum with respect to random errors in temperature and water vapor profile and one might reasonably expect the actual expected signal uncertainties to be less for truly random errors.

REFERENCES

1. Accuracy of Radiosonde Temperature and Pressure-Height Determination, R. W. Lenhard, Bulletin of the American Meteorological Society 51 No. 9, 1970.
2. Mesocale Temperature Changes in the Supersonic Transport Climb Region, Carl W. Kreitzberg, J. of Applied Meteorology 6, Oct. 1967.
3. An Operational Objective Analysis System, George P. Cressman, Monthly Weather Review 87 No. 10, Oct. 1959.

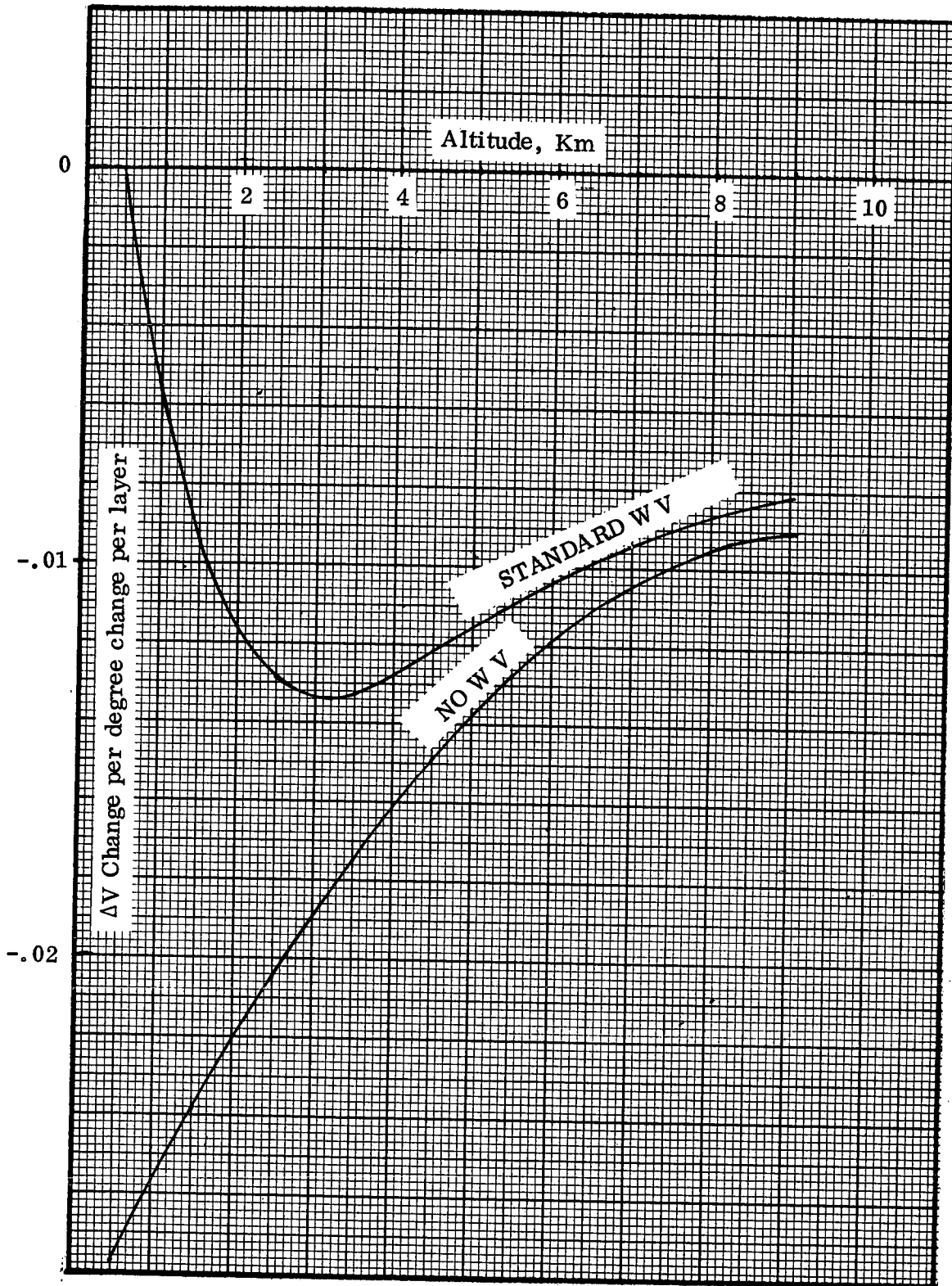


Figure 6-15. Signal difference change per degree change per layer vs. altitude for no water and with water (Gutnick) for CO concentration of 0.2 ppm and ground temp. = 300K.

4. NIMBUS 3 SIRS Pressure Height Profiles as Compared to Radiosondes, C. M. Hayden, Monthly Weather Review 99 No. 9 Sept. 1971.
5. A Regression Method for Obtaining Real-Time Temperature and Geopotential Height Profiles from Satellite Spectrometer Measurements and its Application to NIMBUS 3 SIRS Observations, W. L. Smith, H. M. Woolf and W. J. Jacob, Monthly Weather Review 98, No. 8, August 1970.
6. Retrieval of Atmospheric Temperature Profiles from Satellite Measurements for Dynamical Forecasting, W. L. Smith, H. M. Woolf and H. E. Fleming, J. Applied Meteorology, February 1972.
7. Global Sea-Surface Temperature Distribution Determined from an Environmental Satellite, P. Krishna Rao, W. L. Smith, and R. Koffler, Monthly Weather Review 100 No. 1, January 1972.
8. Vertical Distribution of Atmospheric Water Vapor from Satellite Infrared Spectrometer Measurements, W. L. Smith and H. B. Howell, J. of Applied Meteorology 10, No. 5, October 1971.
9. Estimation of the Effect of Partial Cloud Cover on the Radiation Received by the NIMBUS HRIR, Fred M. Vukovich, Monthly Weather Review 99, No. 11, November 1971.